INVESTIGATION ON THE FEASIBILITY OF TRIFLUOROIODOMETHANE (CF₃I) FOR APPLICATION IN GAS-INSULATED LINES

Lujia Chen

Advanced High Voltage Engineering Research Centre

Cardiff University

A thesis submitted for the degree of

Doctor of Philosophy

July, 2015

DECLARATION

This work has not been submitted in substance for any other degree or award at this or any other university or place of learning, nor is being submitted concurrently in candidature for any degree or other award.

Signed ………………………………………… (Candidate)   Date …………………………

STATEMENT 1

This thesis is being submitted in partial fulfilment of the requirements for the degree of PhD.

Signed ………………………………………… (Candidate)   Date …………………………

STATEMENT 2

This thesis is the result of my own independent work/investigation, except where otherwise stated.
Other sources are acknowledged by explicit references. The views expressed are my own.

Signed ………………………………………… (Candidate)   Date …………………………

STATEMENT 3

I hereby give consent for my thesis, if accepted, to be available for photocopying and for inter-library loan, and for the title and summary to be made available to outside organisations.

Signed ………………………………………… (Candidate)   Date …………………………

ACKNOWLEDGEMENTS

PUBLICATIONS

L. Chen, M. S. Kamarudin, K. H. Elnaddab, A. Haddad, H. Griffiths, "Gas Insulated Transmission Line using CF_3I-CO_2 Gas Mixture", *6th Universities High Voltage Network*, Glasgow (UK), 2013.

M. S. Kamarudin, L. Chen, P. Widger, K. H. Elnaddab, M. Albano, H. Griffiths, and A. Haddad, "CF_3I Gas and its Mixtures: Potential for Electrical Insulation", *CIGRE Session 45*, D1-308, Paris (France), 2014.

L. Chen, P. Widger, C. Tateyama, A. Kumada, H. Griffiths, K. Hidaka and A. Haddad, "Breakdown Characteristics of CF_3I/CO_2 Gas Mixtures under Fast Impulse in Rod-plane and GIS Geometries", *19th International Symposium on High Voltage Engineering*, 547, Pilsen (Czech Republic), 2015.

L. Chen, P. Widger, M. S. Kamarudin, H. Griffiths, A. Haddad, "Potential of CF_3I/CO_2 Gas Mixture in Gas-Insulated Equipment", *IEEE Conference on Electrical Insulation and Dielectric Phenomena*, Michigan (USA), 2015.

L. Chen, M. S. Kamarudin, H. Griffiths, A. Haddad, "Breakdown of CF_3I Gas and its Mixtures under Lightning Impulse in Coaxial-GIL Geometry", *IEEE Transactions on Dielectrics and Electrical Insulation* (Under Review).

SUMMARY

It is widely acknowledged that the world needs to reduce the level of greenhouse gas emissions. It is proposed to use potentially cleaner renewable energy sources to replace fossil fuels, and thus reduce greenhouse gas emissions. A significant challenge facing renewable energy sources, however, is that the power generation facilities are often located far from the load centres, meaning that new high capacity long-distance transmission systems would need to be built. This is a particular issue since there are increasing difficulties in obtaining approval to construct new overhead lines (OHL). An alternative is gas-insulated lines (GIL), a system for the transmission of electricity over long distance and is considered as a viable technical solution in places where OHL cannot be constructed. The currently adopted gas medium in GIL, however, is sulphur hexafluoride (SF_6), which is a potent greenhouse gas. Trifluoroiodomethane (CF_3I) has been proposed as an alternative insulation medium to SF_6 in GIL, and this thesis investigates the potential of using a CF_3I gas mixture in GIL applications. It is hoped that the research can lead to a new form of environmentally friendly power transmission system that could cope with the increasing power demand in large metropolitan areas, and contribute to the reduction of SF_6 usage in the high-voltage industry.

The literature survey reviewed the research work on CF_3I gas and its mixtures to date. Several research gaps were identified, and these informed the investigations carried out in this research. Reduced-scale coaxial test systems with the electric field properties of a full-scale 400 kV GIL were designed, developed and fabricated. The designs were simulated using COMSOL to ensure that the highest field would be along the centre of the conductor. The effective ionisation coefficients of various CF_3I gas mixtures were calculated using BOLSIG+, which provided estimated values for the critical reduced field strength of each gas mixture.

Extensive laboratory tests using a standard lightning impulse (1.2/50) were conducted on the fabricated prototypes using various CF_3I/CO_2 and CF_3I/N_2 gas mixtures to determine the 50% breakdown voltage. The breakdown characteristics of CF_3I gas mixtures were examined for pressure, geometric ratio, impulse polarity, buffer gas and mixture content. Based on the measured breakdown voltage and calculated critical reduced field strength of various CF_3I gas mixtures, a two-stage streamer/leader mathematical model was developed to evaluate the reduction in field strength at higher pressures.

A comparative study was carried out on CF_3I gas mixtures in a rod-plane electrode configuration under standard lightning impulse and steep-front square impulse waveforms. This investigation focused on the V-t characteristics of CF_3I gas mixtures in this particular configuration. A phase equilibrium experiment was also carried out to determine the boiling point of various CF_3I gas mixtures.

CONTENTS

LIST OF FIGURES

LIST OF TABLES

LIST OF ABBREVIATIONS

CF_3I	Trifluoroiodomethane
SF_6	Sulphur hexafluoride
CO_2	Carbon dioxide
N_2	Nitrogen
GIL	Gas-insulated lines
GIS	Gas-insulated switchgear
HV	High-voltage
GWP	Global warming potential
ODP	Ozone depletion potential
LI	Lightning impulse
U_{50}	50% breakdown voltage
U_b	Measured breakdown voltage
U_S	Streamer breakdown voltage
U_L	Leader breakdown voltage
E/p	Pressure-reduced electric field to the corresponding $(\alpha - \eta)$ value
$(E/p)_{crit}$	Critical reduced field strength when $(\alpha - \eta) = 0$
$(E_{max}/p)_B$	Pressure-reduced maximum breakdown field strength
E_L	Leader propagating field
C_S	Radial streamer radius
MPa	MegaPascal
bar	Metric unit of pressure exactly equal to 100,000 Pascal
GC-MS	Gas chromatography mass spectrometry

1 INTRODUCTION

1.1 Gas-Insulated Lines: Role and Problems

In response to the Kyoto Protocol on climate change, governments worldwide have set ambitious targets to reduce greenhouse gas emissions. In high-voltage equipment, such as gas-insulated switchgear (GIS) and gas-insulated lines (GIL), sulphur hexafluoride (SF_6) is the most commonly used dielectric gas medium. This is because SF_6 is chemically stable with a high arc interruption capability and a dielectric strength three times that of air at atmospheric pressure [1]. SF_6, however, is one of the six restricted greenhouse gases identified by the Kyoto Protocol due to the fact that its global warming potential (GWP), for a given time horizon of 100 years, is 23,900 times that of CO_2 [2]. Identifying alternatives to SF_6 for application in high-voltage gas-insulated equipment remains a tantalising problem for researchers. There are gases that exhibit a higher dielectric strength than SF_6, but they all possess at least one negative characteristic, such as a high boiling point, high GWP, low dielectric strength, harmful by-products or voltage-withstand limitations.

An emerging candidate is trifluoroiodomethane (CF_3I), a gas that is chemically inert and nonflammable; and more importantly, has a dielectric strength that is 1.2 times higher than that of SF_6. The weak chemical bond C-I in CF_3I means that it can be decomposed quickly in the atmosphere, which is one of the reasons that CF_3I possesses a GWP of less than 1 over 100 years [3]. This gas was proposed initially by the researchers from Tokyo University as an alternative to SF_6 gas in high-voltage gas-insulated equipment [4]. CF_3I

does have limitations, however, including a high boiling temperature, and the fact that it has to be used in low proportions as part of a binary mixture with CO_2 or N_2 to reduce the overall liquefaction temperature.

Increasing power demands in large metropolitan areas, combined with the fact that new exploitable energy sources are often situated far from load centres, has led to the need for new high capacity transmission systems. The construction of new overhead lines (OHL) introduces challenges in terms of routing and public acceptance. There is, therefore, an interest in developing an affordable alternative transmission technology that has less visual impact whilst being more ecofriendly [5]. The distance over which power may be transferred using traditional AC cables is limited, since there is a need to supply large capacitive charging currents. Furthermore, there is an environmental cost for the materials used to construct the cable. In comparison, GIL have a much lower capacitance and the ability to transfer large amounts of power over longer distances than is possible with AC cables. If CF_3I could be implemented as a replacement to SF_6 in GIL and the cost of GIL were to decrease significantly as the technology matures. There is, therefore, potential for a new form of environmentally friendly power transmission system in the future.

1.2   Aims of the Research Work

This project aims to address a challenging objective related to the future needs of transmission networks. To develop an environmentally friendly GIL for a voltage rating of 400 kV, extensive testing and optimisation would be required before the proposed solution could be deployed in industry. In this study, fundamental research investigations on the properties of CF_3I gas and its mixtures are carried out to analyse the feasibility of using such gases as alternatives to SF_6. There are two main types of work: (i) the gas

analysis of CF$_3$I, which is to evaluate the feasibility of CF$_3$I based on the insulation strength and boiling point of CF$_3$I gas mixtures, and (ii) breakdown tests on CF$_3$I gas mixtures for electrode configurations of varying degrees of field uniformity; this includes fabrication of a reduced-scale coaxial test system due to the high costs of building a full-scale 400 kV GIL test system.

The CF$_3$I-GIL project has a wider significance, since the new gas medium will reduce the environmental impact of all gas-insulated equipment that is currently insulated using SF$_6$ gas. This will open up the prospect of new equipment designs that adopt CF$_3$I as an insulation medium in gas-insulated equipment. GIL, as an emerging transmission technology, may play an integral part in future electrical networks with a low environmental impact. GIL allow large power transmission over long distances (>100 km) without the need for reactive compensation [6], making it potentially suitable for long distance power transmission connecting offshore wind farms to metropolitan areas. The simple functionality and low maintenance level of GIL offer a competitive alternative to HVDC cables for connecting offshore wind farms.

The research programme undertaken for this study is extensive and wide-ranging, with tasks including the design, development and fabrication of prototypes, and simulation modelling. Different types of experimental investigations were also carried out for various CF$_3$I gas mixtures, including lightning impulse breakdown tests to determine their insulation strength, and experiments to determine the conditions that cause liquefaction of various CF$_3$I gas mixtures.

The main aims of this research work are to:

- Develop a reliable test rig for CF_3I gas research which consists of a pressure vessel, gas extraction unit and lightning impulse test setup for the generation and measurement of lightning impulse voltage waveforms.

- Determine the limiting field strength of various CF_3I gas mixtures through the use of BOLSIG+ software which derives the electron swarm parameters. The calculated data would assist the author in choosing the test gas mixture ratio.

- Devise an experiment to measure the boiling points of various CF_3I/CO_2 and CF_3I/N_2 gas mixtures. This will provide fundamental knowledge for the experiments carried out at higher gas pressures to avoid liquefaction. It could also be used as a guideline for future applications of GIL.

- Design, develop and fabricate a reduced-scale coaxial test system that has an electric field distribution similar to that of a full-scale 400 kV GIL. The test system would then be used to provide fundamental knowledge on the breakdown performance of CF_3I gas mixtures under lightning impulses in quasi-uniform field gaps.

- Perform the simulation modelling required to identify high electric field stress regions within the design of the scaled geometry. This will ensure a better understanding of the electric field distribution within the geometry.

- Conduct experimental work on electrode configurations that represent uniform, quasi-uniform and non-uniform field gaps under lightning impulses. The breakdown characteristics are determined by the measurement of 50% breakdown voltage (U_{50}) and voltage-time (V-t) characteristics. The experimental investigation on quasi-uniform field gaps is of greater interest as the field distribution is similar to that of a practical GIL system. The results would

provide an early indication on the feasibility of using CF_3I gas mixtures in GIL applications.

- Perform a comparative study between the standard lightning impulse and steep-front square impulse waveforms for non-uniform field gaps. The use of a steep-front square impulse generator with a rise time of 16 ns enables the V-t characteristics of CF_3I gas mixtures to be surveyed in the nanosecond range.

- Develop a modelling technique that can correlate the critical field strength of each CF_3I gas mixture to the measured breakdown voltage. The breakdown voltage of a gas mixture will change based on factors such as geometry size. The ultimate aim is to use a mathematical model as a means of predicting the breakdown voltage for different coaxial geometries without having to carry out any experimental work.

1.3   Contribution of the Thesis

The main contributions of the present work can be summarised as follows:

- A test rig was developed to perform breakdown testing on CF_3I gas mixtures.

- Reduced-scale coaxial test systems were designed, developed and fabricated.

- Phase equilibrium experiments were conducted to examine the boiling point of CF_3I gas mixtures; this provides a temperature vs pressure plot for gas mixtures with different CF_3I contents, which determines the conditions needed to avoid liquefaction in pressurised gas-insulated equipment using CF_3I gas mixtures.

- A comparative study was carried out on the rod-plane electrode configuration for both steep-front square impulse and standard lightning impulse waveforms.

- A novel experimental investigation was conducted on the breakdown performance of CF_3I gas mixtures in a reduced-scale coaxial test system.

- The calculated E/p values of CF_3I gas mixtures obtained from BOLSIG+ were related to the experimental results for the plane-plane electrode configuration. The comparison shows good agreement between both sets of results. For the coaxial configuration, the experimental values of pressure-reduced maximum breakdown field strength, $(E_{max}/p)_B$ were shown to become saturated towards the $(E/p)_{crit}$ of the gas mixture for positive impulse polarity. The breakdowns for negative impulse polarity drop below the $(E/p)_{crit}$ at a much lower gas pressure.

- A streamer/leader breakdown model was developed based on the measured breakdown results of coaxial GIL geometry for various CF_3I/CO_2 and CF_3I/N_2 gas mixtures and for positive lightning impulses. The breakdown model is able to explain the drop in potential for the measured breakdown voltage at higher gap distances and pressures. More experimental and calculation work is required to develop this model further. It is expected that this model can be used to predict the breakdown voltage for any coaxial geometry up to the maximum operating pressures of full-scale GIL at all rated voltage levels.

1.4   Outline of the Thesis

In the present work, reduced-scale coaxial GIL test systems were fabricated to determine the insulation strength of CF_3I gas mixtures in quasi-uniform field gaps.

The structure of this thesis is as follows:

Chapter 2 – Gas-Insulated Lines and Potential of CF₃I as a Replacement Gas for SF₆: A Review

This chapter reviews the development of GIL and the advantages of this solution in comparison to other transmission technologies, such as OHL and cross-linked

polyethylene (XLPE) cables. The published literature on the potential of CF_3I gas and its mixtures to replace SF_6 is presented; focusing on the potential of CF_3I as an insulation medium for GIL applications.

Chapter 3 – Laboratory Test Equipment and Experimental Techniques

This chapter describes the test equipment and the test methods that were applied for the experiments. Two different test setups were used for the experimental characterisation of CF_3I mixtures. The breakdown characteristics of CF_3I gas mixtures were experimentally investigated using (i) a standard lightning impulse waveform of 1.2/50 and (ii) a steep-front square impulse waveform with a rise time of 16 ns. For the investigation, up-down and multi-level test methods were applied in accordance to international standards.

Chapter 4 – Design and Construction of a Reduced Scale Coaxial GIL

This chapter offers a description of the design and development process of the coaxial-GIL prototypes. Combinations of computer modelling (using COMSOL software) and preliminary testing on a trial prototype were carried out to identify the weaknesses of the design. Based on the findings, modifications were implemented on the prototype for fabrication, which then made possible the experimental investigation of CF_3I gas mixtures as an insulation medium.

Chapter 5 – Field Strength Analysis and Phase Equilibrium Experiment of CF_3I Gas Mixtures

Two types of gas analysis investigations were conducted on CF_3I gas mixtures: (a) the critical reduced field strength, $(E/p)_{crit}$, of CF_3I gas and its mixtures was calculated and compared to SF_6 using the Boltzmann analysis. (b) A phase equilibrium experiment was

also carried out to determine the boiling point of CF_3I gas mixtures as part of a research visit to the Chinese Academy of Sciences in Beijing, China.

Chapter 6 – Breakdown Characteristics of CF₃I Gas Mixtures in Coaxial GIL Geometry

Results for coaxial GIL geometry were obtained from lightning impulse breakdown tests using various CF_3I gas mixtures. The tests were carried out using the up-down method to obtain the measured 50% breakdown voltage, U_{50}. The U_{50} was then converted into pressure-reduced critical field strength, E/p, as a comparison to $(E/p)_{crit}$ of the gas mixture calculated from BOLSIG+ and the practical values obtained from the literature. A two-stage streamer and leader breakdown model was also developed to evaluate and explain the breakdown voltage increasing but at decreasing rate at higher gas pressures.

Chapter 7 – Breakdown Characteristics of CF₃I Gas Mixtures in Uniform and Non-uniform Geometries

This chapter describes the work carried out in collaboration with Tokyo University to investigate the breakdown characteristics of a 30/70% CF_3I/CO_2 gas mixture for a rod-plane electrode configuration. Furthermore, a plane-plane electrode configuration was chosen to represent a uniform field distribution, and this was also tested under lightning impulse voltages.

Chapter 8 – Conclusion and Future Work

This chapter provides the conclusion of the work carried out for this PhD thesis and proposes potential project ideas for continuing research work in the future.

2 GAS-INSULATED LINES AND POTENTIAL OF CF₃I AS A REPLACEMENT GAS FOR SF₆: A REVIEW

2.1   Introduction

Gas-insulated lines (GIL) utilise gas insulation technology for large bulk-power transmission at ultra-high voltage level. The physical structure of a GIL system consists of tubular aluminium conductors encased in a metallic tube that is filled with either SF_6 or an SF_6/N_2 gas mixture as the insulation medium. SF_6, however, is a potent greenhouse gas with a global warming potential (GWP) that is 23,900 times that of CO_2 and an atmospheric lifetime estimated to be of the order of thousands of years [2]. The impact of global warming and the dwindling supply of fossil fuels are affecting the current structure of electric power generation. Renewable energy sources, such as solar, hydropower, geothermal and onshore and offshore wind, are located far from the load centres. In this context, the inevitably increased need for overhead lines (OHL) is problematic, as described in Chapter 1. GIL offer the potential for efficient, long-distance high-power networks to link the generation facilities to the load centres, and the key challenge now is to find a more environmentally friendly gas to replace SF_6.

This chapter provides a review of GIL as a transmission technology. It explores the various features and benefits of GIL technology and compares it with established transmission systems like OHL and cross-linked polyethylene (XLPE) cables. The properties and applications of SF_6 are examined to explain why SF_6 is the most widely

used gas medium in high-voltage gas-insulated equipment and its limitations. Following research into alternative gases to SF_6, CF_3I gas has been proposed as a viable alternative insulation medium. A comprehensive literature review of the properties of CF_3I gas has already been undertaken in two previous PhD theses at Cardiff University [7], [8]. In this thesis, a comparative review was carried out between SF_6 and CF_3I gas and its mixtures. From the review, research gaps such as fast transient study and liquefaction conditions of CF_3I gas mixtures were identified that are relevant to the research programme. Several key factors, for example, the fundamental properties and breakdown characteristics for SF_6, CF_3I gas and its mixtures, were reviewed.

2.2   Review of GIL Technology

2.2.1   Main Features and Benefits of GIL

As can be seen in Figure 2.1, GIL are essentially made of two concentric aluminium pipes in a coaxial cylindrical electrode arrangement with a similar design structure to the bus line of a gas-insulated switchgear (GIS); the main difference being that GIL can be used over longer distances and have a much larger transmission capacity.
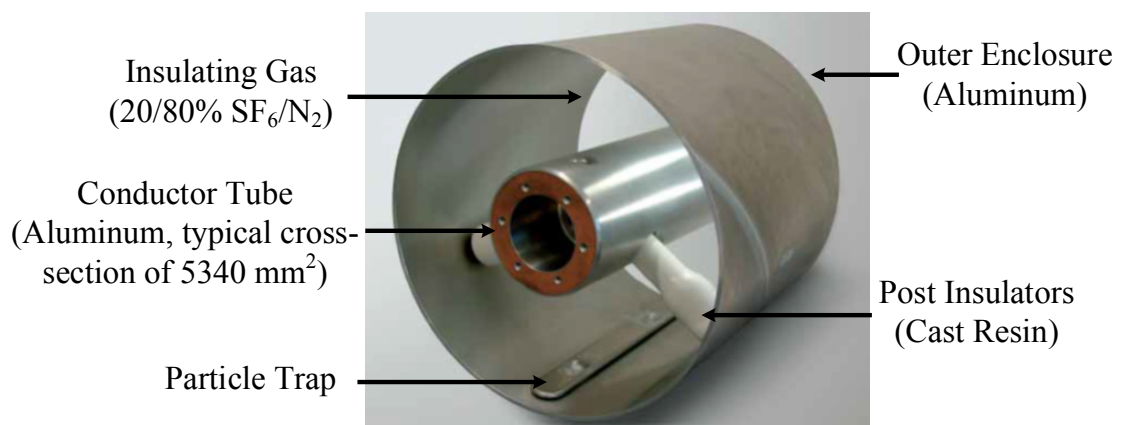
Figure 2.1: Cross-section through a second-generation GIL showing conductor, enclosure, post insulators and particle trap [9].

The established transmission systems, like OHL and AC cables, cannot offer an optimised network of long-distance and high-power transmission. Despite the significant progress in materials, there are still limitations in the power transfer capability of cables and the add-on environmental impact of their materials. More importantly, solid insulation in cables is non-recoverable after breakdown. New OHL projects have found it very difficult to obtain construction approval due to public objections. This has generated interest in the deployment of GIL, a system that has a similar transmission capability to OHL, with a high operational reliability and less visual impact on the environment.

The advantages of using GIL are as follows [5], [9]–[20]:

(i)　　　High Reliability and Long Operational Lifetimes

The sole functionality of GIL is power transmission, with no requirement for a switching/interruption operation. GIL are enclosed within a metallic outer casing, which protects the inner line conductor from the external impact of the surrounding environment. So far, over 200 km of single-phase GIL have been constructed and are in operation, with the first GIL application still operational after nearly 40 years. Thus, GIL technology has proven to be a highly reliable system with no major system failure recorded.

(ii)　　　Lower Transmission Losses

A comparison of the transmission losses is made for 400 kV transmission systems including OHL, cables and GIL. The GIL system has the lowest electrical losses as can be seen in Figure 2.2. As GIL have low resistive losses due to the large cross-section of the conductor and enclosure tubes. The low capacitance in GIL means that no reactive compensation is needed for a distance of up to 100 km [11]. The dielectric losses through insulation medium in GIL are also negligible.

11
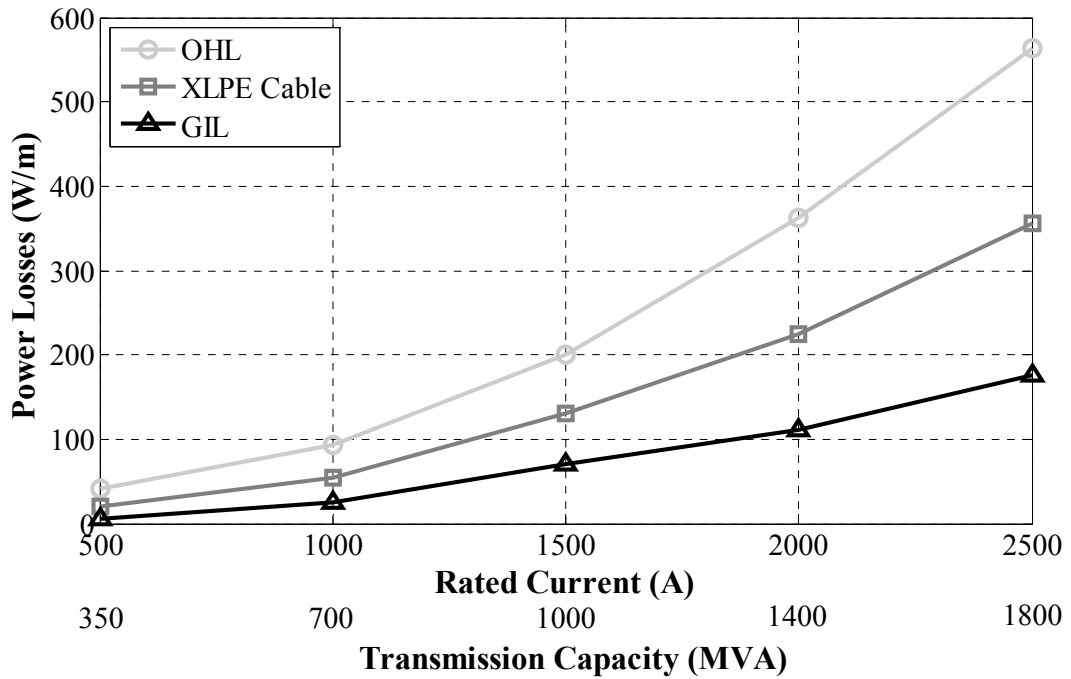
Figure 2.2: Comparison of transmission losses between OHL, XLPE cable and GIL systems [11].

(iii)   High Power Transmission Capability

GIL have a high power transmission capacity of up to 3000 MVA per phase system at a 550 kV rated voltage, which is comparable to that of OHL [11], [15]. Due to the compact structure of GIL, a smaller footprint is required in comparison to OHL. GIL can also be directly buried underground.

(iv)   Nonflammability and High Safety Level

The enclosures and conductors of GIL are made of metal, which can dissipate more heat than an XLPE cable, which is covered by plastic layers. The outer enclosure is solidly grounded with no direct access to the high-voltage conductor, once it is pressurised. As there are no flammable materials, such as oil, GIL are considered to be fireproof [9], [17]. Even in the case of a catastrophic failure in the form of an internal arc, test results have shown that the metallic enclosure has been able to contain the arcing with no damage

observed on the outer enclosure. This allows GIL to be installed in public infrastructures like road and railway tunnels [13].

(v)   Resistance to Ageing

A stable gas medium does not degrade, as gas molecules move around freely, which prevents the accumulation of electrical charges at any location. Solid insulators in GIL are made of cast resin, and the maximum temperature limit of this material is between 105 and 120 °C, so the maximum operating temperature of GIL is designed to be well below this limit. Electrical ageing normally starts when the electric field strength is above 30 to 50 kV/mm, depending on the materials. The dielectric dimensioning of GIL relies on gas insulation, which has a factor 3–4 times lower than the values of the insulators [11], [21]. Therefore, the operating conditions of GIL are too low for any significant electrical or thermal ageing to commence.

(vi)   Electromagnetic Field and Routing Flexibility

The design of GIL achieves low inductive current, since the current in the conductor will induce a reverse current in the enclosure of the same magnitude but with a 180° phase shift. The superposition of both electromagnetic fields is close to zero. GIL are made of an aluminium alloy, which is a malleable material. This makes GIL suitable for complex routing options and flexible for planning new transmission networks close to hospitals and airport control centres, where there are strict regulations on electromagnetic field limitations. Figure 2.3 shows a comparison of magnetic fields in microtesla (μT) for OHL, GIL and cable. The type of OHL is standard in Germany using a bundle of four wires of 240 mm^2 of aluminium and 40 mm^2 of steel (4 × 240/40 Al/St). The field was measured below the lines at 1 m above ground level. The chosen GIL system has a

conductor/enclosure diameter of 180/520 mm and the XLPE cables are used as cross-bonded installations for a 400 kV double system; the GIL and the cable were laid underground at a depth of 2 m and field measurements were taken at 1 m above ground.
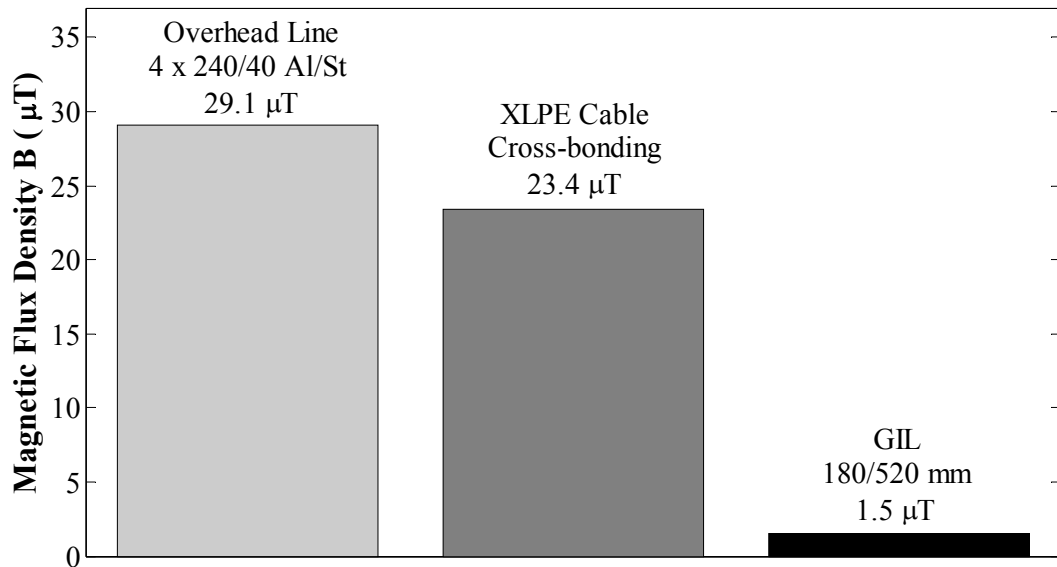
Figure 2.3: A comparison of the magnetic fields for different high-voltage transmission systems [20].

2.2.2   Development of GIL

(i)   First-generation GIL

The first-generation of GIL were filled with 100% SF$_6$ gas, and were then welded or flanged. The construction of the first installation of GIL was in 1975 at the cavern hydropower plant of the "Schluchseewerke" in the Black Forest in Germany at a voltage level of 420 kV. This was the result of a major failure to the oil cable in the pumping storage power plant at Schluchseewerke, which caused significant damage not only to the cable but also to the tunnel. Unlike oil, GIL are nonflammable, as mentioned in Section 2.2.1. The power plant adopted the GIL solution to connect the high-voltage transformers at 420 kV to the OHL through a 700 m tunnel. Figure 2.4 shows the setup of the GIL as part of the Schluchsee hydropower plant. A transformer with a power capacity of 600 MVA (1) is located in the cavern. The GIL connection (4) links the

transformer and the power generator. Gas-insulated surge arresters (2) are used to limit the overvoltage from the generator side, and open-air surge arresters (5) are used to protect the GIL from overvoltage coming from the overhead line (6).
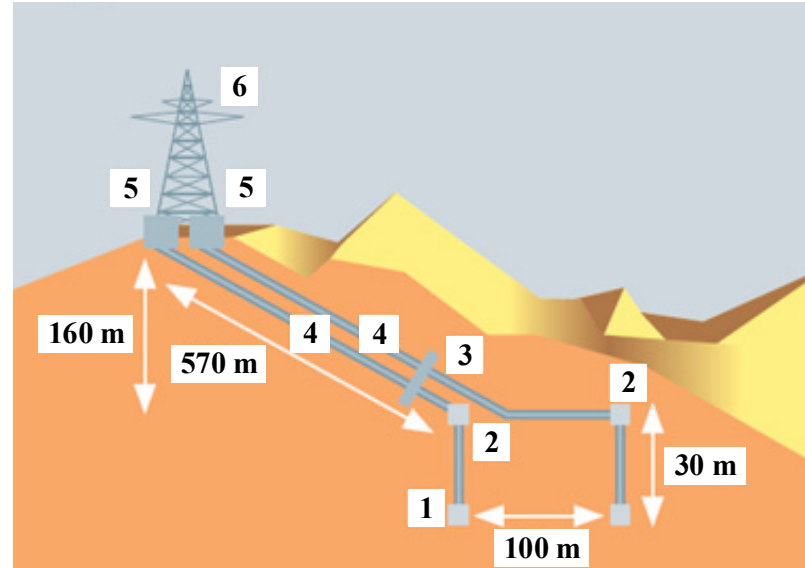
(1) 600 MVA transformer
(2) Encapsulated surge arresters
(3) Transfer switching units
(4) GIL connection
(5) Open-air surge arrester
(6) Overhead line

Figure 2.4: Principle setup of the GIL connection in Schluchsee power plant [17].

Table 2.1 shows the technical data for the GIL in the Schluchsee project. As this was the first application of GIL worldwide, the test voltages for lightning impulse, switching impulse, and power frequency were set at much higher values compared to today's level for a 400 kV system. The GIL went into service at the Schluchsee power plant in 1975, and during a scheduled maintenance check in 2010, after 35 years, practically no ageing effects were detected [11]. This is consistent with the report by CIGRE WG 23.02 which states that there is no need to allow for ageing in gas-insulated systems [10].

Table 2.1: Technical data of the Schluchsee project, Germany [11].

Type	Project
Nominal voltage	380 kV
Nominal current	2000 A
Lightning impulse voltage	1640 kV
Switching impulse voltage	1200 kV
Power frequency voltage	750 kV
Rated short-time current	135 kA
Rated gas pressure	7 bar (abs.)
Insulating gas mixture	100% SF$_6$

(ii)   Second-generation GIL

The application of SF$_6$ in the high-voltage industry is not banned only because there is currently no suitable alternative. The environmental concerns of SF$_6$ combined with the high construction costs of first-generation GIL have led to research and development into second-generation GIL [14]. The proposed solution was to use SF$_6$ in a lower proportion as part of a binary gas mixture with N$_2$ gas (typically 20/80% SF$_6$/N$_2$). A new laying process and technology was also adopted to reduce the overall cost, making GIL a more economical solution for long-distance power transmission [22], [23]. The first application of second-generation GIL was for an international telecommunications exhibition held in Geneva (2003): an existing high-voltage OHL was replaced when building an extension to the Palexpo exhibition venue. The existing 220 kV line had to be laid underground for a length of about 420 m. GIL was chosen because of its low magnetic field and high transmission capacity, amongst other advantages (there was a magnetic field limitation in the exhibition area). The setup of GIL installed beneath the Palexpo exhibition hall is shown in Figure 2.5. The GIL sections were transported through the tunnel opening (1). The straight construction unit (2) was placed into the tunnel and was fixed by steel supports (6). The expansion joints (3) and sliding support structures (5) allowed the

thermal expansion of the structure. The disconnection unit (6) connected the GIL to the overhead line. The technical data for the Palexpo project can be seen in Table 2.2.

(1) Tunnel opening
(2) GIL straight construction unit
(3) Expansion joint
(4) Disconnection unit
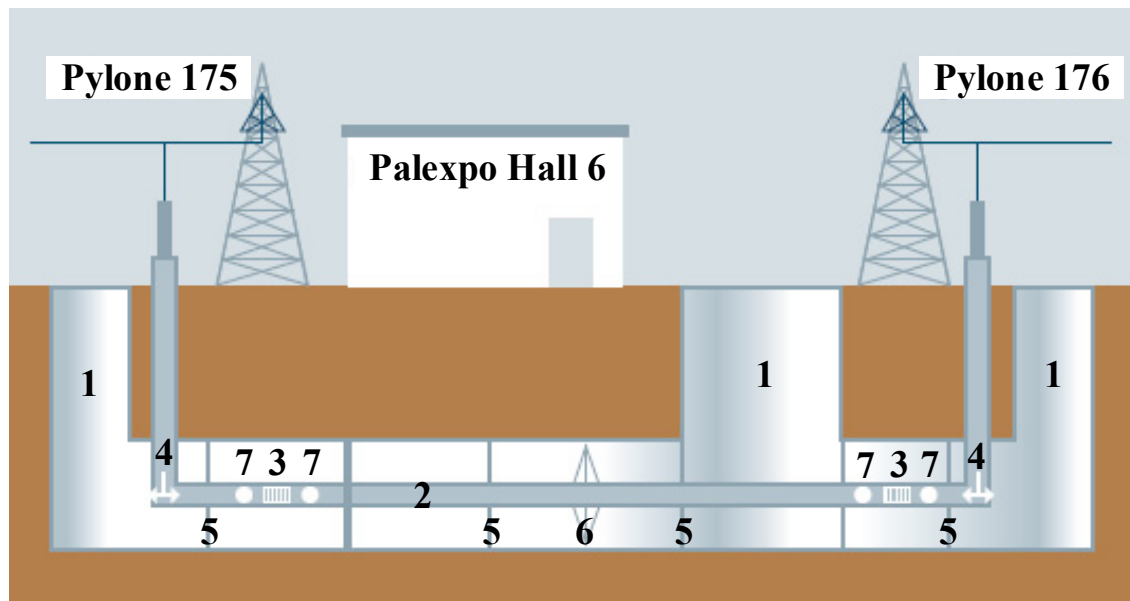
(5) Steel structure (sliding support)
(6) Steel structure (fixed support)
(7) Angle construction unit

Figure 2.5: Setup of GIL in an underground tunnel underneath the Palexpo exhibition hall, Geneva [17].

Table 2.2: Technical data for second-generation GIL [11].

Type	Project
Nominal voltage	300 kV
Nominal current	2000 A
Lightning impulse voltage	1050 kV
Switching impulse voltage	850 kV
Power frequency voltage	460 kV
Rated short-time current	50 kA/1 s
Rated gas pressure	7 bar (abs.)
Insulating gas mixture	20/80% SF_6/N_2

(iii)   Third-generation GIL

Based on the operational experience of GIS/GIL, SF$_6$ gas has proven to be an extremely useful insulating medium. Many studies, however, have shown that SF$_6$ has a high environmental impact that contributes to the greenhouse effect and global warming [2], [24]. For this reason, there has been research into alternative gases with a much lower environmental impact (discussed further in Section 2.4), and one of the emerging candidates is CF$_3$I and its gas mixtures. The aim of this PhD project is to carry out laboratory tests on CF$_3$I gas and its mixtures in order to determine their insulation performance, which, as planned, would lead to the construction of a trial CF$_3$I-GIL demonstrator. If successful, the new CF$_3$I-GIL would become a future generation environmentally friendly transmission system.

In general, GIL do not compete directly with OHL, but rather offer an alternative solution in places where OHL cannot or must not be constructed, for instance, in densely populated areas or environmentally sensitive locations. The very low external magnetic fields allow GIL to be installed in populated areas without violating the local magnetic field regulations. There is also no need for reactive compensation for a single phase distance of up to 100 km due to the very low capacitance of GIL [6], [11].

2.2.3   Worldwide GIL Applications and Laying Options

In this section, some of the typical GIL installation and laying methods are described, starting with the first GIL application at the Schluchsee power plant in the 1970s. Since then, GIL technology has been used successfully worldwide at different voltage levels ranging from 72 ~ 800 kV. Table 2.3 shows some examples of GIL applications across the globe.

Table 2.3: Typical examples on the engineering applications of GIL installation worldwide by AZZ CGIT [11], [16], [19], [25]–[27].

No.	Project Name	Location	Voltage Rating (kV)	Current Rating (A)	No. of Circuits	Phase Length (m)	Date of Order
1	Schluchsee Power Plant	Germany	420	2500	3	700	1975
2	Claireville Substation	Canada	242	3000	8	3480	1976
3	Joshua Falls Line Station	USA	145	2000	3	1638	1978
4	Rowville Substation	Australia	550	3000	1	940	1979
5	Revelstoke Hydro	Canada	550	4000	2	1830	1979
6	Guri Dam	Venezuela	800	1200	5	855	1981
7	Balsam Meadow	USA	242	1200	1	1239	1984
8	Seabrook Nuclear Station	USA	362	3000	3	245	1990
9	Substation 9002 / Power Plant 8	Saudi Arabia	550	1200	3	6800	1994
10	Shinmeika-Tokai	Japan	275	6300	2	3300	1998
11	Ling Ao Nuclear Station	China	550	2000	2	3008	1998
12	Palexpo	Switzerland	400	2000	1	420	2001
13	Hams Hall	UK	420	3150	2	1500	2005
14	Laxiwa Hydropower Station	China	800	4000	2	2928	2005
15	Kelsterbach Airport	Germany	420	2500	1	1000	2007
16	Xiluodu Hydropower Station	China	550	4500	1	12500	2013

Over 200 km phase lengths of GIL are installed worldwide, as shown in Table 2.4. It can be seen that the majority of the GIL installations are for a voltage rating between

362 ~ 550 kV. The phase length supplied by AZZ CGIT accounts for 50% of the world's total phase length of GIL installations, as shown in Table 2.4.

Table 2.4: GIL installations worldwide, status as at 2010 [11], [27].

Voltage Level (kV)	Phase Length by CGIT (km)	Percentage (%)	Phase Length by All Suppliers (km)	Percentage (%)
72/145/172	8542	5.6	38000	13.1
242/300	31024	20.3	33000	11.4
362/420	23173	15.2	125000	43.1
550	83975	55.0	90000	31.0
800	5153	3.4	3000	1.0
1200	768	0.5	1000	0.3
Total	152635	100	290000	100

Most of the laying options are developed in accordance with the requirements for specific situations at the time of construction. In some cases, GIL will be laid in a similar way to pipelines, i.e. laid underground with corrosion protection on the outside, and covered with soil. For applications like hydropower plants with large dams or tunnels inside a mountain where generators are located, GIL would be installed in tunnels. Such is the convenience provided by the flexibility of GIL that only minor changes need to be made to take account of mechanical and thermal stresses. GIL consist of metallic pipes and the physical specifications are fixed. Thus, over a long distance, a few support structures will be needed. The distance between the support structures is related to the pipe diameter and wall thickness, which provides the mechanical stiffness. Since the pipes are made of aluminium, a malleable metal, which can cover the curve of most landscape profiles, GIL technology has the flexibility to be implemented in densely populated or environmentally protected areas as a future solution for transmission networks. Here, three popular laying options, namely, above-ground, tunnel and directly buried installations, are described. It

is noteworthy to highlight that a thermal study is required for each individual design case. This is to avoid non-reversible dry-out of soil when temperature rises above the set limit.

(i)   Above-ground Installation

GIL can be installed above ground on steel structures in power plants or substations. This is a relatively trouble-free option, since GIL systems are unaffected by high ambient temperatures and intensive solar radiation. Corrosion protection is usually not necessary, since the aluminium enclosure pipe develops an oxide layer under atmospheric conditions, which protects the aluminium from corrosion. Those above-ground installations can be low and close to the ground or high enough to allow substation vehicles to pass under them [11], [15], [23].

(ii)   Tunnel Installation

For the tunnel-laying option, a trench is opened from the top and the tunnel segments, constructed using concrete, and would be laid in the open trench and covered with 1–2 m of soil. A tunnel will typically have two GIL systems laid inside, which is accessible for engineers to enter the tunnel and carry out maintenance work on the GIL systems. Natural convection of air in the tunnel allows the transport of heat to the surrounding tunnel walls and then into the soil. If the ventilation is not sufficient, forced ventilation can be introduced by installing a cooling system inside the tunnel [9], [11], [17].

(iii)   Buried Installation

This method is very similar to the pipeline laying method that is used for oil or gas pipelines. The pipeline laying method is a continuous process in an open trench, with the goal being to cover long distances as quickly as possible. Directly buried GIL offer an

economical and fast solution for installing cross-country transmission lines. GIL systems can be laid underneath the soil, thus causing only minor disruption to the local landscape. Once installation is complete, the land can be returned to its original agricultural use [11], [15], [23].

(iv)   Undersea Tunnel for Offshore Wind Farms

A project funded by the EU, "North Sea Network using GIL technology" in the subject area Trans European Energy Network (TEN-E) investigated the feasibility of connecting offshore wind farms using GIL in the North Sea. GIL have very low capacitance and high power capacity. It is the most suitable HVAC transmission method for connecting offshore wind farms [28]. For laying the GIL undersea, an additional pipe casing is used with the GIL positioned inside as a pipe-in-pipe-in-pipe system. A demonstration of such system is shown in Figure 2.6, recreated from [11].
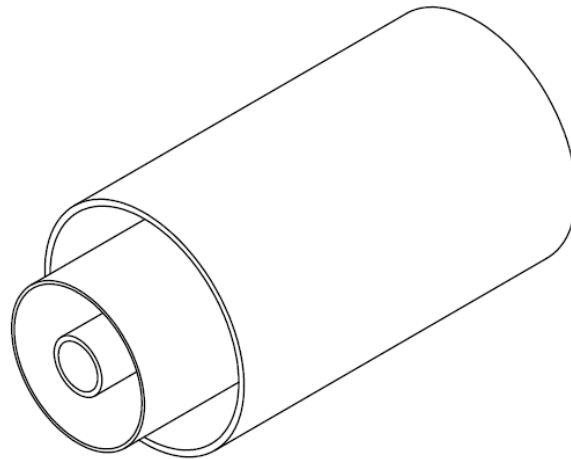
Figure 2.6: Pipe-in-pipe-in-pipe system for offshore applications [11].

2.2.4   Long Distance Power Transmission

It is worth highlighting that a single technology cannot cover every scenario for modern transmission networks. A choice needs to be made based on the suitability of the chosen technology. OHL is by far the cheapest transmission method for any length or capacity.

It also has the highest transmission losses, however, as was illustrated in Figure 2.2, and there is growing public objection to the construction of large pylon projects in metropolitan areas. The emergence of GIL technology offers an alternative underground solution that can transmit the same amount of power as the OHL. Several technical and economic issues need to be addressed in order for GIL to be successfully used for long-distance high-power transmission as part of a large transmission network for both onshore and offshore applications.

2.3   Comparison of the Properties of SF_6 and CF_3I Gases and their Mixtures

A review of the fundamental properties of SF_6 and the proposed replacement gas CF_3I and its mixtures are described in this section. The comparison shows similarities between the two gases and identified weaknesses of using CF_3I as an insulating medium. These, however, are research barriers that need to be overcome for any new proposed gas medium. It is the objective of this thesis to provide solutions to some of the identified weaknesses.

2.3.1   Physical and Chemical Properties

A comparison of the physical and chemical properties of CF_3I and SF_6 is presented in Table 2.5. It can be seen that both gases share a number of similar characteristics, in that they are both colourless and odourless and have slight solubility in water. Both SF_6 and CF_3I are much heavier than air (density $= 1.20$ kg/m³) in terms of density. SF_6 has a much lower boiling point than CF_3I. This means that SF_6 will be able to remain in its gaseous form at much higher gas pressures, which gives the insulating gas higher dielectric strengths. Every gas has a critical point which is defined by the corresponding critical

temperature and pressure. At and above this critical point, the distinction between gas and liquid disappears, which is referred to as the supercritical region. The solubility of a gas decreases as the temperature increases, and vice versa. Bond dissociation energy is the amount of energy required to break the existing bond between two atoms in the gaseous state. It can be seen from Table 2.5 that it requires more energy for an S-F bond to dissociate compared to the energy needed for a C-I bond to break up a single mole.

Table 2.5: Comparison of properties for SF_6 and CF_3I [3], [29]–[32].

Formula	SF_6	CF_3I
Molar mass (g/mole)	146	196
Boiling point at 1 atm (°C)	−63.8	−22.5
Appearance	Colourless gas	Colourless gas
Odour threshold	Odourless	Odourless
Solubility in water	Slight	Slight
Density[1] (kg/m^3)	6.07	8.14 (estimated)
Critical temperature (°C)	45.6	122 (estimated)
Critical pressure (MPa)	3.78	4.04 (estimated)
Bond dissociation energy (kJ/mole)	326	226

[1]Density calculated for absolute pressure of 101325 Pa and at room temperature of 20 °C.

When investigating suitable SF_6 alternatives, one of the key properties is the dielectric strength, which is controlled by parameters such as electron attachment, electron scattering and electron ionization [29]. Highly electronegative compounds containing halogen elements are favoured, therefore, since they can recombine quickly. Both SF_6 and CF_3I have strong electron affinity and able to produce free electrons to form stable negative ions. Due to the weak C-I bond of CF_3I, a succession of breakdown events is likely to produce by-products.

2.3.2   Environmental Impact

The environmental impact is generally based on two parameters: global warming potential (GWP) and ozone depletion potential (ODP). GWP is a relative measure to CO_2 of the heat absorption capability of a greenhouse gas in the atmosphere.

Table 2.6 shows the GWP for a given time horizon of 20, 100 and 500 years for CO_2, SF_6 and CF_3I gases obtained from existing IPCC reports [2], [24]. It can be seen that SF_6 has a very high GWP and a long atmospheric lifetime, making it an undesirable gas medium in high-voltage and other applications. In comparison, CF_3I has a very low GWP. This is helped by the weak C-I chemical bond in CF_3I, which decomposes quickly in the atmosphere [3]. It is noteworthy to highlight that CF_3I has a very short lifetime, and the GWP for such a gas may be subject to error, because gases are unlikely to be evenly distributed globally. Nevertheless, the GWP is still significantly lower than for SF_6, and is considered to be an environmentally friendly alternative.

Table 2.6: Global warming potential for CO_2, SF_6 and CF_3I [2], [24].

Chemical Formula	Life Time (years)	Radiative Efficiency (Wm^{-2} ppb^{-1})	Global Warming Potential for a Given Time Horizon (years)			
			SAR (100)[1]	20	100	500
CO_2	–	1.4×10^{-5}	1	1	1	1
SF_6	3200	0.52	23900	15100	22200	32400
CF_3I	0.005	0.23	–	1	1	<1

[1]SAR: second assessment report on climate change by IPCC

The ODP is the degradation that can be caused to the ozone layer by a greenhouse gas. Previous studies have reported ODP values of <0.008 [33], 0.006 [34] and 0.012 [35] for

CF₃I, which represents an extremely low ODP impact. This is because the C-I bond in CF₃I dissociates due to the absorption of sunlight and, once the released iodine reaches the lower troposphere, it will be removed through rainout. Nonetheless, a very small fraction of the iodine will reach the stratosphere and cause damage to the ozone layer, hence, the reported low ODP values for CF₃I gas. An opposing example would be CF₃Br, which absorbs sunlight less effectively and has a much longer atmospheric lifetime of around 60 years. Once CF₃Br reaches the stratosphere, the Br atoms are directly released and affect the ozone layer. It is interesting to note that iodine atoms are three to six times more potent than Br atoms at destroying ozone in the stratosphere [35], [36]. Considering that GIL are installed at the ground level, the leakage or release of CF₃I will be from the ground. Implementation of CF₃I gas in GIL applications should not, therefore, pose a significant threat to the ozone layer.

2.3.3   Boiling Point and Appropriate CF₃I Gas Mixture

The boiling temperature or the saturation vapour pressure of pure CF₃I gas was measured by Duan et al. [37], and an analytical correlation (2.1) was derived from the experimental data for the vapour pressure calculation of CF₃I.

$$\ln\left(\frac{P}{P_c}\right) = (A_1\tau + A_2\tau^{1.25} + A_3\tau^3 + A_4\tau^7)T_c/T \qquad (2.1)$$

where $\tau = 1 - T/T_c$, $A_1 = -7.19045$, $A_2 = 1.34829$, $A_3 = -1.58035$, $A_4 = -5.46680$, $T_c = 395.05$ K and $P_c = 3.8617$ MPa.

The parameters of (2.1) were provided by [37], and the boiling temperature curve for a pressure range of 1 to 10 bar for CF₃I, CO₂ and SF₆ was plotted, as shown in Figure 2.7. As the pressure of a gas increases, the dielectric strength also increases. Based on operational experiences of gas-insulated systems, high reliability is found in the range of

26

4 to 8 bar for insulating gas pressures. There is only a small improvement in insulation capability above 8 bar. It is also noteworthy that a vessel pressurised above 8 bar is no longer considered to be a low-pressure vessel, which requires a more difficult and costly design approach [11]. However, liquefaction of CF₃I gas occurs above 4 bar and at room temperature (293 K). As a result, CF₃I has to be used in a smaller proportion as part of a binary gas mixture with CO_2 or N_2.
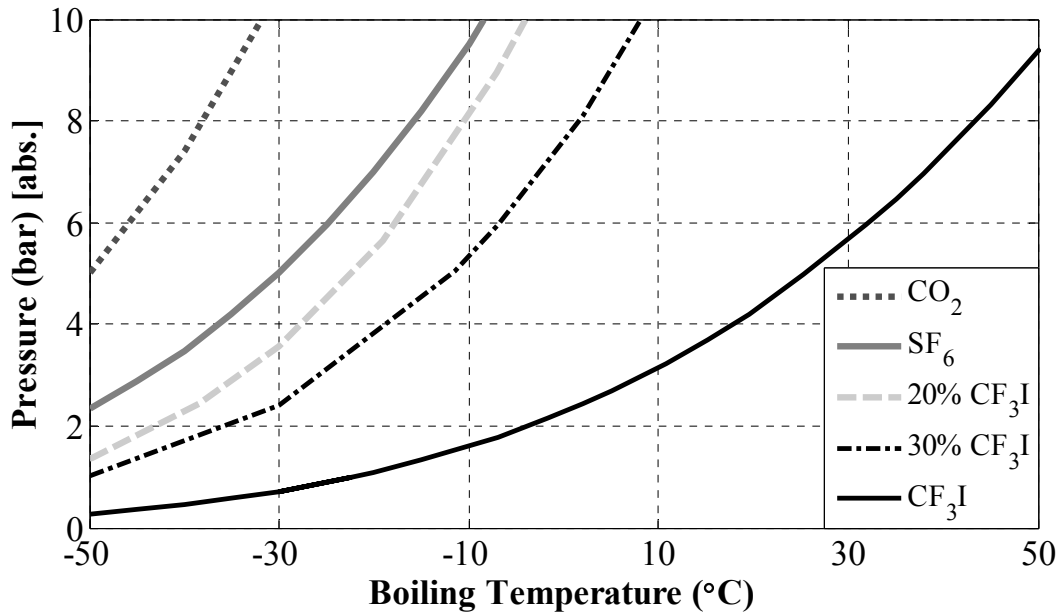
Figure 2.7: Saturation vapour pressure curves for SF₆, CF₃I, CO₂, 20% and 30% CF₃I content [38].

Currently, no measured data are available on the boiling temperature of CF₃I gas mixtures. In [39], the author suggested that the boiling temperature of the partial pressure of CF₃I gas can be calculated based on the van der Waals equation for partial pressure, as expressed in (2.2) and (2.3).

$$\left(kP_m + \frac{a}{V^2}\right)(V - b) = RT_m \tag{2.2}$$

$$\left(kP_0 + \frac{a}{V^2}\right)(V - b) = RT_0 \tag{2.3}$$

The T_0 and P_0 are assumed to be the primary temperature and pressure of the gas mixture, T_m and P_m are the temperature and pressure at liquefaction, R is the molar gas constant,

and *a* and *b* are the van der Waals constants, which for CF$_3$I, a = 1.1967 Pa·(m^3/mol)^2 and

b = 1.0626·10^{-4} m^3/mol. By solving Equations (2.1), (2.2) and (2.3) using Matlab software,

the boiling temperature of various proportions of CF$_3$I of total gas mixture was calculated

for a pressure range of 1 to 10 bar (abs.), as can be seen in Figure 2.8 [39].

This calculation method assumes that the buffer gas, for example, N$_2$ and CO$_2$, behaves

like an ideal gas. This assumption may be valid for N$_2$ gas, since there is a large difference

in the boiling temperature compared to CF$_3$I. However, there is more uncertainty

regarding the calculated results for the CF$_3$I/CO$_2$ gas mixture since this has a boiling

temperature much closer to that of CF$_3$I. It is, therefore, important to measure the boiling

temperature of CF$_3$I/CO$_2$ and CF$_3$I/N$_2$ gas mixtures experimentally.
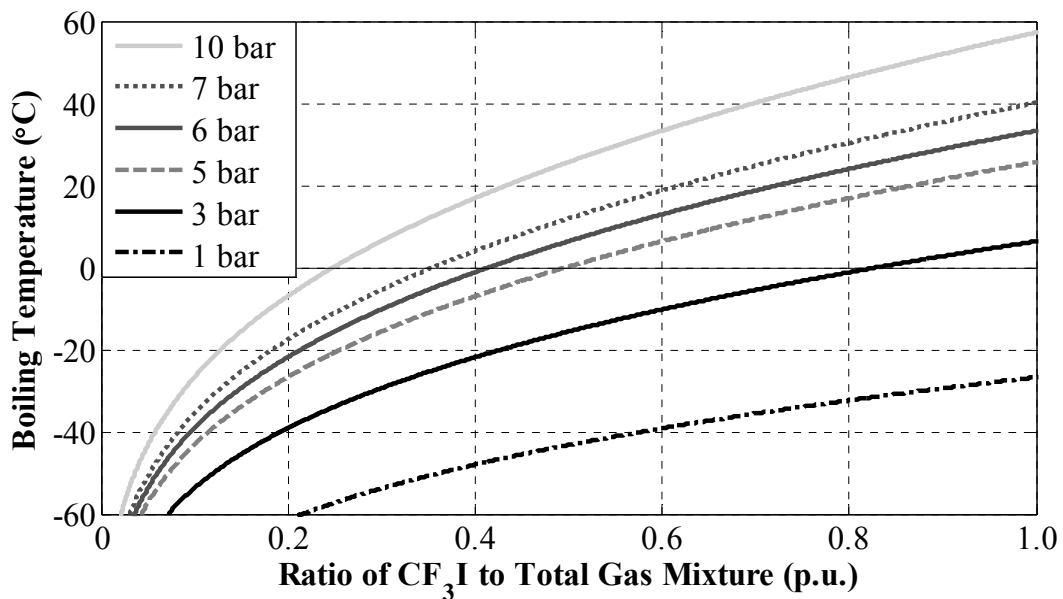
Figure 2.8: Calculated boiling temperature as a function of CF$_3$I content [39].

2.3.4   By-products Analysis

It was reported in [40] that there is a build-up of by-products after a significant number

of electrical discharges. For 25, 500, 1000 and 1300 electrical discharges, by-products

analysis determined the generation of C$_2$F$_6$, C$_2$F$_4$, CHF$_3$, C$_3$F$_8$, C$_3$F$_6$ and C$_3$F$_5$I during the

breakdown of CF₃I gas. The lowest obtained breakdown voltage (after 1300 discharges) was 11% lower than the breakdown voltage when virgin gas and test electrodes were used. However, GIL are designed to have no breakdown occurrence at all, therefore, a significant build-up of by-products inside the GIL is not expected. Table 2.7 shows the measurement conditions of the by-product analysis of CF₃I. A hemisphere-plane test configuration was used to represent a uniform electric field. A non-uniform electric field was represented by a conical rod and plane test configuration. A surface discharge experiment was also carried out on ring electrodes with a PTFE dielectric spacer.

Table 2.7: Measurement conditions for the by-product analysis [40].

	Uniform Electric Field	Non-uniform Electric Field	Surface Discharge
Insulation gas	CF_3I (0.1 MPa)	CF_3I (0.1 MPa)	CF_3I (0.1 MPa)
Electrode	100 mm hemisphere	Conical rod	Ring electrodes
Gap length	10 mm	10 mm	10 mm
Field utilization factor	0.89	0.095	–
Measurement frequency	Par 100 times of sparkover (up to 1300 times)	Par 200 times of sparkover (up to 1400 times)	Par 200 times of sparkover (up to 800 times)

The main by-product of CF₃I is C₂F₆ and Figure 2.9 shows the build-up of C₂F₆ concentration over a number of discharges for three different test configurations: uniform electric field, non-uniform electric field and surface discharge. Table 2.8 shows the conditions (applied voltage, charge quantity and discharge energy) and by-products (ppm) generated per discharge. It can be seen that the concentration of by-products is higher for the uniform electric field, which may have been due to the higher discharge energy. This is inconclusive, however, since the surface discharge experiment had a higher applied

voltage and charge energy than the rod-plane configuration, but with a slightly lower concentration for some of the by-products (C$_2$F$_6$ and C$_2$F$_4$).
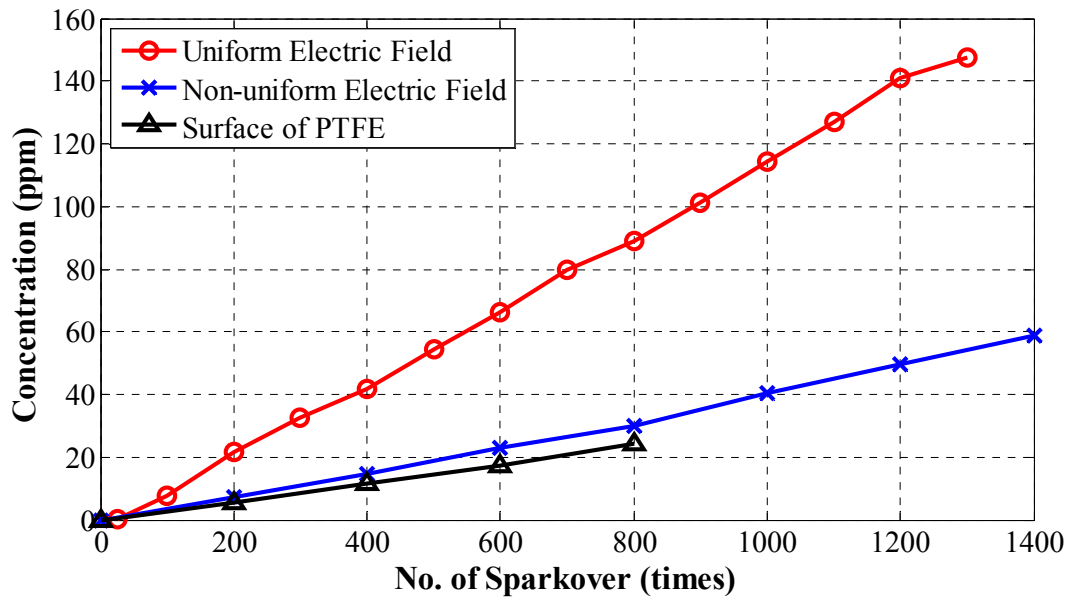
Figure 2.9: The relationship between the number of sparkover events and the concentration of the C$_2$F$_6$ by-product of CF$_3$I [40].

Table 2.8: By-products generated per sparkover or surface flashover [40].

	Uniform Electric Field	Non-uniform Electric Field	Surface Discharge
Applied voltage (kV)	135	43	83
Charge quantity (mC)	5.63	1.79	3.46
Discharge energy (J)	380	38	141
C$_2$F$_6$ (ppm)	0.119	0.0423	0.0317
C$_2$F$_4$ (ppm)	0.0057	0.00348	0.00294
CHF$_3$ (ppm)	0.0147	–	–
C$_3$F$_8$ (ppm)	0.0112	0.00452	0.00718
C$_3$F$_6$ (ppm)	0.00122	0.000501	0.000683
C$_3$F$_5$I (ppm)	0.00739	0.00335	0.00522

An experimental investigation was carried out by Katagiri et al. [41] on the density of by-products such as iodine and fluorine in CF$_3$I gas and its mixtures. Fluorine is a toxic and expected by-product for fluorinated gases, like SF$_6$, and Figure 2.10 shows the measured

density of fluorine for SF_6, CF_3I and a 30/70% CF_3I/CO_2 gas mixture. It can be seen that there is a much lower fluorine density measured for CF_3I than for SF_6. It is also encouraging to observe that there is almost no fluorine content detected for the 30/70% CF_3I/CO_2 gas mixture after current interruption.
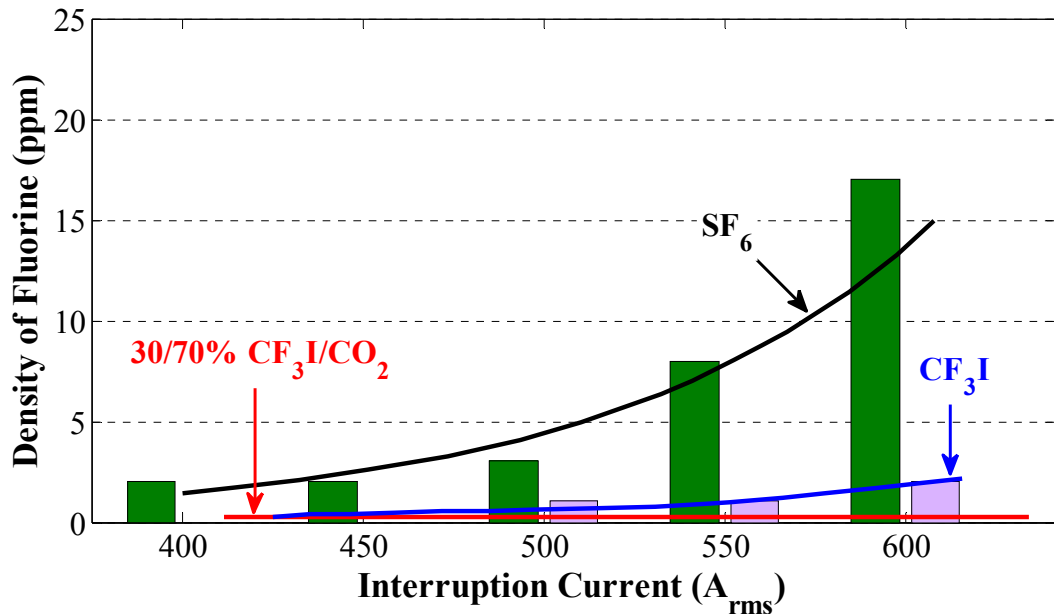
Figure 2.10: Comparison of measured density of fluorine from the experimental investigation on SF₆, CF₃I and a 30/70% CF₃I/CO₂ gas mixture [41].

Due to the weak C-I bond, iodine is a likely by-product of CF_3I after every gas discharge occurrence. Figure 2.11 shows that a 30/70% CF_3I/CO_2 gas mixture produces only 1/3 of the iodine content in comparison to pure CF_3I gas when 400 A_{rms} was interrupted, which is almost proportional to the percentage of CF_3I as part of the mixture. The figure also indicates an exponential growth of iodine content with the current for a pure CF_3I and CF_3I gas mixture. It can be seen in both Figure 2.10 and Figure 2.11 that more by-products of fluorine and iodine were generated at higher levels of interruption current. This indicates that higher discharge energy contributes to more by-products generated per discharge, as shown in Table 2.8.
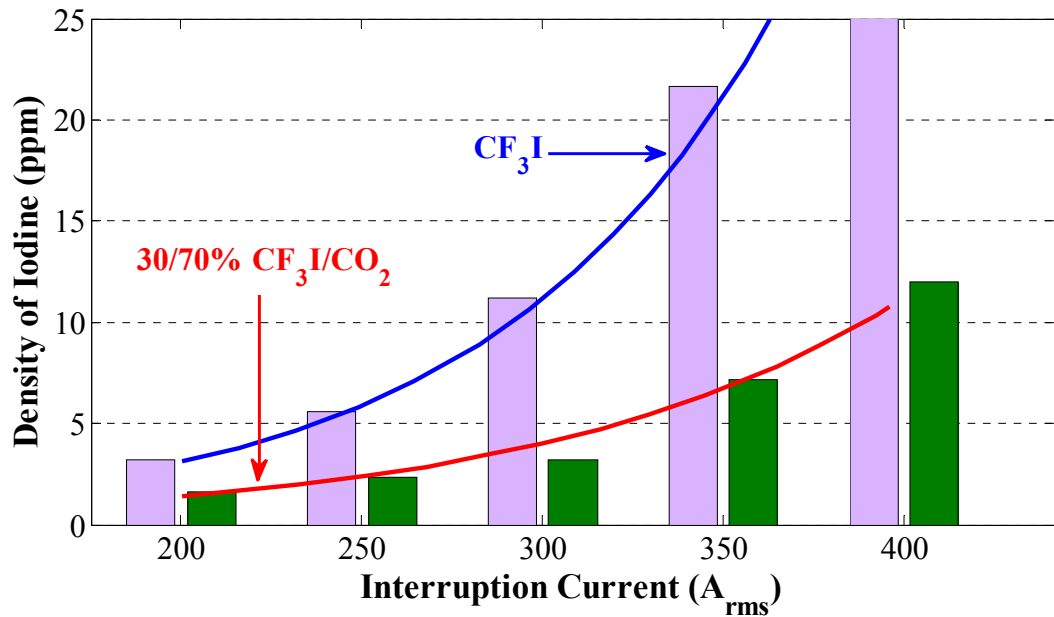
Figure 2.11: Comparison of measured density of iodine from the experimental investigation on CF₃I and a 30/70% CF₃I/CO₂ gas mixture [41].

2.3.5 Toxicity Review of SF₆ and CF₃I

As a pure gas, SF₆ has no known dangerous toxicity or hazardous level. Since SF₆ is denser than air, if a substantial level of SF₆ is released and allowed to settle in an enclosed space (e.g. tunnel), then SF₆ presents the risk of asphyxiation for any personnel that enters the area. The chemical by-products of SF₆, such as SOF_2, SO_2, HF and S_2F_{10}, pose a significant health threat to personnel working with gas-insulated equipment [42]. In terms of the toxicity of CF₃I, a published report [32], based on inhalation tests carried out on animals, shows that CF₃I is a slightly toxic gas. The US National Research Council's (NRC) committee on toxicology has recommended that CF₃I has no observed adverse level (NOAEL) on cardiac sensitization if the concentration is 0.2%, whereas the lowest observed adverse level (LOAEL) is at 0.4%.

The median lethal concentration (LC_{50}) of CF₃I was reported to be 27.4% performed on Sprague-Dawley rats, a value that would classify CF₃I as nontoxic. This is only an

approximate value determined using two concentration levels (24 and 28.8%) for 15 min exposures, which makes the value questionable as LC_{50} requires at least three concentrations and where the animals are exposed to a longer duration (4 to 6 hrs) [43]. However, it was stated in the CGA standard that CF_3I is a nontoxic gas [44]. Since CF_3I is proposed only to be used in relatively low proportions as part of a gas mixture in high-voltage equipment, the overall toxicity level of the CF_3I gas mixture can be calculated using (2.4) [45].

$$LC_{50} = \frac{1}{\sum_i \dfrac{C_i}{LC_{50}}} \qquad (2.4)$$

where C_i is the mole fraction of the ith toxic component present in the gas mixture, LC_{50i} is the lethal concentration of the ith toxic component [($LC_{50} < 5000$ ppm (by volume)].

2.4   Review of SF₆ and its Alternatives

SF_6 is a well-known gas; it has been comprehensively researched worldwide and is used mainly as an interruption/insulation medium in high-voltage GIS/GIL applications. Due to the aforementioned environmental concerns, there has been research into using lower proportions of SF_6 in a gas mixture or completely replacing SF_6 with a new gas, with the aim of identifying and developing a new gas medium with a much lower environmental impact. Since there is a lot of published work on SF_6 gas, only the most important papers will be included in this review.

2.4.1   Previous Investigations into SF₆ Gas

Works and Dakin [46] investigated the breakdown characteristics of SF_6 in a non-uniform field. The experimental setup involved a 1.6 mm diameter hemispherical point and a 152.4 mm diameter plane placed inside a 304.8 mm diameter steel tank. The pressure and

gap length effects were extensively tested for positive and negative DC voltages, positive lightning impulse and 60 Hz AC. It was found that a considerable increase in electrode separation would not yield any appreciable increase in breakdown voltage. Quasi-uniform field gaps represented by the coaxial-cylindrical and sphere-plane electrode configurations investigated for SF$_6$ by Philp [47], Doepken [48], Menju [49] and Legros [50] were tested using lightning and switching impulses. The results show that the measured breakdown voltage of SF$_6$ is approximately three times higher than in N$_2$ or CO$_2$, up to pressures of 10 bar (abs.). This difference in breakdown voltage was reduced at much higher pressures. The breakdown performance of SF$_6$ in uniform field gaps was reported by Malik [51] for a gap distance of 1 to 60 mm and at pressures up to 2 bar (abs.). It was reported that for uniform field gaps, the test results follow Paschen's law until higher pressures are reached; an increase in the pressure resulted in deviation to the Paschen's law at higher pd. Other factors, such as voltage waveform, impulse polarity and electrode surface roughness, could also affect the breakdown voltage of SF$_6$.

2.4.2   Research into Alternatives to SF$_6$

Since the discovery of the high GWP of SF$_6$, there has been research into alternative gases. Initially, the research focused on using low proportions of SF$_6$ as part of a mixture. Several papers [52]–[57] have reviewed the breakdown characteristics of SF$_6$ when mixed with various percentages of air, N$_2$, CO$_2$, N$_2$O, CHF$_3$ or CF$_4$, tested in both uniform field and non-uniform field electrode configurations. Of these, SF$_6$/N$_2$ gas mixtures had the most promising results, and this is why an insulating medium of 20/80% SF$_6$/N$_2$ gas mixture was implemented in the first application of second-generation GIL.

Due to its long atmospheric lifetime, the percentage of SF_6 in our atmosphere will continue to increase and will cause sustained global warming impact. The ideal scenario would be to replace completely the use of SF_6 in high-voltage applications. A report by Brand [58] compared alternative gases in terms of their dielectric strength, boiling point and toxicity (see Appendix A). Brand's results revealed that while gases exist with higher dielectric strengths than SF_6, they all possess one or more negative characteristics, such as a high boiling point, high GWP or high toxicity. Recent reports by Rabie et al. [59]–[61] have investigated the possibility of identifying potential insulation gases through computational screening methods based on electrical, environmental and safety characteristics. Out of 56,000 compounds from the PubChem database, a few promising candidates for further evaluation were identified from 1234 (CID number) compounds.

At the CIGRE Paris Session 2014, Alstom Grid and 3M announced a new gas medium named Fluoronitrile as a replacement for SF_6 in high-voltage GIS [62]. This gas was reported to have a dielectric strength 2.2 times higher than that of SF_6. Due to a high boiling point of –4.7 °C, it can only be used as a gas mixture with CO_2. A 20/80% Fluoronitrile/CO_2 gas mixture was proposed as a gas medium, which has a dielectric strength of 85 to 100% that of SF_6 depending on the operating temperature and pressure for switchgear applications. Tests were conducted on a 145 kV GIS prototype, and the toxicity was found to be in the same class as SF_6 for both the new and the polluted gas. The GWP of Fluoronitrile was calculated as 2300 relative to CO_2 for a time horizon of 100 years and, more importantly, this decreases to 380 for a 20% Fluoronitrile and 80% CO_2 gas mixture. However, the chemical composition of Fluoronitrile is unknown since it has not been released by the company, and so far there is only a limited amount of information available regarding this gas.

2.5   Experimental Investigations on CF$_3$I Gas and its Mixtures

In the literature, the breakdown characteristics of CF$_3$I gas and its mixtures have been reported mainly by researchers from Tokyo University [63]–[66], Tokyo Denki University [67], Kyushu Institute of Technology [68] and from two previous PhD theses at Cardiff University [7], [8]. The work at Tokyo University was conducted using a steep-front square impulse generator with a very fast rise time of 16 ns. Investigations have focused on the voltage-time (V-t) characteristics of CF$_3$I gas and its mixtures and results were compared to SF$_6$. At Cardiff, the experimental investigations were carried out using a 400 kV impulse generator with a standard lightning impulse waveform of 1.2/50. There has also been other reported experimental work that focused on the electron swarm parameters of CF$_3$I gas and its mixtures [69]–[72].

2.5.1   Breakdown Characteristics under Lightning Impulse

Kamarudin [73] investigated the breakdown characteristics of CF$_3$I/CO$_2$ gas mixtures using various electrode configurations under a standard lightning impulse waveform of 1.2/50. The effect of gas pressure was experimentally examined at gas pressures of 1, 1.5 and 2 bar (abs.) for a rod-plane configuration as shown in Figure 2.12. The breakdown voltage increases linearly against gap distance at lower gaps. At higher gap distances, a saturation trend can be observed from the test results. It can also be seen that the breakdown results for negative impulse polarity are higher than those for positive impulse polarity in rod-plane configurations at 1, 1.5 and 2 bar (abs.).
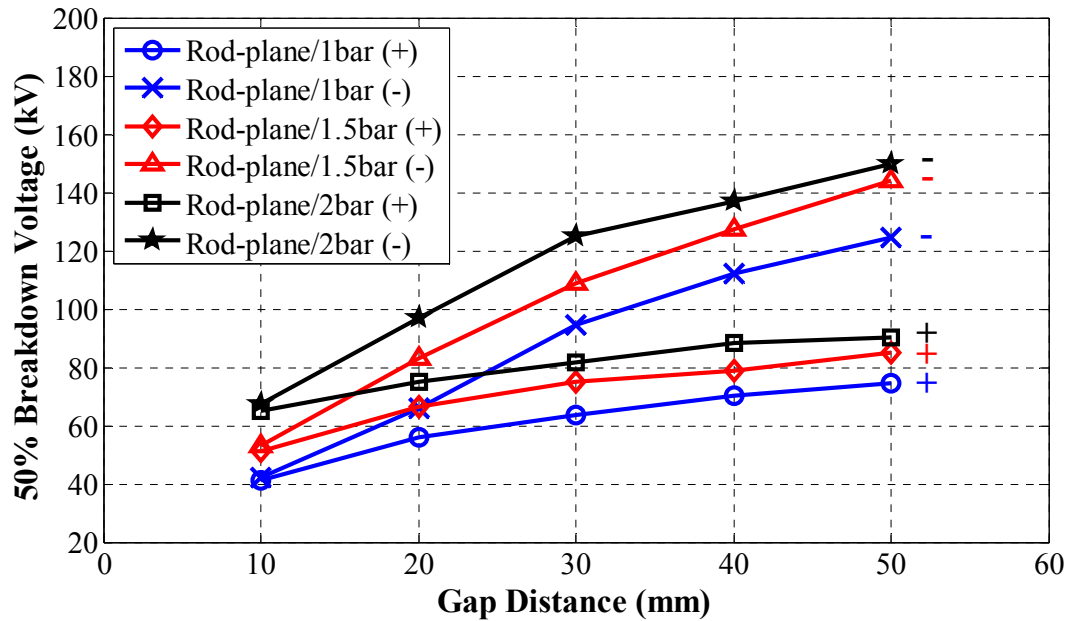
Figure 2.12: U_{50} against gap distance of 10 to 50 mm in a rod-plane electrode configuration and investigated for a 30/70% CF_3I/CO_2 gas mixture at pressure of 1, 1.5 and 2 bar (abs.) and for both lightning impulse polarities [73].

The effect of gap distance was tested in sphere-sphere, plane-plane and rod-plane electrode configurations. As can be seen in Figure 2.13, for all electrode configurations, the breakdown voltage increases as the gap distance increases. The breakdown voltage for positive impulse polarity was higher than that for negative impulse polarity, with the exception of rod-plane gaps. It was reported by Kuffel in [74] that negative breakdown voltage is higher than the positive breakdown voltage in gaps with marked asymmetrical fields. In the case of a positive rod-plane, ionization is accelerated by electron collision in the high field region near the rod. Electrons are readily drawn towards the anode and in time the field strength near the rod is sufficiently high to initiate a complete breakdown. For a negative rod-plane, the electrons are accelerated into the low field region by the cathode and in the process become attached to strongly attaching gases like CF_3I or SF_6 [75]. This slows down the ionization process, which then requires a higher voltage to initiate a complete breakdown. In uniform or quasi-uniform gaps the characteristics are

reversed with negative breakdown voltage lower than positive breakdown voltage, which were reported for a coaxial electrode configuration in [49] for SF_6 and in [74] for N_2. This indicates that there are other influencing factors including a polarity effect for reduced breakdown voltage in quasi-uniform field gaps.
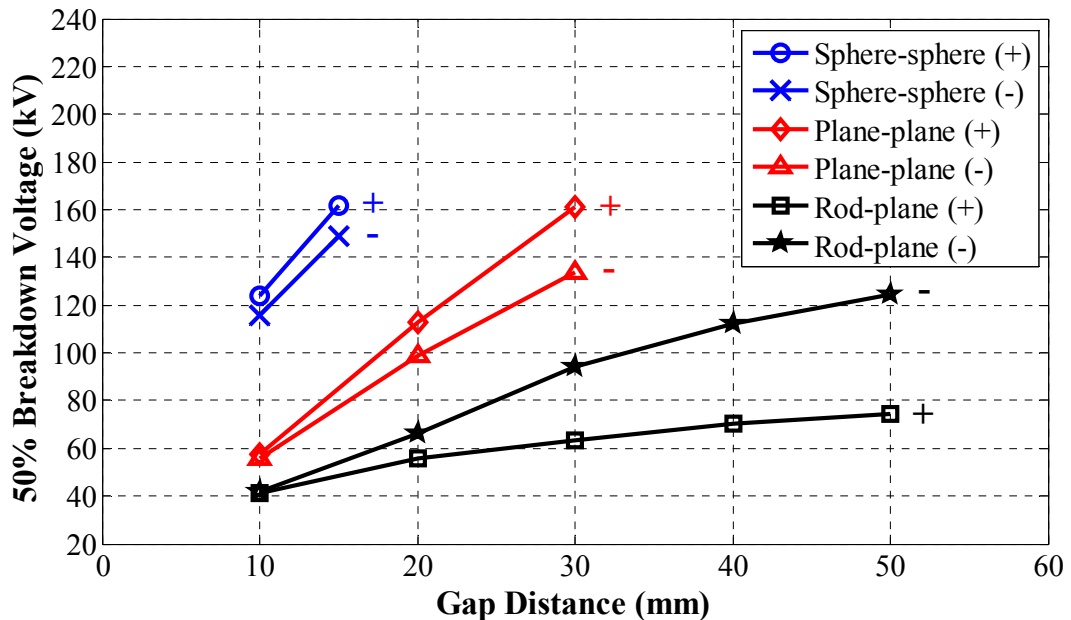
Figure 2.13: U_{50} against gap distance of 10 to 50 mm in sphere-sphere, plane-plane and rod-plane electrode configurations, tested using a 30/70% CF₃I/CO₂ gas mixture at 1 bar (abs.) and for both lightning impulse polarities [73].

An investigation was also carried out [73] for CF_3I/CO_2 gas mixture ratios of 20/80%, 30/70% and 40/60%. Tests were carried out at a pressure of 1 bar (abs.) in rod-plane and plane-plane electrode configurations, with maximum gap distances of 50 mm and 30 mm respectively. The test results are shown in Figure 2.14 and Figure 2.15. It can be seen from the figures that changing the CF₃I content has more effect on U_{50} in a rod-plane configuration for both lightning impulse polarities. In a plane-plane configuration, a 20% increase in CF₃I content resulted in a similar increase in the percentage of the breakdown voltage for a positive lightning impulse. An increase in CF₃I content would result in a higher breakdown strength, as illustrated in Figure 2.12 and Figure 2.13. For a CF₃I gas

mixture with high CF$_3$I content, however, lower pressures are required for liquefaction and more by-products would also be generated.
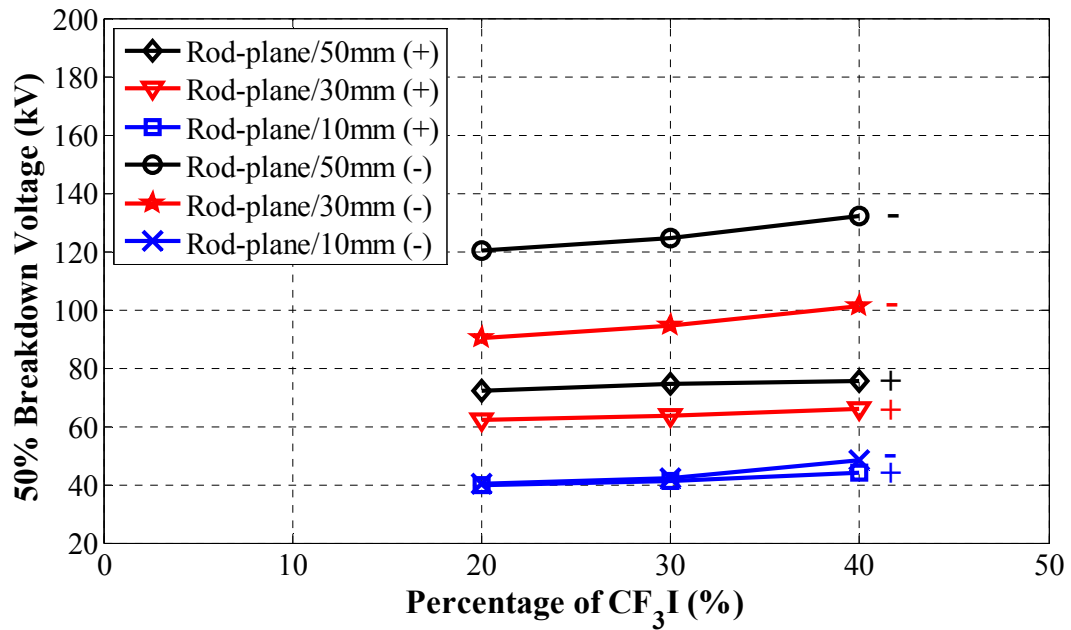
Figure 2.14: U$_{50}$ investigated for various CF$_3$I/CO$_2$ gas mixtures in a rod-plane electrode configuration for gap distances of 10 to 50 mm at 1 bar (abs.) and for both lightning impulse polarities [73].
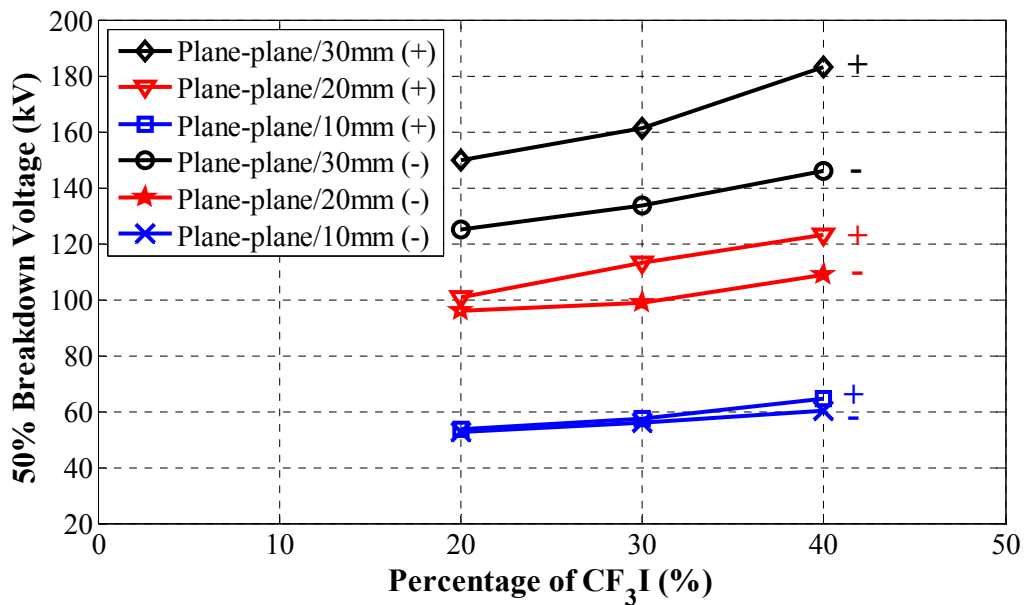
Figure 2.15: U$_{50}$ investigated for various CF$_3$I/CO$_2$ gas mixtures in a plane-plane electrode configuration for gap distances of 10 to 50 mm at 1 bar (abs.) and for both lightning impulse polarities [73].

2.5.2   Breakdown Characteristics under Steep-front Square Impulse

Investigations were carried out on the breakdown characteristics of CF_3I gas and its mixtures [63]–[66]. A steep-front square impulse generator was used to generate a square impulse waveform with a very steep rise time of 16 ns. The research determined experimentally the V-t characteristics of various CF_3I and SF_6 gas mixtures. The generic V-t characteristics trends for uniform and non-uniform gaps are shown in Figure 2.16. In uniform or quasi-uniform field gaps, as the overvoltage level increases, the breakdown time decreases, which results in a steep rising slope. The flat curve of the V-t trend in a uniform gap is also the breakdown level under DC. For non-uniform field gaps, there is a greater statistical spread in the V-t results and, the data appear to manifest itself at shorter breakdown time as indicated by the dotted lines in Figure 2.16.
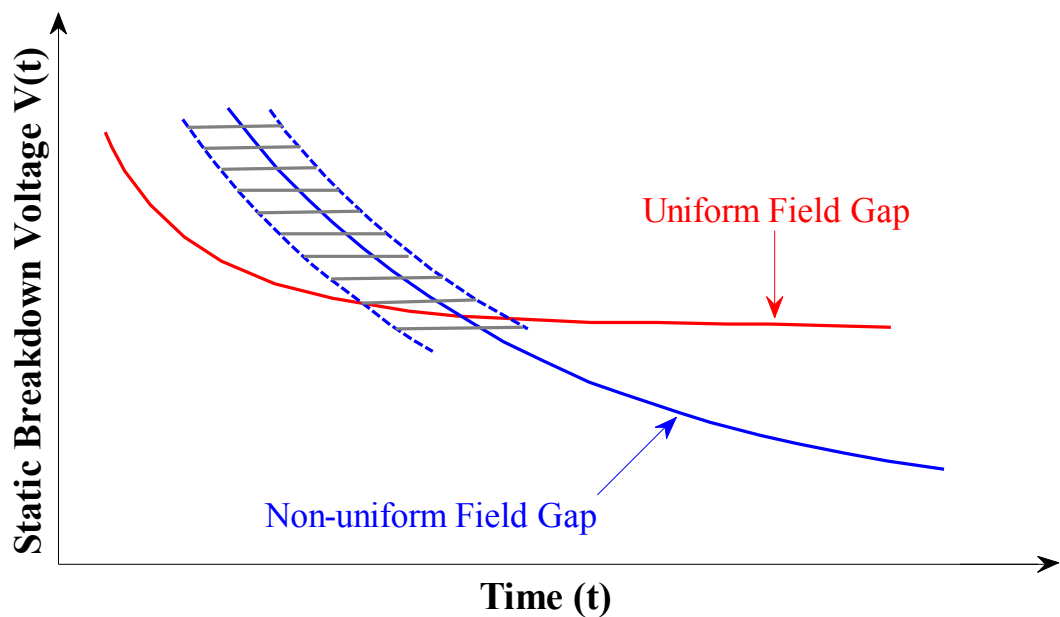
Figure 2.16: V-t characteristics of uniform and non-uniform field gaps [74].

From this research, the following observations could be made:

- Measured voltages at instants of breakdown for CF_3I are lower than for SF_6 in non-uniform electric field gaps (needle-plane configuration).

- Measured voltages at instants of breakdown for CF₃I are higher than for SF₆ in uniform electric field gaps (hemisphere-plane configuration).

- The obtained V-t results demonstrate its similarity to the generic V-t trends for uniform and non-uniform gaps shown in Figure 2.16, where the results for non-uniform gaps indicate greater dispersion.

Figure 2.17 shows the U_{50} of CF₃I and SF₆ for a needle-plane and a hemisphere-plane configurations, which represent a non-uniform and a uniform electric field respectively. It can be seen from the figure that the U_{50} results of CF₃I are lower than their SF₆ equivalent. Conversely, CF₃I has higher U_{50} than SF₆ tested in a hemisphere-plane configuration at a gap of 10 mm. It is unclear whether negative U_{50} results will be lower in uniform field gaps as was observed for lightning impulse, since there is no report of negative U_{50} for CF₃I tested in a hemisphere-plane configuration using steep-front square impulse.
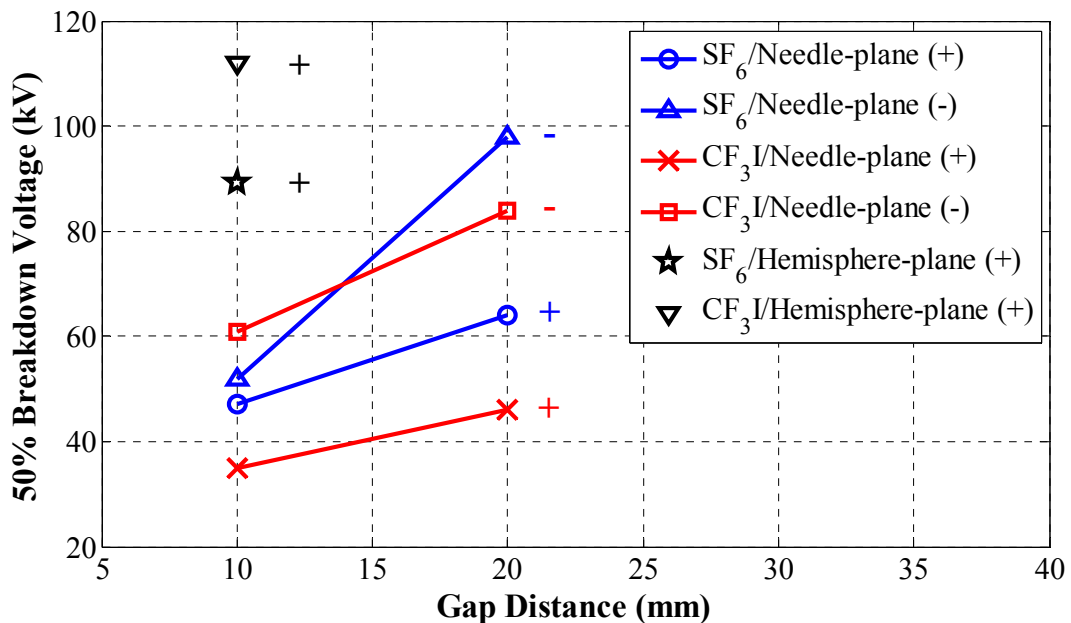
Figure 2.17: Breakdown voltage, U_{50}, for SF₆ and CF₃I gases tested for needle-plane and hemisphere-plane configurations at 1 bar (abs.) and for steep-front square impulse [76].

2.5.3   Electron Swarm Parameters of CF$_3$I

Electron swarm parameters were investigated by de Urquijo [69], reporting the measurement of the electron drift velocity, the longitudinal diffusion coefficient, and the effective ionization coefficient for CF$_3$I and CF$_3$I/N$_2$ gas mixtures. Of these, the effective ionization coefficient is the parameter of the greatest interest, since it provides an indication of the dielectric strength of each gas or gas mixture based on the (E/N)$_{crit}$ value. The critical field strength of pure CF$_3$I at the point where ionization is equal to attachment was found to be 437 Td, which is around 1.2 times higher than that of pure SF$_6$ (361 Td). A comparison was made in terms of (E/N)$_{crit}$ for CF$_3$I/N$_2$ and SF$_6$/N$_2$ gas mixtures, as can be seen in Figure 2.18. The CF$_3$I/N$_2$ gas mixture outperforms its SF$_6$/N$_2$ counterpart when the percentage of N$_2$ decreases to less than 40%. It also shows that a gas mixture with 70/30% CF$_3$I/N$_2$ has almost the same (E/N)$_{crit}$ value as pure SF$_6$, however, such mixture ratio is unlikely to be used in practice due to concerns regarding liquefaction. It is noteworthy that the (E/N)$_{crit}$ trend for CF$_3$I gas mixtures is relatively linear in comparison to their SF$_6$ equivalent, which perhaps indicate that CF$_3$I has better gas stability.
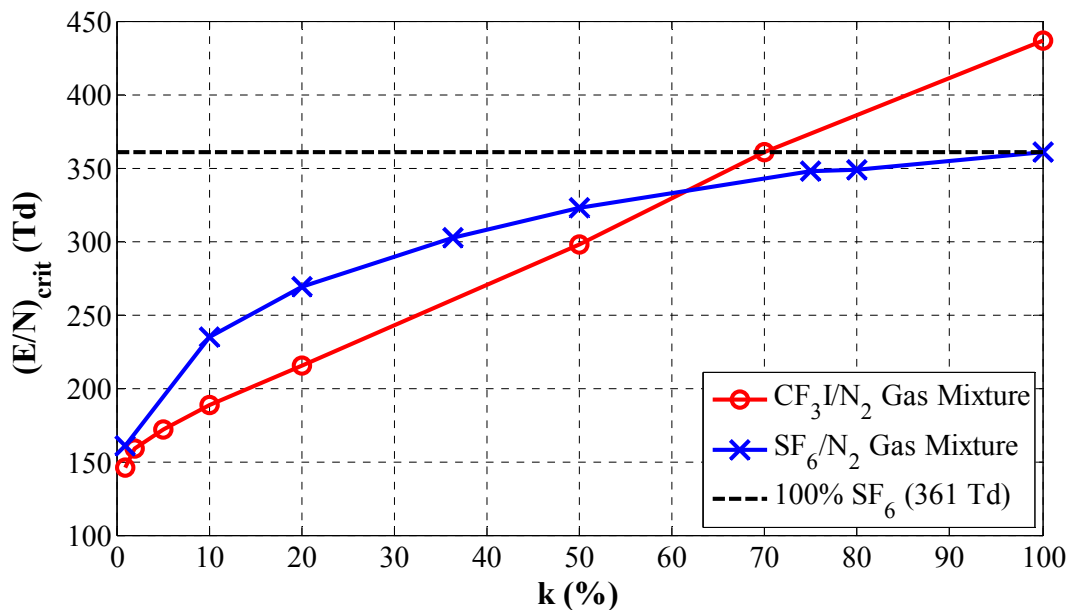
Figure 2.18: Comparison of the critical field strength, (E/N)$_{crit}$, as a function of CF$_3$I or SF$_6$ gas content, k, for both CF$_3$I/N$_2$ and SF$_6$/N$_2$ gas mixtures [69].

2.6   Conclusion

This chapter has provided an overview of the existing literature on GIL, SF$_6$ and CF$_3$I. From this literature review, several research gaps can be identified that are important to the realisation of a CF$_3$I-GIL system. These are listed as follows:

- Experimental investigation on the boiling point of CF$_3$I gas mixtures to determine the conditions leading to liquefaction. This would establish a temperature/pressure threshold for the CF$_3$I-GIL to avoid liquefaction.

- Calculation and comparison of the effective ionisation coefficients of CF$_3$I/N$_2$ and CF$_3$I/CO$_2$ gas mixtures so as to develop an initial understanding of the dielectric strength of each gas mixture.

- Development of a reduced-scale coaxial test system based on the dielectric design of a full-scale GIL system for the purpose of experimental work, since there is limited published data on the breakdown performance of CF$_3$I in coaxial geometry.

- Experimental investigations on the breakdown characteristics of CF$_3$I gas mixtures in the coaxial prototype in terms of the impact from gas pressure, gap distance, impulse polarity, mixture content and buffer gas.

- Comparative study of the steep-front square impulse and standard lightning impulse waveforms for CF$_3$I gas mixtures.

All of the above mentioned actions will form the basis of the fundamental knowledge needed to characterise CF$_3$I gas and its mixtures as an insulation medium in GIL applications. It is hoped that this would lead to the successful implementation of a CF$_3$I gas mixture in a full-scale GIL demonstrator system.

3 LABORATORY TEST EQUIPMENT AND EXPERIMENTAL TECHNIQUES

3.1   Introduction

CF_3I gas and its mixtures have been studied in this thesis as a potential replacement for SF_6 in GIL applications. In this investigation, direct breakdown experiments were conducted to examine the breakdown strength of CF_3I gas mixtures. Different electrode configurations, namely rod-plane and plane-plane, were chosen to represent non-uniform and uniform field distributions respectively. A coaxial cylindrical electrode was used to represent a scaled prototype of the full-scale GIL geometry. A digital oscilloscope (10 GS/s, 600 MHz) was used to record the breakdown voltages for a chosen waveform. In this PhD project, (i) a standard lightning impulse waveform of 1.2/50 and (ii) a steep-front square impulse waveform with a rise time of 16 ns and a time duration of 10 μs were used. This chapter first describes the development of a pressure vessel to carry out gas research and then reviews the test setups and the experimental techniques that were used in this investigation.

3.2   Test Equipment

A cylindrical pressure vessel was manufactured out of mild steel, with a maximum pressure limit of 10 bar (abs.). The design of the pressure vessel was developed in a previous PhD project [8]. Figure 3.1(a) shows the dimensions of the vessel: a height of 500 mm, an outer radius of 250 mm and a wall thickness of 10 mm, which gives the vessel a volume of 0.0982 m^3, or 98.2 litres at atmospheric pressure. After fabrication, the vessel

was filled with dry nitrogen gas at 10 bar (abs.) and was held for 30 minutes as part of a pressure inspection test. During which, all joints were checked using a gas leak detector spray and no indication of any pressure drop was detected.

3.2.1 Pressure Vessel

Figure 3.1(b) shows the fabricated pressure vessel. The side window was made of polycarbonate; this is a tough thermoplastic material that has a high level of transparency, making it a suitable material for observing the discharge phenomena occurring inside the vessel. At the bottom of the vessel, there are multiple inlets and outlets for the processes of pressurising and evacuating the vessel.
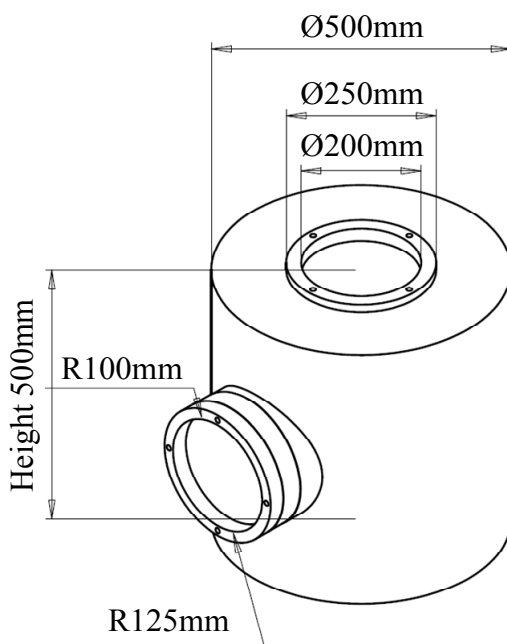
(a)   (b)

Figure 3.1: (a) Schematic diagram with the dimensions of the pressure vessel and (b) a picture of the fabricated pressure vessel.

Two pressure gauges were installed beneath the vessel to provide readings of the pressure inside the vessel as can be seen in Figure 3.2: (a) a vacuum gauge for measuring pressure

of less than 1 bar (abs.), normally used when evacuating air from the vessel before filling any test mixtures; and (b) a pressure gauge ranging from 0–7 bar (atm.), which allows the user to carry out experiments at much higher pressures.
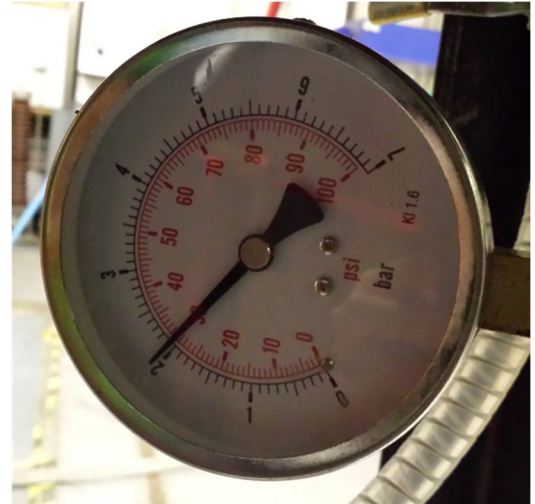
(a)   (b)

Figure 3.2: (a) Vacuum gauge and (b) a pressure gauge from 0–7 bar (atm.).

At the bottom of the pressure vessel, a pressure release valve was fitted, as shown in Figure 3.3. The relief valve was designed with a pre-determined set pressure of 6 bar (abs.). If the pre-determined set pressure is exceeded, the relief valve is released, and this provides an auxiliary passage for the gas to evacuate the vessel.

Figure 3.3: Pressure relief valve.

3.2.2 Bushing

The main function of a high-voltage bushing is to help the applied impulse voltage to safely reach the high-voltage electrode inside the pressure vessel. It prevents the possibility of flashovers to the grounded metal, provided that the withstand voltage of the bushing is not exceeded. The bushing used in this research has a copper conductor, which forms a part of the terminal end, surrounded by silicone rubber (see Figure 3.4). There is a 10 mm inner thread at the bottom of the copper conductor to which the high-voltage electrode can be connected. This also ensures that the electrode configurations are mounted concentrically within the pressure vessel. The bushing specification was provided by the manufacturer (see Appendix B). For a bushing with a dry power frequency withstand voltage of 70 kV, the equivalent dry lightning impulse withstand voltage is then limited to 170 kV peak [77]. The applied impulse voltage during the experiment should not, therefore, exceed 170 kV.
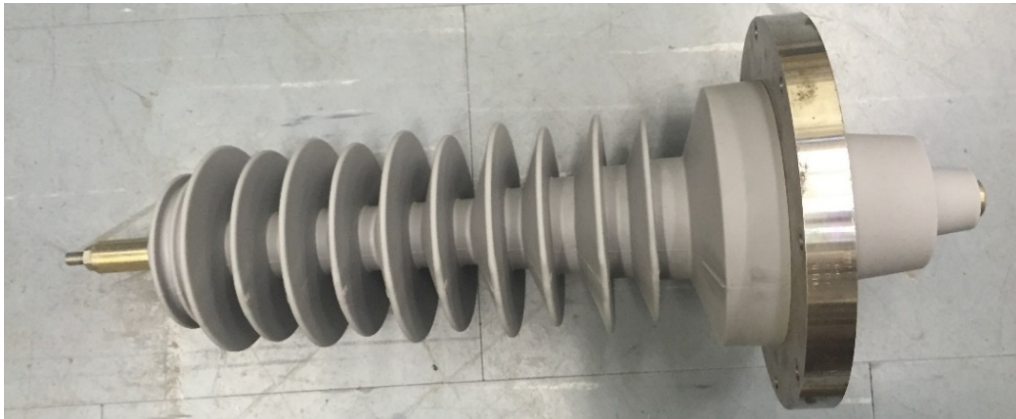
Figure 3.4: 38 kV dry bushing.

3.2.3 Linear Actuator

Experimental investigations were conducted on rod-plane and plane-plane electrode configurations to examine the effect of gap length under pressurised CF_3I gas mixtures. This required a system that could be controlled from outside of the vessel and to adjust

the gap distance while the vessel is pressurised. A Firgelli linear actuator and controller [78] was connected using wires that feed through from inside to outside while the vessel is pressurised. To avoid gas leaking from the wires, a compression seal fitting, also known as a sealing gland, was attached onto the bottom of the vessel with wires coming through the centre, as can be seen in Figure 3.5. The sealing gland provides the connection between the linear actuator inside the vessel and the controller which is on the outside. Loxeal engineering adhesives were applied to the connection joint to prevent any gas leakage along the wires.

Figure 3.5: Sealing gland for external wiring connections.

Figure 3.6 shows the setup of the linear actuator that was placed inside the pressure vessel. A Firgelli linear actuator is attached to the ground electrode, providing linear movement in either an upwards or a downwards direction. Outside the vessel, a linear actuator controller made by Phidgets [79] ensures the actuator moves the ground electrode to the exact location required before starting any experiment. The controller is powered by a

USB port through a laptop or desktop computer. The linear actuator and the controller are connected using wires that pass through the compression sealing gland. Once the gap is setup, the controller is then disconnected from the linear actuator before the experiment.
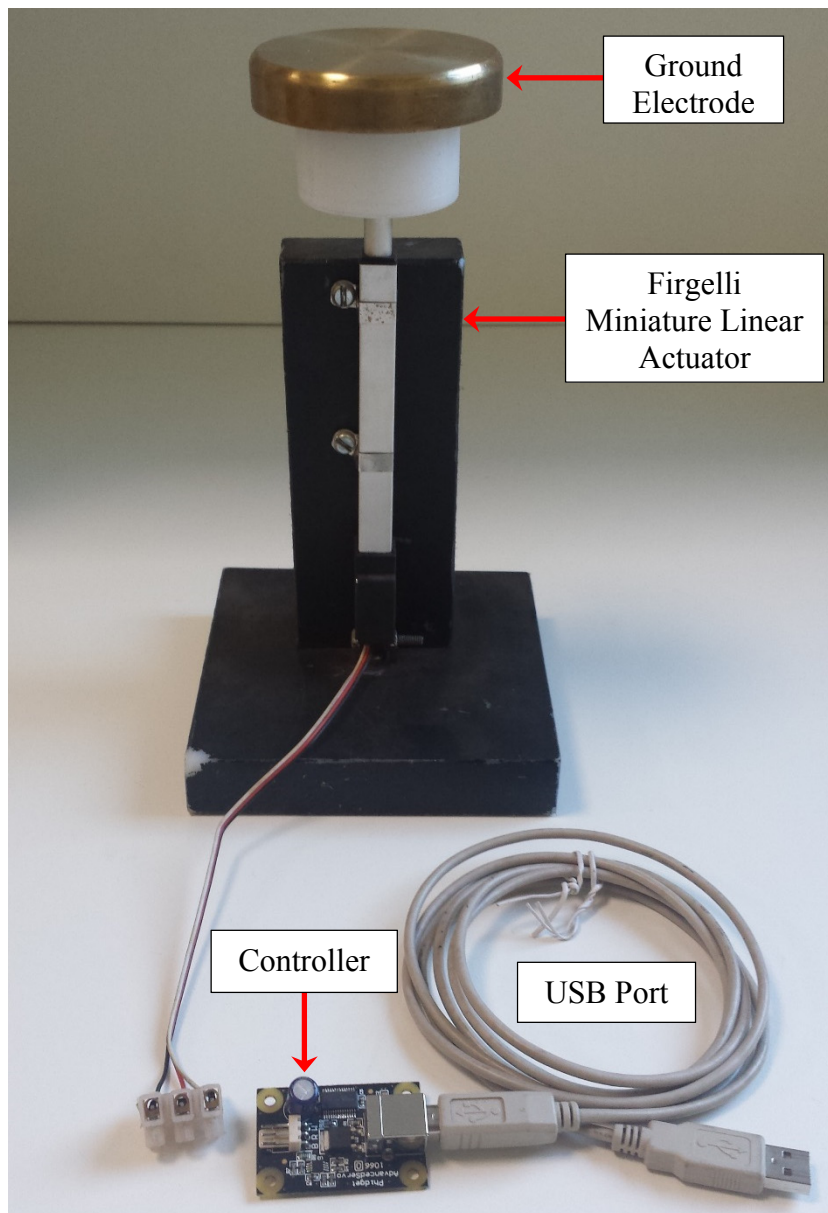
Figure 3.6: Firgelli linear actuator and controller [78].

3.2.4   Gas Extraction Unit

For the purposes of gas mixing, a 15 kg bottle of CF_3I gas with ~100% purity was used. Bottles of compressed N_2 and CO_2 gases were also purchased to allow preparation of CF_3I gas mixtures. It was clear from the cost of the CF_3I gas that it would be an expensive

investigation to carry out, necessitating the recycling of gas for further tests. Several empty green gas storage cylinders were also purchased from DILO for storing CF_3I/CO_2, and two grey storage cylinders were used for storing CF_3I/N_2 mixtures, as shown in Figure 3.7.
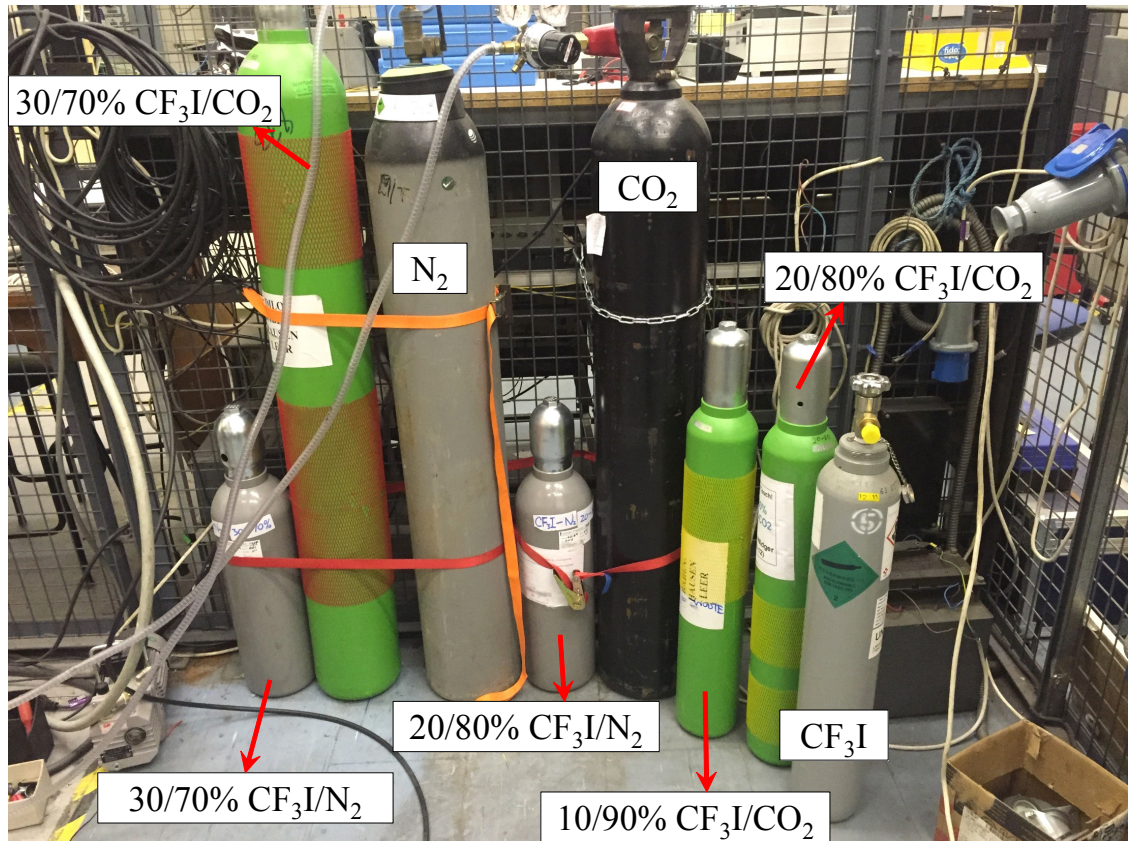
Figure 3.7: Gas storage cylinders for different CF₃I gas mixtures.

A mini-series extraction unit Z579R03, as shown in Figure 3.8, was purchased from DILO, to carry out the vacuuming and gas recycling processes. This service cart contains a vacuum compressor, vacuum pump, compressor, pre-filter unit and other fittings. One of the main reasons for purchasing this machine is because all the connections have O-rings incorporated to minimise gas leakage.
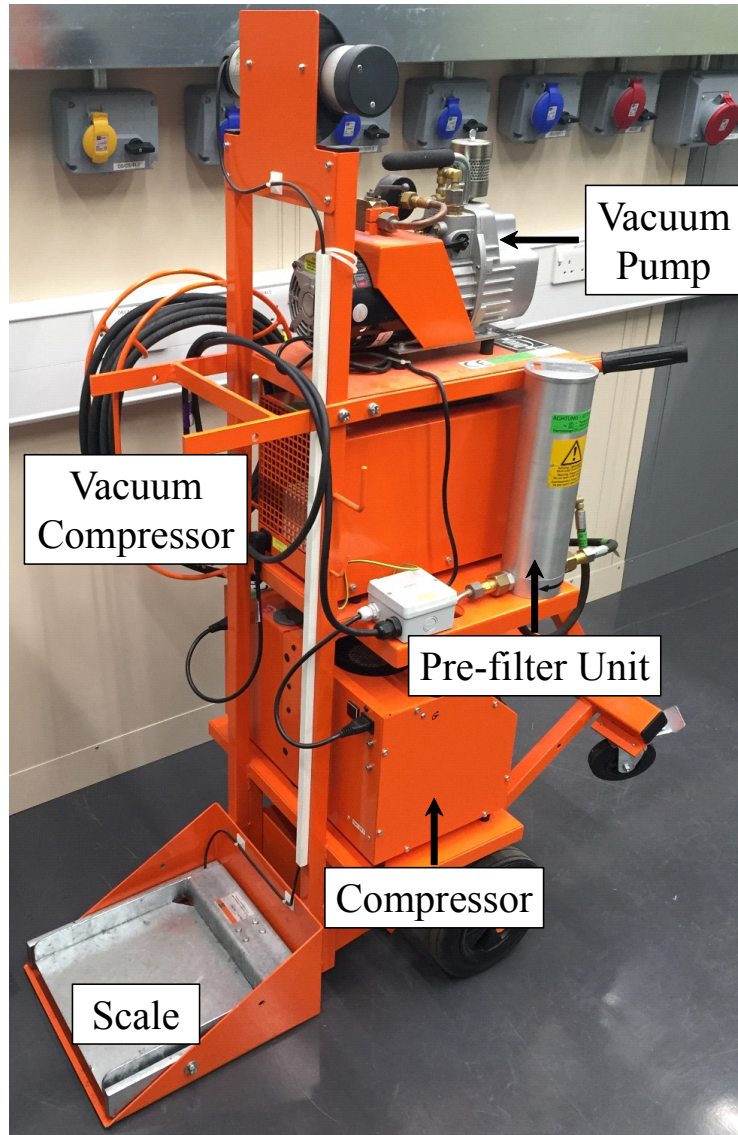
Figure 3.8: DILO mini-series for vacuuming and gas extraction from the pressure vessel.

All pressure measurements in this thesis are stated as absolute values in bar. A wireless temperature and humidity sensor was placed inside the pressure vessel and, for all the tests, the room temperature varied within ±2 °C. Before the start of any experiment, the electrodes were metal polished and cleaned thoroughly with alcohol. Any possible remaining dust particles were removed using pressurised air before the electrodes were inserted into the pressure vessel.

Figure 3.9 illustrates the operation of gas mixing and extraction. At the start of every experiment, the vacuum pump unit was used to ensure the evacuation of air from the vessel. It was possible to achieve a final vacuum of <1 mbar.
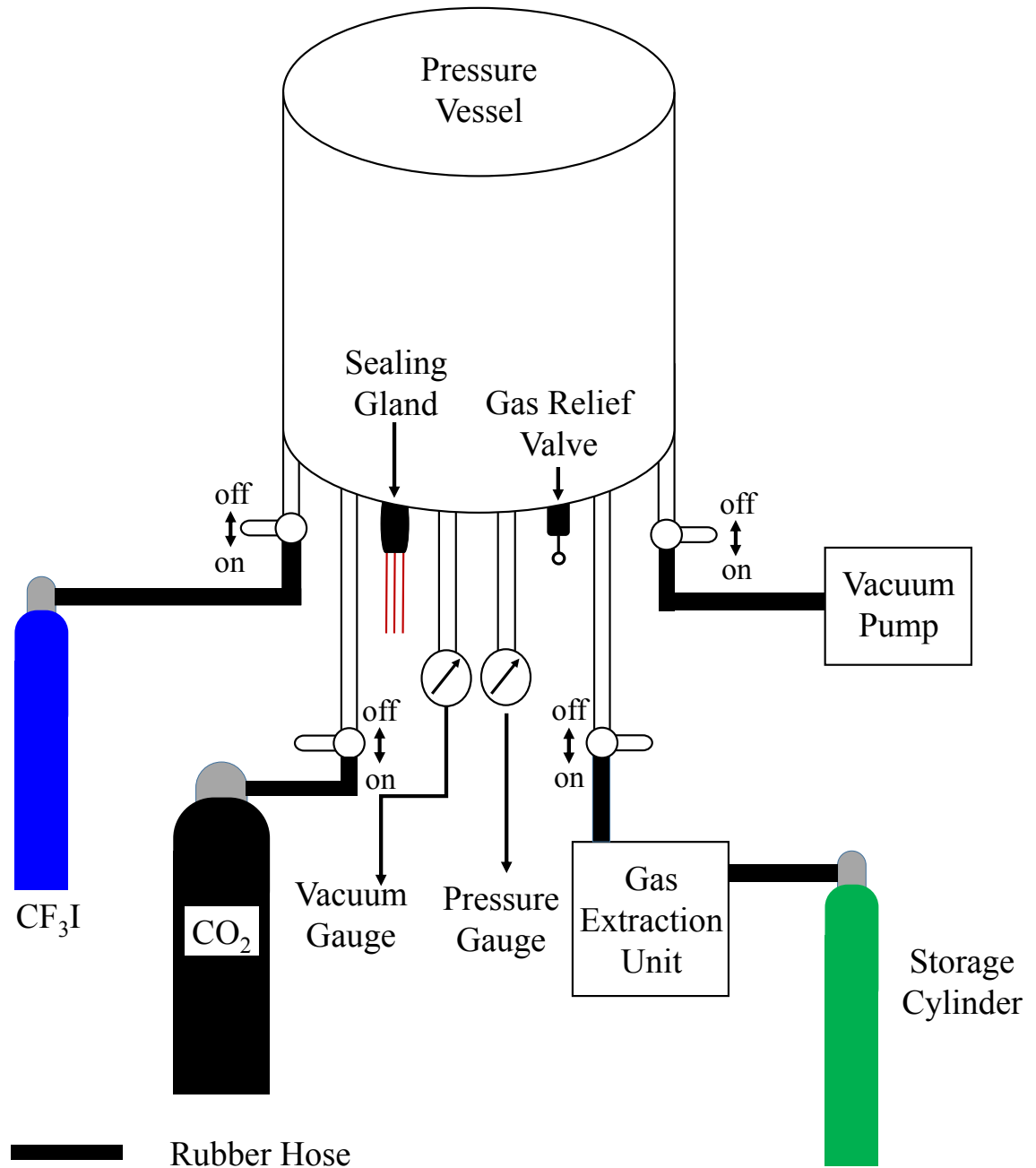
Figure 3.9: Schematic diagram of gas filling and extraction system.

To establish a 20/80% CF_3I/N_2 gas mixture at 1 bar (abs.), the gas with the lower proportion has to be filled first. In this case, the vessel is filled to 0.2 bar (abs.) with CF_3I

gas, then 0.8 bar (abs.) of N_2 gas, meaning that the pressure gauge should read 1 bar (abs.).

It was reported in [80] that the test results showed good repeatability when the gas mixture

was left to mix for 24 hours prior to carrying out each experiment. At the end of an

experiment, the tested CF_3I gas mixture was pumped out of the vessel and into a storage

cylinder via the mini-series extraction unit. The gas first encounters the pre-filter unit

which purifies and dries the gas with the particle filter and dry filter installed inside the

unit. This then leads to the recovery of the gas via the vacuum compressor unit, which is

capable of pumping down to a final pressure of <10 mbar. The maximum operating

overpressure is 10 bar (abs.) for both the compressor and vacuum compressor unit. The

whole gas extraction process takes between 1 to 2 hours depending on the gas pressure

inside the vessel.

For the user to re-use any CF_3I gas mixture that has been stored inside a storage cylinder,

a DILO gas refilling device 3-393-R002 shown in Figure 3.10 can be used to refill the

vessel with the CF_3I gas mixtures stored inside the storage cylinder.

Figure 3.10: DILO gas refilling device 3-393-R002.

3.3   Generation and Measurement of Lightning Impulses

In high-voltage experiments, lightning impulse voltages are used to investigate the breakdown mechanisms. A standard lightning impulse voltage reaches its peak voltage in 1.2 microseconds and then gradually declines, eventually reaching zero. The peak value of impulse voltages is measured by a digital oscilloscope, which is used to record the complete time characteristic of the voltage.

3.3.1   Test Setup of Lightning Impulse Experiment

For the laboratory work, a 400 kV Haefely impulse generator was used for the generation of lightning impulse voltages that led to gas discharges for either positive or negative impulse polarity for any test electrode configuration. The circuit diagram of a Haefely impulse generator is shown in Figure 3.11.
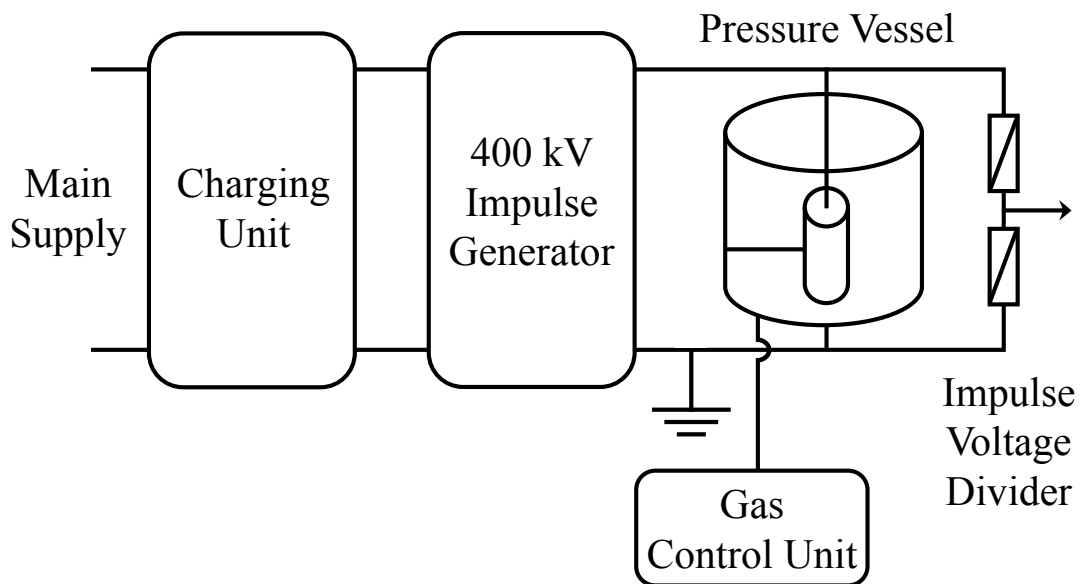
Figure 3.11: Test circuit of impulse voltage generator.

Figure 3.12 shows a graphical representation of the impulse generator that was used extensively for the experimental investigations carried out in this thesis. The applied

impulse voltage can be pre-set using the Haefely impulse generator's control system. The power supply is converted into a DC source by the charging rectifier and then gradually increased to the per-stage charging voltage of the generator. If the applied lightning impulse voltage is sufficiently high, a breakdown occurs across the electrode gap inside the test vessel. The lightning impulse voltage is measured by the capacitive impulse voltage divider with a ratio of 27931 to 1 and a 50 ns rise time. A digital oscilloscope (10 GS/s, 600 MHz) is then used to capture the impulse voltage waveform. The high-voltage equipment and test vessel are grounded using flat tinned copper braid wires with a cross-section area of 100 mm^2 and connected to earth via a star point.
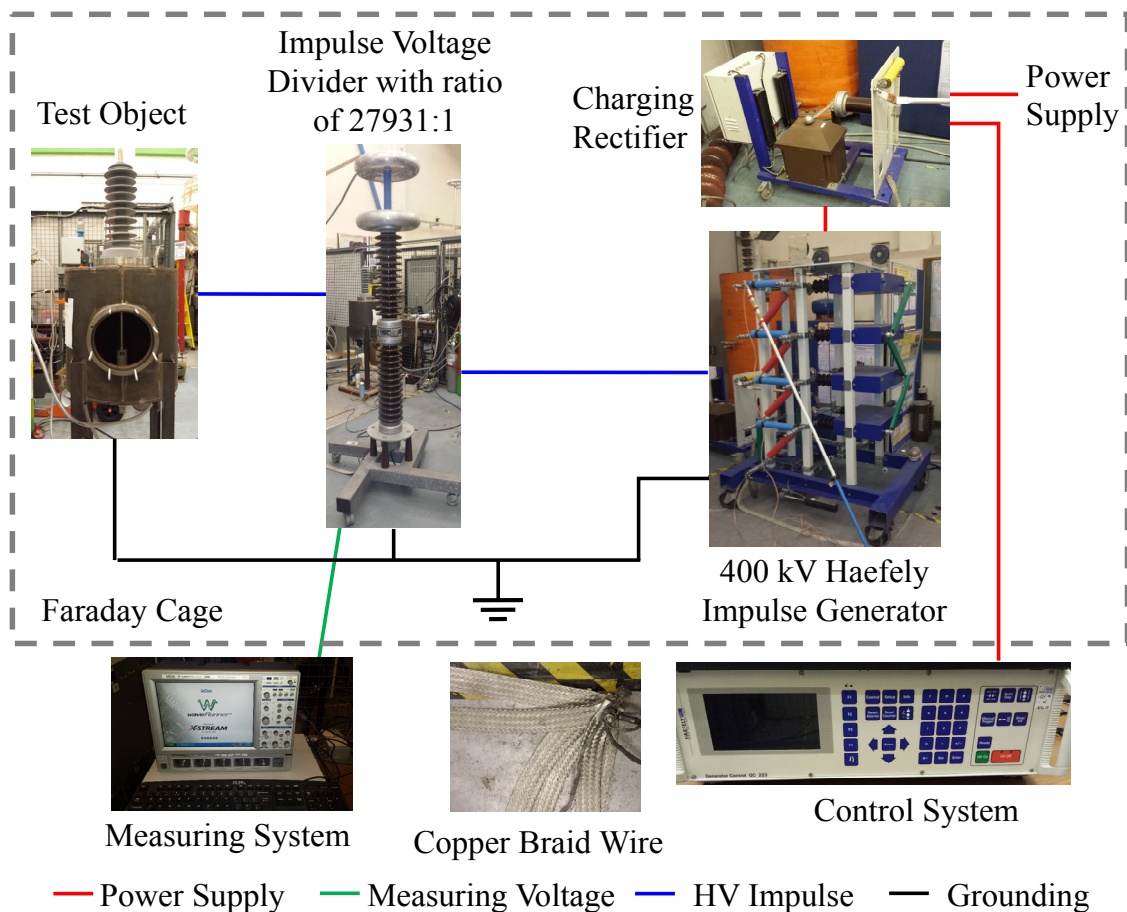
Figure 3.12: Setup of high-voltage and grounding connections for the lightning impulse experiment.

3.3.2   Standard Lightning Impulse Voltage Waveform

The international standard defines a lightning impulse voltage as having a front time, T_1, of 1.2 μs with a tolerance of ±30% and a tail time, T_2, of 50 μs, with a tolerance of ±20%. The measured peak value, U_{peak}, should be within ±3% of the applied voltage [81]. It is always important to check whether the measured lightning impulse voltages conform to the standard before each set of experiments. A trial impulse shot of a 120 kV lightning impulse is shown in Figure 3.13. The measured results for T_1, T_2 and U_{peak} were all within the tolerance level as stated in the standard [81].
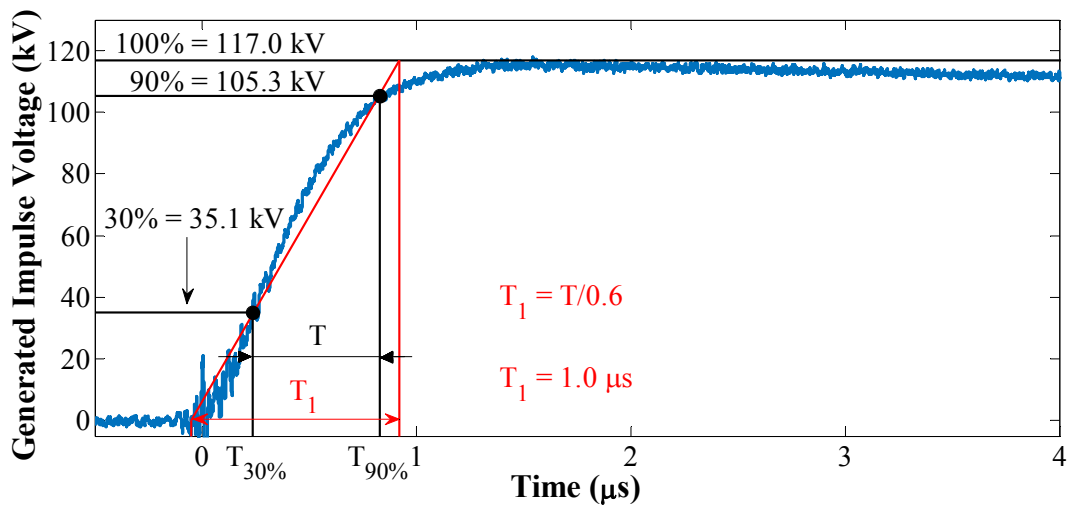
(a)   Front time measurement
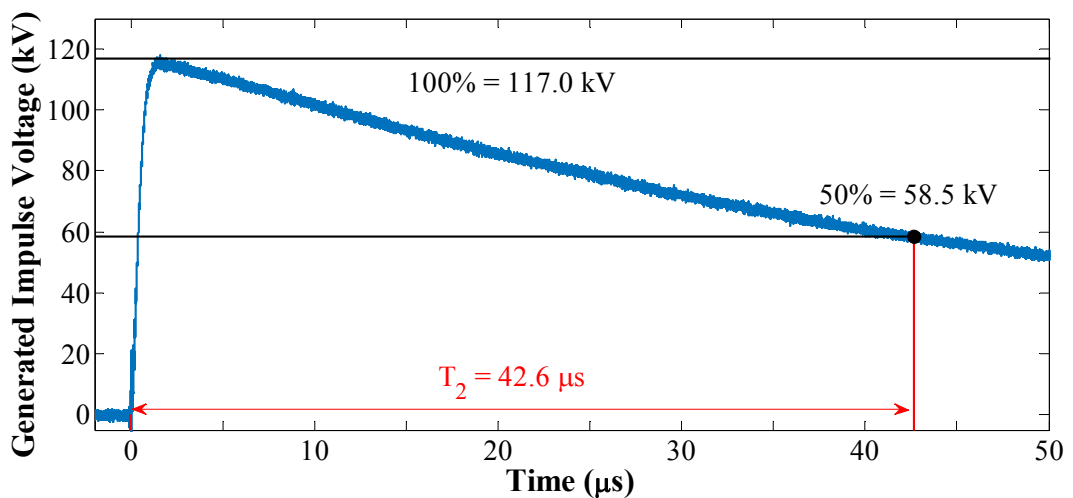
(b)   Tail time measurement

Figure 3.13: Measurement of a 120 kV lightning impulse shot.

3.4 Generation and Measurement of Steep-front Square Impulses

In collaboration with Tokyo University, a comparison of the breakdown characteristics of CF_3I gas mixtures for both standard lightning impulse and steep-front square impulse waveforms was carried out. This section will discuss the generation and measurement of a steep-front square impulse voltage.

3.4.1 Steep-front Square Impulse Voltage Generator

As can be seen in Figure 3.14, a steep-front square impulse voltage generator consists of three main sections: a Marx circuit, a laser triggering system and a discharge chamber. The circuit diagram of the generator is shown in Figure 3.15. During the operation, an impulse voltage with a peak value of 40–200 kV was generated by the Marx circuit, and the charges in the circuit were then transferred and stored in a capacitor. This equipment has a rise time of 16 ns, which allowed a maximum steepness of 12.5 kV/ns to be achieved. Inside the laser triggering chamber pressurised with SF_6 gas, a pair of sphere electrodes act as the spark gap. In Figure 3.16, a beam from an Nd:YAG laser short-circuits the spark gap inside the laser triggering chamber. As a result, in this research, a steep-front square impulse was generated and applied to the test electrode in the discharge chamber. Two capacitive dividers were used to measure the voltage waveform: a high-frequency divider to measure the wave front and a low-frequency divider to measure the entire waveform. Voltage waveforms were recorded using a Tektronix TD3034B digital oscilloscope with 300 MHz band width and 2.5 GS/s sampling rate. To minimise noise, the oscilloscope is placed in a shield box. The measured data were then transferred to a PC and post-processed using Matlab.
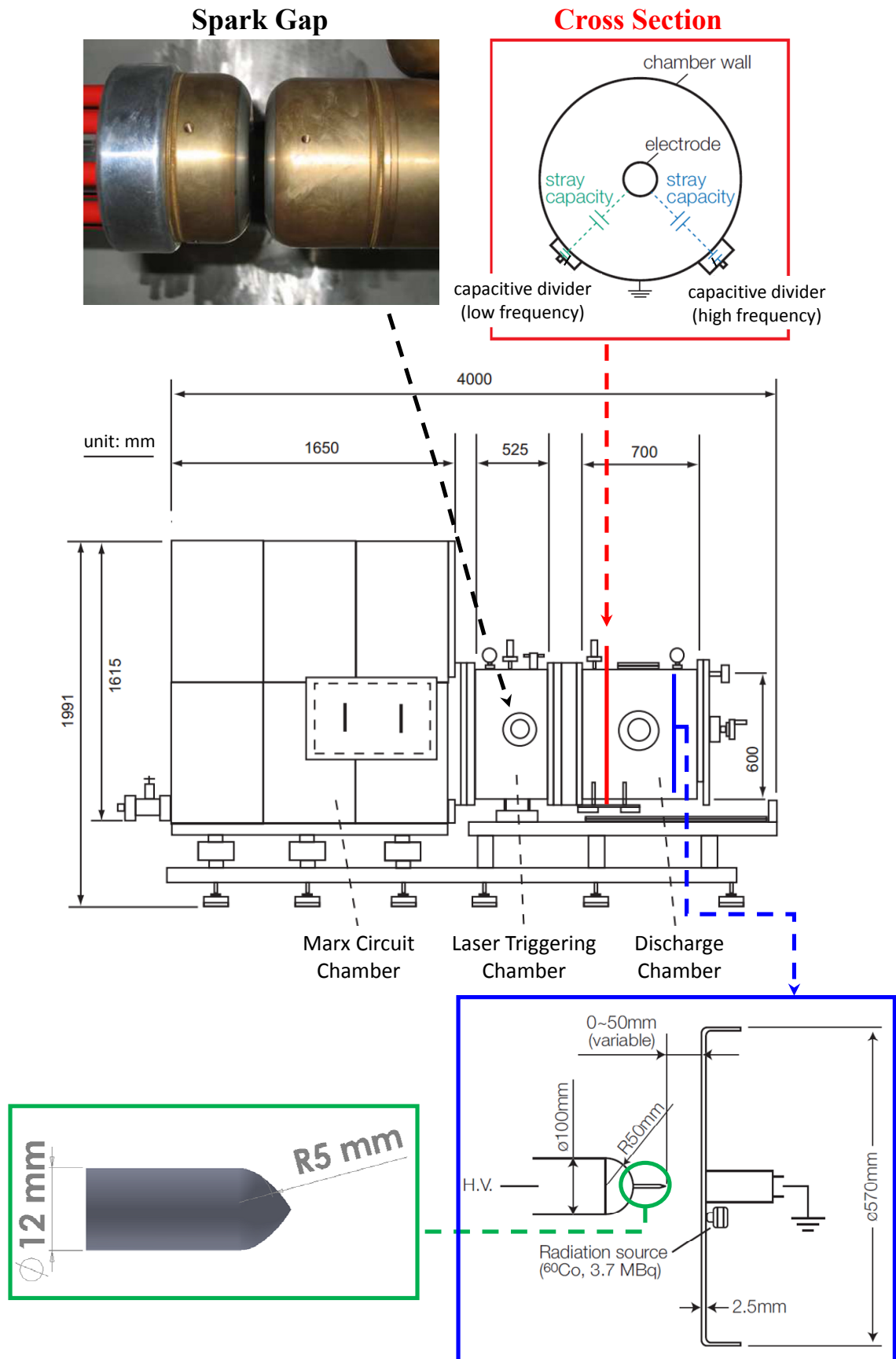
Figure 3.14: Cross-sectional view of the generator[66], [76], [82], [83].
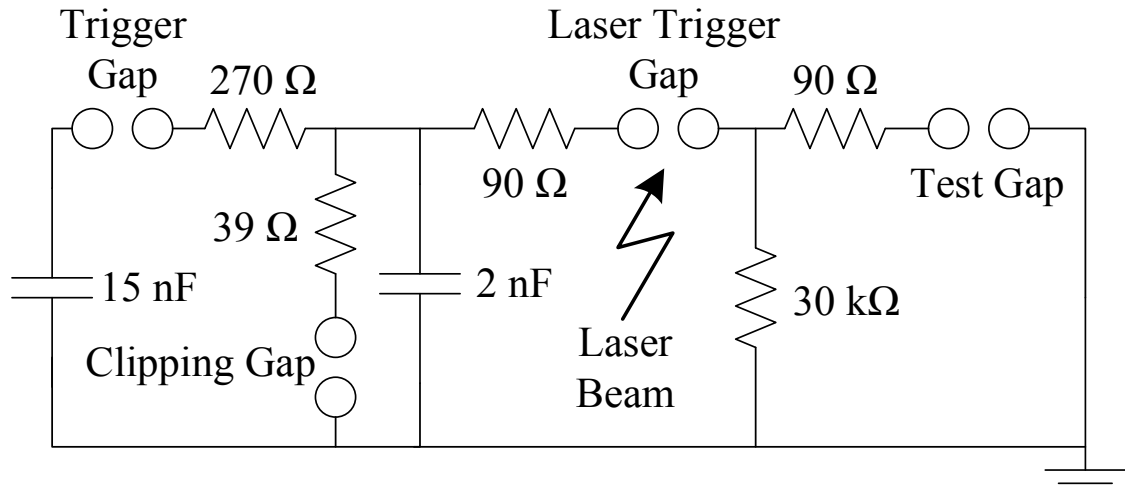
Figure 3.15: Test circuit for the steep-front square impulse voltage generator [76].
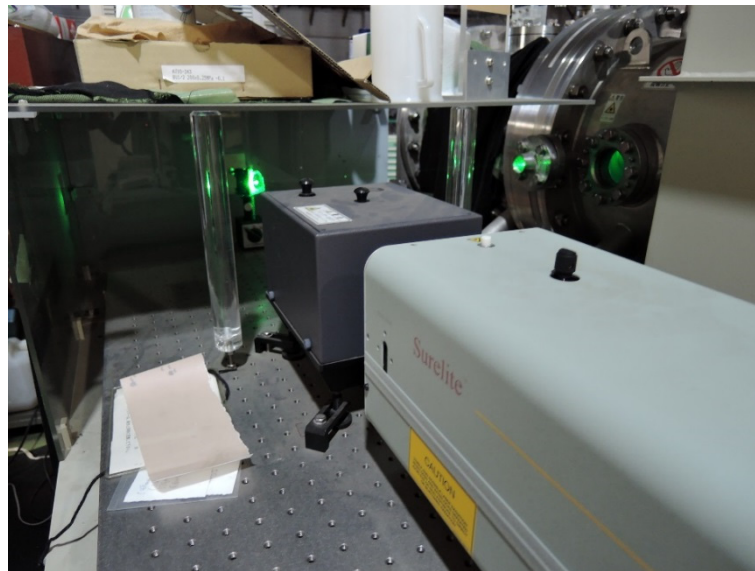
Figure 3.16: Photograph of the laser triggering the series gap.

3.4.2   Steep-front Square Impulse Voltage Waveform

The wave front of the recorded waveform is shown in Figure 3.17(a). It can be seen that the voltage reached its peak at around 16 ns. This is measured using the high-frequency divider which has a response time of less than 10 ns [66]. The full square waveform is shown in Figure 3.17(b), and it was set by the maximum time duration of the equipment, which is set at 10 μs. The specification of the generated voltage is shown in Table 3.1.
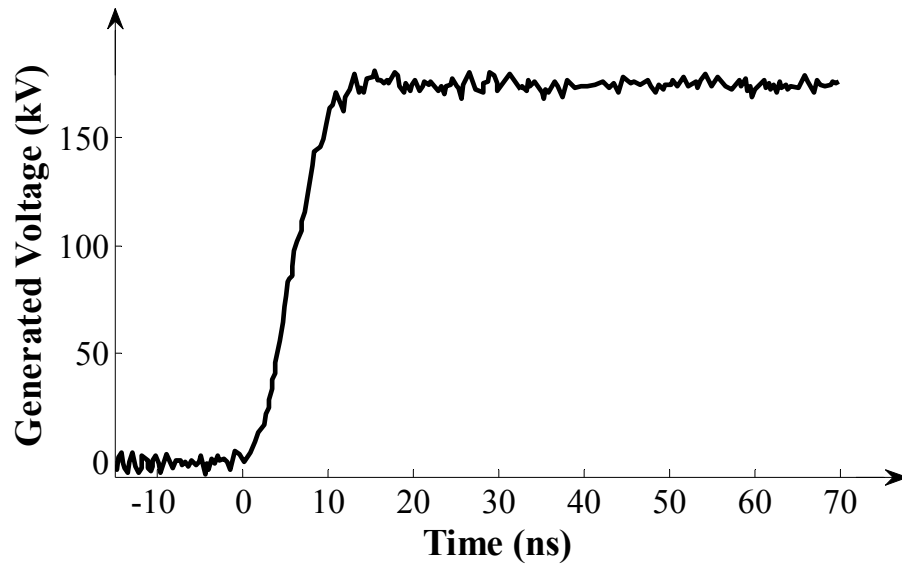
(a)   Wave front
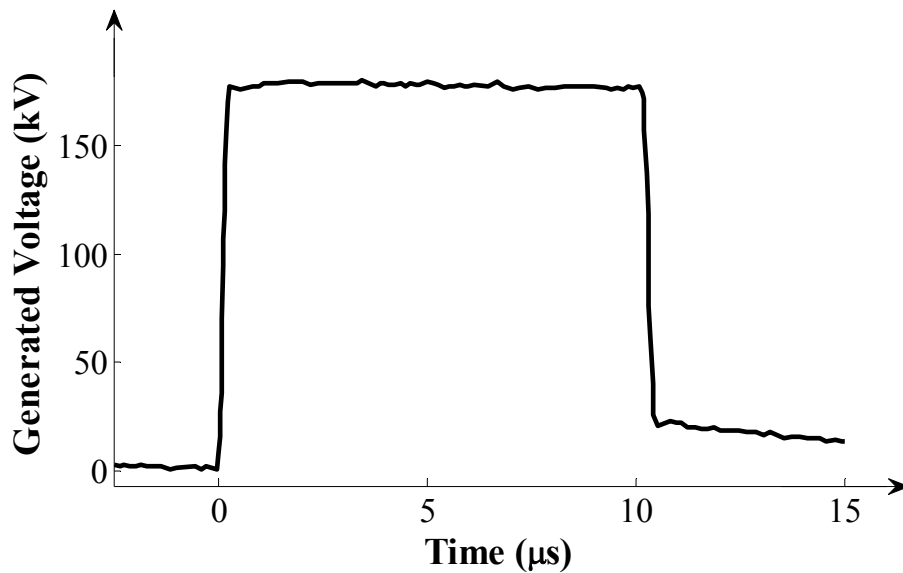
(b)   Full waveform

Figure 3.17: Steep-front square impulse voltage waveform [66], [76].

Table 3.1: Parameters of the steep-front square impulse generator.

Rise time	16 ns
Peak value	40–200 kV
Time Duration	Maximum 100 µs (set at 10 µs)
Damping factor	Less than 2.5% after 10 µs elapsed

3.5   Experimental Techniques

Two experimental techniques, namely, up-down and multi-level techniques, were applied according to the IEC/BS EN 60060-1 standard [81]. The up-down method was used to carry out experiments using the new CF_3I gas mixtures in order to obtain the 50% breakdown voltage while the multi-level method was applied to obtain the V-t characteristics of the CF_3I gas mixtures.

3.5.1   Up-down Method

As mentioned earlier in this chapter, due to the cost of purchasing additional CF_3I gas, the gas mixtures were recycled and stored. The aim of the present investigation is to obtain the breakdown characteristics of CF_3I gas and its mixtures in different electrode configurations that were tested under different polarities, gap distances and gas pressures. This required a large number of tests and would have required even more if the tests were to be conducted using virgin gas mixtures for each shot. Considering these factors, the up-down method is well suited for this purpose [81] since it is a testing method that is able to determine the 50% breakdown voltage, U_{50}, of an electrode configuration within a small number of discharges. Therefore, it requires minimal experimental time to achieve a good level of accuracy.

At the start of the experiment, an initial estimated breakdown voltage of U and a voltage interval ΔU of 3% were chosen. An impulse voltage with a peak value of U was injected into the test object. If there were no breakdown, the next impulse would be $U + \Delta U$. If a breakdown occurred, however, the next impulse would be $U - \Delta U$. This process would continue based on the previous breakdown event of the applied impulse. There is a minimum time interval of two minutes between each impulse shot, which allows the gas

to recover its insulation strength after a breakdown event. For every test arrangement, there were a minimum of 30 impulse voltage applications, and every peak value U_i ($i = 1, 2, \ldots, n$) obtained was recorded. From those data, a mean 50% breakdown voltage U_{50} was determined using (3.1).

$$U_{50} = \sum_{i=1}^{n} k_i U_i \ /m \qquad (3.1)$$

where k_i is the number of groups of stresses at the recorded voltage level, U_i, and m is the total number of voltage applications. The lowest voltage level taken into account should not differ from U_{50} by more than $2\Delta U$. A graphical demonstration of this method is shown in Figure 3.18.
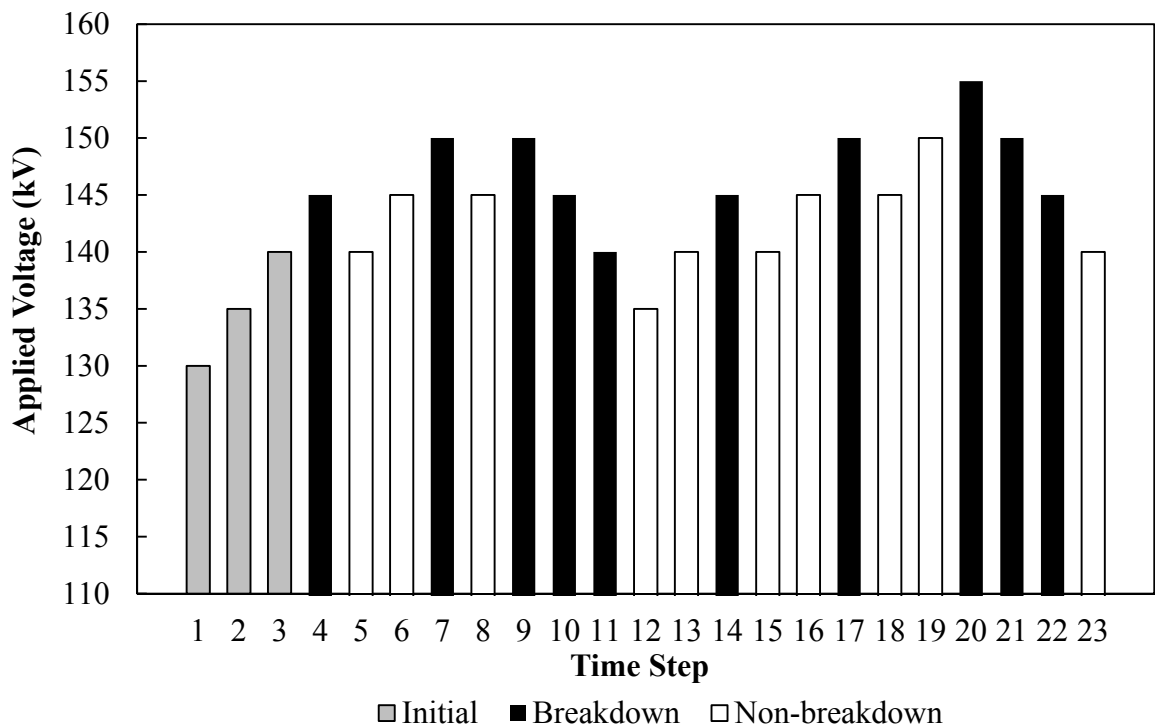
Figure 3.18: Example of an up-down test procedure.

The standard deviation of a test series can be calculated based on the following expression:

$$\sigma = \sqrt{\frac{1}{n}\sum_{i=1}^{n}(U_{i\_50} - \overline{U_{50}})^2} \qquad (3.2)$$

Where $\overline{U_{50}}$ is the mean of all the measured U_{50} values in a test series, and U_{i_50} is the individual values of U_{50}. A large number of measurements, $\sum n_i$, would be required to obtain a better estimation of the standard deviation.

The U_{50} can also be determined using either (3.3) or (3.4), depending on the breakdown or non-breakdown events.

$$U_{50} = U_0 + \Delta U \left(\frac{A}{k} - 0.5\right) \tag{3.3}$$

$$U_{50} = U_0 + \Delta U \left(\frac{A}{q} + 0.5\right) \tag{3.4}$$

U_0 is the lowest breakdown voltage recorded in the series, k is the number of breakdown events, and q is the number of non-breakdown events. The smaller of the two events will decide which equation is to be used for calculating the U_{50}; a detailed explanation for this can be found in [84]. Although both calculation methods provide similar U_{50} values, it was decided to follow the international standard and use (3.1) for calculating U_{50} values.

3.5.2   Multi-level Method

According to the standard, the multi-level method requires more than four voltage levels and $n_i \geq 10$ impulses per level [81]. An initial estimated breakdown voltage, U, and a voltage interval, ΔU, of 3% were chosen. The following voltage level was $U + \Delta U$, until it reached a voltage level where the majority of the applied voltages resulted in breakdowns. Figure 3.19 shows an example of multi-level testing with seven recorded voltage levels. Once the results were obtained, they could be plotted on a probability paper with the y axis ranging from 0.01% to 99.9% in a logarithm scale. The applied voltages could be plotted against the probability of gas breakdowns in the given voltage level. A line of best fit could be drawn based on the results and, from the graph, U_{50} could

be obtained graphically. The corresponding values of U_{16} and U_{84} could then be used to determine the standard deviation of the test series. The difference between $U_{84} - U_{50}$ must be equal to the value of $U_{50} - U_{16}$.
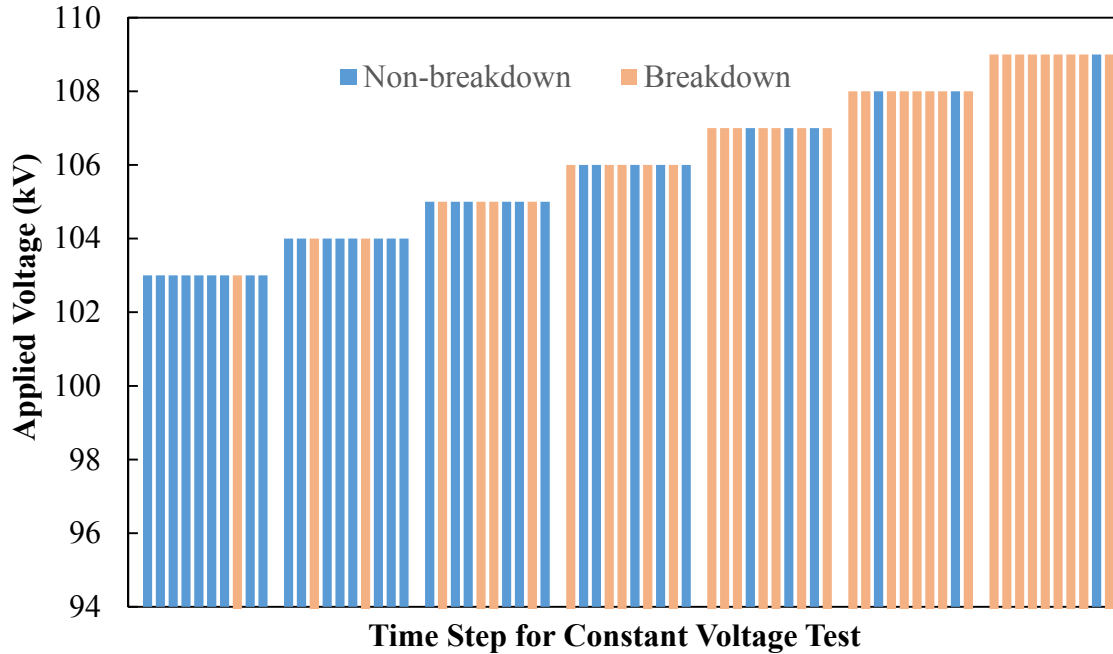
Figure 3.19: Example of a multi-level test procedure.

3.5.3   Measurement of V-t Characteristics

V-t characteristics represent the breakdown voltage as a function of breakdown time. Breakdown can occur before, at, or after the instant of peak voltage. The value of the voltage when the breakdown occurs and its associated time lag are recorded and used to plot the V-t characteristics. A lightning impulse voltage of 148 kV was applied to a test gap which resulted in a direct breakdown as shown in Figure 3.20. The measured impulse voltage is ±1.7% of the applied peak voltage, which is within the ±3% variation allowed for the test voltage value. It can be seen that the voltage recorded at the instant of breakdown is the same as the measured peak voltage at 1.6 µs.
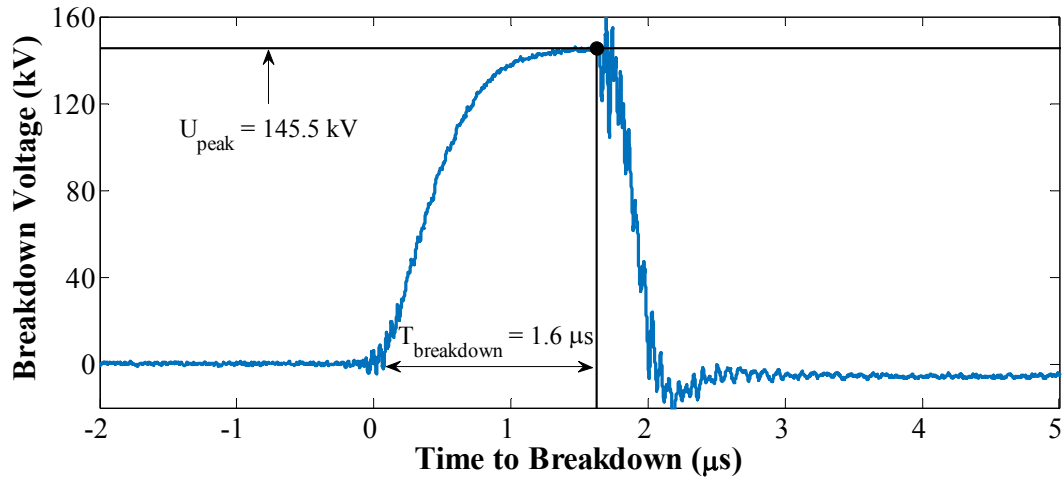
Figure 3.20: Example of breakdown voltage waveform after being subjected to a standard lightning impulse voltage of 148 kV.

A different example is shown in Figure 3.21; when the time to breakdown is longer than 2 µs, the voltage at the instant of breakdown will be lower than U_{peak}. The measured values of time and voltage are taken at the point where the voltage drops sharply to zero, inferred here as the breakdown voltage, which follows the IEC/BS EN 60060-1 standard. A significant number of measured V-t results will give a good indication of the breakdown characteristics as a function of time for CF_3I gas mixtures.
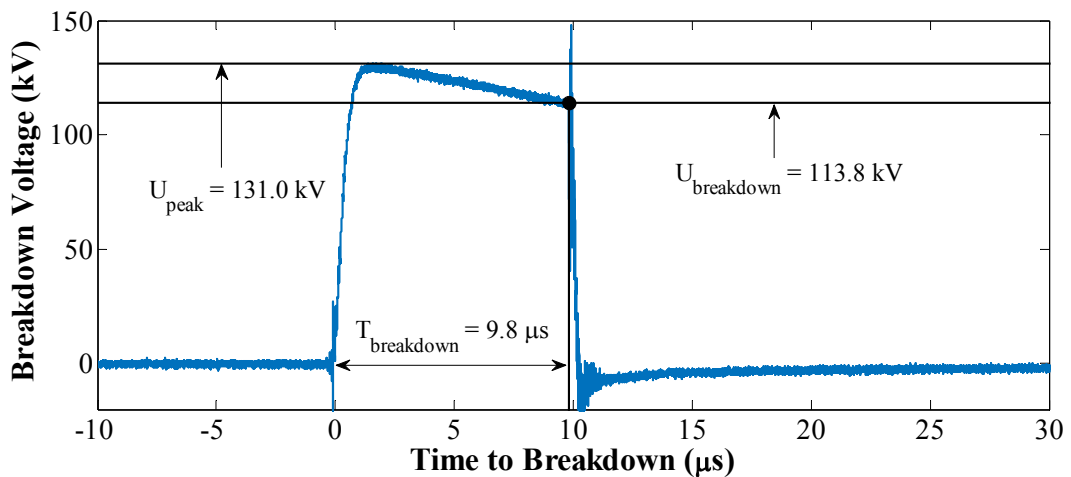
Figure 3.21: Example of breakdown voltage waveform after being subjected to a standard lightning impulse voltage of 132 kV.

3.6   Conclusion

This chapter has described the functions of several experimental setups: a purpose-built pressure vessel, a gas recycling unit and an experimental setup that generates a standard lightning impulse waveform to investigate the breakdown characteristics of CF_3I gas mixtures. The test rigs were developed at Cardiff University. The author undertook a research visit to Tokyo University and carried out a V-t characteristics investigation of a rod-plane configuration for steep-front square impulse waveforms in the context of a CF_3I gas mixture. The basic operations related to the generation and measurement of a steep-front square impulse voltage generator were described. Furthermore, the up-down and multi-level experimental techniques that were applied in the CF_3I gas experiments were also discussed.

The multi-level method was applied to obtain the breakdown characteristics of a rod-plane configuration for the steep-front square impulse waveforms, whereas the up-down method was applied for the lightning impulse waveforms. In order to minimise CF_3I gas costs, it was more cost-effective to use the up-down method for the lightning impulse experiment since it requires a smaller number of shots. Since both methods are recommended by the international standards, it is assumed that the difference in the obtained U_{50} would be negligible.

4 DESIGN AND CONSTRUCTION OF A REDUCED SCALE COAXIAL GIL

4.1   Introduction

Existing gas-insulated lines (GIL) are essentially constructed from two concentric pipes made from an aluminium alloy and filled with either SF_6 or a mixture of 20/80% SF_6/N_2 gas mixture which acts as the insulation medium. The research aims to investigate the feasibility of using CF_3I gas and its mixtures in GIL applications. Since GIL is coaxial cylinder electrode configuration, a reduced-scale coaxial prototype was designed to investigate the breakdown characteristics of CF_3I gas mixtures in a quasi-uniform field geometry similar to that of GIL. The scaled coaxial prototype was positioned inside a mild-steel cylindrical pressure vessel for the purpose of carrying out high-voltage experiments on CF_3I gas mixtures. This experimental investigation was intended to provide new results regarding the breakdown characteristics of CF_3I gas and its mixtures in a coaxial GIL test system.

This chapter first describes the initial process of the design and development of a reduced-scale coaxial GIL prototype, hereafter referred to as the Trial Prototype. Simulation and experimental work were carried out on the design. Subsequently, improvements were made to the Trial Prototype based on the findings. As a result, two modified coaxial GIL test systems were fabricated and used for the main experimental investigation in this thesis, hereafter referred to as Prototypes I and II. A finite element software package, COMSOL, was used to build models of the two prototypes. The simulation results

revealed that the electric field distribution inside the geometry can be controlled adequately through refined geometry and selection of materials.

4.2   Preliminary Design of a Coaxial GIL Trial Prototype

GIL have a similar structure to the busline of GIS. Complete GIS systems are much more complex, however, with the functionality of circuit breaker, disconnector, earthing switch, busbar, and current and voltage transformers. In comparison, the sole function of GIL is power transmission or connections with GIS. GIL have an inner conductor within an outer enclosure casing, both made out of aluminium alloy. Inside GIL, the locations with higher field strengths are usually associated with the location of the insulators. Other than that, the dielectric dimensioning of GIL is simply a quasi-homogenous electric field distribution.

4.2.1   Design Principles

The flowchart in Figure 4.1 shows the processes of developing the coaxial prototype. It starts with the conceptual design, taking into account the relevant design constraints, for instance, the physical constraint of fitting a scaled coaxial test system inside the pressure vessel or the associated cost involved in fabricating a large scale test system along with the extra cost of the higher volume of CF_3I gas required. The next step was to carry out simulation analysis in COMSOL to evaluate the electric field distribution within the model and identify the high field stress regions. Once the simulation results were deemed satisfactory, the design was fabricated by the mechanical workshop at Cardiff University. The aim was to carry out high-voltage experiments using up-down method on the coaxial test systems for different CF_3I gas mixtures to determine a suitable CF_3I gas mixture candidate to be used in a full-scale GIL demonstrator.
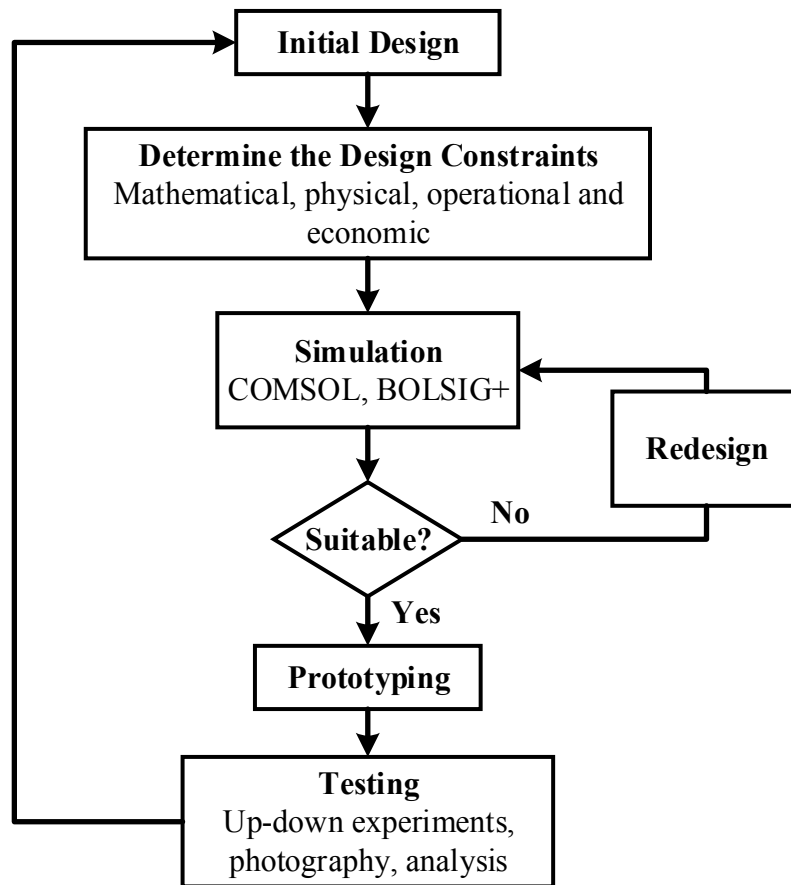
Figure 4.1: Processes leading to the testing of the coaxial GIL prototype.

From the dielectric design perspective, GIL effectively have a coaxial cylindrical electrode configuration, as can be seen in Figure 4.2, where the outer radius of the solid conductor is R_a and the inner enclosure radius is R_b.
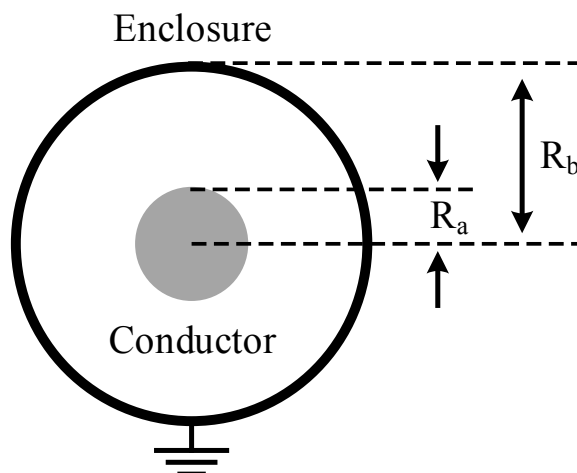
Figure 4.2: Cross-section view of a coaxial GIL geometry.

There are several influencing factors regarding the design of GIL. For the design of a reduced-scale coaxial test system, however, the most important parameter is the dielectric dimensioning. Typically, GIL have a maximum allowed field strength of 20 kV/mm [85]. In a coaxial design, the maximum electric field strength can be calculated based on the test voltage, the size of the conductor, and the enclosure of the GIL. The highest electric field should occur at the surface of the inner conductor located in the centre of the coaxial geometry, where breakdown is most likely to occur. Expression (4.1) was applied to determine the dimensions of R_a and R_b for the scaled prototype for a given maximum voltage and required field strength. The selection of R_a and R_b was also based on the practical constraints of fitting the test system inside the pressure vessel and the voltage limitation of the high-voltage bushing (approx. 170 kV lightning impulse) as described in Chapter 3.

$$E = \frac{U}{R_a \cdot \ln(\frac{R_b}{R_a})}$$
(4.1)

When the voltage stress along the conductor reaches the breakdown field strength, E_b, (4.1) can be re-written as

$$U_b = E_b \cdot R_a \cdot \ln(\frac{R_b}{R_a})$$
(4.2)

An important factor that needs to be taken into consideration for the design is the optimisation of the quantity $\ln(R_b/R_a)$ [74]; a value of unity is considered the optimal ratio for gap distance and field uniformity in a coaxial geometry. Assuming E_b to be a constant value, then, by keeping R_b constant, the optimal design of a coaxial geometry can be achieved by

$$\ln\left(\frac{R_b}{R_a}\right) = 1; \quad \left(\frac{R_b}{R_a}\right) opt = e = 2.718$$

and

$$(U_b)_{max} = E_b \cdot R_a \qquad (4.3)$$

Figure 4.3 shows the relationship of the breakdown voltage and the radius of the inner conductor R_a while having a fixed radius of the outer enclosure R_b. It can be seen that the maximum breakdown voltage is attained when R_b is 2.718 times larger than R_a.
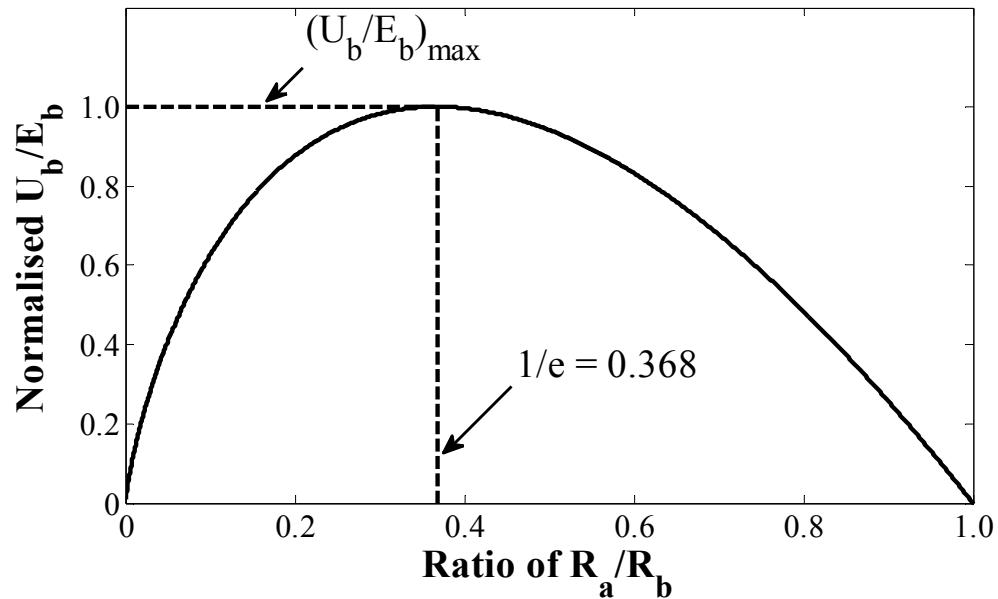
Figure 4.3: Relationship between the ratios of normalised U_b/E_b against R_a and R_b in a coaxial geometry.

Existing GIL systems have adopted this optimal ratio for their geometric dimensioning, as can be verified by reports from the literature [11], [86]–[89]. The report from AZZ CGIT, a major manufacturer of GIL worldwide, details the dimensions of all the GIL systems from a rated voltage of 145 kV to 1200 kV. The equivalent lightning impulse withstand voltages were plotted against the geometric ratios of the GIL and are shown in Figure 4.4. It can be seen that the majority of the dimensions are between a ratio of 1 to 2.718 (optimal) or 3. The R_a/R_b ratio is designed to be slightly larger (1:3) than the optimal ratio (1:2.718) to reduce the maximum electric field at R_a. For the dimensions of 800 kV and 1200 kV rated GIL systems, however, the geometric ratio is much larger than for the

71

GIL at a lower voltage rating. This indicates that at a very high voltage rating, the factor of gap spacing governs the field uniformity of the inner geometry of the GIL.
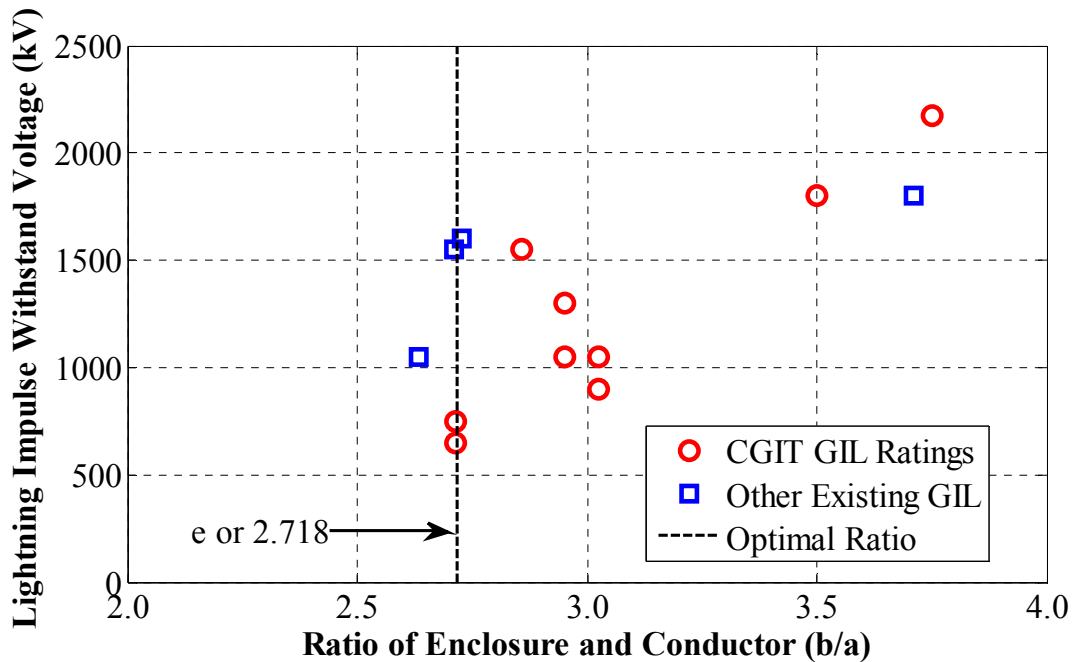
Figure 4.4: Relationship between lightning impulse withstand voltage and geometric dimension in existing GIL systems [11], [86]–[89].

4.2.2   Geometric Dimensions of the Trial Prototype

A full-scale 400 kV SF$_6$ GIL system manufactured by Siemens has a rated lightning impulse voltage of 1425 kV, an outer conductor radius of 90 mm, and an enclosure inner radius of 240 mm [11]. By applying expression (4.1), the maximum electric field found along the surface of the inner conductor was calculated, as in (4.4).

$$E_{max} = \frac{1425 \cdot 10^3}{90 \cdot \ln(\frac{240}{90})} = 16.14 \; kV/mm \qquad (4.4)$$

For the dimensions of the reduced-scale coaxial test system, a similar maximum electric field strength was achieved with a U$_{applied}$ of 85 kV, as can be seen from the calculated result in (4.5).

$$E_{max} = \frac{85 \cdot 10^3}{5.56 \cdot \ln(\frac{14.25}{5.56})} = 16.24 \; kV/mm \qquad (4.5)$$

The dimensions of metal are normally given in imperial units, as commonly used by suppliers in the UK. As can be seen in Figure 4.5, these imperial values were converted into SI metric units, which were used for the design of a simulation model. It can be seen that an inner conductor rod acting as the high-voltage conductor was centred within the outer cylinder, which was earthed. The insulators were designed with several circular shaped holes, providing pathways for gas circulation.
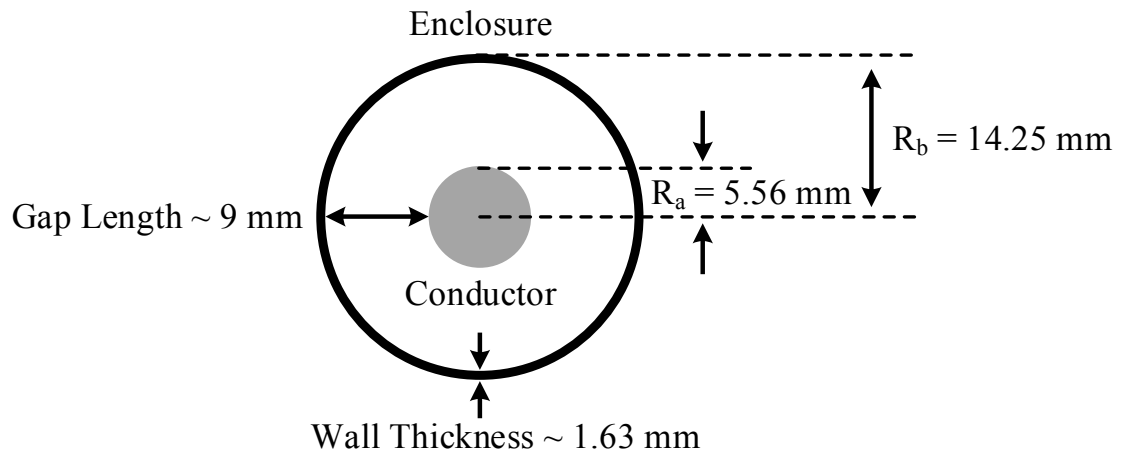
(a) Top view
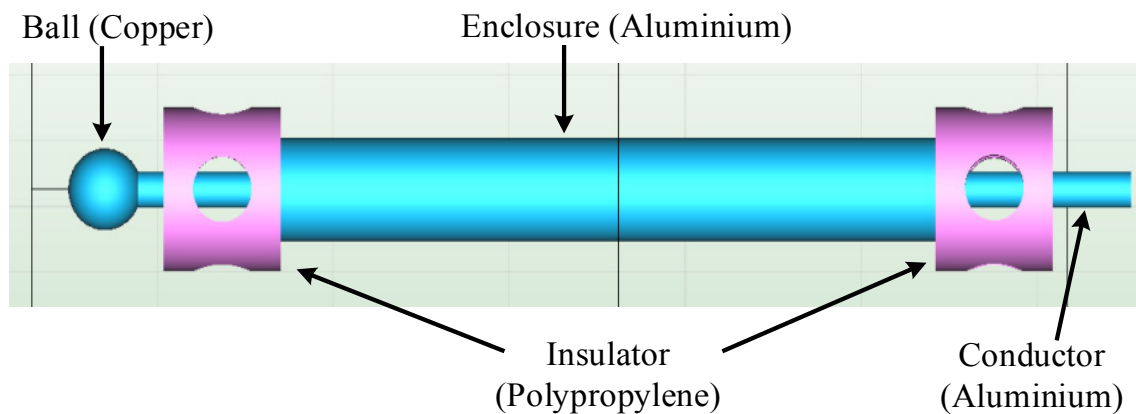
(b) Side view

Figure 4.5: Initial design of the Trial Prototype.

4.3   Finite Element Modelling: COMSOL Software

Finite Element Modelling (FEM) is a numerical method which provides an approximated solution to many different types of simulation studies: thermal analysis, fluid flow analysis, electrical analysis, etc. For this work, a commercial finite element software, COMSOL Multiphysics version 5.0 was used to perform electric field computations on the prototype coaxial geometries. FEM analysis is carried out in three stages:

- *Modelling* is the design of a model geometry, discretising the model into smaller sectors through the process of meshing, and defining the material properties and boundary conditions.

- *Solution* is the execution of the simulation using a particular mathematical model for a stationary or a time/frequency dependent study.

- Finally, the *visualisation* of the simulation results can be shown in 1D, 2D, or 3D plots depending on the model and the user's preference.

4.3.1   Geometrical Structure

Most FEM simulation processes start with the import of a CAD drawing of the object into the software, which may result in broken surfaces in the model that cannot be meshed. For this reason, the drawings of coaxial geometries were all constructed using the graphical interface available on COMSOL. A 2D axisymmetric model was chosen because the coaxial prototype, pressure vessel and high-voltage bushing were radially and circumferentially symmetrical in shape. The accuracy of the results of a 2D model will be similar to that of a 3D model as long as the geometric shape is completely cylindrical. In addition, by using a 2D cut-plane function, the user can directly compare the simulation results between 2D and 3D. The advantage of using an axisymmetric model is that the computation time is significantly reduced.

Figure 4.6 shows the geometrical structure of the axisymmetric model, which was established to represent the actual model closely. In the model, the high-voltage bushing was positioned centrally at the top of the pressure vessel. An inner cylinder, acting as the conductor, was then attached onto the bushing and centred inside the vessel. Around the conductor, the thin wall of a cylindrical enclosure formed the outer cylinder of the coaxial system. The two cylinders were kept apart and centred by two support insulators; this also reduces the likelihood of breakdown between the conductor and the vessel. Two toroid rings were also added on both edges of the outer cylinder to reduce the end effects along the rims of the outer cylinder.
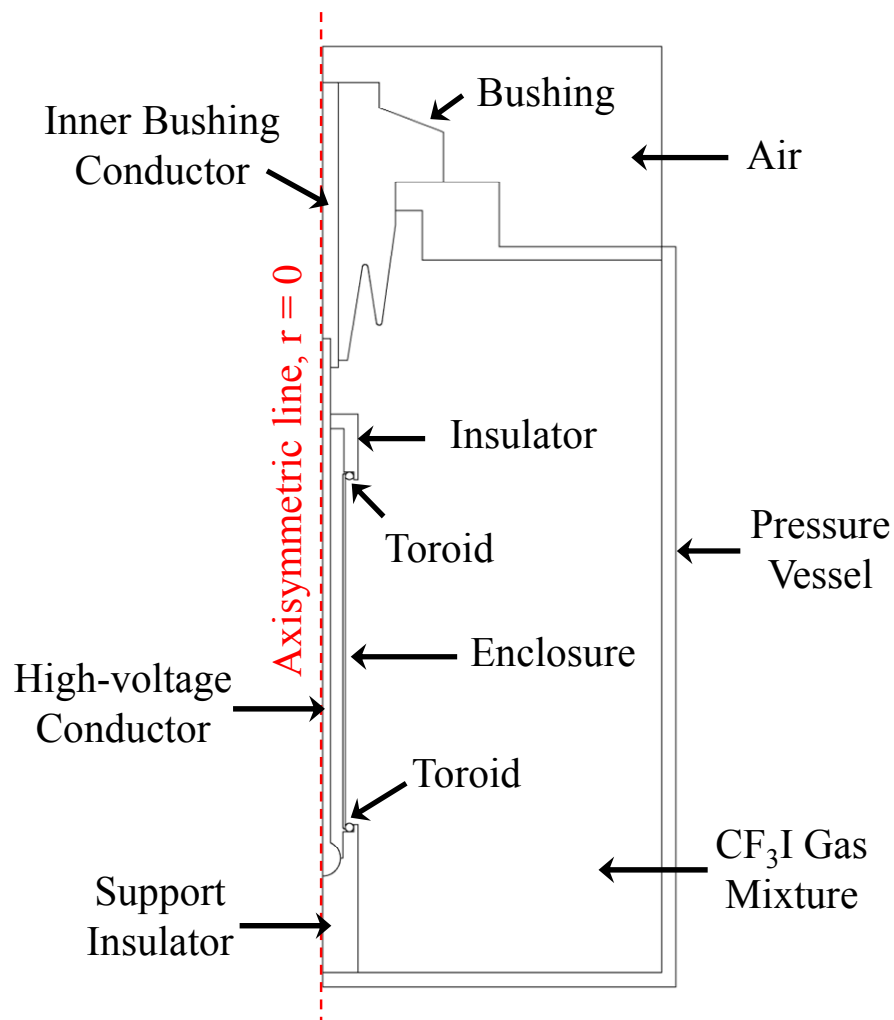
Figure 4.6: 2D axisymmetric model of the Trial Prototype within a fully assembled pressure vessel built using COMSOL.

4.3.2   Specifying Simulation Conditions

The parameters for the physics of the study, material properties and boundary conditions need to be defined before processing any simulation. For the *physics* function of the study, the electrostatics interface was chosen to model the electric fields with a stationary study [90]. Many engineering systems consist of more than one material. The properties of materials can be defined and assigned to represent each domain. An important property for any electrostatic study is the relative permittivity. For a gas, unless it is under very high pressure, the relative permittivity will be 1 [30]. Table 4.1 shows the relative permittivity of the materials used [91] and the components that they were assigned to.

Table 4.1: Properties of materials used for COMSOL modelling.

Materials	Relative Permittivity, ε_r	Components
Silicone rubber	3.1	Bushing
Polypropylene	2.2	Insulators
Air /CF_3I	1.0	Remaining domains

For the boundary conditions, only the high-voltage terminal and the ground need to be defined. The ground is set as 0 V and is defined on the outer enclosure, the toroid of the coaxial prototype and the metal wall of the pressure vessel. The terminal is where the high voltage will be applied during the experiment, which would be the conductor and inner bushing conductor. A value of 85 kV was assigned to the inner conductor so that the selected coaxial geometry would obtain a maximum electric field similar to that of a 400 kV full-scale GIL. Varying this voltage value would alter the value of E_{max}, but it would not change the distribution of the electric fields along the conducting electrode.

4.3.3   Meshing

Mesh generation is an important process in FEM simulation; it involves the meshing/discretising of the model geometry into smaller sectors of regular shapes, such as triangles or squares. The reason for the subdivision of the model is to represent a complex geometry more accurately. If the model is complex, there may be no standard mathematical formula to perform the calculation directly. There are formulas for calculations on a standard shape, such as a triangle or a square. By meshing the domain into smaller elements, an approximated solution can be generated easily. The solutions of all the smaller elements can then form the overall solution of the domain. This places great emphasis, however, on the quality and accuracy of the mesh in order to generate accurate results. Triangular meshing is the preferred way to create meshes. In comparison, quadrilateral elements will provide higher accuracy in the simulated results, although it is also more difficult for them to be generated automatically [92].

A finer mesh can be generated depending on the selection of the meshing process; extra manual refinement can also be carried out in the region of interest. For the model shown in Figure 4.6, extra refined meshing was applied to the domain along the conducting electrode, since this is where the maximum electric field is expected to occur. Further refinement will produce higher accuracy in the simulated results but, at the same time, will increase the processing time. To reduce the processing time, a coarser mesh was applied in domains such as CF_3I outside the coaxial enclosure and in regions that would not compromise the simulated results. Figure 4.7 shows the discretisation of the Trial Prototype; in the area of interest, extra refinement was applied to ensure the accuracy of the results, whereas in regions far from the conductor, the mesh elements are coarser.
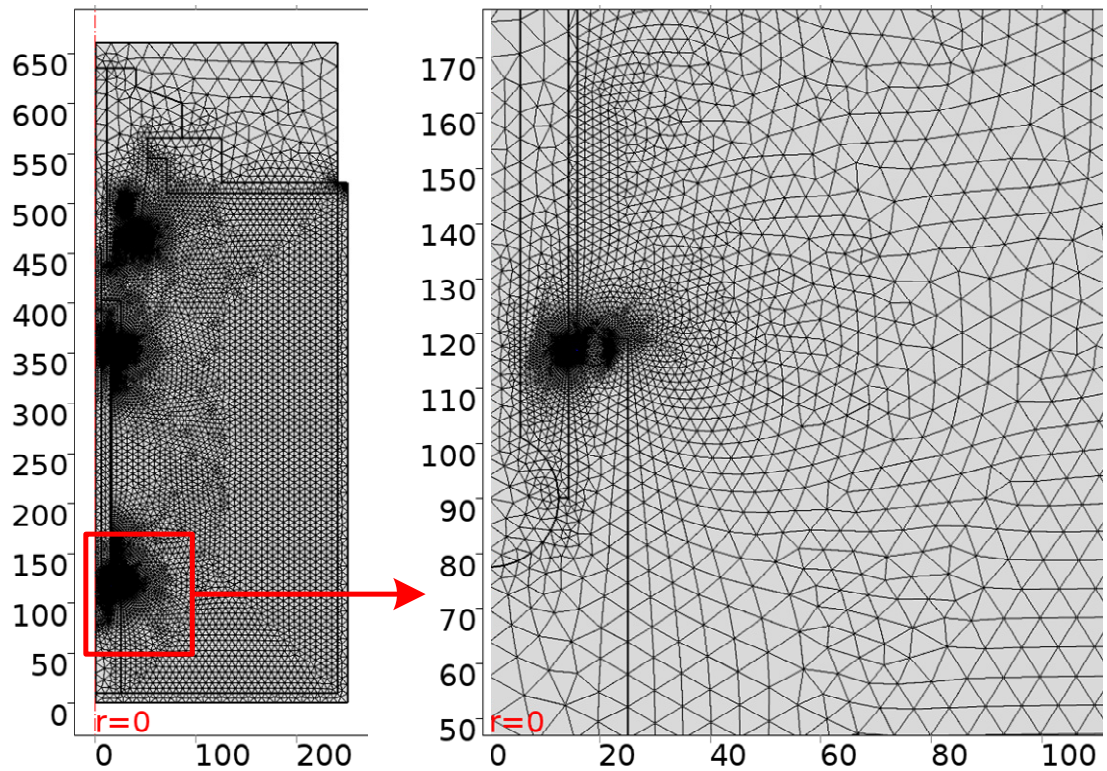
Figure 4.7: Triangular meshing of FEM model of Trial Prototype with extra refinement near the conductor terminal.

4.3.4   Simulation Results

A simulation was carried out on the Trial Prototype to identify high field stress regions. For the simulation, the voltage on the conductor was set at 85 kV and the enclosure was grounded. High field stress regions were identified on the edges of the enclosure, and these were alleviated by adding two grading rings on these edges, as shown in Figure 4.8. This was to minimise the end effects at the edges of the enclosure, which otherwise has the potential to affect the results. The next step was to compare the simulated and calculated values of E_{max}. It was determined from (4.5) that the calculated E_{max} was 16.24 kV/mm; in Figure 4.8, it can be seen that the calculated E_{max} from COMSOL of 16.10 kV/mm was reasonably close. It is noteworthy to highlight that the E_{max} is identified along the conductor region that is near to the edge of the enclosure.

Contour: Electric Field Normalised (kV/m)
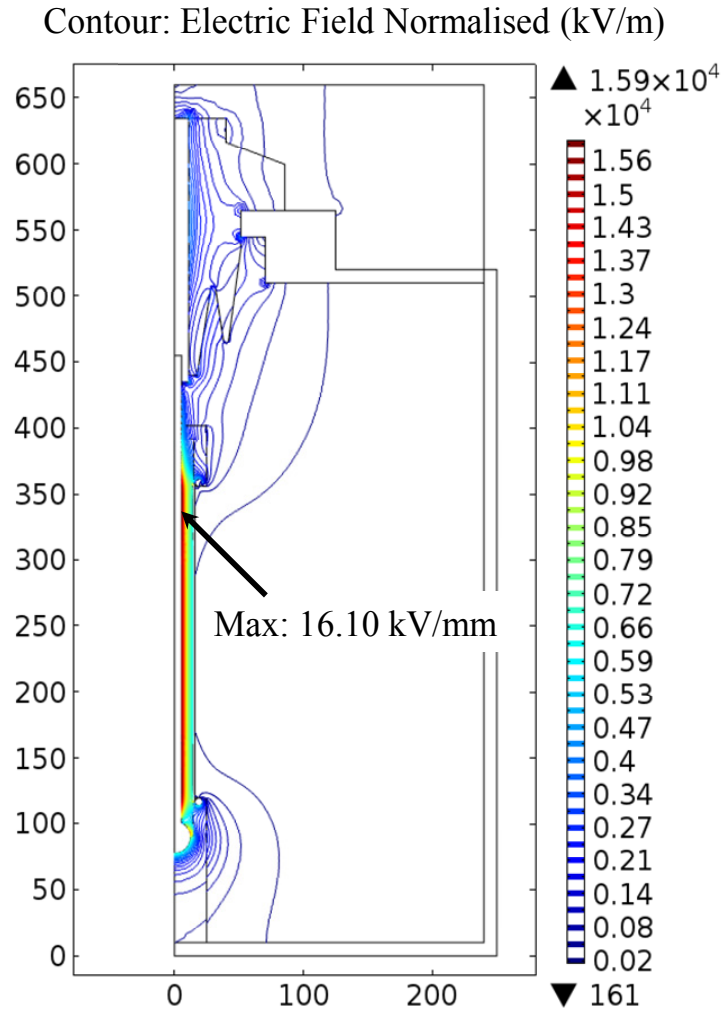
Figure 4.8: Plot of the electric field distribution showing that the maximum electric field was found along the centre of the conductor (E_{max} = 16.10 kV/mm).

4.4   Evaluation of the Trial Prototype

To gain a better understanding, the coaxial design of this Trial Prototype was fabricated and preliminary tests were carried out. The breakdown results and other data were then evaluated to inform further design improvements.

4.4.1   Preliminary Results

Based on the simulation model, the coaxial GIL prototype was fabricated; this is shown in Figure 4.9. The enclosure and conductor were both made out of aluminium; a metal

strip was welded onto one of the toroid rings, and this was used for connection to ground. On the tip of the conductor, there is a 10 mm thread that is used for attaching the coaxial prototype onto the high-voltage bushing inside the pressure vessel. Support insulators were made out of a natural polypropylene rod, a material with a dielectric strength of 52 kV/mm [93], that is, three times higher than the E_{max} of Trial Prototype, as illustrated in Figure 4.8. Holes were drilled in some of the insulators to provide airways for the circulation of CF_3I gas mixtures inside the prototype.
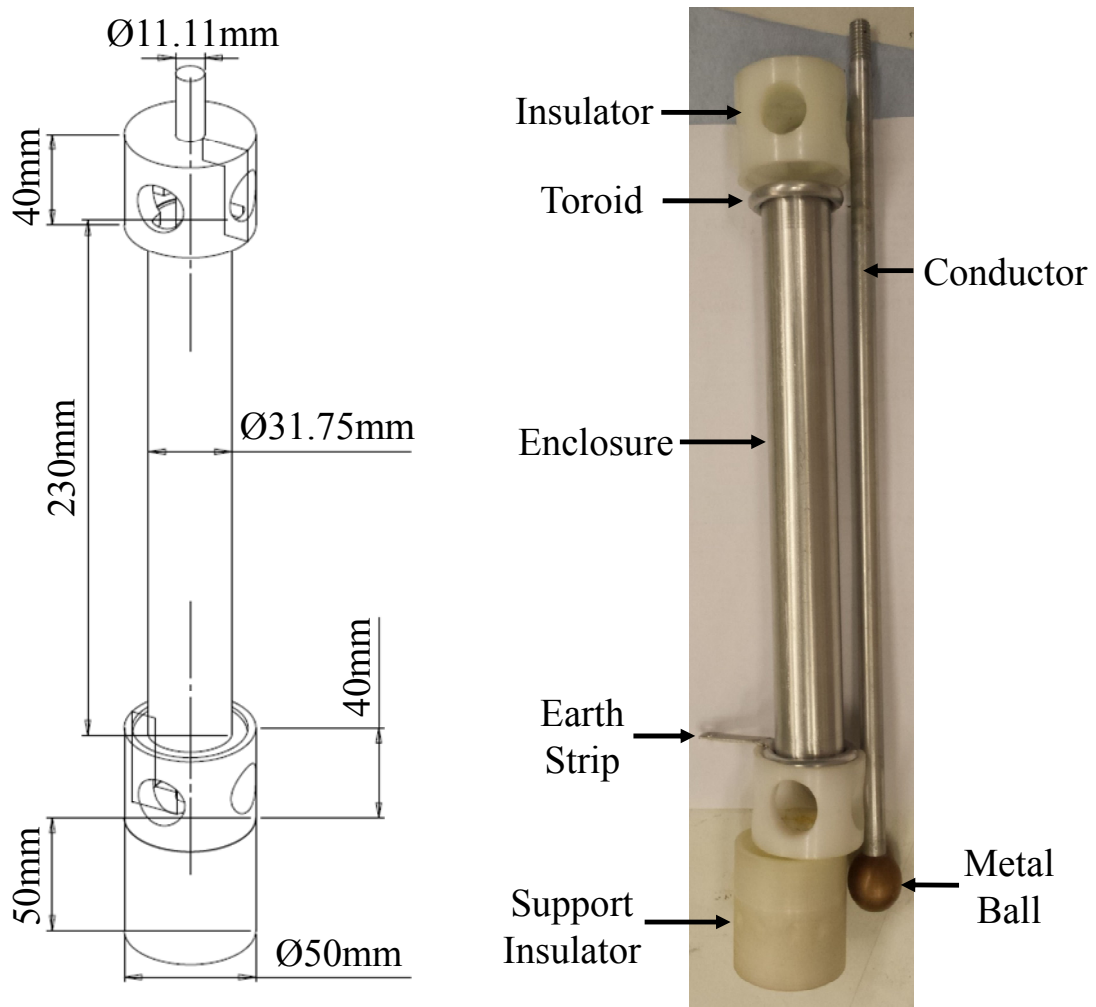
Figure 4.9: Solidworks design and photograph of the fabricated Trial Prototype.

A standard lightning impulse waveform (1.2/50) was used for the preliminary experiment, and the up-down method was applied to obtain the 50% breakdown voltage U_{50}. The

experiment was carried out over a pressure range of 0.5 to 3.0 bar (abs.) in steps of 0.5 bar for positive lightning impulse polarity.

The results are displayed in Figure 4.10 and, as expected, the U_{50} increases against increasing pressure. At 2 bar (abs.), the U_{50} value is around 84 kV and a test was also conducted for air under the same gas pressure. The measured U_{50} was 38 kV; thus, the U_{50} of a 30/70% CF_3I/CO_2 mixture is 2.2 times higher than air in a coaxial geometry. The trend indicates that the breakdown voltage is increasing but with a decreasing rate towards higher pressures.
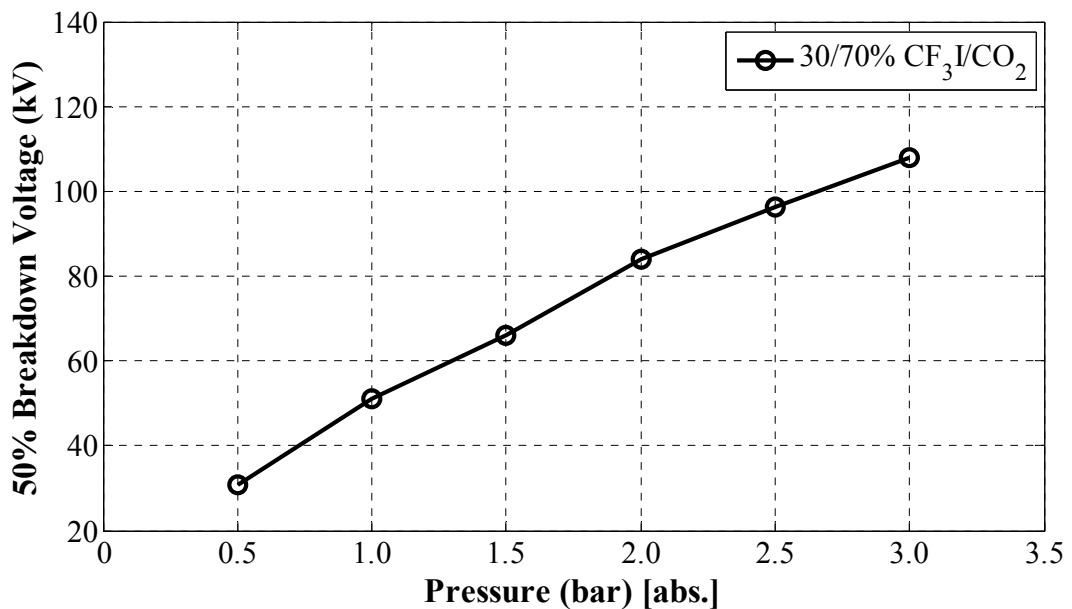
Figure 4.10: 50% breakdown voltage, U_{50}, as a function of pressure for a 30/70% CF_3I/CO_2 gas mixture in a coaxial test system of 11.1/28.5 mm and for positive lightning impulse polarity (Trial Prototype).

4.4.2   Evidence of Breakdown Events

For any breakdown experiment in a coaxial test system, there should be a random distribution of breakdown occurrences along the conductor. If the majority of the breakdowns occurred near the edges of the enclosure, however, it is safe to assume that

the recorded results were distorted by the end effects. A coaxial geometry is a fully enclosed system with no way of observing and determining the location of the breakdown during the experiment. It is, however, possible to determine the locations of breakdown events by visual examination of the inner conductor after tests and identify pits (arc sites) on the conductor. As shown in Figure 4.11, there is a random distribution of black markings along the conductor. The rule indicates the distance from the metal ball at the conductor end.
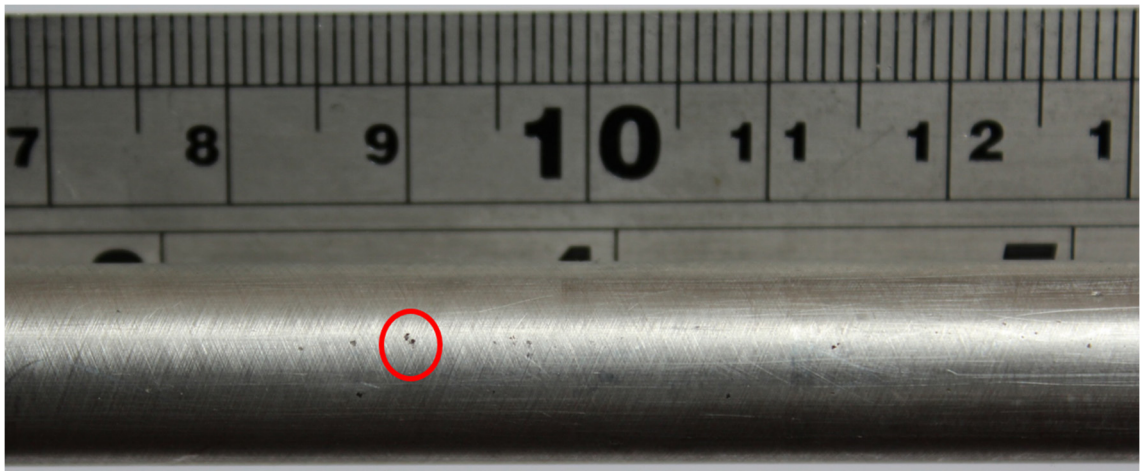
Figure 4.11: Photograph of breakdown evidence on the conducting electrode.

A microscope was used to obtain a clearer view of the black pitting at the circled location, as shown in Figure 4.12. It can be seen in Figure 4.13, however, that there are markings on the metal ball and around the edges of the enclosure. This suggests that some of the breakdown events may have occurred due to the end effects because the toroid ring did not reduce the field stress sufficiently, as was expected from the simulation results. Design modifications were required to ensure that breakdowns in future experiments would occur in the area of interest.
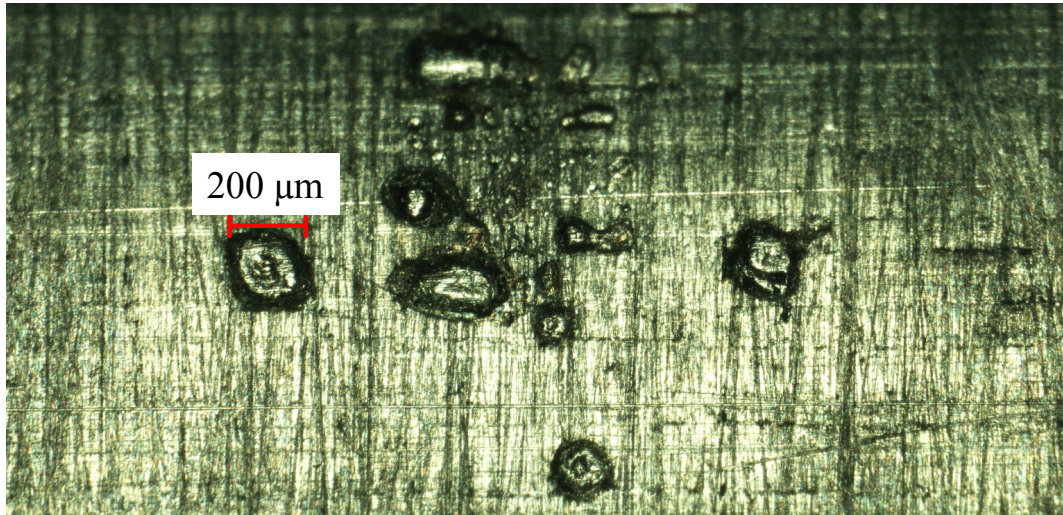
Figure 4.12: Microscopic imaging of the pits (arc sites) in the area that was circled in Figure 4.11.

Figure 4.13: Markings on the enclosure wall and metal ball indicating occurrences of flashover around the edges of the enclosure.

4.5   Development of Prototypes I & II

This section discusses the changes made to the Trial Prototype and the development of Prototype I. Prototype II was then designed using the same geometric ratio as Prototype I but three times bigger.

4.5.1   Identifying the Problems and Design Modifications

In Section 4.4.2, the photographs taken after the experiment showed breakdown occurrences at the end of the enclosure wall. This could be due to non-uniformities in the practical geometry because the simulation model assumes that the coaxial cylinder and toroid rings are perfectly circular. In reality, the enclosure and the toroid rings are made of aluminium sheets rolled and welded into a tube shape. The conductor was cut into a smaller length from a long rod of aluminium metal. Three main problems were identified based on the preliminary investigation on the Trial Prototype:

(i) The field stress at the contact regions between the end of the enclosure and the toroid rings can be much higher than anticipated from the simulated results; a potential improvement is to discard the toroid rings and simply increase the thickness of the enclosure wall, so that the inner enclosure wall can be flared out at each end. The flaring of the wall will achieve widening of the gap distance towards the end of the enclosure, thereby, reducing the likelihood of breakdown on the edges of the enclosure and avoiding extra contact regions.

(ii) The other problem is to ensure that the gap spacing between the inner and the outer cylinders remains constant. Assuming that the conductor has a bending radius of a few mm, it would have a large effect on the randomness of the breakdown distribution. This is especially the case considering that the reduced-scale coaxial prototype has a relatively small gap spacing of less than 10 mm. This may be improved by having the parts machined to the exact dimensions. In this research, to simplify the measurement and fabrication process, the dimensions were designed to the nearest mm.

(iii) As shown by the breakdown evidence illustrated in Figure 4.13, flashover occurred from the metal ball to the enclosure end. The metal ball was used for reducing the field stress at the conductor end, but the flashover distance between the enclosure end and the metal ball was not long enough. To avoid this, the ball was removed and the conductor was designed to be positioned deeper inside the support insulator. In this way, the flashover distance between the conductor end and the enclosure wall was maximised. Although this reduced the distance between the conductor and the base of the vessel to 40 mm, the high dielectric strength of the polypropylene material of the support insulator means that an extremely high electric field resulting from a high value of applied voltage would be required to cause a dielectric failure and a flashover to the base of the vessel.

4.5.2   Dimensions of Prototype I

Based on the suggested improvements described in Section 4.5.1, a new coaxial geometry was designed using a conductor radius to enclosure radius of 1:3, that is, a ratio similar to the majority of existing 400 kV GIL systems. Practical radius values of R_a = 5 mm and R_b = 15 mm and an applied voltage of 85 kV were chosen for the simulation model. The utilization factor, f, of a 400 kV GIL system and Prototype I can be calculated using (4.6); the values are calculated as 0.58 and 0.55 respectively.

$$f = \frac{R_a \cdot \ln(\frac{R_b}{R_a})}{R_b - R_a} \tag{4.6}$$

The maximum electric field strength, E_{max} along the conductor is calculated by (4.7), and the value is similar to the E_{max} of a full scale GIL system.

$$E_{max} = \frac{85 \cdot 10^3}{5 \cdot \ln(\frac{15}{5})} = 15.5 \; kV/mm \tag{4.7}$$

85

Based on the values of R_a and R_b, the new model geometry was built and simulated as shown in Figure 4.14. It can be seen that the inner enclosure wall is flared out at each end of the enclosure. The process of the simulation was the same as described in Section 4.3. The E_{max} is shown to be at the centre of the conductor, which is in the region of interest.
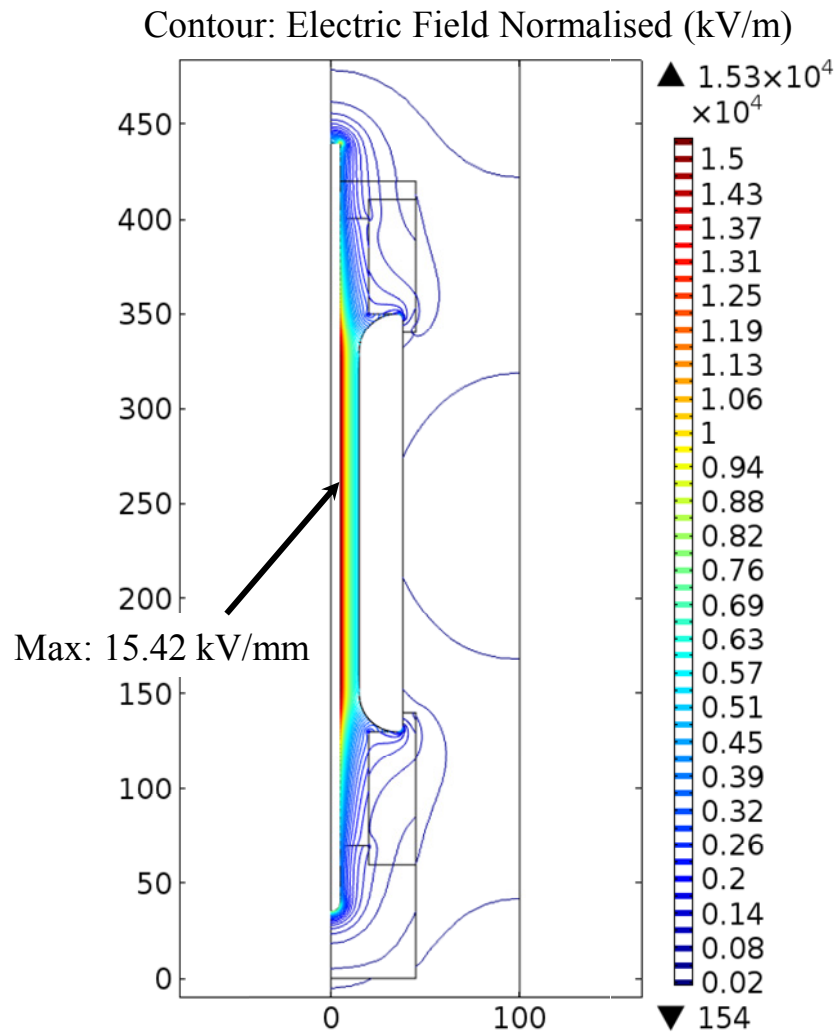
Figure 4.14: Plot of electric field distribution showing the maximum electric field was found along the centre of the conductor (E_{max} = 15.42 kV/mm).

4.5.3   Fabrication Process

This section discusses the fabrication process and the steps taken to achieve the good accuracy regarding the prototype dimensions. Solidworks was used to design all the individual parts so they could then be exported to different machinery in order to carry

out the relevant fabrication process. In Figure 4.15, the section view of the fully

assembled prototype is shown in part (d). Around the assembled prototype, individual

parts are displayed with their dimensions.
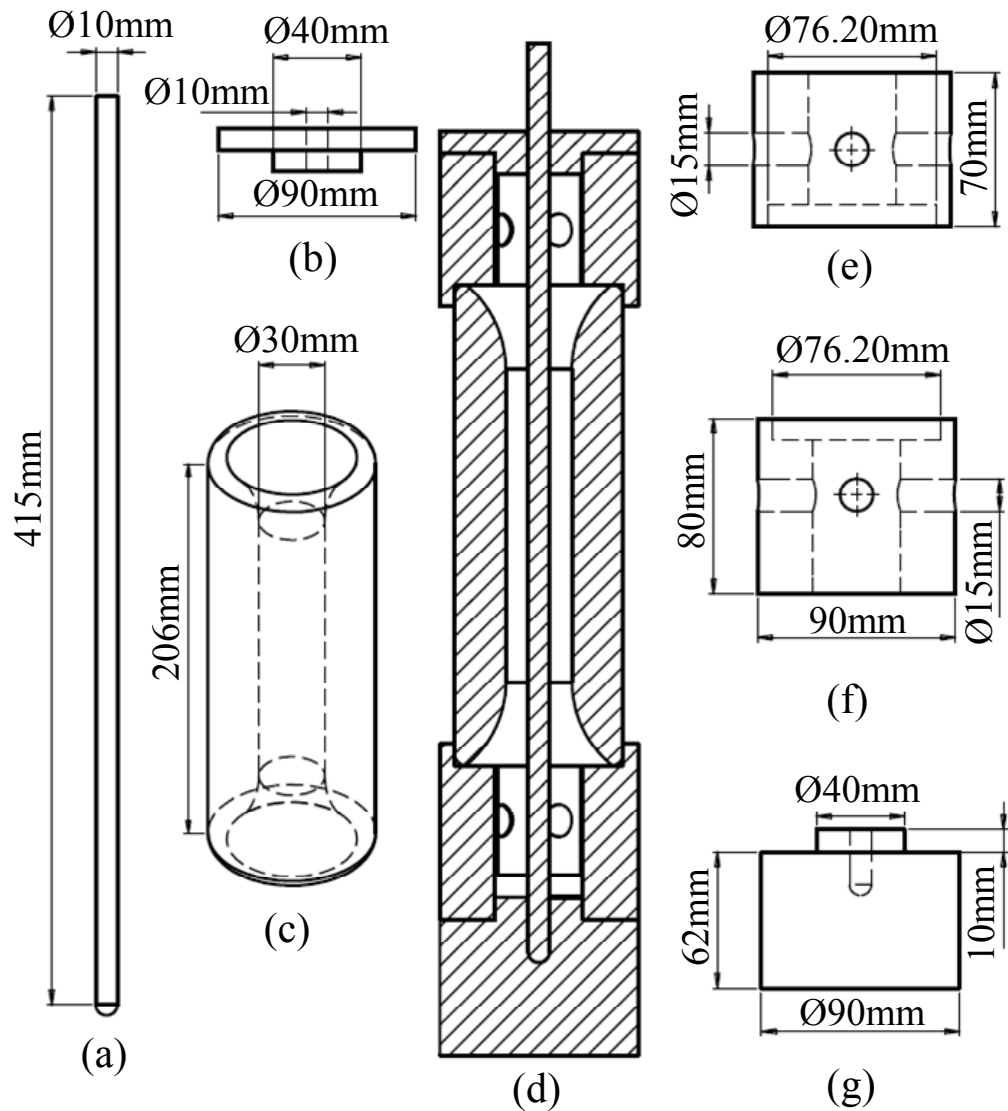
Figure 4.15: Design schematic of Prototype I – (a): conductor, (b): top insulator, (c): enclosure, (d): cross-section view of the fully assembled prototype, (e): support insulator_1, (f): support insulator_2 and (g): bottom insulator.

The same design principle was applied in the design of Prototype II, with the exception

that Prototype II has an inner enclosure and outer conductor diameter three times the size

of Prototype I while maintaining the same geometric ratio, as can be seen in Figure 4.16.

Experimental results from Prototype II were used as part of an evaluation process for a streamer and leader breakdown model, which will be discussed further in Chapter 6.
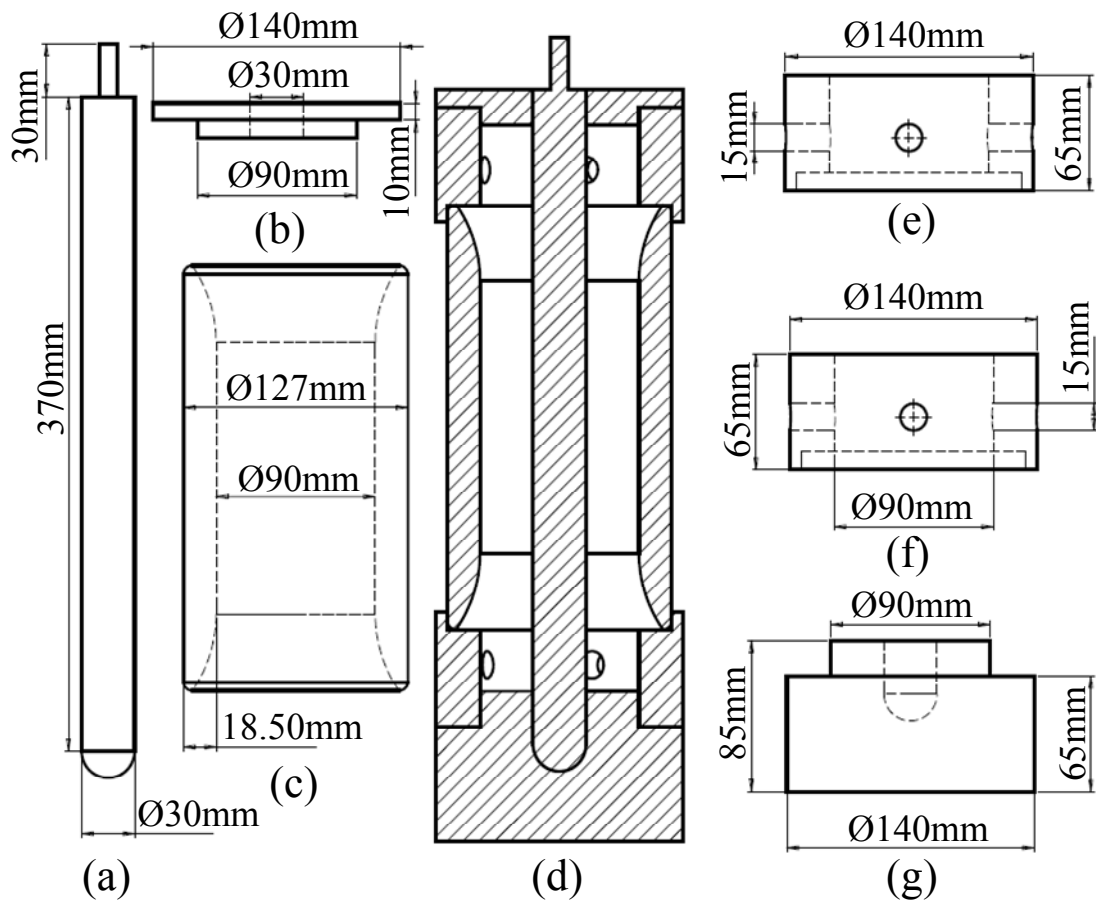
Figure 4.16: Design schematic of Prototype II – (a): conductor, (b): top insulator, (c): enclosure, (d): cross-section view of the fully assembled prototype, (e): support insulator_1, (f): support insulator_2 and (g): bottom insulator.

Out of all the fabrication stages, the most important aspect was to ensure the accuracy of the diameter of the inner enclosure and the outer conductor. For Prototype I, an aluminium bar of 76.2 mm diameter and 250 mm length was purchased. The extra length was required for the 3 jaw self-centring chuck to hold the bar tightly in position before any drilling. Initially, a ball nose cutter with a diameter of 28 mm was used to machine away a large majority of the required portion of the metal in the centre. A 30 mm cutter was not used directly because the drilling process creates a rough finish. Instead, a wire-cutting

machine was used to expand the inner enclosure diameter from 28 mm to the exact

required 30 mm gap spacing and provide a smooth finish. The setup described above can

be seen in Figure 4.17; after drilling, the extra length that was used for holding the bar

was then cut off.
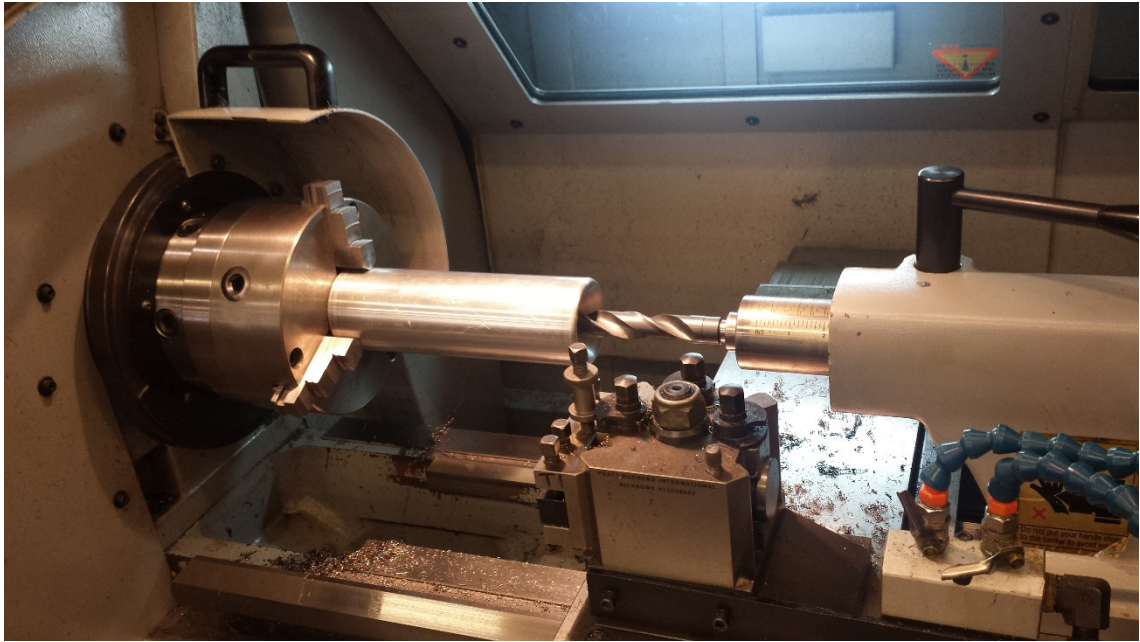
Figure 4.17: Photograph of aluminium bar held in position before the drilling process (Prototype I).

The next step was to add a curvature radius onto both ends of the enclosure; this was

achieved by using a computer numerical controlled (CNC) milling machine, as shown in

Figure 4.18. A 3 jaw chuck was again used to hold the aluminium bar inside the

machinery. The Solidworks drawing was imported electronically into the control panel

of the CNC machine to then start the automatic milling process. A 10 mm ball nose cutter

was used to drill in a circular motion, and this gradually went down in steps. This was

then able to produce the curvature while ensuring a smooth finish.
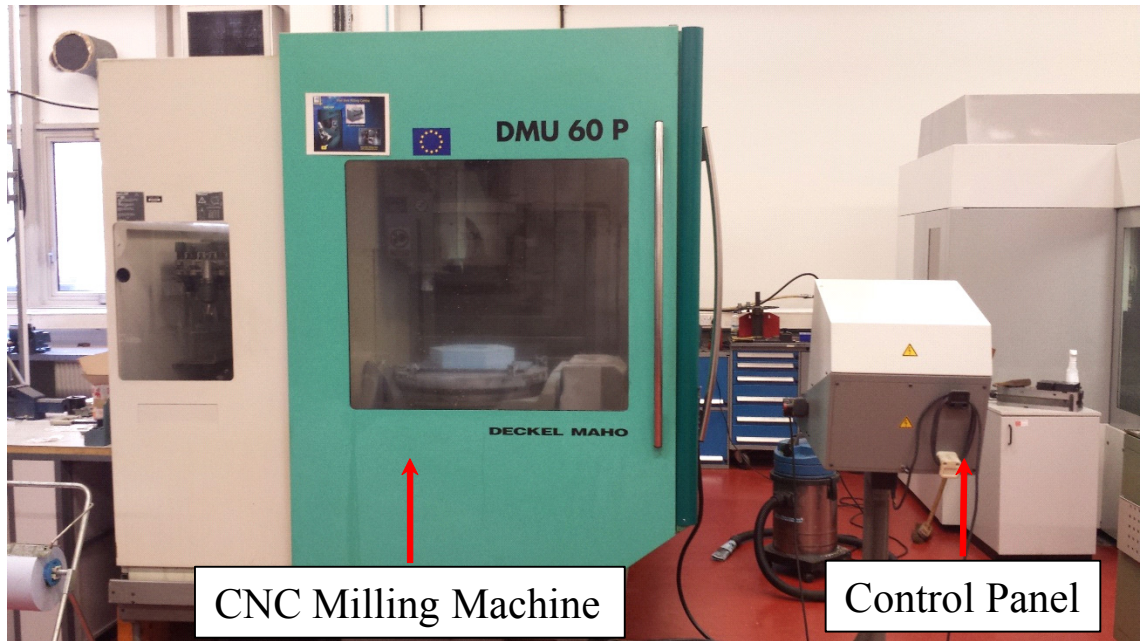
Figure 4.18: CNC milling machine for producing the curvatures on the enclosure ends.

Figure 4.19: Photograph demonstrating the procedure of milling a curvature.

The final step was to use an AGIE Wire Cut machine to apply the finishing touches, as shown in Figure 4.20. The machine was programmed on the control panel to take off an extra 2 mm of materials to an accuracy of up to 0.1 mm. The wires were run through a rotary system, and then a circular motion allowed grinding of the surface of the inner enclosure. Extremely hot temperatures were generated during the surface grinding process. Thus, the machined part had to be placed inside a water basin to reduce the temperature and prevent damage to the Wire Cut machine. The degree of smoothness is based on the types of wire used, and a much longer machine time is required for a surface finish finer than 0.1 mm.
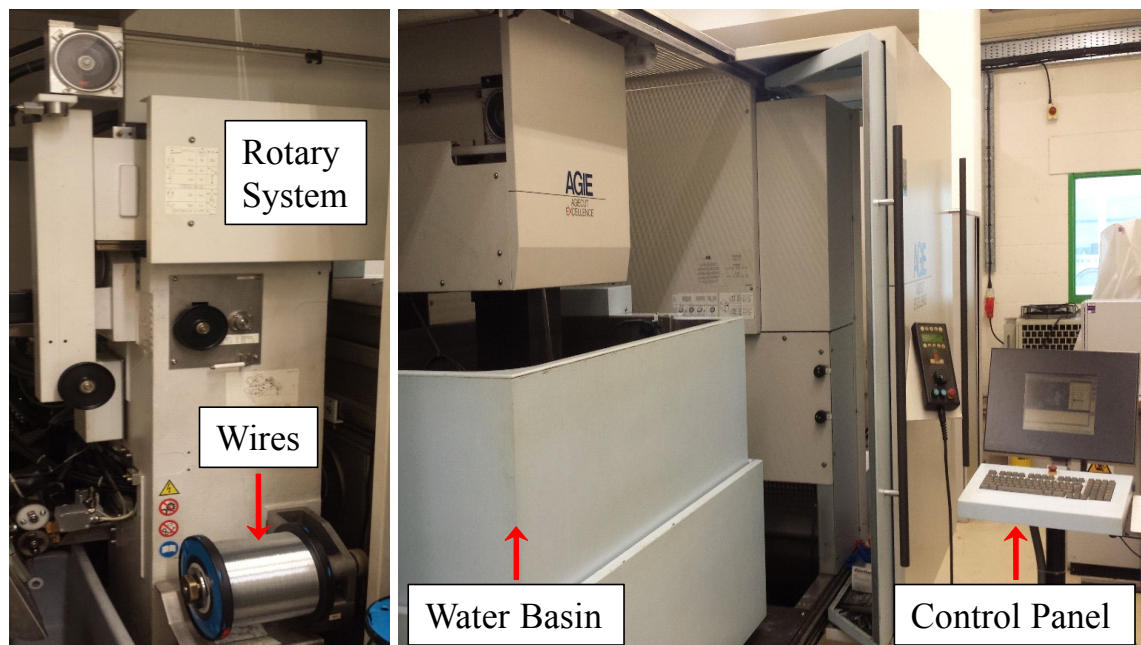
Figure 4.20: AGIE Wire Cut machine for providing a smooth surface finish.

Polypropylene support insulators were fabricated using the CNC milling machine. Figure 4.21 shows all the components that were used in the testing. The same enclosure was used so that the radius of R_b was fixed, and different sized conductors were also manufactured to investigate fully the effect of gap spacing in coaxial geometry when filled with CF_3I gas mixtures. The same fabrication process was also carried out for Prototype II.
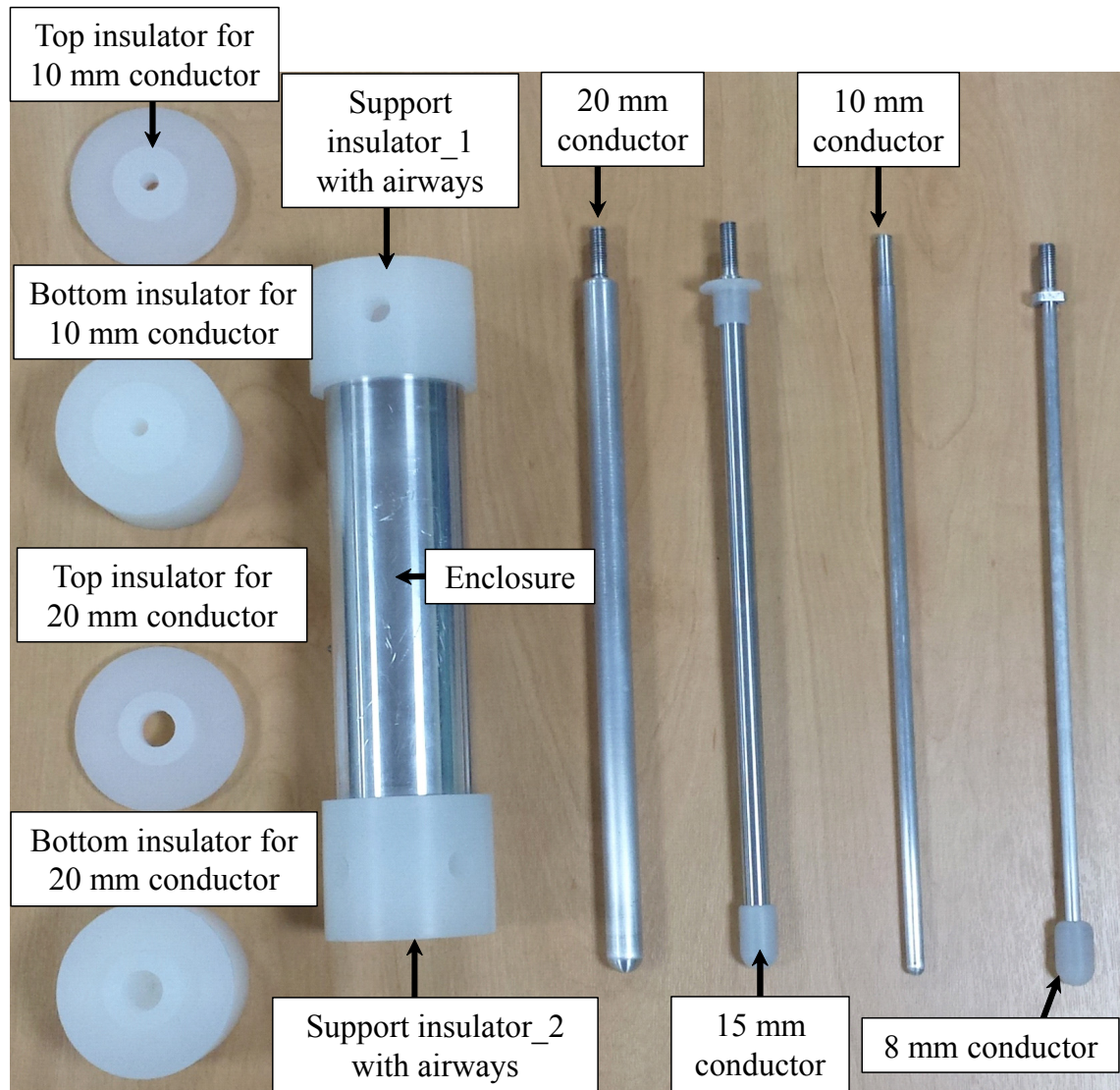
Figure 4.21: Fabricated components for the coaxial GIL test system.

As shown in Figure 4.21, there are four different sized conductors. To avoid wasting materials, rather than making more insulator parts, small adapters were made. As demonstrated in Figure 4.22, a conductor with a 15 mm diameter will have a 10 mm thread at the top of the conductor, which then allows the connection into the high-voltage bushing. Two polypropylene adapters were also fabricated for the 15 mm conductor to fit into insulators that were initially designed for a 20 mm sized conductor. A metal adapter was also manufactured for an 8 mm conductor to thread into and then attached onto the high-voltage bushing, also shown in Figure 4.22.
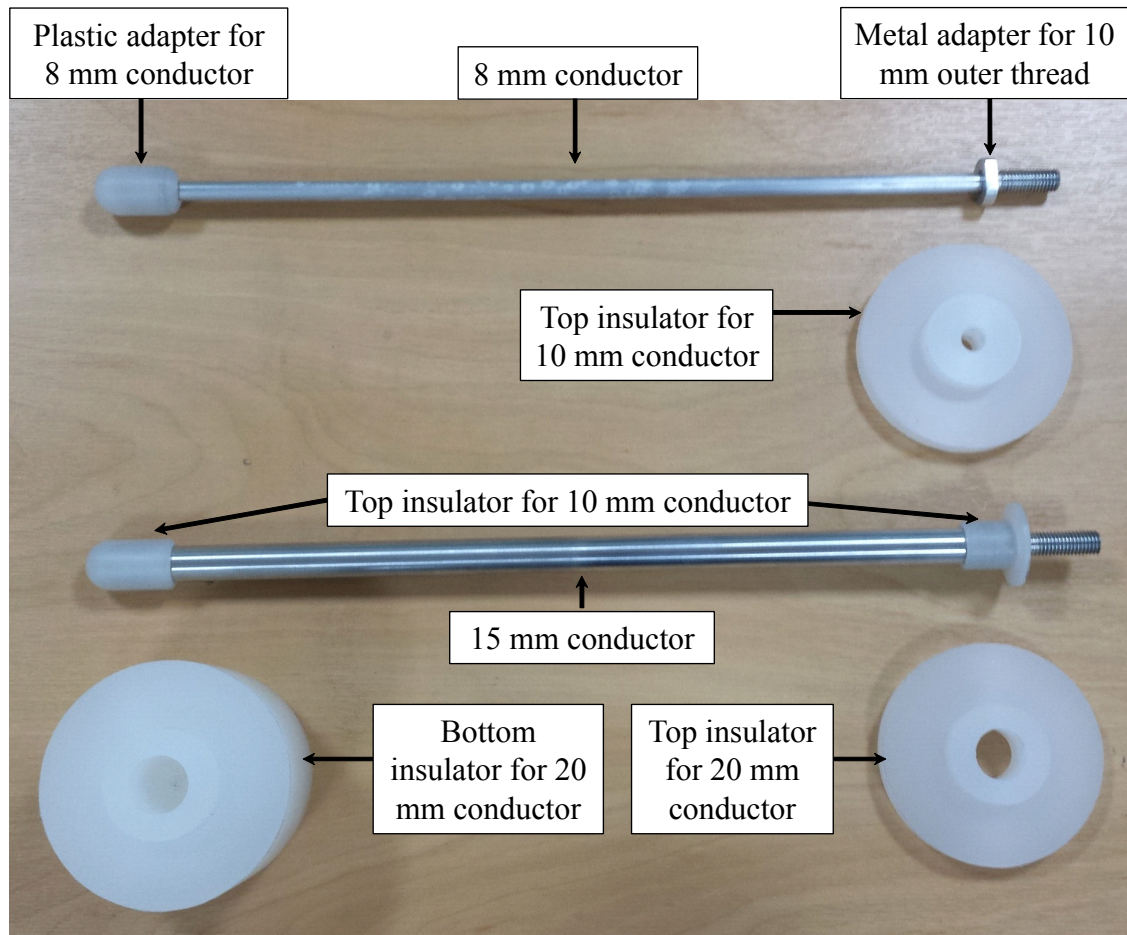
Figure 4.22: Metal and plastic adapters for different sized conductors.

The fully assembled views of Prototypes I and II can be seen in Figure 4.23 and Figure 4.24 respectively. Prototype II was designed to have the same geometric ratio of 1 to 3 as Prototype I, but the gap distance is three times larger.

Figure 4.23: Prototype I with inner enclosure diameter of 30 mm and conductor diameter of 10 mm.

Figure 4.24: Prototype II with inner enclosure diameter of 90 mm and conductor diameter of 30 mm.

4.6   Conclusion

This chapter has described the process of the design and construction of coaxial prototypes. First of all, it was pointed out that the maximum breakdown voltage can only be achieved when the geometric ratio and quantity $\ln(R_b/R_a)$ of the coaxial system is at unity. The first coaxial prototype was designed and fabricated close to the unity ratio. A preliminary experiment that was carried out on the prototype and photographic evidence shows that some of the breakdown events occurred near the rim of the enclosure. This raises the question of whether the breakdown was affected by the end effects. Based on the findings, practical improvements were made to the initial design to minimise the uncertainty of the end effects on the breakdown locations. The fabrication process of Prototype I has been discussed in detail to show the precautions taken to ensure that the dimensions were machined accurately. COMSOL simulations were performed on the coaxial geometry to identify high field stress regions prior to the fabrication of a prototype.

5 FIELD STRENGTH ANALYSIS AND PHASE EQUILIBRIUM EXPERIMENT OF CF₃I GAS MIXTURES

5.1 Introduction

Researchers have spent years trying to find an alternative insulation medium to replace SF_6 in high-voltage gas-insulated equipment. To date, only SF_6/N_2 gas mixtures and synthetic air have been proposed as serious alternatives in GIL applications [94]. There are gas candidates that have a much higher dielectric strength than SF_6; however, they would liquefy under the typical operating pressures of SF_6 GIS/GIL (4 to 8 bar) or at outdoor temperatures below –20 °C. This has led to research into the use of a smaller proportion of those gas candidates as part of a binary gas mixture with N_2 or CO_2. To investigate the feasibility of CF_3I gas and its mixtures, two sets of investigations were carried out: (i) gas analysis of CF_3I, which was to evaluate the insulation strength and the boiling point of each CF_3I gas mixture; and (ii) the breakdown characteristics of CF_3I gas mixtures, which were obtained through large numbers of breakdown tests for various electrode configurations.

This chapter describes the process of gas analysis of CF_3I gas mixtures. First, the critical field strength of CF_3I gas and its mixtures was calculated and compared to air and SF_6 using the Boltzmann analysis. The calculated results provided estimates of the breakdown performance of CF_3I gas mixtures before any experiment was carried out. To determine the boiling point of CF_3I gas mixtures, the author undertook a research visit to the

Technical Institute of Physics and Chemistry, Chinese Academy of Sciences (TIPC, CAS), China, to carry out the phase equilibrium experiment on CF_3I/CO_2 and CF_3I/N_2 gas mixtures. Researchers at the institute have previously investigated liquefaction temperature of CF_3I/propane gas mixtures for application of refrigerants [95]. The research focus of TIPC, CAS was to investigate the potential of using CF_3I as a replacement for the traditional chlorofluorocarbon (CFC) refrigerants. The purpose of this collaborative work was to measure saturation vapour pressures of CF_3I gas mixtures to be used in GIL applications. A model was created based on the measured data to evaluate various CF_3I gas mixtures over a temperature range of –40 °C ~ +50 °C (233 K ~ 323 K) and their corresponding saturation vapour pressures. The obtained results were then used to provide an estimate of the pressure and temperature required for the liquefaction process to take place for any CF_3I/CO_2 or CF_3I/N_2 gas mixture.

5.2   BOLSIG+ Calculation of CF₃I Gas Parameters

The effective ionisation coefficients of different gases and gas mixtures were computed using BOLSIG+ software, which applies the two-term approximation of the Boltzmann equation [96]. The Boltzmann equation for an ensemble of electrons in an ionised gas is

$$\frac{\partial f}{\partial t} + v \cdot \nabla f - \frac{e}{m} \mathrm{E} \cdot \nabla_v f = C[f]$$
(5.1)

where f is the electron distribution, v are the velocity coordinates, e is the elementary charge, m is the electron mass, E is the electric field, ∇_v is the velocity-gradient operator and C represents the rate of change in f due to collisions [96].

This software was used to obtain the critical reduced field strength, $(E/p)_{crit}$, for different gases or gas mixtures. The data required for the modelling of CF_3I/CO_2 and CF_3I/N_2 gas

mixtures were obtained from measured experimental results in the literature [71], [72]. In here, α is the ionisation coefficient and η is the electron attachment rate. A common way of showing the results is by plotting the effective ionisation coefficient, $(\alpha - \eta)$, as a function of the corresponding pressure-reduced electric field value, E/p. At $(\alpha - \eta) = 0$, the corresponding $(E/p)_{crit}$ value represents the cut-off point in terms of pressure-reduced critical field strength for each gas or gas mixture. In the coaxial prototype, when the electric field becomes higher than the $(E/p)_{crit}$ value, it will result in a build-up of ionisation that eventually leads to electrical breakdown. Figure 5.1 shows the calculated pressure-reduced ionisation coefficient, $(\alpha - \eta)/p$, as a function of electric field strength for SF_6 and CF_3I. It can be seen that CF_3I gas, like SF_6, has a linear characteristic. CF_3I also has a higher gradient, exceeding SF_6 at 21.3 kV/mm.
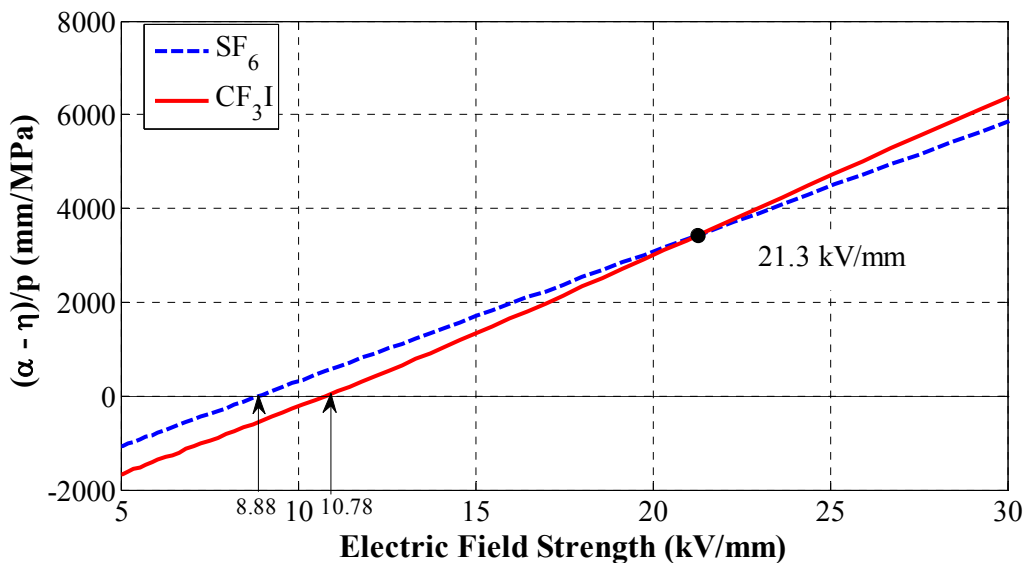
Figure 5.1: Pressure-reduced effective ionisation coefficient, $(\alpha - \eta)/p$ is plotted against electric field strength for both SF_6 and CF_3I.

Figure 5.2 shows the effective ionisation coefficient as a function of E/p for different pure gases (SF_6 and CF_3I) and CF_3I gas mixtures. It can be seen that the E/p is calculated to be 10.78 kV/mm/bar for CF_3I at $(\alpha - \eta) = 0$, and 8.88 kV/mm/bar for SF_6. This is consistent with the existing experimental results reported in [4], which show that CF_3I has a

dielectric strength around 1.2 times higher than that of SF_6. The steepness of the slope for SF_6 and CF_3I indicates that α is sensitive to changes in E/p. The insulation integrity of the gases is precarious near to the $(E/p)_{crit}$, since breakdown in SF_6 is known to happen very fast as a strong growth of ionisation would occur in the region where $E/p > (E/p)_{crit}$, especially in the presence of defects in the gas-insulated equipment [1]. CF_3I gas mixtures show a less linear characteristic than pure CF_3I and are less sensitive to changes in E/p. The simulated results from BOLSIG+ software were compared with the experimental results from the literature. The result for SF_6 was compared to those reported in [1], while the results for CF_3I gas mixtures were compared with results in [3] and [7]. All the simulated results were in good agreement with the published results in the literature.
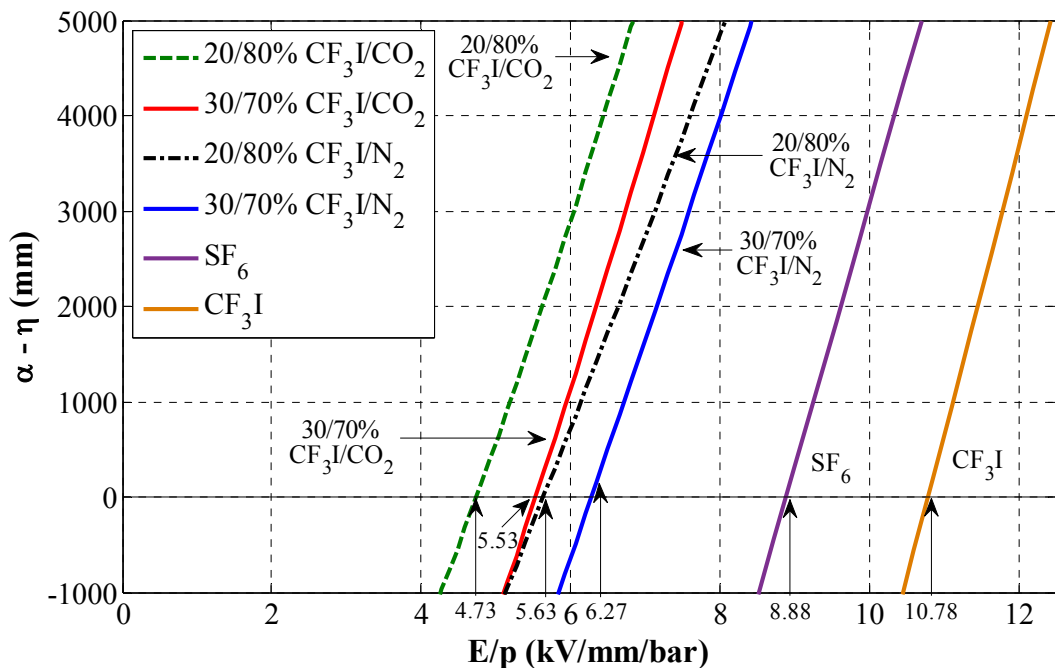
Figure 5.2: Effective ionisation coefficients in pure gases (SF_6 and CF_3I) and CF_3I/CO_2 and CF_3I/N_2 mixtures (20/80% and 30/70%).

Critical E/p values of various CF_3I gas mixtures can be obtained graphically by finding the point of E/p when the quantity $(\alpha - \eta)$ intersects 0 on Figure 5.2. The data of E/p for gases (SF_6 and CF_3I) and gas mixtures (CF_3I/CO_2 and CF_3I/N_2) are shown in Table 5.1.

The E/p of the CF$_3$I gas mixtures was found to decrease with a lower CF$_3$I content, and the CF$_3$I/N$_2$ gas mixtures have comparably higher E/p values than the equivalent CF$_3$I/CO$_2$ gas mixtures, as can be seen in Figure 5.2 and Table 5.1.

Table 5.1: Tabulated E/p values at ($\alpha - \eta$) = 0 for CF$_3$I, SF$_6$ gas and different CF$_3$I/N$_2$ and CF$_3$I/CO$_2$ gas mixtures.

CF$_3$I Content	CF$_3$I/N$_2$ E/p (kV/mm/bar)	CF$_3$I/CO$_2$ E/p (kV/mm/bar)
5%	4.45	3.30
10%	4.92	3.85
20%	5.63	4.73
30%	6.27	5.53
40%	6.91	6.30
50%	7.54	7.05
70%	8.82	8.55
100% CF$_3$I	10.78	
100% SF$_6$	8.88	

5.3 Phase Equilibrium Experiment

In Chapter 2, it was highlighted that there is no experimental data available on the boiling point of CF$_3$I gas mixtures. Considering the amounts of CF$_3$I gas required to fill a full-scale GIL test system, it is important to know the exact conditions that would lead to liquefaction of CF$_3$I gas mixtures. The boiling point is effectively the point where the vapour to liquid phase transition occurs. This can be measured using the phase equilibrium method, which is a quick and efficient way of obtaining the equilibrium properties of gas mixtures. Experimental data of the vapour and liquid phases of a gas mixture were measured to develop a model, which could then be used to calculate other temperature range and equilibrium properties of the gas mixture without recourse to

experiment. To have an effective model, a highly accurate and reliable experimental setup and measurement procedure was necessary. A brief description of the setup and the test method of the phase equilibrium experiment are provided in the following sections. Comparative analysis shows that there is a good agreement between the experimental and calculated results. Therefore, the model is then applied for the calculation of the entire operating temperature range of a GIL system for CF$_3$I/CO$_2$ and CF$_3$I/N$_2$ gas mixtures.

5.3.1   Experimental Setup

The experimental setup used for this work was based on the vapour-phase recirculation method; a schematic of which is shown in Figure 5.3. The setup was designed by Dong et al. [95], [98] and has produced publishable results in the past for the measurement of vapour pressures and phase equilibrium for gas mixtures containing CF$_3$I [99]–[102].

A cylindrical pressure cell made of stainless steel with a volume of 150 ml was fabricated to carry out the gas experiment. This vessel was located inside an isothermal liquid bath that had a volume of 6.5 L and was filled with alcohol. A digital controller was used to regulate a refrigerating machine and an electric heater to adjust the temperature of the liquid bath. The temperature was measured using a 25 Ω standard platinum resistance thermometer, which was inserted inside the 150 ml equilibrium cell. A uniform temperature distribution was achieved with two speed-controlled mixers inside the liquid bath. For pressure measurement, a Mensor series 6000 digital pressure transducer with a scale of up to 12.5 bar and uncertainties of ±0.0025 bar was used for this experiment. Both the cell and the bath were placed inside a larger stainless steel vessel at vacuum pressure; this was adopted (i) to avoid frosting on the surface of the bath, and (ii) to minimise any impact on the experiment caused by the temperature of the surrounding

environment. A gas chromatograph (GC) was used to measure the composition of gas mixtures in terms of vapour and liquid phases. It can be seen from the figure that the vessel was equipped with viewing windows made of quartz glass to allow observation of the phase interaction during an experiment.
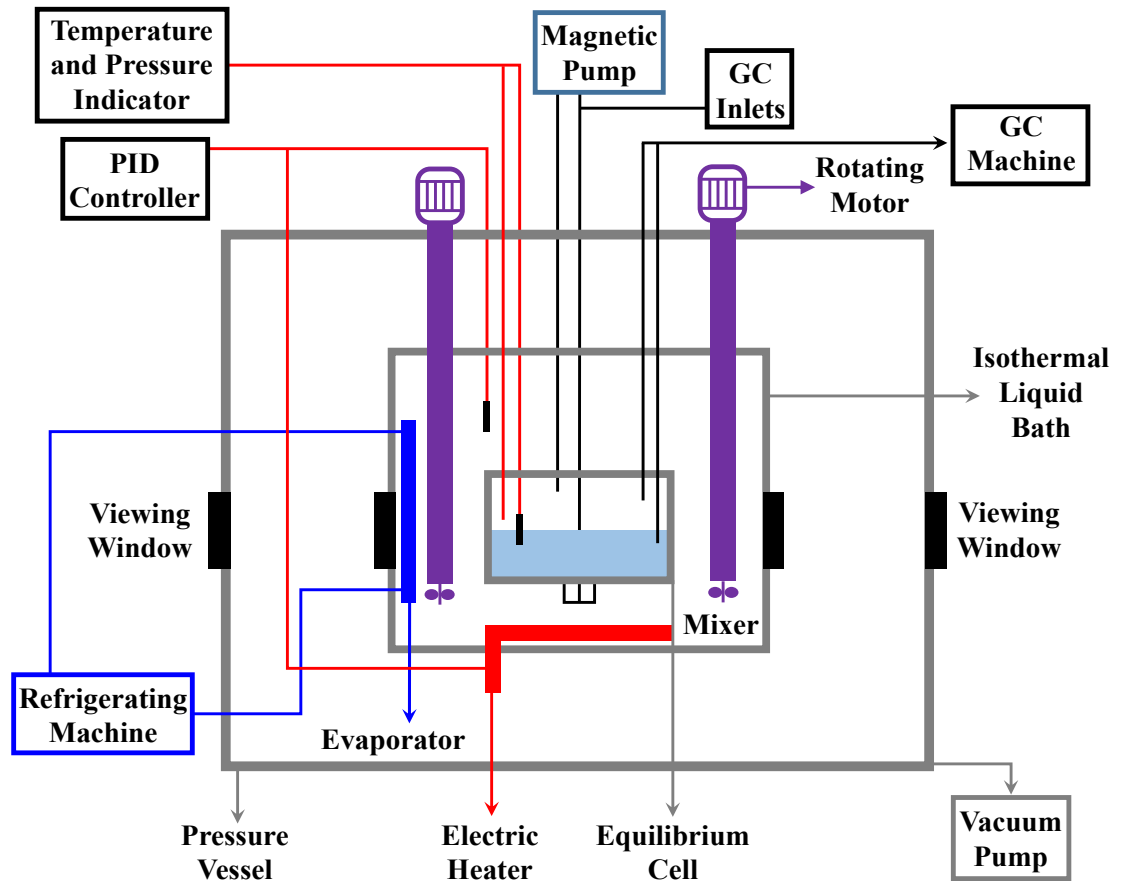
Figure 5.3: Schematic diagram of the phase equilibrium experimental setup [95].

5.3.2   Sample Calibration Procedure

The GC analysis cannot directly provide the desired value since, it is simply measuring the height and area of the peak of various substances analysed from the GC column. There are two types of GC column: capillary and packed. Columns have different types of absorbents on the inner wall which is necessary for analysing different gas compositions. For this work, a metal packed GC column with Sebaconitrile as the absorbent was used, as recommended by the manufacturer in analysing CF₃I gas compositions.

The gas composition measured by the GC may be quite different from the actual gas composition. This difference may be caused by the sensitivity of the GC column or the GC analyser towards CF$_3$I gas mixtures. To obtain accurate experimental data, the gas composition must first be calibrated by the GC, which provides the correction factor for the following experiments. This requires the initial reading of the gas compositions to be highly accurate before the start of the calibration process. For this work, the standard weighing method was applied for the calibration of the GC, and the process of calibration was as follows:

(1) To calculate the ratio of mass for each gas, the gas mixture compositions were set (for example, 30% CF$_3$I and 70% CO$_2$), based on the weighing method.

(2) An empty gas bottle was vacuumed and then weighed. The bottle was weighed again once it had been filled with CF$_3$I gas, then the same process was repeated for the buffer gas. The measured weight values provided the exact composition of the gas mixture inside the gas bottle.

(3) The gas mixture sample from the bottle was released into the GC inlet for analysis. After a detection period, the GC analyser recorded two main peaks for CF$_3$I and the buffer gas (N$_2$ or CO$_2$), and also measured the area of the two peaks. This then produced a calibrated ratio for the gas mixture sample.

(4) The method was repeated until the analysis of five sets of molar ratio showed a result deviation of less than 0.001.

(5) From the obtained results, the set that had the closest value to the average of the five sets of results was selected.

(6) All of the above steps were then repeated for the same gas mixture but for different mixture ratios. Data points at a low percentage (20%) and a high percentage (80%) were chosen to enhance the accuracy of the calibration plot.

In Figure 5.4 and Figure 5.5, the values measured by the weighing method were plotted against the measured values from the GC analyser for both the CF_3I/CO_2 and CF_3I/N_2 gas mixtures respectively. The fitting equations shown on both figures were applied for the conversion between the measured experimental data and the actual values.

$$y = 9.2506E^{-4} + 2.6223x - 3.7051x^2 + 3.3356x^3 - 1.2537x^4$$
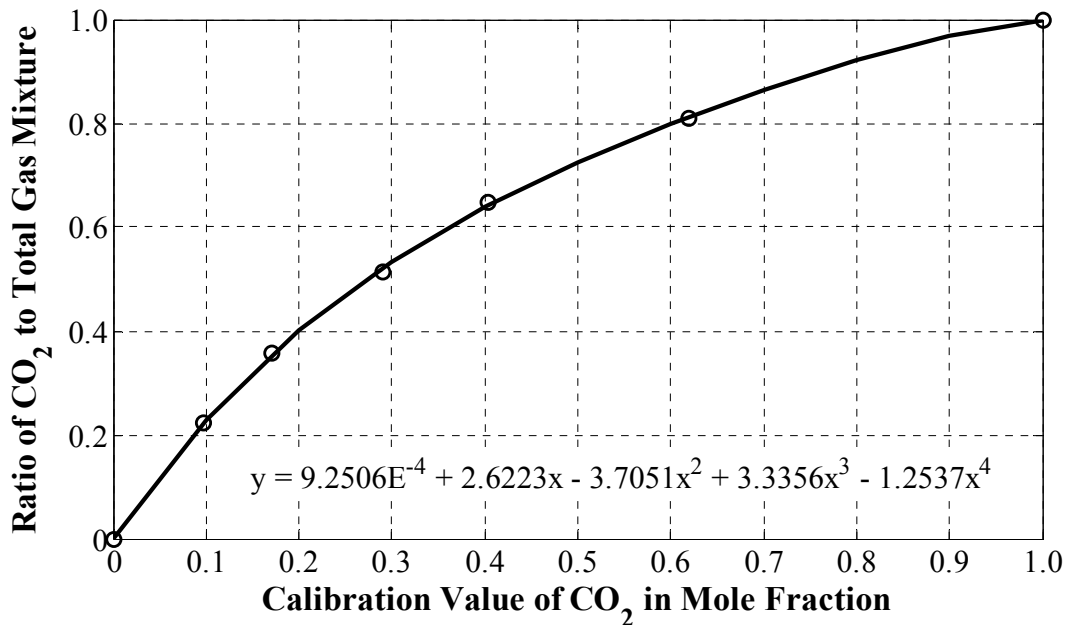
Figure 5.4: Calibration plot for CF₃I/CO₂ gas mixtures in mole fraction.

$$y = 2.9402E^{-4} + 3.2084x - 5.6073x^2 + 5.5189x^3 - 2.1204x^4$$
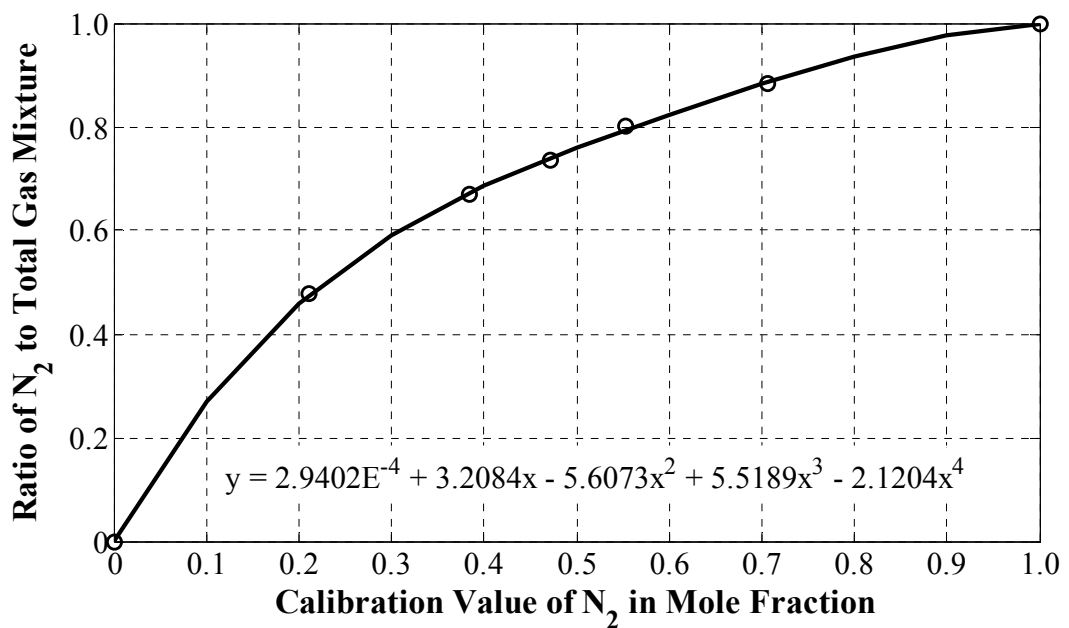
Figure 5.5: Calibration plot for CF₃I/N₂ gas mixtures in mole fraction.

5.3.3 Experimental Method

There are two ways of carrying out the experiment. The first method is to mix the desired gas mixture in a gas bottle to a significantly high pressure, then release the gas mixture into the GC via the inlets until the liquefaction process occurs; this method requires visual observation of the phase change inside the cell. The second is to drive a large amount of CF_3I gas into the cell until a proportion of the gas turns into liquid, which can be observed through the viewing window as shown in Figure 5.6. During the experiment, various percentage of the buffer gas, either CO_2 or N_2, is released into the cell to prepare the desired CF_3I gas mixture, which is then analysed using the GC.
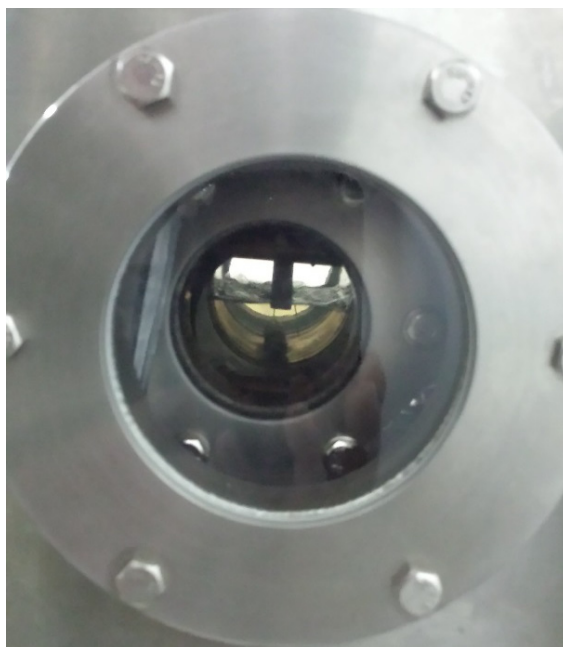
Figure 5.6: Photograph of the VLE process for CF₃I gas mixtures observed through the viewing window.

The first method needs large amounts of gas mixed according to the desired mixture ratio before the experiment, and there is a high possibility of error if the instance of phase change can be recorded only by visual observation. The second method was preferred, therefore, since the measured results are used to improve the accuracy of the calculation model, which can then provide the full range of data for any mixture ratio. A calculation

model was developed based on the Peng-Robinson equation of state (PR EoS) and van der Waals (vdW) mixing rules used to correlate the experimental and calculated data. The model was developed as part of a commercial software package and provided by the research group in TIPC, CAS, for all the calculations in this chapter. As this is in a different field of research, and is not the main concern of this PhD work, the process of the calculation will not be discussed further in this thesis; detailed explanations were reported in [103].

The second method was adopted for the experimental investigation. First, the equilibrium cell was vacuumed to remove any residual impurities. CF$_3$I, the gas with the higher boiling point, was the first gas released into the equilibrium cell. The temperature could be regulated through the refrigerating machine or the electric heater. Once the temperature was stabilised, that is, when the temperature fluctuation in the cell was less than ±3 mK and the pressure fluctuation was no more than ±0.002 bar for at least 10 minutes, then it could be considered that the equilibrium state was reached. A pre-determined value of the gas with the lower boiling point was released into the equilibrium cell to mix with the CF$_3$I gas. When the equilibrium state was once again reached for the gas mixture, the GC was used to measure the liquid and vapour phase of the sample. Each phase was measured at least three times, unless two adjacent measurements had a deviation of less than 0.002, whereupon an average value was taken. The process was then repeated for different compositions of CF$_3$I gas mixtures.

5.3.4   Experimental Analysis of CF$_3$I Gas Mixtures

The PR model was used to calculate the equivalent of each set of the measured results, and the comparison can be seen in Table 5.2 and Table 5.3 for the CF$_3$I/CO$_2$ and CF$_3$I/N$_2$

gas mixtures respectively. It can be observed from the results that there is a small discrepancy in the calculated results, with a difference mostly below 2%. The model was considered satisfactory and was then applied to obtain the liquid and vapour phase equilibrium (VLE) diagrams for a temperature range of –40 °C to +50 °C for the full range of gas compositions of CF_3I/CO_2 and CF_3I/N_2 gas mixtures.

The suitability of CF_3I gas mixtures was analysed for the maximum and minimum ambient air temperatures for outdoor GIS equipment. As stated in the international standards IEC/BS 62271-203 [104], the minimum allowed outdoor temperature is stated to be either –25 °C or –40 °C, and the maximum allowed outdoor temperature is +40 °C. Case studies of VLE diagrams were plotted for CF_3I gas mixtures under temperatures of –25 °C, –40 °C and +40 °C. At extremely low temperatures of –25 °C and –40 °C, low values of saturation vapour pressure are required for the CF_3I gas mixtures to turn into liquid state, as can be seen from Figure 5.7 to Figure 5.10.

Table 5.2: Comparison of measured and calculated data for CF_3I/CO_2 mixtures at different pressures and temperatures.

Temperature (K)	Pressure (bar) [abs.]	CO_2 Content Measured	CO_2 Content Calculated	Discrepancy (%)
233.2	10.06	0.689	0.693	0.60
248.2	6.17	0.635	0.640	0.65
253.2	4.94	0.680	0.688	1.25
253.2	3.80	0.724	0.728	0.51
263.2	3.29	0.737	0.745	1.10
263.2	6.76	0.655	0.673	2.67
273.2	5.63	0.721	0.729	1.10
273.2	4.19	0.745	0.755	1.38
283.2	2.43	0.828	0.827	0.22

Table 5.3: Comparison of measured and calculated data for CF_3I/N_2 mixtures at different pressures and temperatures.

Temperature (K)	Pressure (bar) [abs.]	N_2 Content Measured	N_2 Content Calculated	Discrepancy (%)
253.919	6.997	0.807	0.822	1.83
255.929	7.128	0.808	0.811	0.31
255.938	7.144	0.805	0.811	0.82
257.878	7.296	0.798	0.803	0.74
257.934	7.313	0.794	0.803	1.22
258.941	7.431	0.789	0.799	1.32
260.939	7.145	0.795	0.775	2.59
263.350	6.539	0.740	0.734	0.73
263.351	7.122	0.759	0.753	0.75
263.349	7.131	0.760	0.754	0.85
270.379	6.995	0.679	0.680	0.04
271.374	7.112	0.678	0.674	0.69
271.379	7.124	0.677	0.674	0.47

A VLE diagram consists of three parts: liquid phase, vapour phase, and a mixed phase of both liquid and vapour. This trend can be clearly observed for CF_3I/CO_2 gas mixtures, as shown in Figure 5.7. In the case of CF_3I/N_2 gas mixtures, due to the extremely low boiling point of N_2 gas, the cross-over of liquid and vapour phases would occur at a much higher gas pressure. Given that the operating pressure of most gas-insulated equipment is below 10 bar, the VLE diagrams for CF_3I gas mixtures will only be shown up to 20 bar for –25 °C and –40 °C. A much higher pressure is required to liquefy a gas mixture under a high surrounding temperature of +40 °C, therefore, the VLE diagrams are shown up to 60 bar. As shown in Figure 5.7 and Figure 5.8, the two mixture ratios of particular interest are 20/80% and 30/70% corresponding to mole fractions of 0.8 and 0.7 respectively. For

operating temperature of –25 °C, the 20/80% and 30/70% CF_3I gas mixtures would liquefy if pressurised above 4.1 bar and 2.8 bar respectively.
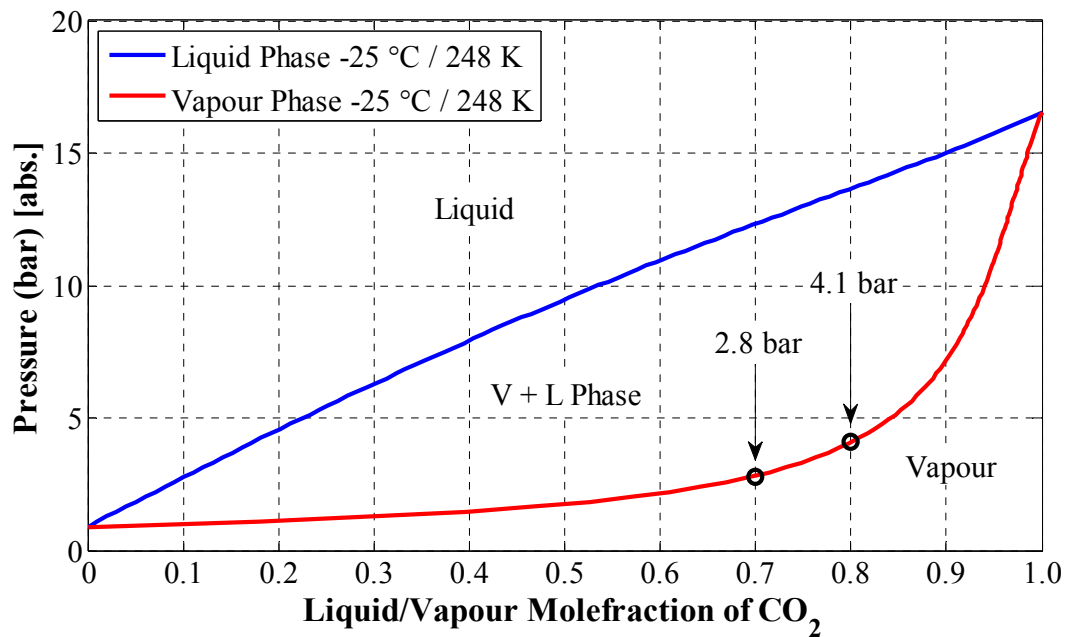
Figure 5.7: Liquid and vapour mole fraction of CO_2 gas as a function of pressure for CF_3I/CO_2 gas mixtures at a temperature of –25 °C (248 K).
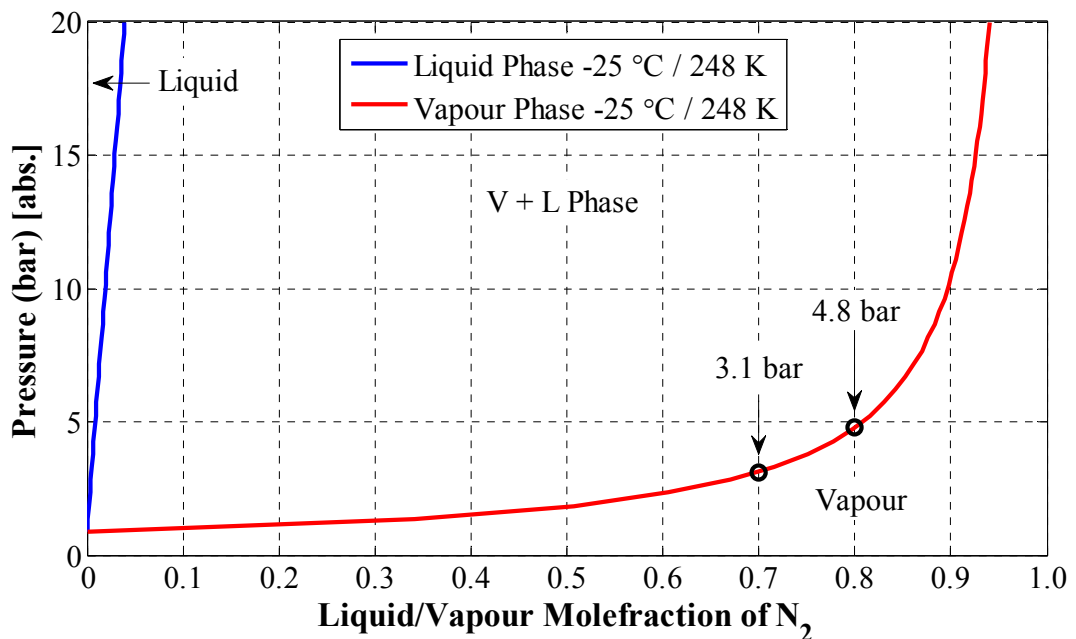
Figure 5.8: Liquid and vapour mole fraction of N_2 gas as a function of pressure for CF_3I/N_2 gas mixtures at a temperature of –25 °C (248 K).

In Figure 5.9 and Figure 5.10, for a temperature of –40 °C, it can be seen that the saturation vapour pressure required for liquefaction reduces.
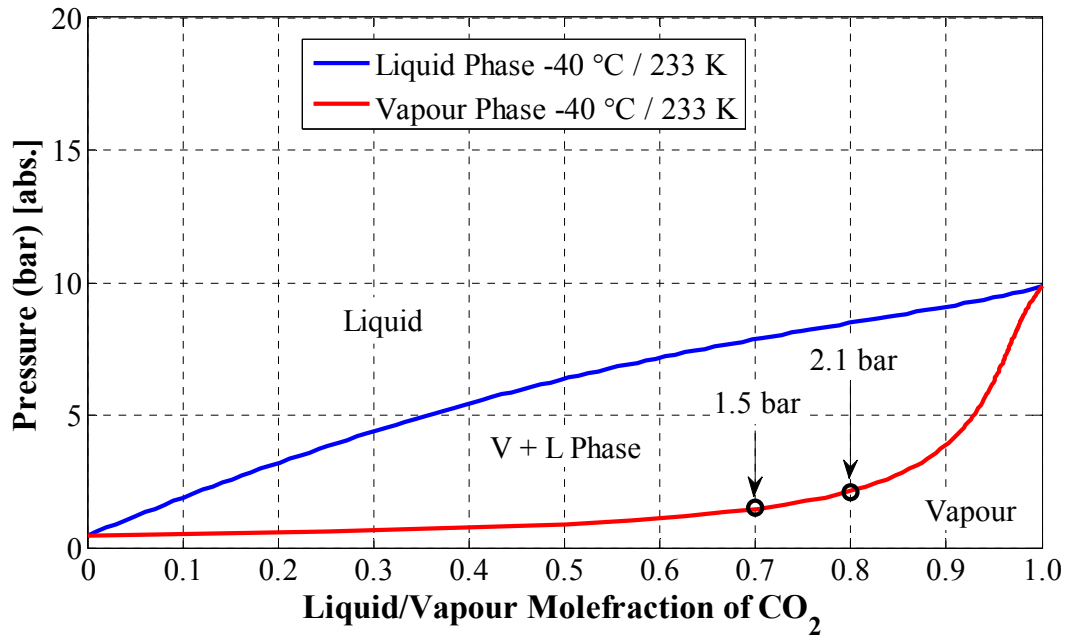
Figure 5.9: Liquid and vapour mole fraction of CO_2 gas as a function of pressure for CF_3I/CO_2 gas mixtures at a temperature of –40 °C (233 K).
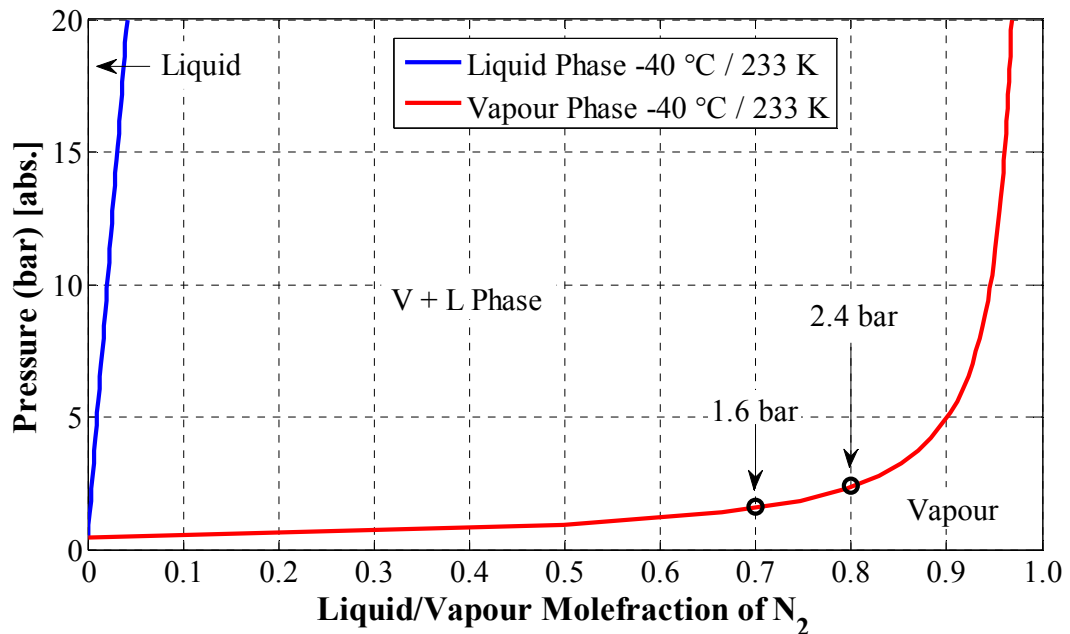
Figure 5.10: Liquid and vapour mole fraction of N_2 gas as a function of pressure for CF_3I/N_2 gas mixtures at a temperature of –40 °C (233 K).

The results in Figure 5.11 and Figure 5.12 indicate that, the CF$_3$I gas mixtures can be used in GIL applications for higher temperatures (at maximum operating temperature of 40 °C) without the danger of liquefaction to the gas medium.
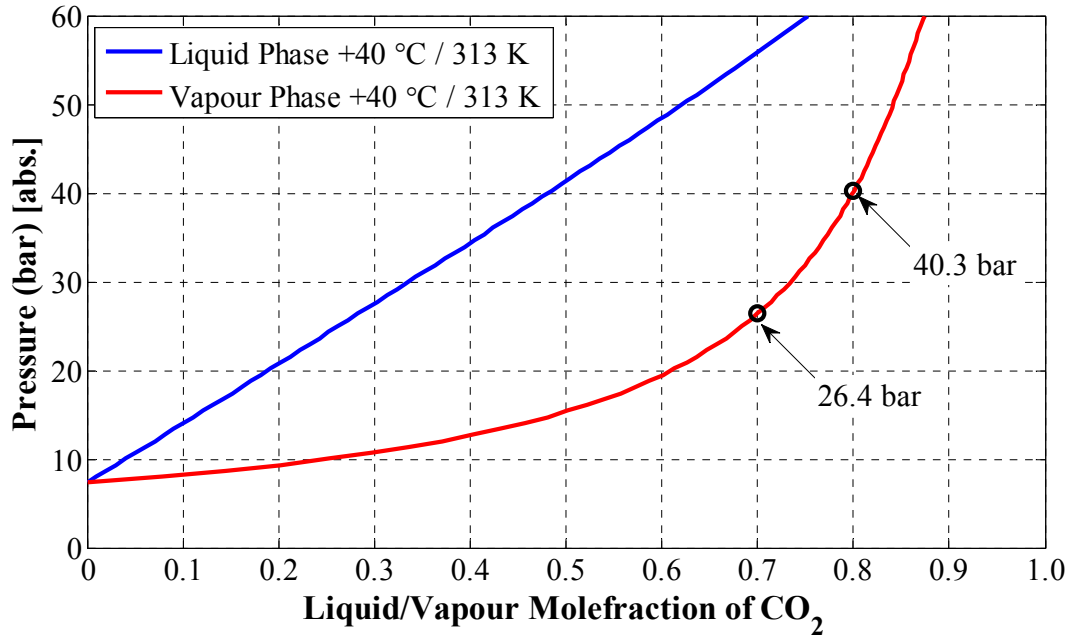
Figure 5.11: Liquid and vapour mole fraction of CO$_2$ gas as a function of pressure for CF$_3$I/CO$_2$ gas mixtures at a temperature of +40 °C (313 K).
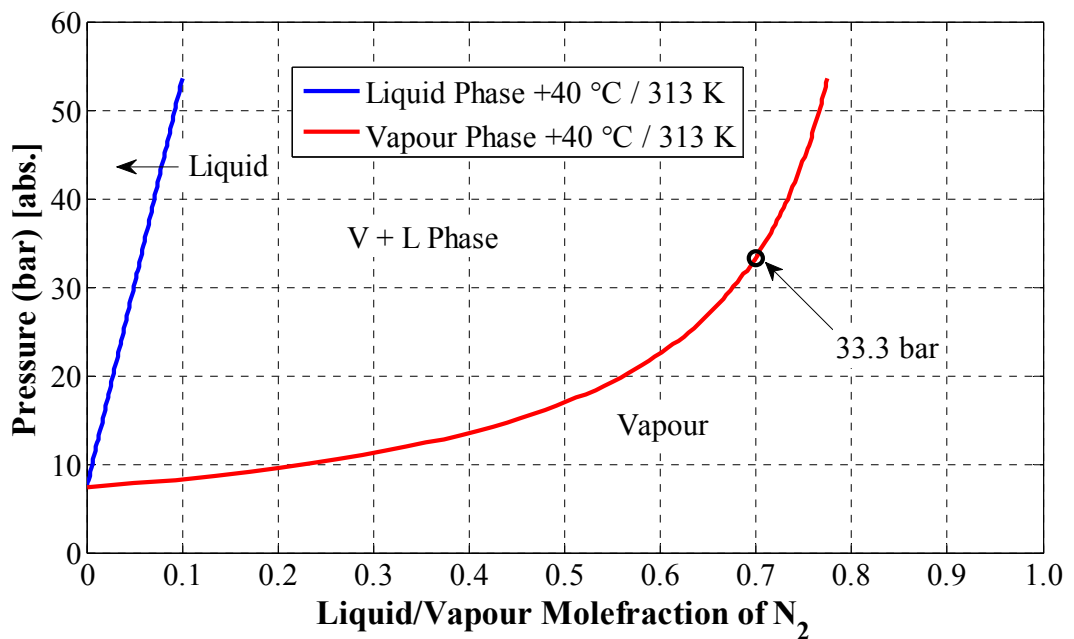
Figure 5.12: Liquid and vapour mole fraction of N$_2$ gas as a function of pressure for CF$_3$I/N$_2$ gas mixtures at a temperature of +40 °C (313 K).

110

Figure 5.13 shows the relationship between saturation vapour pressure and boiling temperature for gases including N_2 [105], CO_2 [106], [107] SF_6 [108] and CF_3I [37], and mixture ratios of 20/80% and 30/70% for both CF_3I/CO_2 and CF_3I/N_2 gas mixtures. For temperature range between 10 °C and 40 °C (maximum operating temperature), the four CF_3I gas mixtures shown on Figure 5.13 would not liquefy under the typical operating pressure (4–8 bar) of GIL. However, at minimum temperature of –25 °C, the operating pressure should be below 4 bar for the 20/80% CF_3I gas mixtures to avoid liquefaction.
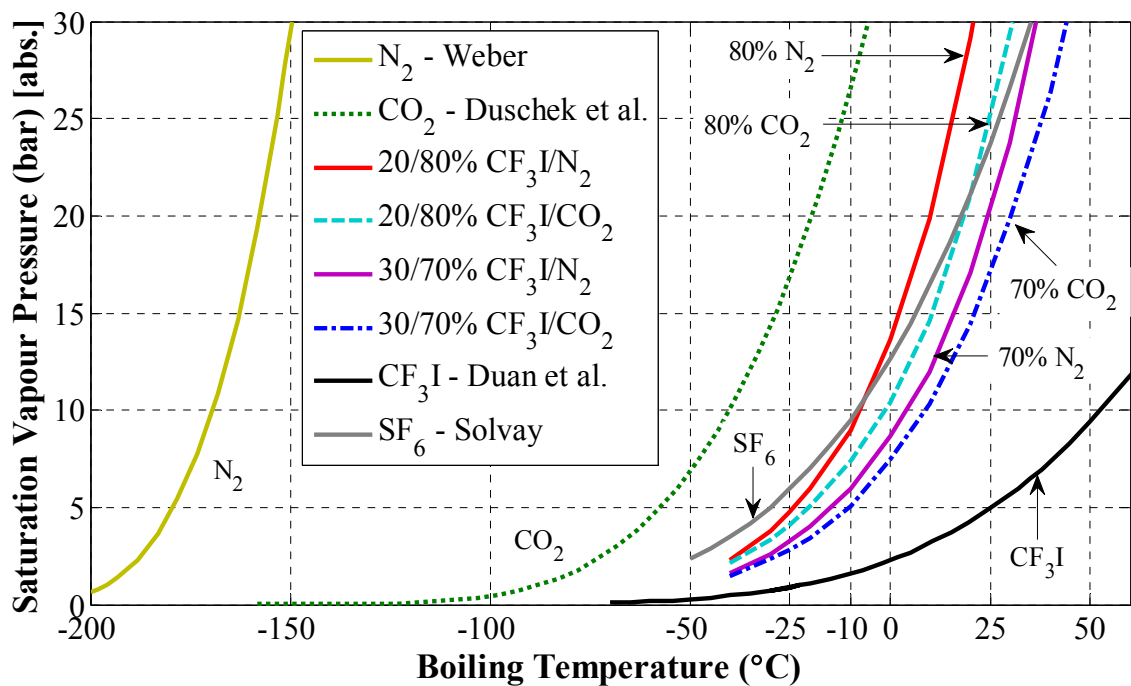
Figure 5.13: Saturation vapour pressure as a function of boiling temperature for pure gases (N_2 [105], CO_2 [106], [107], SF_6 [108] and CF_3I [37]) and gas mixtures (ratios of 20/80% and 30/70% for both CF_3I/CO_2 and CF_3I/N_2 gas mixtures).

5.4   Conclusion

This chapter has carried out two gas analysis investigations on CF_3I gas and its mixtures. The numerical software BOLSIG+ was used to calculate the E/p values of different CF_3I gas mixtures. The calculated results gave an indication of the critical field strength of each gas or gas mixture. For the design of GIL using a CF_3I gas mixture, the interior

dimensions must be significantly lower than the $(E/p)_{crit}$ of the chosen gas mixture. In this way, the possibility of direct breakdown occurring in the GIL is minimised. The calculated data show that using 20% ~ 30% of CF_3I content would provide insulation strength of 5 ~ 6 kV/mm/bar, such would be appropriate for GIL applications.

Experiments were conducted to determine the boiling point of CF_3I/CO_2 and CF_3I/N_2 gas mixtures as part of a research visit to TIPC CAS, China. The measured results were correlated using a calculation model developed based on Peng-Robinson equation of state and van der Waals mixing rules. A comparison between the measured and the calculated results indicated a relatively small difference. It was observed that CF_3I/N_2 gas mixtures have lower boiling points than their CF_3I/CO_2 equivalents. At high temperatures, higher pressures would be required for the gas to liquefy. Conversely, lower pressures were recorded for tests carried out at lower temperatures for CF_3I gas mixtures. This is as expected since N_2 has a much lower boiling point than CO_2. Based on the obtained data, it is suffice to say that 20% ~ 30% of CF_3I content mixed with CO_2 or N_2 would not liquefy at the test pressures up to 4 bar (abs.) for the breakdown laboratory work. The obtained results would provide a benchmark for any future work that involves testing at higher pressure for CF_3I gas mixtures.

Normally, for gas-insulated equipment, a heating device is switched on when the temperature drops below –25 °C. The device was installed since SF_6 gas would liquefy above 6.0 bar at –25 °C. For the CF_3I-GIL to be used in an extremely cold area, a similar heating device would be required to heat up the line sections if the temperature drops below a pre-determined value.

6 BREAKDOWN CHARACTERISTICS OF CF₃I GAS MIXTURES IN COAXIAL GIL GEOMETRY

6.1 Introduction

A coaxial cylindrical geometry has an electric field arrangement analogous to that of a GIL system. In Chapter 4, the design and fabrication process of a reduced-scale coaxial GIL model was described. The coaxial test system consists of a metal enclosure with a fixed diameter and several different-sized conductors to provide a varied gap spacing, and it can be mounted vertically inside a pressure vessel. To carry out the experimental investigation, a 400 kV Haefely impulse generator was used for the generation of a standard lightning impulse waveform (1.2/50).

The breakdown characteristics of four different CF₃I gas mixtures were investigated using the coaxial test system. Based on the measured results of coaxial GIL geometry in CF₃I gas mixtures in this thesis, a two-stage streamer/leader model was developed by Waters from Cardiff University [109]. The breakdown modelling determines the streamer/leader discharge for every breakdown result. For the leader discharge, a critical-field ratio 'k' and leader-channel electric field gradient E_L were obtained mathematically. The modelling technique was then applied to a larger scale coaxial test system to estimate the theoretical breakdown strength, and it was found that both the theoretical and experimental results were in good agreement. The study carried out in this chapter provides indications on (i) the feasibility of CF₃I gas and its mixtures for application with

GIL, (ii) an appropriate CF_3I gas mixture to be used in a full-scale GIL demonstrator, and (iii) development of a modelling technique that can be used for estimating the breakdown strength of full-scale GIL without recourse to experiment.

6.2   Breakdown of CF₃I Gas Mixtures in Coaxial Geometry

In this section, the investigation focuses on the coaxial geometry closest to the optimal ratio of R_a/R_b (10/30 mm) in terms of breakdown voltage and U_{50} as a function of pressure for CF_3I/CO_2 and CF_3I/N_2 gas mixtures in different ratios.

6.2.1   Conditioning Effect and Repeatability of Test Results

The up-down method was used [81] for the experimental work; this was discussed in more detail in Chapter 3. For every experiment, a minimum of 30 impulse voltages n_i were applied and every peak value U_i obtained was recorded. The recorded results were then used to determine the 50% breakdown voltage, U_{50}, and the population standard deviation from a given set of data. It is well known that the presence of dust particles [110], [111] or surface roughness [112]–[114] on the electrode will have a significant effect on the breakdown characteristics. In the preparation before every experiment it was, therefore, important that the surface of the electrodes was polished and was then cleaned carefully using alcohol.

For tests carried out under higher gas pressures, the initial breakdown voltages could be considerably lower than expected. According to the reviewed literature, a polished electrode will need to be conditioned by a number of breakdowns before a high breakdown strength can be obtained [115]. The conditioning effects have been reported for SF_6 in highly non-uniform field gaps [116], for quasi-uniform field gaps [47], [117],

and in uniform field gaps [117], [118]. A similar effect was also observed in different field gaps under a vacuum [119]–[121]. For CF_3I gas mixtures, it was observed during experiments that a higher number of breakdowns are required for conditioning CF_3I/N_2 gas mixtures in comparison to CF_3I/CO_2 gas mixtures.

One of the fundamental issues of any experimental work is whether there is repeatability in the results. Due to the high cost of CF_3I gas and the high volume of experimental work, the repeat experiments were carried out using recycled gas. For verification, comparative tests were carried out between newly mixed and recycled gas mixtures for a pressure range of between 1 and 4 bar (abs.), as shown in Figure 6.1. After 200 lightning impulse discharges, the gas was left in a storage bottle to recover. The tests on recycled gas was carried out a month after the initial investigation on new gas. It can be seen from Figure 6.1 that the recycled CF_3I gas mixtures retained most of the original insulation strength, a clear indication that there is repeatability in the results.
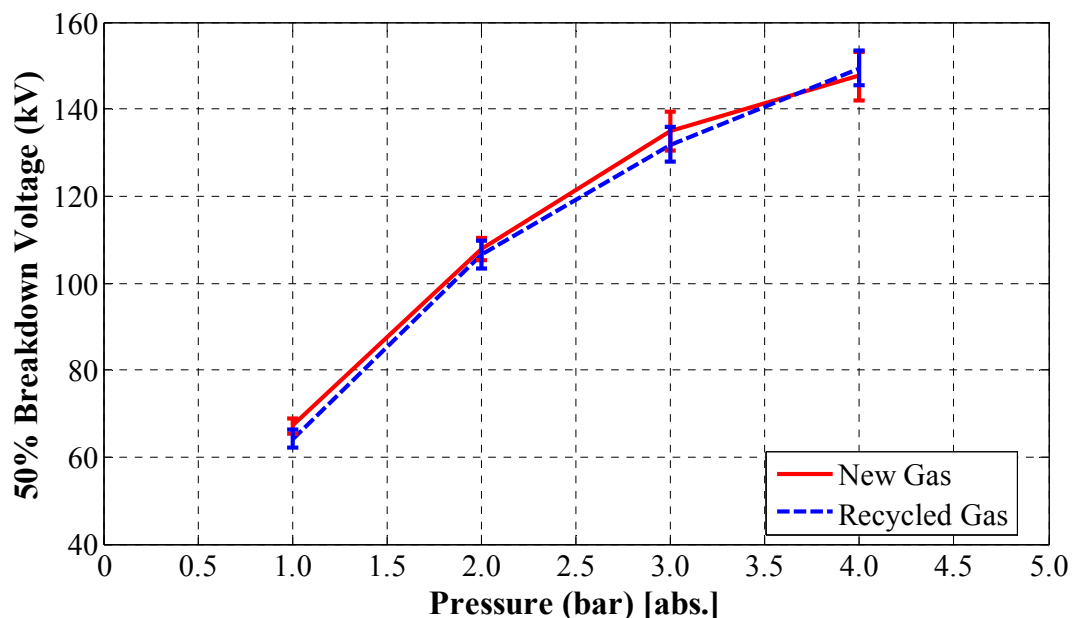
Figure 6.1: Comparison of breakdown voltage, U_{50}, between newly mixed and recycled 30/70% CF_3I/CO_2 gas mixtures at a pressures of 1 to 4 bar (abs.) tested on a coaxial test system of 10/30 mm and for positive lightning impulse polarity.

It was reported that the breakdown voltage for CF$_3$I gas after 1,300 discharges in uniform field gaps is reduced by 11% [40]. For the study at Cardiff, the number of discharges applied to the new gas before recycling was much lower than this and, therefore, the drop in U$_{50}$ should be a lot smaller, as illustrated in Figure 6.1.

6.2.2　Effect of CF$_3$I Content and Mixing Gas

The partial pressure of CF$_3$I in the mixture is generally selected based on a trade-off between three factors: the boiling point of the gas mixture, insulation strength and the by-products of the gas mixture upon each electrical discharge. Based on these factors, a comparative study was carried out using a 10/30 mm coaxial geometry in different CF$_3$I gas mixtures to examine their breakdown properties. The results obtained at 1 bar (abs.), as shown in Figure 6.2, gave an initial indication that the mixtures containing CO$_2$ had a higher breakdown performance than the mixtures with N$_2$ gas. It can be seen that there was only a small difference between the 20/80% and 30/70% CF$_3$I/CO$_2$ gas mixtures.
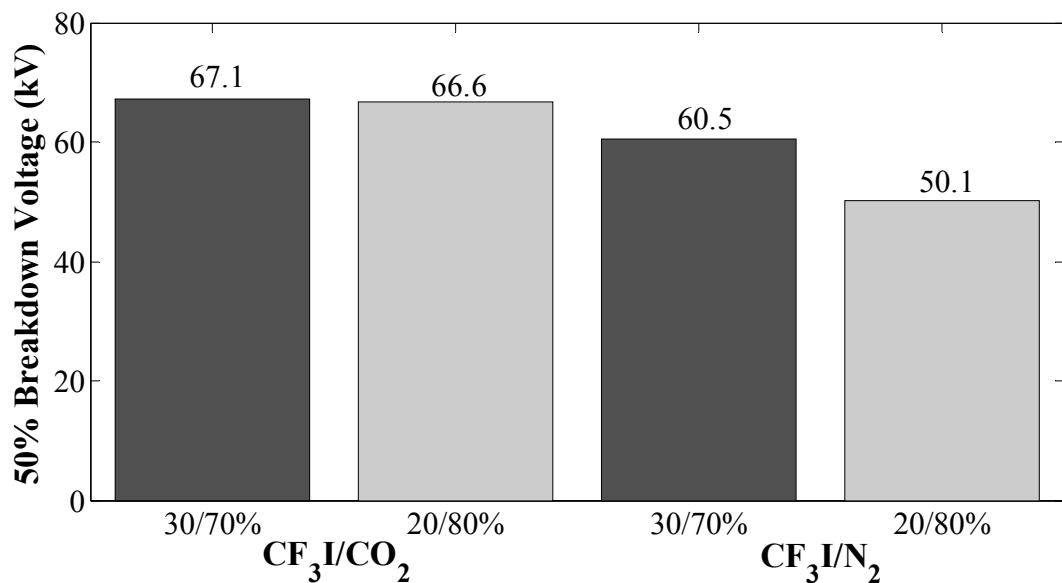
Figure 6.2: Effects of CF$_3$I contents and buffer gas on breakdown strength at pressure of 1 bar (abs.) (tested on a coaxial test system of 10/30 mm and for positive lightning impulse polarity).

A more comprehensive investigation was conducted at mixture ratios of 20/80% and 30/70% for CF_3I/CO_2 and CF_3I/N_2 gas mixtures for positive impulse polarity with different pressures. The results are shown in Figure 6.3, from which the following observations can be made: (i) at low pressure, there is a small difference in terms of U_{50} for 20/80% and 30/70% CF_3I/CO_2 gas mixtures; (ii) under higher gas pressures, a gas mixture with a higher CF_3I content will have a higher U_{50}, and, (iii) CF_3I/CO_2 gas mixtures have a higher breakdown strength than their equivalent CF_3I/N_2 gas mixtures. The standard deviation was obtained based on the individual set of results for each data point; these are indicated in the form of error bars on Figure 6.3.
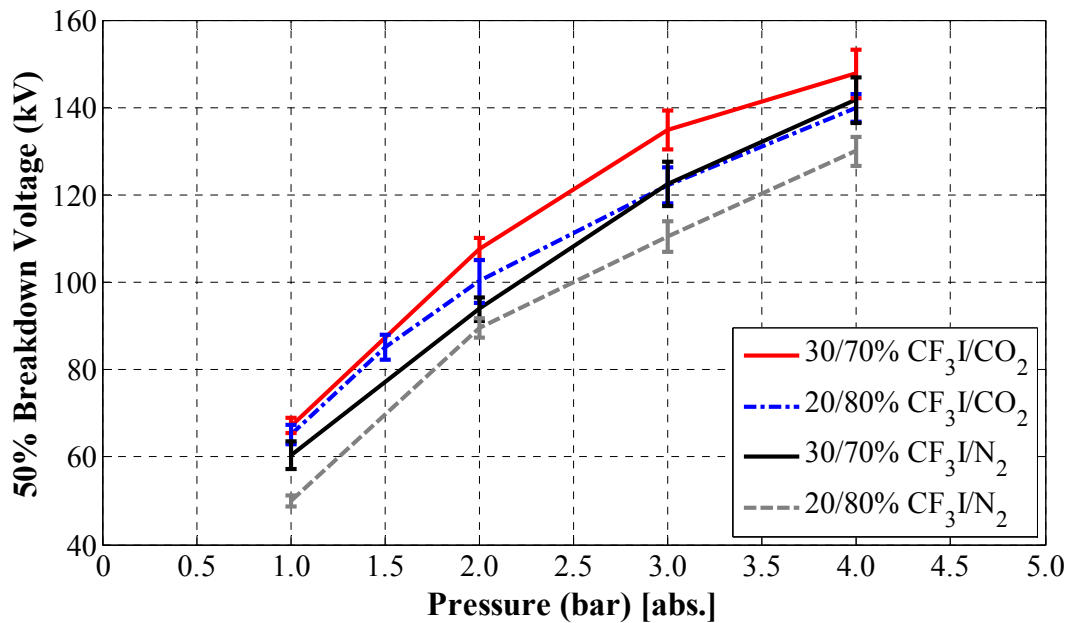
Figure 6.3: Breakdown voltage, U_{50}, as a function of pressure from 1 to 4 bar for CF_3I/CO_2 and CF_3I/N_2 gas mixtures with ratios of 20/80% and 30/70% (tested on a coaxial test system of 10/30 mm and for positive lightning impulse polarity).

6.2.3 Effect of Pressure and Polarity

To quantify and gain a better understanding of the effect of gas pressure and impulse polarity, experiments were carried out for pressures of 1, 2, 3 and 4 bars (abs.) for both positive and negative impulse polarities on gas mixture with ratios of 20/80% and 30/70%

for both CF_3I/CO_2 and CF_3I/N_2. The breakdown data were then plotted. These are displayed in Figure 6.4 and Figure 6.5 for CF_3I/CO_2 and CF_3I/N_2 gas mixtures respectively. From the figures, four observations can be made: (i) the breakdown voltage increases with increasing pressure, (ii) higher CF_3I content results in a higher breakdown voltage, (iii) the breakdown voltages obtained for positive impulse were higher than their equivalent for negative impulse, and, (iv) the differences between positive and negative breakdown voltages were smaller for CF_3I/N_2 gas mixtures in comparison with CF_3I/CO_2 gas mixtures.

The polarity effect can be seen in the breakdown voltage results for the coaxial test system; breakdown voltages obtained for the negative impulse were much lower than for the positive impulse, particularly at higher pressures. As can be seen in Figure 6.4 and Figure 6.5, the breakdown voltages increase more linearly with pressure for a negative lightning impulses than for a positive lightning impulses.
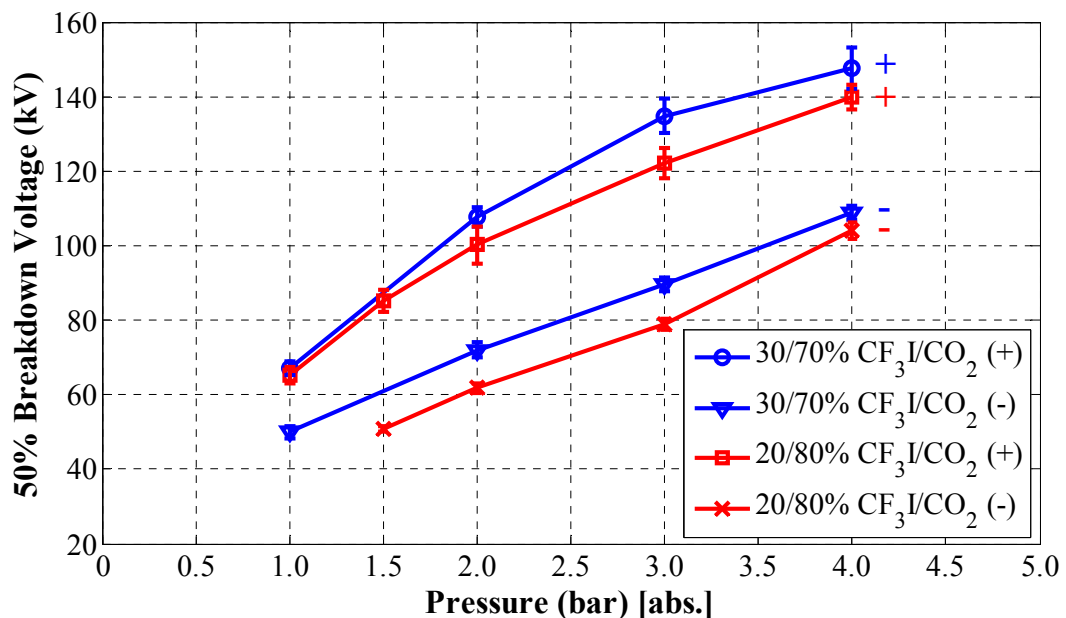
Figure 6.4: Breakdown voltage, U₅₀, at a pressure range of 1 to 4 bar (abs.) for various CF₃I/CO₂ gas mixtures, tested on a coaxial test system of 10/30 mm and for both lightning impulse polarities.
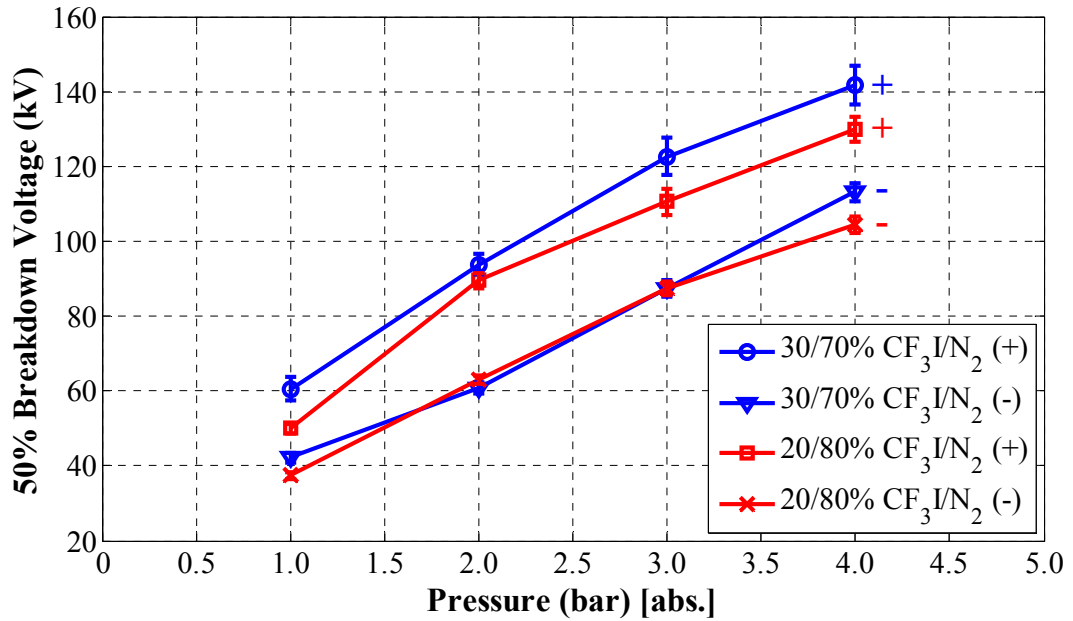
Figure 6.5: Breakdown voltage, U_{50}, at a pressure range of 1 to 4 bar (abs.) for various CF₃I/N₂ gas mixtures, tested on a coaxial test system of 10/30 mm and for both lightning impulse polarities.

6.3　Pressure-reduced Maximum Breakdown Field Strength

In Section 5.2, a dataset of pressure-reduced electric field, E/p, values against corresponding $(\alpha - \eta)$ values were computed using BOLSIG+ software for each CF₃I gas mixture. The E/p value at $(\alpha - \eta) = 0$ is referred to as the critical reduced field strength, $(E/p)_{crit}$, of each CF₃I gas mixture. An intense build-up of ionisation will occur in the regions when $E/p > (E/p)_{crit}$, which may lead to a complete breakdown of the insulating gas across the gap within the equipment. To analyse the breakdown data, the measured U_{50} were used in Equation (6.1) to obtain the pressure-reduced maximum breakdown field strength $(E_{max}/p)_B$. This is given by the calculated field strength at the inner cylinder when the breakdown voltage $U_b = U_{50}$. If we assume that, at breakdown, this breakdown field strength is exceeded at the inner cylinder, then the expression (6.1) can be applied in order to calculate the $(E_{max}/p)_B$ for CF₃I gas mixtures. The experimental $(E_{max}/p)_B$ values are shown in Figure 6.6 and Figure 6.7 for CF₃I/CO₂ and CF₃I/N₂ gas mixtures respectively.

119

$$(E_{max}/p)_B = \frac{U_{50}}{R_a \cdot \ln(R_b/R_a) \cdot p} \tag{6.1}$$

where $(E_{max}/p)_B$ is the pressure-reduced maximum breakdown field strength, R_a and R_b are respectively the inner and outer radii of the coaxial geometry.

As can be observed in Figure 6.6 and Figure 6.7, the $(E_{max}/p)_B$ decreases with a steep slope in the low pressure range and, thereafter, with a gradual slope. From the BOLSIG+ computations, an estimation of the critical value of the gas mixture $(E/p)_{crit}$ was obtained for different CF_3I gas mixtures as shown in Section 5.2. It is expected that, below the $(E/p)_{crit}$, there should be no occurrence of any breakdown but $(E_{max}/p)_B$ values at higher pressures for negative polarity can be smaller than the critical value of $(E/p)_{crit}$ for CF_3I gas mixtures. This may be attributed to the existence of an electron avalanche with the support of electron emission from the microscopically irregular surface on the cathode.
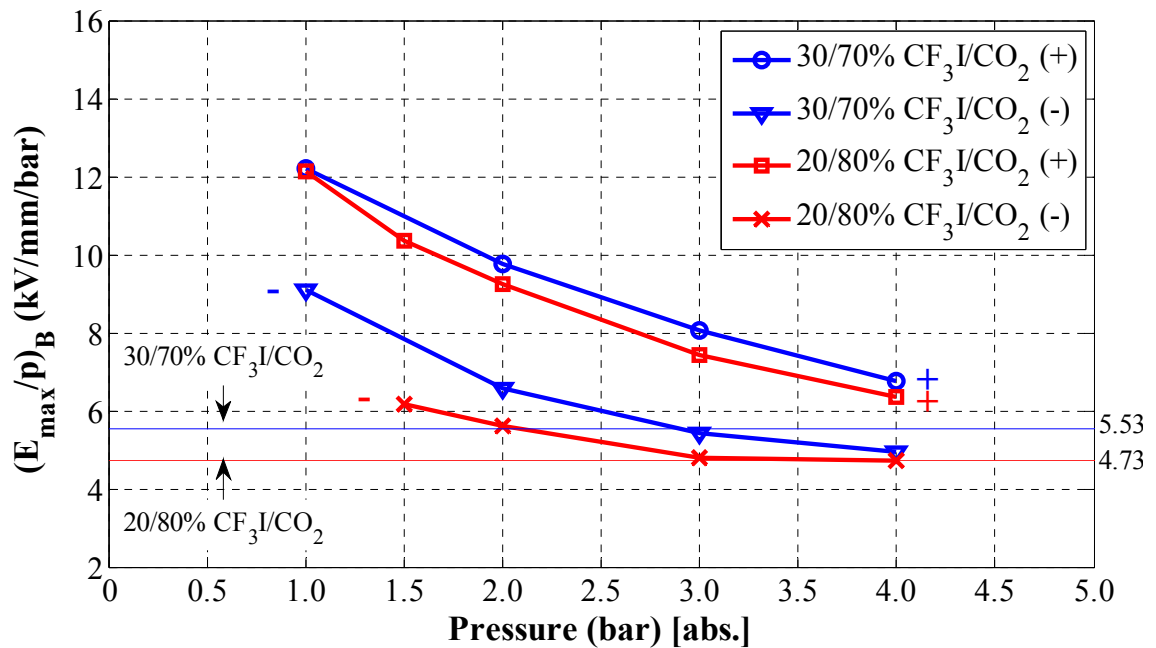
Figure 6.6: Characteristics of $(E_{max}/p)_B$ for various CF_3I/CO_2 gas mixtures at a pressure range of 1 to 4 bar (abs.), tested on a coaxial test system of 10/30 mm and for both lightning impulse polarities.
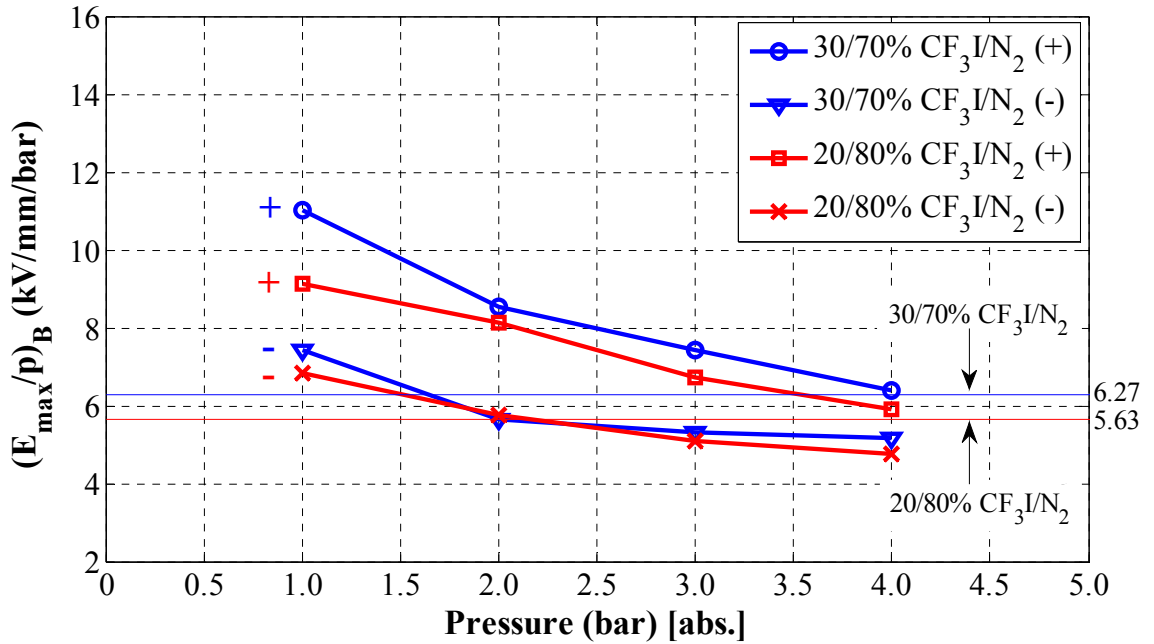
Figure 6.7: Characteristics of $(E_{max}/p)_B$ for various CF₃I/N₂ gas mixtures at a pressure range of 1 to 4 bar (abs.), tested on a coaxial test system of 10/30 mm and for both lightning impulse polarities.

As can be seen on Figure 6.6 and Figure 6.7, the results for negative impulse show a lower breakdown strength compared with their equivalent for positive impulse. An anode conductor, when subjected to a lightning impulse with a fast rise time, may require a much higher applied field and thus a larger critical volume where $(E_{max}/p)_B > (E/p)_{crit}$, so that initiatory electrons near the anode conductor can start the electron avalanche. This phenomenon will take place when the corona inception field strength, E_{corona}, is reached. To bridge the gap in a coaxial test system via a direct breakdown, the $(E_{max}/p)_B \sim (E/p)_{corona}$ has to be exceeded. In the case of a cathode conductor, the electrons could be more readily emitted from the conductor. Based on the lower measured breakdown voltages for negative impulse polarity, it can be assumed that the electron avalanche will take place at a lower electric field, inferred here as $E_{cathode}$. Hence, the $E_{cathode}/p < (E/p)_{corona}$, and the $(E_{max}/p)_B$ value would be smaller for negative than for positive impulse polarity, as demonstrated by the results shown in Figure 6.6 and Figure 6.7. A schematic

diagram is shown in Figure 6.8 illustrating the difference in the breakdown process under positive and negative polarities. In essence, the avalanche growth would be stronger when directed in the field of increasing strength. Electron avalanche develops more strongly towards an anode.
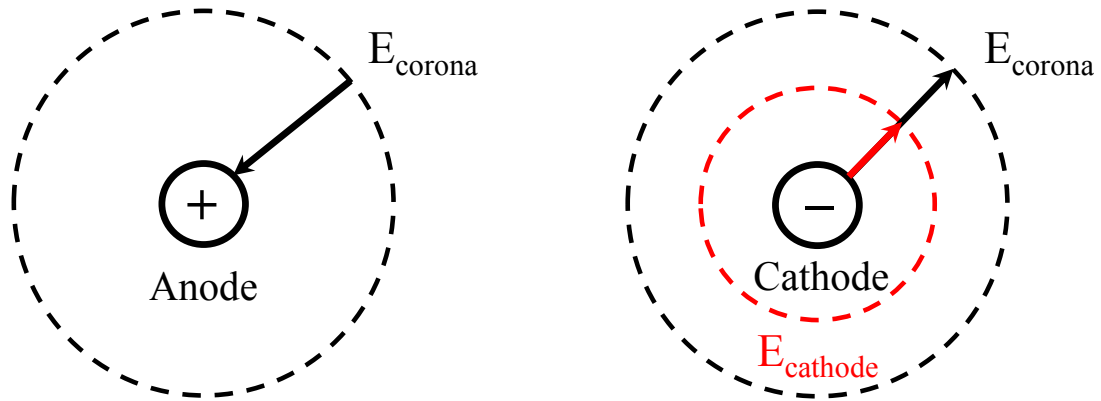
Figure 6.8: Schematic drawing of breakdown electric field in a coaxial geometry for both polarities, arrows indicating the direction of avalanche growth.

The breakdown results of CF_3I gas mixtures were then compared to SF_6 data from the literature. In [49], lightning impulse experiments were carried out on coaxial geometries of 32/96 mm and 50/96 mm over the pressure range from 1 to 14.7 bar (abs.) for positive and negative polarities. The 32/96 mm geometry has the same R_b/R_a ratio as the coaxial test system that was investigated in this work and, hence, has the same field utilization factor. However, the gap distance is different for the two models, which makes a direct comparison of the breakdown voltage not suitable. This, then, led to a comparative study using $(E_{max}/p)_B$ values, as shown in Figure 6.9 for SF_6, and for the 30/70% ratio of CF_3I/CO_2 and CF_3I/N_2 gas mixtures. It can be observed that, under positive polarity at low pressure, CF_3I gas mixtures have a higher $(E_{max}/p)_B$ than SF_6 gas and, at higher pressures this decreases much more quickly than with SF_6. At 4 bar (abs.), the $(E_{max}/p)_B$ of a 30/70% CF_3I gas mixture is around 80% that of SF_6. The critical value $(E/p)_{crit}$ of each gas mixture was calculated using BOLSIG+ when $(\alpha - \eta) = 0$. For a CF_3I/CO_2 gas

mixture, the $(E_{max}/p)_B$ drops below the $(E/p)_{crit}$ at a much higher pressure than their SF_6 or CF_3I/N_2 equivalent.
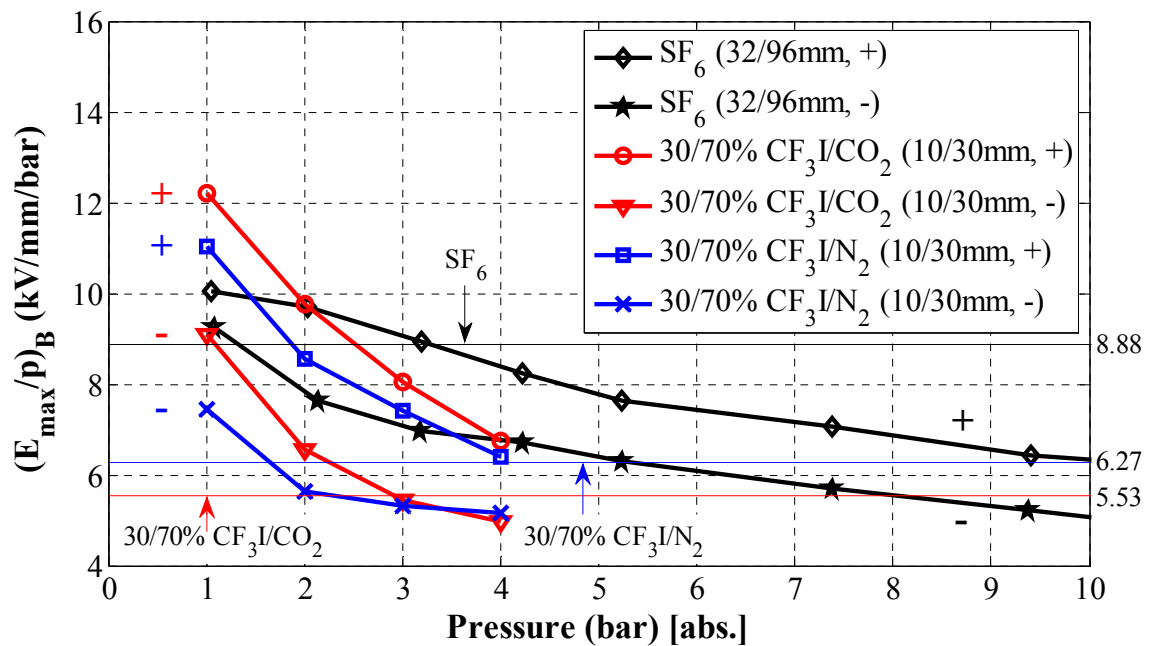
Figure 6.9: A comparative study on $(E_{max}/p)_B$ as a function of pressure for SF_6 and a 30/70% ratio of CF_3I/CO_2 and CF_3I/N_2 gas mixtures for coaxial test systems with geometric ratios of 1/2 and 1/3 and for both lightning impulse polarities.

6.4 Investigation of 30/70% CF₃I Gas Mixtures in Coaxial Geometry

Based on the results shown previously, the 30/70% CF_3I/CO_2 gas mixture had the most promising breakdown characteristics. Breakdown tests were then carried out on the 30/70% CF_3I/CO_2 and CF_3I/N_2 gas mixtures in a coaxial test system using different sized inner conductors. The V-t characteristics were also examined under a standard lightning impulse waveform.

6.4.1 Effect of Gap Spacing on 30/70% CF₃I/CO₂ Gas Mixture

The utilization factor f of a coaxial geometry is given by:

$$f = \frac{E_{mean}}{E_{max}} = \frac{R_a}{(R_b - R_a)} \cdot \ln(\frac{R_b}{R_a}) \tag{6.2}$$

where R_a is the outer conductor radius and R_b is the inner enclosure radius.

Table 6.1 shows the field utilization factor in percentages; the 10/30 mm coaxial geometry has an f value of 0.55 and is the closest to the optimal ratio. The previous experiments were carried out on a coaxial geometry with a ratio close to the optimal ratio as is used in full scale GIL. Using the same enclosure diameter, different-sized inner conductors were manufactured to investigate the effect of gap spacing in coaxial test systems. It was stated in the literature [74] that the highest breakdown voltages can be reached with ratios of R_b/R_a, which is very close to the optimum value of 2.718. It can be seen in Figure 6.10 that the relationship between breakdown voltage and pressure is almost linear irrespective of the gap spacing. As pressure increases, the voltage will increase less linearly, as observed by other researchers [49]. An inner conductor with a diameter of 20 mm has a higher geometric uniformity than a 10 mm diameter conductor, but it will also lead to a lower breakdown voltage due to the gap spacing between the inner and outer coaxial conductors being smaller. In contrast, an 8 mm diameter conductor has a larger gap spacing than a 10 mm diameter conductor, but the breakdown voltage is lower due to the geometry providing a less uniform field distribution.

Table 6.1: Field utilization factor for coaxial cylindrical electrode configurations.

2·(R_a/R_b) (mm)	f
8/30	0.48
10/30	0.55
15/30	0.69
20/30	0.81
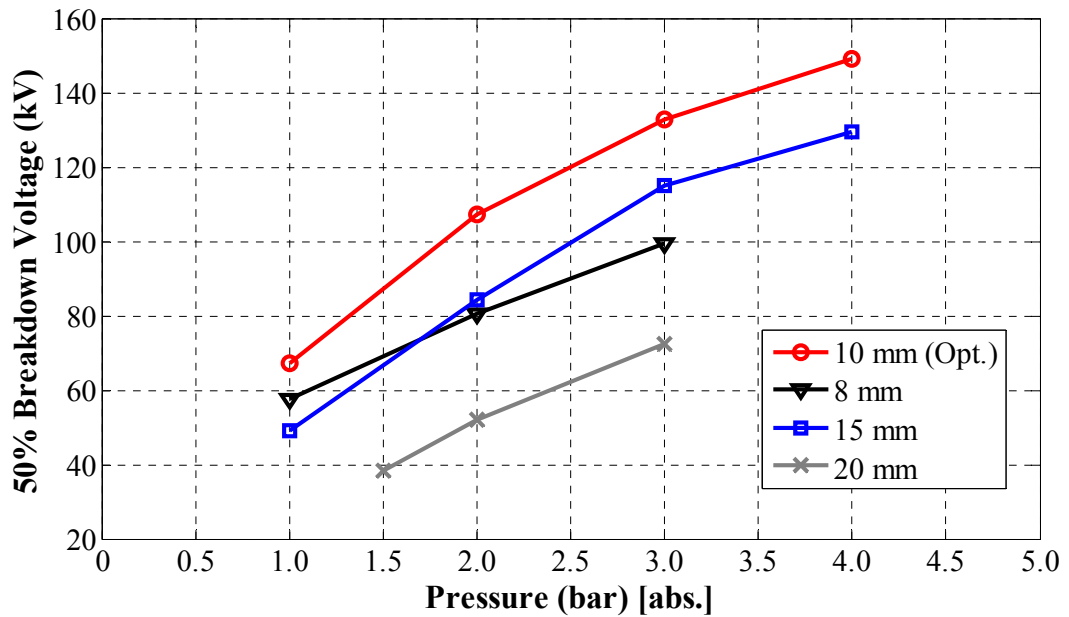
Figure 6.10: Breakdown voltage, U_{50}, for a 30/70% CF_3I/CO_2 gas mixture at a pressure range of 1 to 4 bar (abs.), for different diameters of the inner conductor in the coaxial test system and for positive lightning impulse polarity.

Figure 6.11 shows the pressure-reduced maximum breakdown field strength at breakdown for a 30/70% CF_3I/CO_2 gas mixture for different diameters of the inner conductor under pressures of 1 to 4 bar (abs.). Varying the diameter of the conductors alters the electric field uniformity, and the measured results suggest that all the curves are saturating towards the calculated critical reduced field strength, $(E/p)_{crit}$, of the 30/70% CF_3I/CO_2 gas mixture at 5.53 kV/mm/bar. At higher pressures, the $(E_{max}/p)_B$ values will drop below the critical value $(E/p)_{crit}$ of the CF_3I gas mixture as indicated by the SF_6 data shown in Figure 6.9, which is derived from [49].
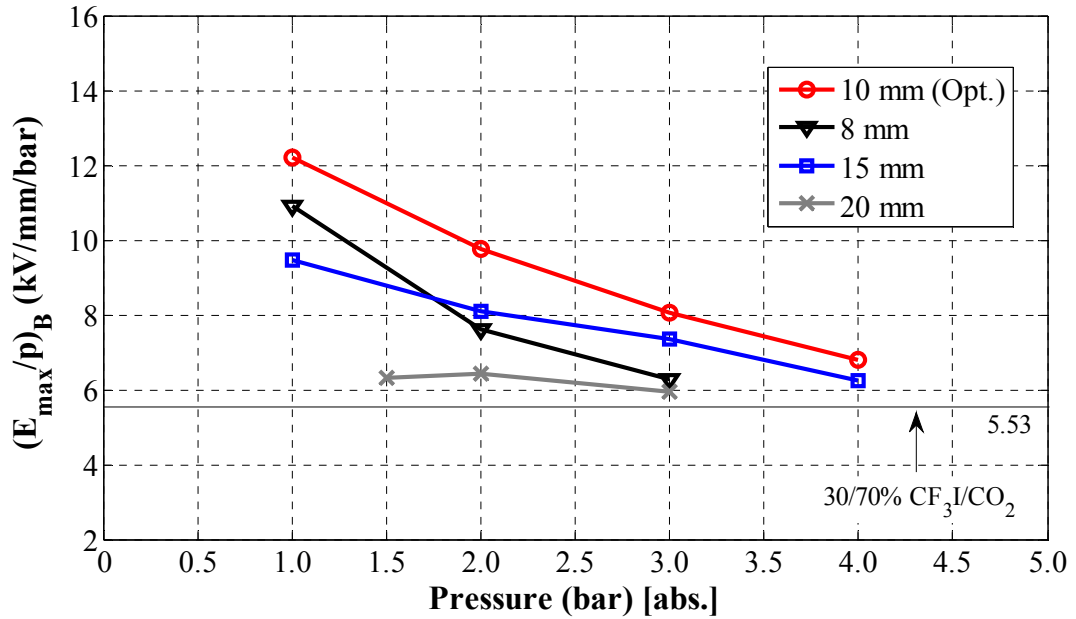
Figure 6.11: $(E_{max}/p)_B$ as a function of pressure tested for a 30/70% CF_3I/CO_2 gas mixture at a pressure range of 1 to 4 bar (abs.), for different diameters of the inner conductor in the coaxial test system and for positive lightning impulse polarity.

6.4.2   Effect of Gap Spacing on 30/70% CF_3I/N_2 Gas Mixture

The breakdown performance for different-sized conductors was also investigated in a 30/70% CF_3I/N_2 gas mixture. Figure 6.12 shows the breakdown voltage as a function of pressure for different-sized conductors. The coaxial geometry 10/30 mm has the highest breakdown strength, and all U_{50} data show a saturating trend except when $U_b = E_{crit} \times$ gap length. The $(E_{max}/p)_B$ values of a CF_3I/N_2 gas mixture for 8, 10 and 15 mm conductor diameters show the $(E_{max}/p)_B$ slope gradually decreasing to the $(E/p)_{crit}$ of the gas mixture at 6.27 kV/mm/bar calculated via BOLSIG+ as shown in Figure 6.13. These behavioural trends were also observed for a CF_3I/CO_2 gas mixture, but with a higher breakdown strength. However, for a non-uniform gap provided by an 8/30 mm geometric ratio, the breakdown strength is shown to be higher for the CF_3I/N_2 gas mixture. This is an indication that, for a coaxial geometry with lower field uniformity, the CF_3I/N_2 gas mixtures may outperform the equivalent CF_3I/CO_2 gas mixture. Further experimental

work is therefore required on a larger scale coaxial geometry and on conductor/enclosure ratios that provide lower field uniformity.
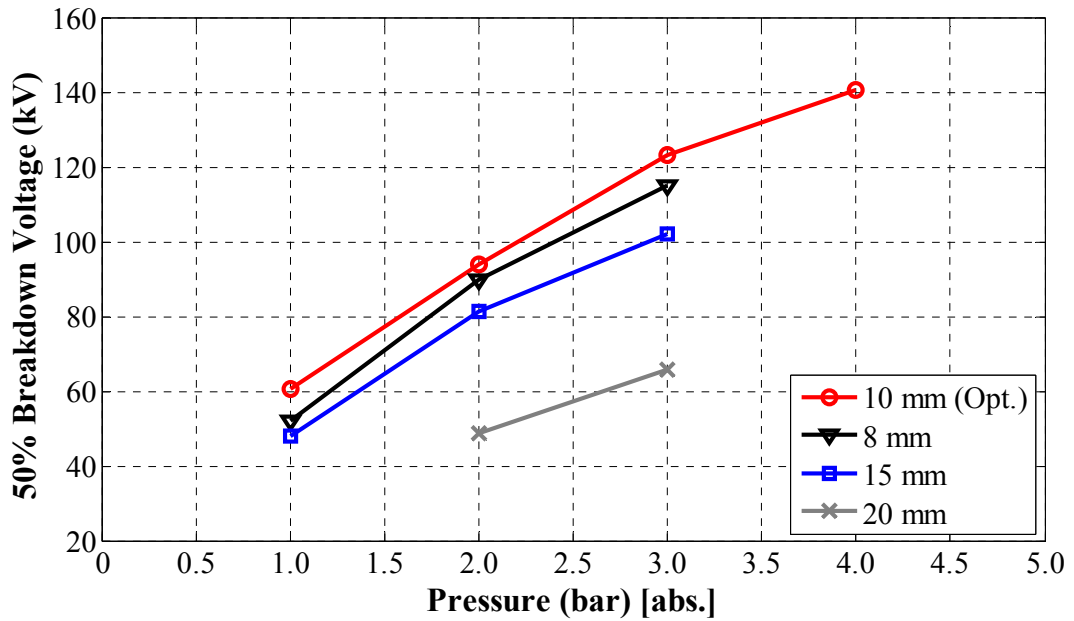
Figure 6.12: Breakdown voltage, U_{50}, for a 30/70% CF_3I/N_2 gas mixture at a pressure range of 1 to 4 bar (abs.), for different diameters of the inner conductor in the coaxial test system and for positive lightning impulse polarity.
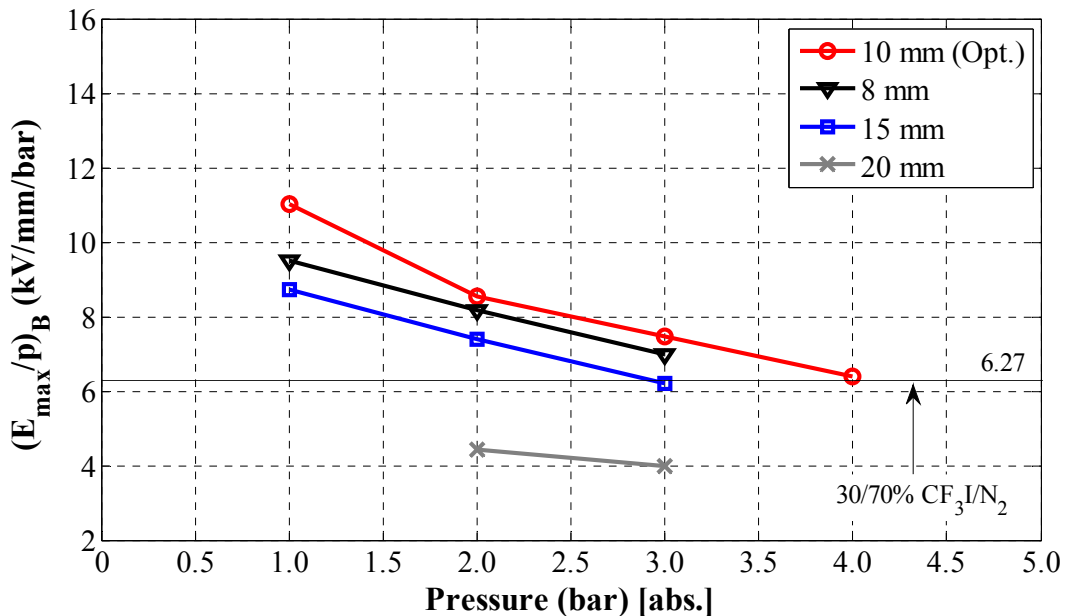
Figure 6.13: $(E_{max}/p)_B$ as a function of pressure tested for a 30/70% CF_3I/N_2 gas mixture at a pressure range of 1 to 4 bar (abs.), for different diameters of the inner conductor in the coaxial test system and for positive lightning impulse polarity.

Two of the coaxial geometries that were investigated in this work had similar geometric ratios to the 32/96 mm and 50/96 mm geometries reported in [49] for SF$_6$ gas. A comparative study was carried out, and the results are reported in Figure 6.14. A similar behavioural trend can be seen from both sets of coaxial test systems. The set of systems with a 1/3 ratio (close to optimal) has higher $(E_{max}/p)_B$ values and requires higher pressure to give values lower than the $(E/p)_{crit}$ value. This was expected since there is a steeper slope of the curve $(\alpha - \eta) = 0$ as a function of E/p in CF$_3$I and its mixtures with N$_2$. Therefore, it is important to design the GIL system to be well below the $(E/p)_{crit}$ of the chosen gas mixture to avoid a complete breakdown of the insulation.
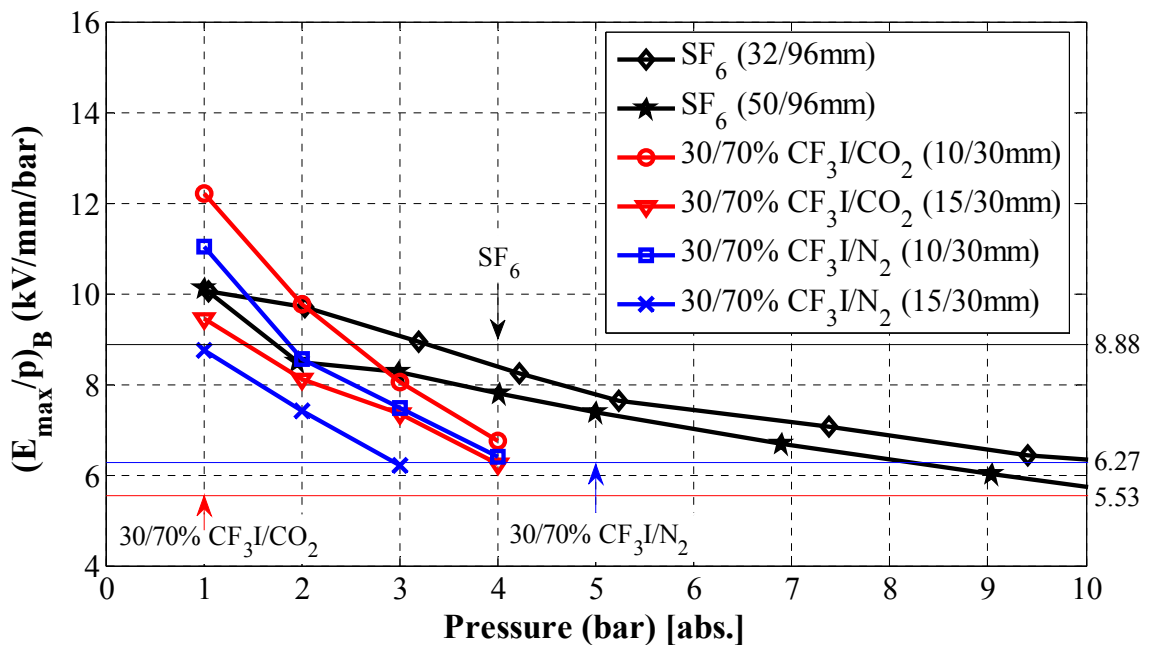
Figure 6.14: $(E_{max}/p)_B$ as a function of pressure for SF$_6$ and 30/70% mixture ratio of CF$_3$I/CO$_2$ and CF$_3$I/N$_2$ gas mixture in coaxial test systems with geometric ratios of 1/2 and 1/3 and for positive lightning impulse polarity.

6.4.3   V-t Characteristics

The V-t characteristics for the coaxial geometries were investigated for different CF$_3$I content, conductor thickness, gas pressure and impulse polarity. Two main patterns can be observed from Figure 6.15 to Figure 6.17: (a) mostly flat V-t curves or (b) V-t curves

rising steeply in the short-time region. The second pattern can be visibly observed at low pressure and small gap spacing.

Figure 6.15 shows the V-t characteristics for different CF_3I gas mixtures at 1 and 4 bar. At 1 bar, most of the breakdown events occurred in less than 5 μs. In the case of 4 bar, at a much higher gas density, there was more dispersion in the V-t results with more breakdown occurrences above 5 μs. It can be seen from the figure that the time to breakdown is more sensitive with the rise in breakdown voltage at a higher pressure of 4 bar. A higher breakdown voltage has a shorter average time to breakdown. There is no clear indication, however, that the time to breakdown was affected by changing the proportion of CF_3I as part of a binary mixture or the buffer gas (CO_2 or N_2). Based on these results, the V-t characteristics are shown to be more dependent on the applied voltage and the gas pressure between the inter-electrode gaps of the coaxial test system.
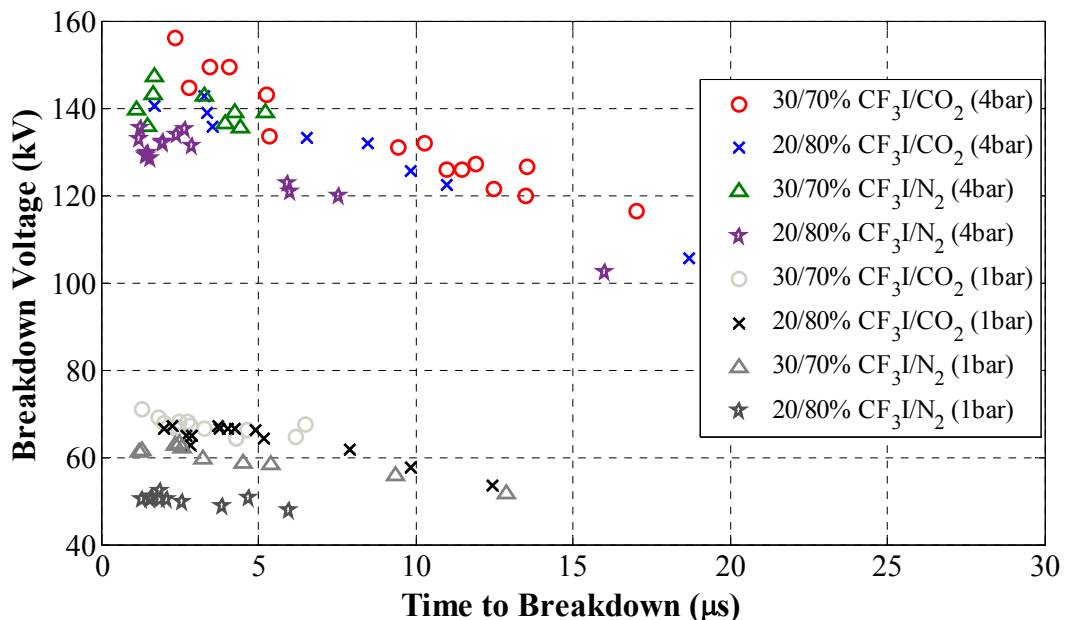
Figure 6.15: V-t characteristics for 20/80% and 30/70% mixture ratios of CF₃I/CO₂ and CF₃I/N₂ gas mixtures at 1 and 4 bar (abs.) pressure, tested on a coaxial test system of 10/30 mm and for positive lightning impulse polarity.

The V-t characteristics for the 30/70% CF_3I/CO_2 gas mixture were compared for both positive and negative polarities, as shown in Figure 6.16. The breakdown process under a positive impulse takes longer whereas, under a negative impulse, most of the breakdown events occur in less than 5 µs, with a few breakdown occurrences between 5 to 10 µs. It was found in the literature [65] that for a rod-plane electrode system with an Ø12 mm hemispherical capped rod and a field utilization factor of 0.45 that, the average time to breakdown for CF_3I gas at 1 bar (abs.) is longer for positive than for negative impulse polarity. The 10/30 mm coaxial geometry has a similar field utilization factor at 0.55, however, a direct comparison is not suitable, as both electrode configurations are different.
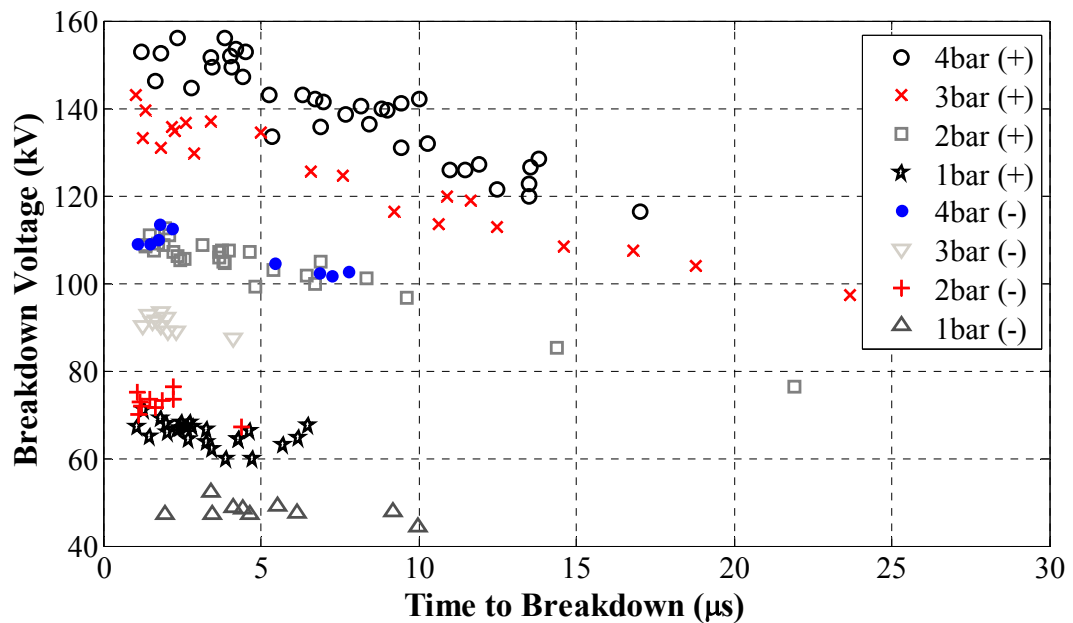
Figure 6.16: V-t characteristics of a 30/70% CF₃I/CO₂ gas mixture at a pressure of 1 to 4 bar (abs.), tested on a coaxial test system of 10/30 mm and for both lightning impulse polarities.

In Figure 6.17, when the pressure was fixed at 3 bar (abs.), the highest breakdown voltage was recorded for a 10 mm conductor rather than an 8 mm conductor, which exhibits a higher gap spacing. This is because, in a coaxial test system, the highest breakdown voltage is dependent on the trade-off between gap spacing and field uniformity, i.e., when

the ratio of R_b/R_a is closest to 'e = 2.718'. For a gas pressure of 3 bar, the highest breakdown voltage was recorded for a 10 mm conductor rather than an 8 mm, which has a higher gap spacing, as the ratio for 10/30 mm is closer to 'e'. The V-t results for negative impulse show that most of the breakdown events occurred below 5 μs, a trend that is also seen in Figure 6.16. Thus, the average breakdown voltage is lower for a negative breakdown, and the time to breakdown is not dependent on the change of breakdown voltage. This result supports the explanation earlier regarding E_{corona} and $E_{cathode}$ for positive and negative polarities. For a negative breakdown, the field stress $E_{cathode}$ is lower in comparison to a positive breakdown; therefore, a much lower breakdown voltage is needed. For a cathode conductor, electrons are readily available; in other words, less statistical time is required for the initial electrons to start the avalanche process. This, then, reduces the time to breakdown in comparison to a breakdown initiated for positive impulse.
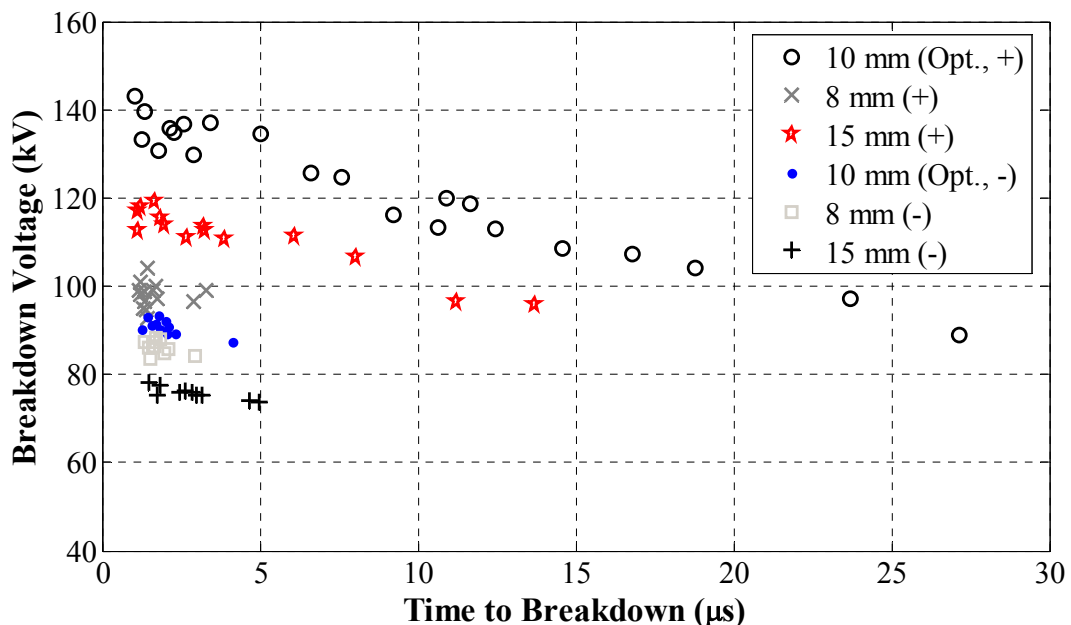
Figure 6.17: V-t characteristics of a 30/70% CF₃I/CO₂ gas mixture for various conductor diameters at 3 bar (abs.) pressure and for both lightning impulse polarities.

6.5   Modelling Technique for Streamer and Leader Breakdown

Full-scale GIL demonstrators are expensive, and experimental investigation of CF_3I gas mixtures via breakdown tests in such a demonstrator would risk damaging it. A reduced-scale test system was, therefore, developed to investigate the breakdown characterisation of CF_3I gas mixtures. It would be more useful, however, to have a modelling technique that could evaluate the breakdown strength for larger coaxial geometries. In this thesis, based on the principle of a streamer/leader discharge mechanism and obtained breakdown data for the coaxial test system, equations for the breakdown model were developed by Waters [109]. The model was developed for positive breakdown data, since there is another influencing factor for negative impulse polarity due to $E_{cathode}/p$, which is lower than the $(E/p)_{crit}$. Furthermore, comparisons were carried out for a larger scale coaxial test system (Prototype II) and data obtained from the literature for SF_6 to verify the breakdown model.

6.5.1   Streamer/Leader Breakdown of Electronegative Gas

For the breakdown model, U_b refers to the measured breakdown voltage, U_S is the calculated streamer breakdown voltage and U_L is the calculated leader breakdown voltage. For an electronegative gas such as CF_3I, the build-up of ionisation will occur when the pressure-reduced field $(E_{max}/p)_B$ exceeds the critical value $(E/p)_{crit}$ of CF_3I, that is, around 10.78 kV/mm/bar. As observed from the BOLSIG+ plot of $(\alpha - \eta)/p$ against E/p, CF_3I is a brittle gas; when the $(E/p)_{crit}$ is exceeded, the ionisation builds up very quickly, and this leads to a direct breakdown of the gas insulation through the formation of a discharge channel. However, adding a large proportion of CO_2 or N_2 gases as part of a binary mixture, the slope becomes less steep when compared to pure CF_3I gas, and this indicates that the build-up of ionisation would be slower. However, the value of $(E/p)_{crit}$ is reduced

in gas mixtures; for example, in a 30/70% CF_3I/CO_2 gas mixture, the value of $(E/p)_{crit}$ is 5.53 kV/mm/bar.

The difference between a streamer and a leader channel can be explained by the ideal gas law (6.3).

$$p = \frac{nRT}{V} \qquad (6.3)$$

where p is the pressure of the gas, V is the volume of the gas, n is the number density of the gas, R is the ideal gas constant, and T is the temperature of the gas.

The critical reduced field strength, $(E/p)_{crit}$, is effectively determined by the critical gas density E/N. In a streamer channel, the temperature increase remains relatively small. In a leader channel, by contrast, the temperature increases due to increased current density in the channel, which lead to gas expansion. This results in further increase in current and a much lower gas density, following (6.3). The effective ionisation coefficient $(\alpha - \eta)$ is increased and free electrons are produced at a lower field strength [122], so that the measured U_b at breakdown is lower than U_s.

In the past, Wiegart et al. [123]–[125] developed a theory for predicting the breakdown voltage of SF_6 in a non-uniform field. A Schlieren photograph of breakdown in SF_6 was taken to illustrate the basic structure of flashover in a non-uniform field: initial dense channels of streamer near the high-voltage electrode may be extended further by fewer and broader streamer channels. The gas discharge phenomenon may occur as a streamer or leader breakdown. With the assumption that the applied voltage is sufficiently high, if the primary streamers bridge the inter-electrode coaxial gap between the conductor and the enclosure, a discharge channel may develop, and a single-stage streamer breakdown

may be initiated when $U_b = U_S$. The boundary of the streamer discharge in a coaxial test system can be represented by the radial streamer extent, C_S, and when $C_S = R_b$, throughout the streamer region, the electric field will be E_{crit}. At longer gaps, the streamer radius C_S may be shorter than R_b. For the breakdown to initiate, a secondary streamer channel may undergo internal heating and then rapid gas expansion. This process takes place very quickly, and a self-propagating leader channel is formed in the streamer region ($R_b - C_L$), where $C_S = C_L < R_b$ at the breakdown voltage U_b, which eventually leads to a leader breakdown across the coaxial gap [126]. At U_b, the electric field across the ($C_L - R_a$) region will be the E_{crit} of the insulation gas medium, and the electric field for the region ($R_b - C_L$) will be the leader propagating field, E_L. The criteria C_L and E_L can be deduced based on the measured breakdown voltage, U_b.

6.5.2   Breakdown Modelling in a Coaxial Geometry

In a coaxial test system with a geometric ratio $R = R_b/R_a$, when the field strength on the conductor R_a exceeds the critical field strength of the gas mixture, the corona inception can occur at a voltage $U > U_i$. Assuming that no leader channel was formed, the streamer breakdown voltage U_S can be calculated by (6.4).

$$U_S = E_{crit} \cdot (R_b - R_a) \tag{6.4}$$

The radial streamer extent C_S can provide an indication of whether the breakdown is under the streamer or the leader category. This criterion can be obtained using (6.5).

$$E_{crit} \cdot (C_S - R_a) = U \cdot [\ln(C_S/R_a) / \ln R] \tag{6.5}$$

The expression on the right-hand side represents the potential at radius C_S before streamer development, and the expression assumes that this potential will remain unchanged by the radially symmetrical critical field streamer growth defined by the left-hand expression.

If the breakdown voltage is known, then C_S at breakdown can be calculated. This can be determined systematically as shown in Figure 6.18.
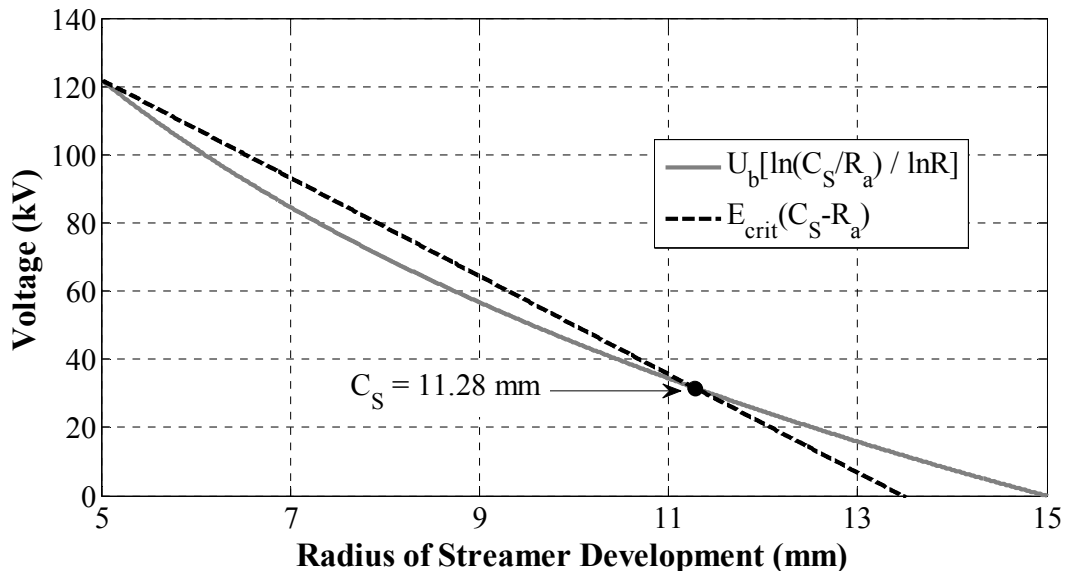
Figure 6.18: Voltage as a function of radius of a streamer development to determine the streamer extent, C_S, at an applied voltage of 120 kV for a 20/80% CF₃I/CO₂ gas mixture at 3 bar (abs.) pressure (tested on a coaxial test system of 10/30 mm and for positive lightning impulse polarity).

Equation (6.5) can be rewritten as

$$f\left(\frac{C_s}{R_a}\right) = \frac{\frac{C_S}{R_a} - 1}{\ln(\frac{C_S}{R_a})} = \frac{U}{R_a \cdot E_{crit} \cdot \ln R} \tag{6.6}$$

Unlike (6.5), which calculates the radius C_S for a single breakdown data, (6.6) can provide a plot of $f(C_S/R_a)$ that can calculate the C_S of any coaxial geometry, as can be seen in Figure 6.19. Using the measured breakdown voltage into the right-hand expression in (6.6) gives a value for $f(C_S/R_a)$, which can be used to determine C_S/R_a, and then C_S graphically, as seen in Figure 6.19.
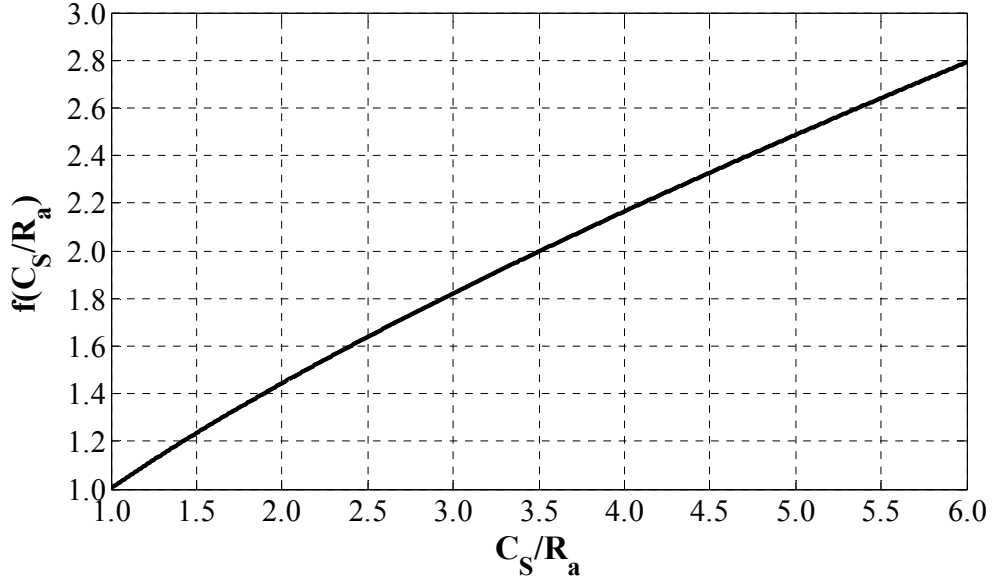
Figure 6.19: Calculation of streamer radius C_S for various geometric ratios.

If the streamer extent $C_S = C_L < R_b$, the measured breakdown voltage U_b may be below

U_S. For the lower U_b, a leader propagating field, E_L is introduced as a criterion which is

based on the mean voltage gradient across $(R_b - C_L)$. In other words, a self-propagating

leader channel is formed in the region ahead of the corona streamers $(R_b - C_L)$, and then

eventually, this initiates the leader breakdown. The relationship of E_L to the critical field

of the CF₃I gas mixture is not known but must be sufficient to sustain leader growth across

$(R_b - C_L)$. It will be shown in Section 6.5.3 that the E_L criterion can be deduced

experimentally based on the measured breakdown voltage for the coaxial test system. The

occurrence of a breakdown at a voltage below U_S is possible because the E_L in the leader

channel is lower than $(E/p)_{crit}$ in the CF₃I gas mixture. U_L is calculated by (6.7).

$$U_b = E_L \cdot (R_b - C_L) + E_{crit} \cdot (C_L - R_a) \tag{6.7}$$

The ratio of the mean field E_L in the leader channel to the critical field E_{crit} can be

represented by the field ratio, K as shown in (6.8).

$$K = E_L \ / \ E_{crit} \tag{6.8}$$

6.5.3 Analytical Study Using the Breakdown Model

The model was applied to the positive breakdown data in a coaxial geometry to analyse the results further. Table 6.2 shows the comparison between the measured U_b and the calculated streamer breakdown voltage U_S in a coaxial geometry of 10/30 mm.

In Table 6.2, the streamer breakdown voltage was calculated using (6.4), which is simply the product of E_{crit} and gap spacing ($U_S = E_{crit} \times g$). E_{crit} is the boundary that represents the critical field strength for each CF_3I gas mixture. It assumes that as a result of streamer development a value of $(E/p)_{crit}$ will become constant throughout the coaxial gap. Therefore, the breakdown voltage will increase linearly with the pressure and gap spacing. It can be seen that U_b and U_S are comparable only for low gas pressures, which suggests that a two-stage leader breakdown occurred at the higher pressures. This is when the streamer extent $C_S < R_b$ for the measured breakdown voltage. The leader extent C_L is calculated and shown in Table 6.3.

Table 6.2: Comparison of measured U_b and the calculated U_S.

Pressure	30/70% CF₃I/CO₂			30/70% CF₃I/N₂		
	U_b	E_{crit}	U_S	U_b	E_{crit}	U_S
bar (abs.)	kV	kV/mm	kV	kV	kV/mm	kV
1	67.1	5.5	55.3	60.5	6.3	62.7
2	107.7	11.1	110.6	93.8	12.5	125.4
3	134.9	16.6	165.9	122.6	18.8	188.1
4	147.7	22.1	221.2	141.7	25.1	250.8

The distance C_L is determined from (6.6); a leader breakdown is indicated when $C_S = C_L < R_b$. Equations (6.7) and (6.8) are used to calculate criteria K and E_L/p using the same set of measured U_b data from Table 6.2. The pressure-reduced leader field criterion,

E_L/p, shows that streamer breakdown is possible around 1 bar for 30/70% CF$_3$I/CO$_2$, whereas for 30/70% CF$_3$I/N$_2$, the streamer breakdown is possible only below 1 bar.

Table 6.3: Calculations of C$_L$, K and E$_L$/p values from measured U$_b$.

Pressure bar (abs.)	30/70% CF$_3$I/CO$_2$				30/70% CF$_3$I/N$_2$			
	U$_b$ kV	C$_L$ mm	K	E$_L$/p kV/mm/bar	U$_b$ kV	C$_L$ mm	K	E$_L$/p kV/mm/bar
1	67.1	–	–	–	60.5	14.1	0.60	3.80
2	107.7	14.3	0.60	3.32	93.8	9.0	0.58	3.65
3	134.9	10.5	0.59	3.23	122.6	7.0	0.57	3.57
4	147.7	7.3	0.57	3.13	141.7	5.3	0.55	3.48

6.5.4   Evaluation Model for Breakdown Results

The investigation of gap distance was extended to a larger coaxial test system of Prototype II, which has the same geometric ratio as Prototype I but with a gap spacing that is three times larger. Due to limitations of the high-voltage bushing, the test was only carried out for 0.5 bar (abs.). The theoretical breakdown voltage was calculated using Equation (6.4); with the assumption that if the breakdown occurred at 0.5 bar (abs.), there would be a streamer discharge. A comparison of the breakdown voltages for experimental and theoretical breakdown strength is shown in Figure 6.20. It can be seen that there is a small difference in the breakdown results for 30/70% CF$_3$I/CO$_2$ and 30/70% CF$_3$I/N$_2$ gas mixtures. This was also observed for the breakdown comparison at 0.5 bar (abs.), as shown in Figure 6.2. It can be seen, however, that there is a significant difference between the experimental and theoretical results for 30/70% CF$_3$I/N$_2$. This indicates that a leader breakdown model needs to be applied on the measured U$_b$, and the results of this are shown in Table 6.4.
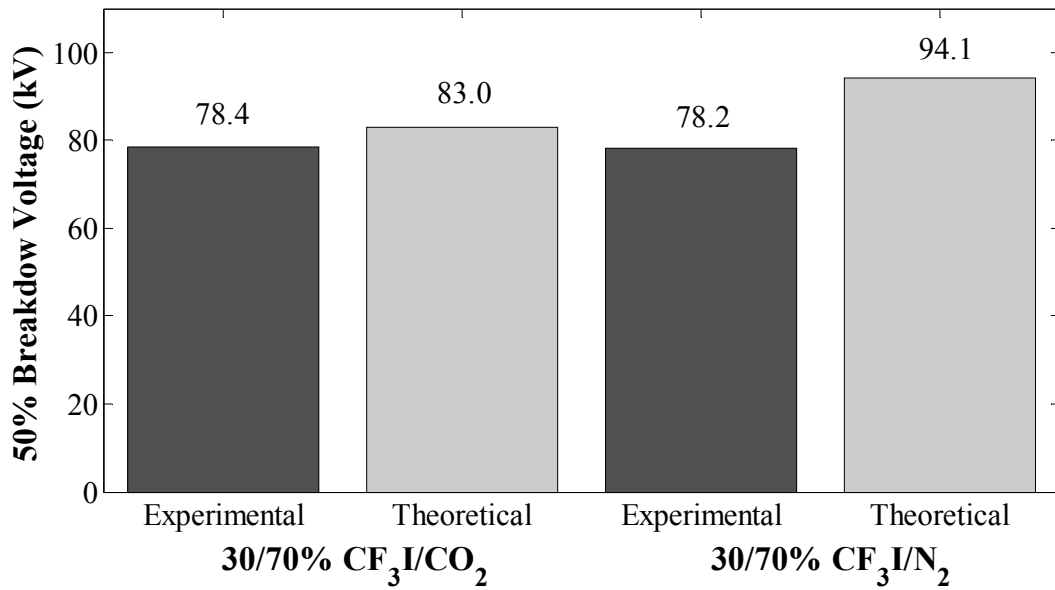
Figure 6.20: Effects of CF$_3$I contents and buffer gas on breakdown strength between experimental and theoretical results at pressure of 0.5 bar (abs.) tested on a coaxial test system of 30/90 mm for positive lightning impulse polarity.

Table 6.4 shows that if $C_L < R_b$, a leader breakdown has taken place. It was observed in Table 6.3, that the difference for E_L/p of CF$_3$I gas mixtures can be equated to the difference in $(E/p)_{crit}$ of gas or gas mixtures, which were calculated by BOLSIG+, as can be seen for the E_L/p results in Table 6.4. The criterion K obtained for 30/90 mm is similar to the results obtained in Table 6.3 for a 10/30 mm geometry. This suggests that E_L/p is not dependent on pressure, field utilization factor and gas mixture.

Table 6.4: Comparison of measured U_b at 0.5 bar (abs.) with calculated U_S and U_L.

Gas Mixture	Measured U_b	U_S	U_L	C_L	K	E_L/p
	kV	kV	kV	mm		kV/mm/bar
30/70% CF$_3$I/CO$_2$	78.4	83.0	78.42	40.9	0.60	3.31
30/70% CF$_3$I/N$_2$	78.2	94.1	78.24	32.7	0.59	3.71

The breakdown voltage is likely to be very high (beyond the laboratory test capability) for a full-scale GIL test system. It can be seen in the tables that the potential gradient does

not increase linearly against gas pressure. This breakdown model is able to account for

the drop in potential at higher gas pressures by introducing ratio K, which are obtained

using the experimental data. Figure 6.21 shows a comparison of ratio K as a function of

pressure for mixture ratios of 20/80% and 30/70% for both CF_3I/CO_2 and CF_3I/N_2 gas

mixtures and 100% SF_6 gas [49] tested on three sets of coaxial test systems: 10/30 mm,

30/90 mm and 32/96 mm, which all have the same geometric ratio of 1/3. It is noteworthy

that, for the available data, the calculated field ratio, K, in Figure 6.21, is almost

independent of the insulation medium, gas pressure and, more importantly, the size of the

coaxial geometry, as long as the geometric ratio remains the same.
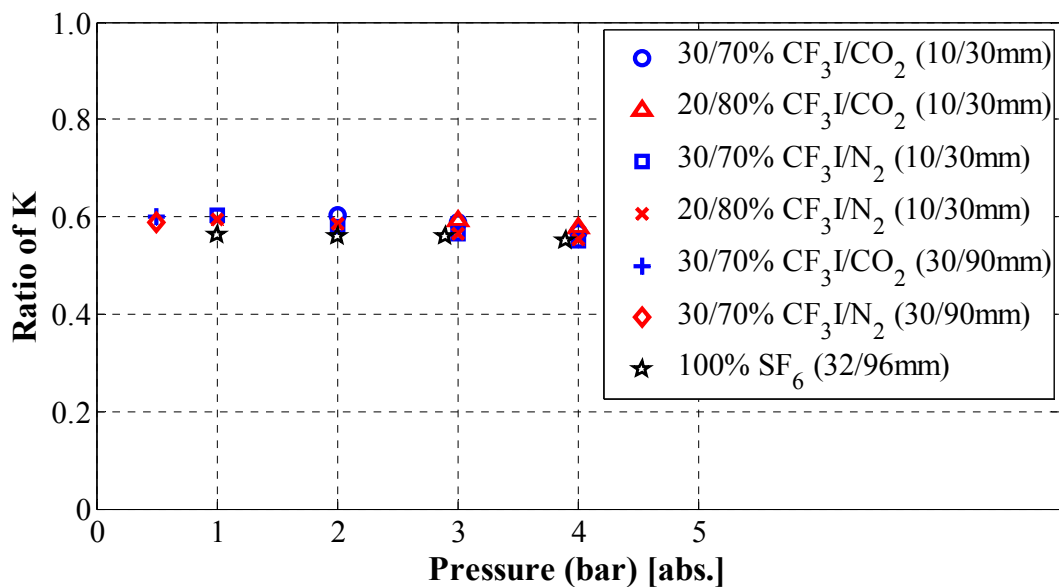
Figure 6.21: Ratio of K as a function of pressure for SF₆ and mixture ratio of 20/80% and 30/70% for both CF₃I/CO₂ and CF₃I/N₂ gas mixtures, tested on three sets of coaxial test systems (10/30mm, 30/90mm and 32/96mm) with the same geometric ratio R of 1/3 and for positive lightning impulse polarity.

6.5.5   Applying the Breakdown Model for SF₆ Data

The streamer and leader breakdown model was also applied to published breakdown data

for SF_6 in a coaxial test system of 32/96 mm, obtained from the literature [49]. The SF_6

test system, although much larger, has the same near-optimum value of R = 3 as the

coaxial test system of 10/30 mm investigated for CF$_3$I gas mixtures in this thesis. At higher gas pressures, the C$_L$ distance can be identical to the gap spacing within the coaxial test system. In this case, the value K can be calculated using (6.9).

$$K = \frac{U_b}{(R_b - R_a) \cdot E_{crit}} \tag{6.9}$$

The calculated criterions of K and E$_L$/p are shown in Table 6.5. It is found that over the pressure range of 1 to 4 bar (abs.), the K ratio for SF$_6$ is in the same range, 0.55–0.60, as has been found here for CF$_3$I data tested on a 10/30 mm coaxial test system. It was shown in Table 6.5 that at higher pressures of up to 12.7 bar, which are not in the range useful for GIL design, the calculated K values of SF$_6$ decline to 0.38. It is unknown whether this would be the case for CF$_3$I gas mixtures at higher pressures.

Table 6.5: Calculated K and E$_L$/p criterions for measured U$_b$ of SF$_6$.

Pressure	U$_b$	C$_L$	K	E$_L$/p
bar (abs.)	kV	mm		kV/mm/bar
1.0	180.0	21.1	0.56	5.01
2.0	350.0	19.9	0.56	4.99
2.9	500.0	19.4	0.56	4.97
3.9	610.0	16.1	0.55	4.89
4.9	700.0	–	0.50	4.46
6.9	920.0	–	0.47	4.17
8.8	1060.0	–	0.42	3.76
10.8	1230.0	–	0.40	3.56
12.7	1360.0	–	0.38	3.35

For different insulation gases, the E$_L$/p decreases only slightly with gas pressures up to 4 bar (abs.), as can be seen in Table 6.3 and Table 6.5. When comparing two different insulation gases, for example, around 4 bar, the E$_L$/p of SF$_6$ and a 30/70% CF$_3$I/N$_2$ gas mixture is 4.9 and 3.5 respectively. The ratio of the two E$_L$/p values is almost the same as

the ratio of $(E/p)_{crit}$ between SF$_6$ gas and a 30/70% CF$_3$I/N$_2$ gas mixture, which is 8.88

and 6.27 kV/mm/bar respectively. By applying this comparison to any CF$_3$I gas mixture

and to SF$_6$ gas, as long as the coaxial geometric ratio is the same, the ratio of E_L/p is found

to be almost identical to the ratio of $(E/p)_{crit}$.

6.5.6   Arrested Leader Length of SF$_6$ in Uniform Field

Seeger et al. [127] studied the breakdown mechanism of SF$_6$ in a plane-plane electrode

configuration with a 1 mm protrusion length and a gap distance set at 20 mm.

A configuration that represents a quasi-uniform field similar to a coaxial cylindrical

configuration. The experiment was conducted using a Van der Graff generator with a long

time duration of 60 s. In the paper, the authors introduced a dimensionless ratio, referred

to as the reduced background field, x, which can be calculated using (6.10).

$$x = \frac{E_0}{E_{cr,0}} = \frac{U/d \cdot p}{(E/p)_{crit}} \qquad (6.10)$$

where E_0 is the mean reduced applied field, $E_{cr,0}$ is the critical reduced field, U is the

applied voltage, d is the gap distance, p is the pressure and $(E/p)_{crit}$ is the critical reduced

field strength of the insulation gas.

For this long duration of applied voltage, the leader frequently arrested (stopped) during

the development. The lengths of arrested leaders were roughly evaluated from the video

frames of a high speed camera and are shown in Figure 6.22. It can be seen that the leader

length also increases as the applied background field, x, increases. There is almost no

arrested leader present when x >0.6 for both polarities at pressures of 2 and 4 bars. This

indicates when x ≥ 0.6, a leader discharge is initiated. It is noteworthy that the maximum

value of x ≈ 0.6 is the same value as the ratio K deduced from the experimental data for

CF$_3$I gas mixtures, as illustrated in Figure 6.21. It can, therefore, be assumed that x ≡ K

when a leader discharge occurs ($x \equiv K \geq 0.6$). The figure also shows that as pressure increases, the arrested leader length decreases. If we assume $x \equiv K$, similar reduction was also observed at higher pressure for the K values of SF_6, as shown in Table 6.5. Although it is a different definition from the ratio K used in this thesis, it is a useful parameter for comparison with the K values of CF_3I data.
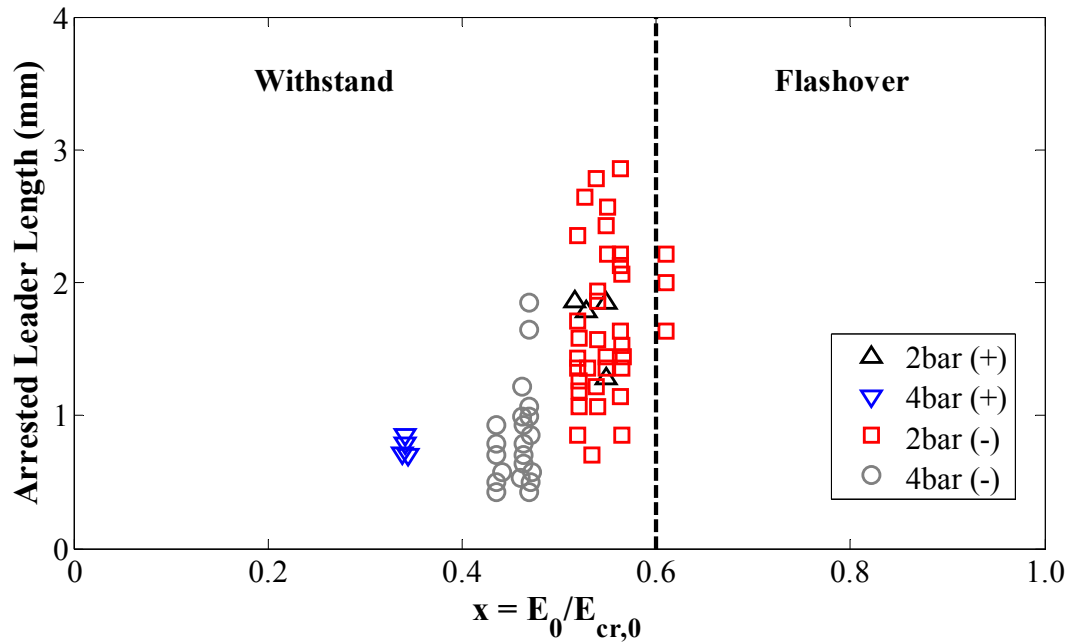
Figure 6.22: Arrested leader length as a function of reduced background field x at pressures of 2 and 4 bar (abs.) and for both polarities [127].

6.6   Conclusion

The breakdown characteristics of CF_3I/CO_2 and CF_3I/N_2 gas mixtures were experimentally examined in a reduced-scale coaxial test system using different-sized inner conductors. The results have demonstrated the potential of CF_3I gas and its mixtures as candidates to replace SF_6 gas as an insulation medium in high-voltage equipment, particularly in GIL applications.

Investigations were carried out in this system with variations in CF_3I gas content, buffer gas, gas pressure, gap distance and impulse polarity. In general, increasing the CF_3I content and pressure resulted in a higher breakdown voltage. It was also found that CF_3I/CO_2 gas mixtures had higher U_{50} compared to CF_3I/N_2 gas mixtures, despite the higher $(E/p)_{crit}$ values for the N_2 mixtures. The polarity effect was present in the coaxial test system due to the practicality of having a perfectly smooth inner surface. The breakdown results were converted into $(E_{max}/p)_B$ and compared with results obtained from the literature for SF_6 on coaxial test systems with a similar geometric ratio. It was demonstrated that for a 30/70% CF_3I gas mixture, the $(E_{max}/p)_B$ value at breakdown under 4 bar (abs.) pressure is around 80% that of SF_6. Thus, it can be inferred that CF_3I gas and its mixtures have a promising insulation capability and may be a feasible alternative to SF_6 in a GIL system.

A study was also conducted on the V-t characteristics of CF_3I/CO_2 gas mixtures under a quasi-uniform field distribution represented by the coaxial cylindrical configuration. The test results have confirmed that the characteristics depend on the conditions of the gap and the gas pressure and, on average, the breakdown process in a coaxial geometry for positive polarity takes longer. The literature, however, reports that for a rod-plane configuration, the breakdown time under a negative impulse can take longer in comparison with a positive impulse, and this needs further investigation. To address the various points identified in this work that are not fully explained, tests using a larger scale coaxial test system will be required.

A two-stage streamer and leader breakdown model was developed based on the obtained breakdown results. The model was applied to all breakdown data obtained for various

coaxial geometries. There is a reduction in the measured breakdown voltage per unit pressure at higher gap distances and pressures. The idea behind the development of the breakdown model is to explain the reduction in the gradient using criteria such as leader channel extent, C_L, and leader field, E_L, which were deduced from the measured U_b. This breakdown model cannot be used to predict the breakdown results of larger coaxial test systems without first determining the general validity of the value of the leader field E_L, which was obtained from the breakdown tests. From the test results obtained here, it can be observed that the values for E_L/p are relatively constant.

Based on the evaluation from the streamer/leader breakdown model, the experimental data indicated the following:

1. At lower pressures, the breakdown occurs at a voltage given by $E_{crit} \cdot (R_b - R_a)$.

2. At higher pressures, the breakdown occurs at a voltage given by $K \cdot E_{crit} \cdot (R_b - R_a)$.

3. For a useful range of pressure and electrode geometry, the value of K has been shown to be independent of the electronegative gas and pressure for the data that are available.

4. At intermediate pressures, the breakdown voltage lies between these limits, and will be dependent upon the criteria that are necessary for streamer to leader transition within the gap space from conductor to enclosure. This would require further experimental investigation on CF$_3$I gas mixtures, and more comprehensive published SF$_6$ data on coaxial configurations would also have to be obtained.

7 BREAKDOWN CHARACTERISTICS OF CF₃I GAS MIXTURES IN UNIFORM AND NON-UNIFORM GEOMETRIES

7.1   Introduction

This chapter describes the collaborative work carried out at Cardiff University and Tokyo University to investigate the breakdown characteristics of 30/70% CF_3I/CO_2 gas mixture. A rod-plane electrode configuration was used to represent a non-uniform field distribution. The experiments for the 30/70% CF_3I/CO_2 gas mixture were carried out using two different experimental setups to examine the rod-plane configuration: a 400 kV Haefely impulse generator from Cardiff University was used for the generation of a standard lightning impulse waveform (1.2/50). The author then undertook a research visit to Tokyo University and carried out experiments using a steep-front impulse voltage generator (rise time of 16 ns) which produces square impulse waveforms. The fast rise time allowed examination of the V-t characteristics of the 30/70% CF_3I/CO_2 mixture in the nanosecond to microsecond range.

The breakdown characteristics of a 30/70% CF_3I/CO_2 gas mixture were investigated for different gap distances under various gas pressures. The V-t characteristics are presented in the range 20 ns to 20 μs. Furthermore, a plane-plane electrode configuration was chosen to represent a more uniform field distribution. In terms of the design of coaxial GIL, the experimental findings from this chapter demonstrate the breakdown performance of CF₃I gas mixtures in non-uniform and uniform field distributions.

7.2   Designing and Conditioning the Experiment

7.2.1   Electrode Configurations

A rod-plane electrode configuration, as shown in Figure 7.1, was chosen to represent a non-uniform electric field distribution. The rod electrode had a 45° angle and the tip had a radius of 0.5 mm. The plane electrode used for these investigations had a diameter of 90 mm with 2.5 mm rounded profile along the rim of the electrode. Both electrodes were made of a brass alloy. Each conducting electrode had a M10 size inner thread for fitting onto the high-voltage bushing using an Ø10 mm rod. Before each series of tests, the electrodes were polished and cleaned thoroughly using propanol. The breakdown characteristics were investigated for a varied gap distance of 10, 30 and 50 mm under an increasing pressure of 1, 2 and 3 bar (abs.). The 50% breakdown voltages and V-t characteristics were measured and compared for both the standard lightning impulse and the steep-front square impulse waveforms.
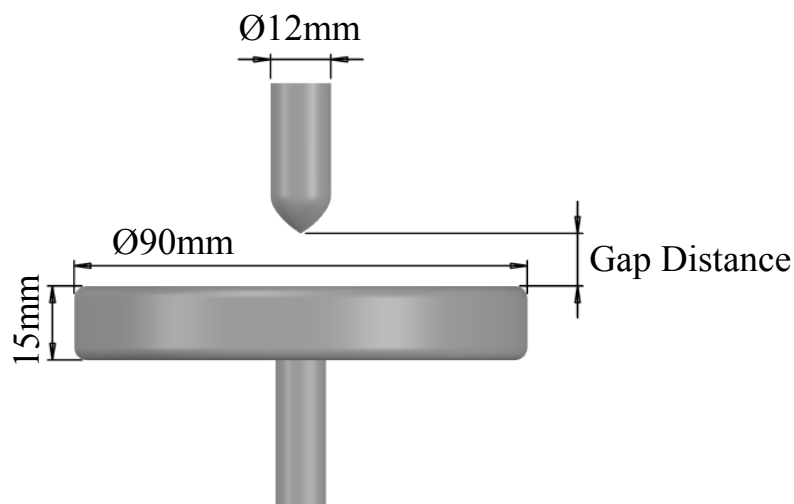
Figure 7.1: Rod-plane electrode configuration.

Figure 7.2 shows a schematic drawing of two plane electrodes, fabricated out of brass alloy, with a diameter of 90 mm and a 2.5 mm rounded profile along the rim of each

electrode. It was expected that higher applied voltages would be required to achieve direct breakdown in the gap, which was filled with CF_3I gas mixtures, compared to a rod-plane configuration. To ensure that a dielectric failure would not occur to the high-voltage bushing, it was essential that the applied impulse voltage was lower than the withstand voltage of the bushing. For this reason, the gap length of the plane-plane experiment was investigated only up to 30 mm and under atmospheric pressure. For uniform field gaps, a rule of thumb proposes a 5:1 ratio for distance-width. The plane-plane electrode configuration shown in Figure 7.2 has a ratio of 2:1 which suggests that the field arrangement would be slightly non-uniform.
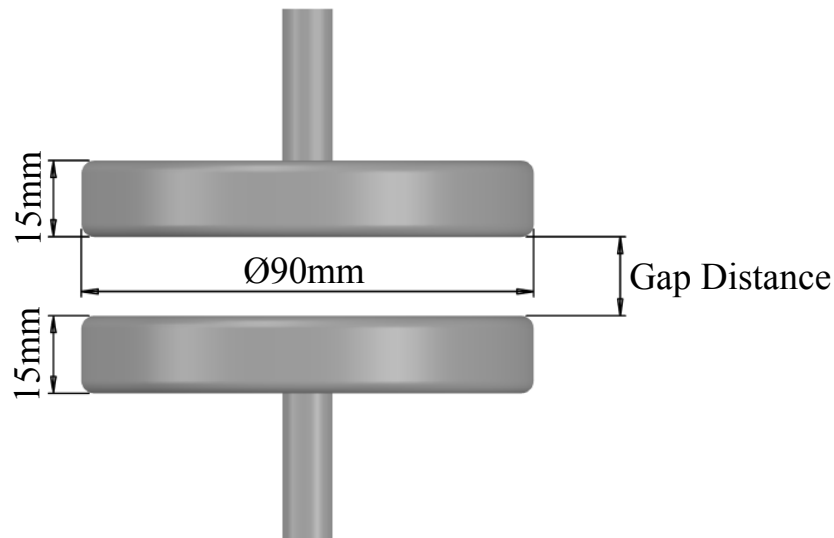
Figure 7.2: Plane-plane electrode configuration.

7.2.2   Electrode Preparation

Prior to any testing, the plane electrode was polished using a Strurers Tegramin-25 machine with a 250 mm disc, as shown in Figure 7.3. Once the preparation step begins, the disc starts turning slowly and then the turning speed can be regulated by the user. Different polishing cloths can be used to achieve an efficient removal process. The hardest abrasive is the diamond grinding disc, as displayed in Figure 7.3.

The initial stages listed below were used to remove the coarse surface on the electrode:

- Diamond grinding disc

- SiC foil 320 grit, 600 grit and 1200 grit with water

- Fine grinding disc and 9 μm diamond suspension

- Coarse polishing cloth and 3 μm diamond suspension

Polishing cloths and ultra-fine aluminium oxide polishing powder were then used to apply a smooth surface finish to the electrode.
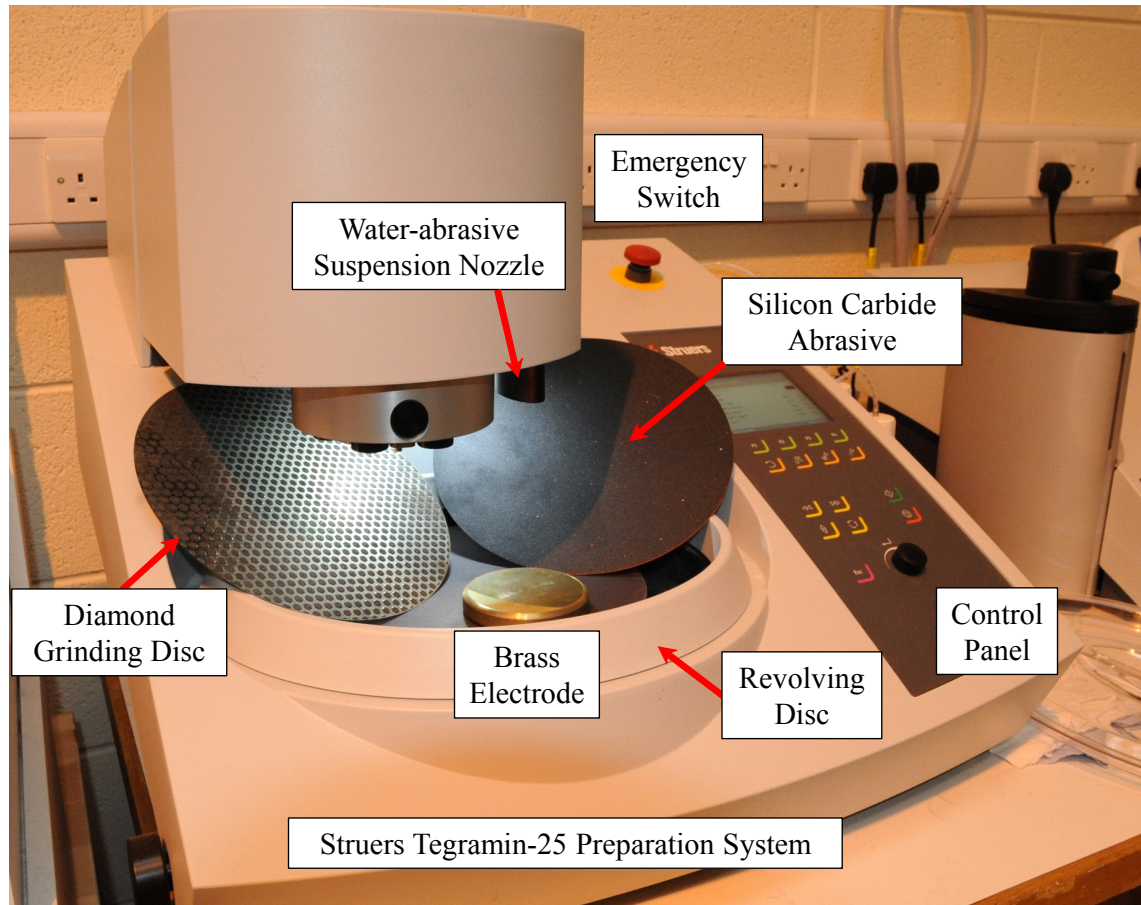
Figure 7.3: Struers Tegramin-25 preparation system for a 250 mm disc.

There will be residual dirt on the surface due to the nature of polishing. In this research, an ultrasonic bath, as shown in Figure 7.4, was used to remove all the dirt by a combined process of ultrasound and water rinsing, which ensures effective cleaning without the use

of cleaning agents or alcohol. This was then followed by a high-speed spin-drying process. This is a necessary procedure at each step of the polishing process since, otherwise, during the next polishing stage, the diamonds left on the surface of the object would contaminate the fine cloths and leave scratches on the electrode.

Figure 7.4: Ultrasonic bath for removing dirt on the surface of the electrode.

7.2.3 Breakdown Distribution

A trial experiment was carried on a rod-plane configuration to determine the location of breakdown events. This was to ensure that there was a random distribution of breakdowns with the majority happening in the centre of the plane electrode. After polishing the plane electrode, a microscope used optical light to image the central area of the polished surface, as shown in Figure 7.5. The operation and functionality of this microscope can be found in [128]; it will not be discussed in depth here since it is not the main concern of this study.
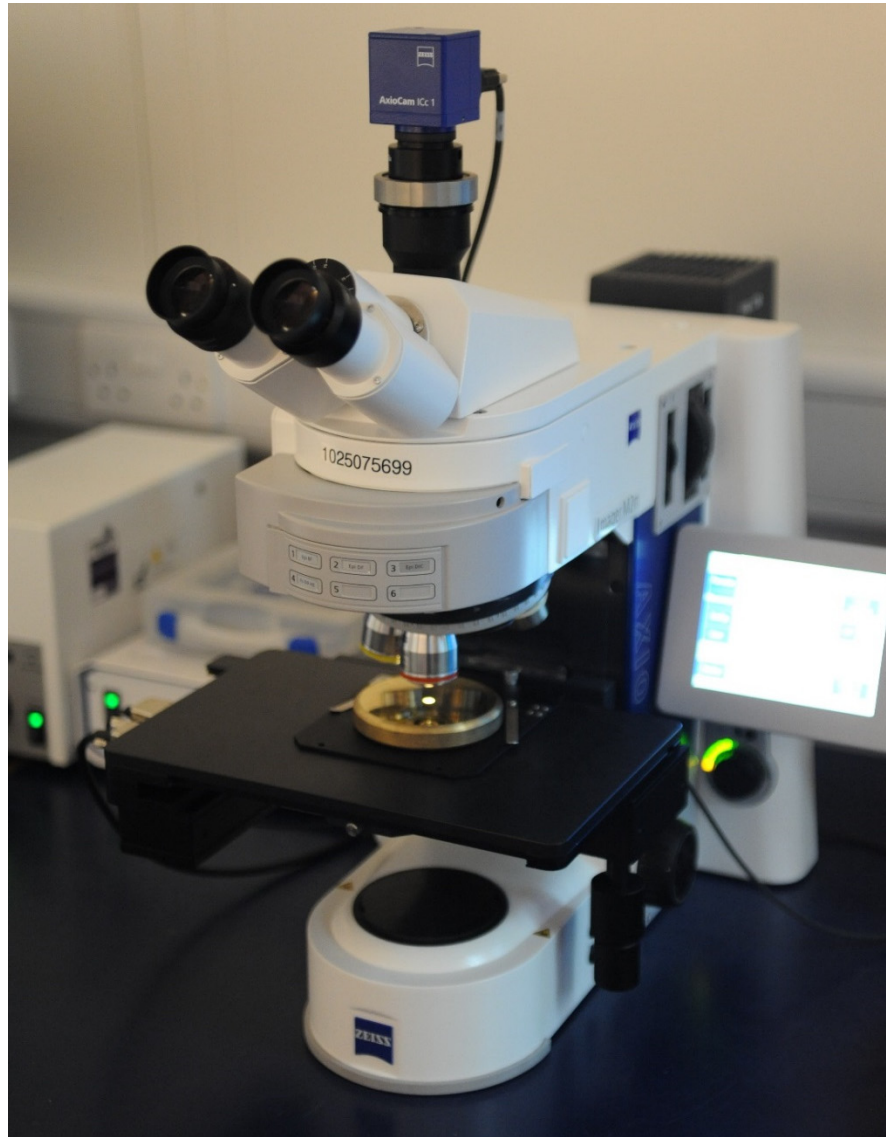
Figure 7.5: Axio Imager 2 Research Microscope.

In Figure 7.6, the image produced by the microscope was able to capture in-depth details, such as machined lines from the previous polishing process. After the trial experiment, another image was made of the same area to determine the locations of breakdown attachment and whether the number of recorded breakdown events matched those on the image. The gap distance of the rod-plane configuration was fixed at 50 mm, and it was subjected to a set of 14 positive lightning impulses.
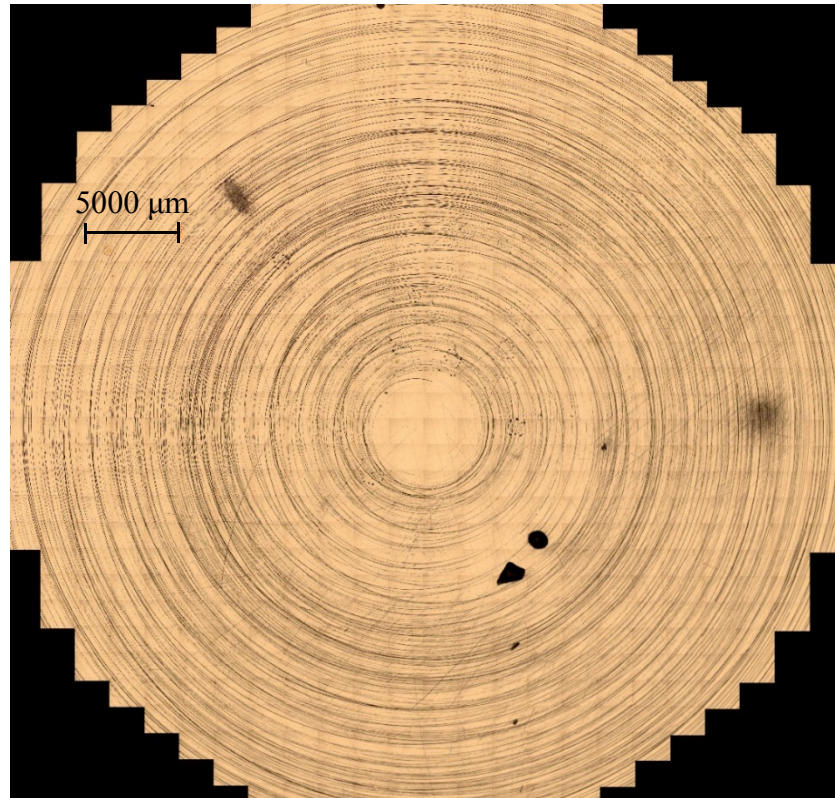
Figure 7.6: Microscope imaging on the polished surface of the plane electrode before the experiment.

Table 7.1: Data record of the trial experiment using a rod-plane configuration.

No.	Applied Voltage (kV)	Breakdown (Y/N)	U_{peak} (kV)	$U_{breakdown}$ (kV)	$T_{breakdown}$ (µs)
1	88.0	Y	81.0	81.0	0.82
2	88.0	N	87.4	–	–
3	88.0	Y	86.0	86.0	1.14
4	88.0	Y	85.4	85.4	1.09
5	88.0	Y	82.0	82.0	0.93
6	88.0	N	87.4	–	–
7	88.0	Y	84.0	84.0	0.98
8	88.0	Y	83.6	83.6	0.99
9	88.0	Y	87.4	87.4	1.28
10	88.0	N	87.0	–	–
11	88.0	Y	87.6	87.6	1.31
12	88.0	Y	79.4	79.4	0.85
13	88.0	Y	87.4	87.4	1.36
14	88.0	Y	86.6	85.4	2.67

The data recorded in Table 7.1 show eleven breakdown occurrences, which can be seen graphically in the photograph taken after the experiment (see Figure 7.7). It can be seen from the photograph that each breakdown shows a nearly circular area that may have been caused by the impact from the electrical breakdown with pitting positioned in the centre of each circular area. Out of the eleven breakdowns, nine occurred around the centre and two breakdowns occurred near the rim of the electrode. Breakdowns in the centre region of the electrode are axial breakdown. For breakdowns near the edge of the electrode, a longer breakdown path length (curved arc trajectory) is required which may have occurred after establishment of corona.
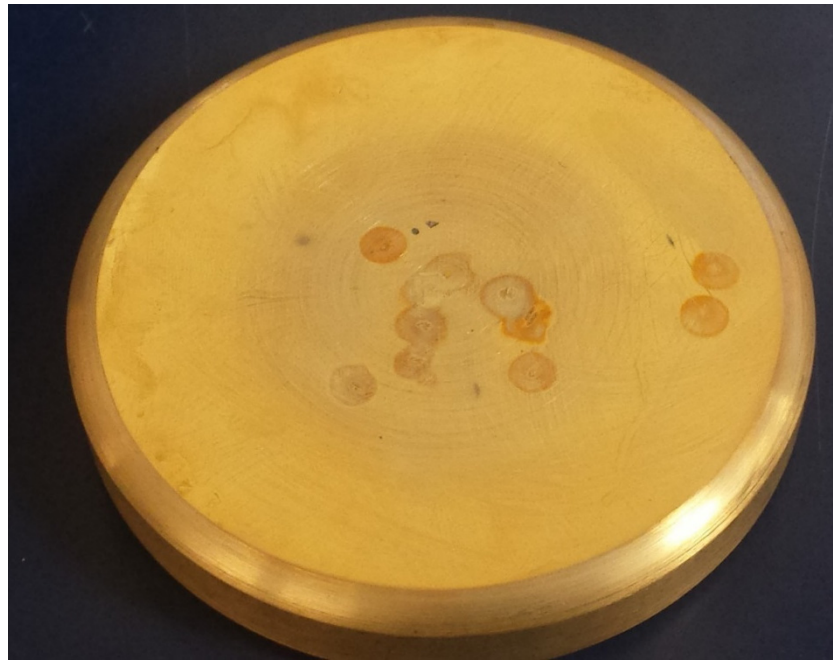
Figure 7.7: Photograph of the plane electrode after the experiment.

Since there were two distinct areas in which the breakdown events occurred (at the centre and along the rim of the plane electrode), two separate microscope images were taken, as shown in Figure 7.8 and Figure 7.9 respectively. The microscope software allows the diameter of the affected area to be measured. This provides a general idea of the size of the impact from a breakdown. The results recorded for U_{peak}, $U_{breakdown}$ and $T_{breakdown}$ gave

no clear indication that the breakdown voltage or time could be correlated to the location of discharge. Although the majority of the breakdown discharges occurred around the centre of the rod-plane configuration, there was no other discernible pattern to the location of those breakdown.
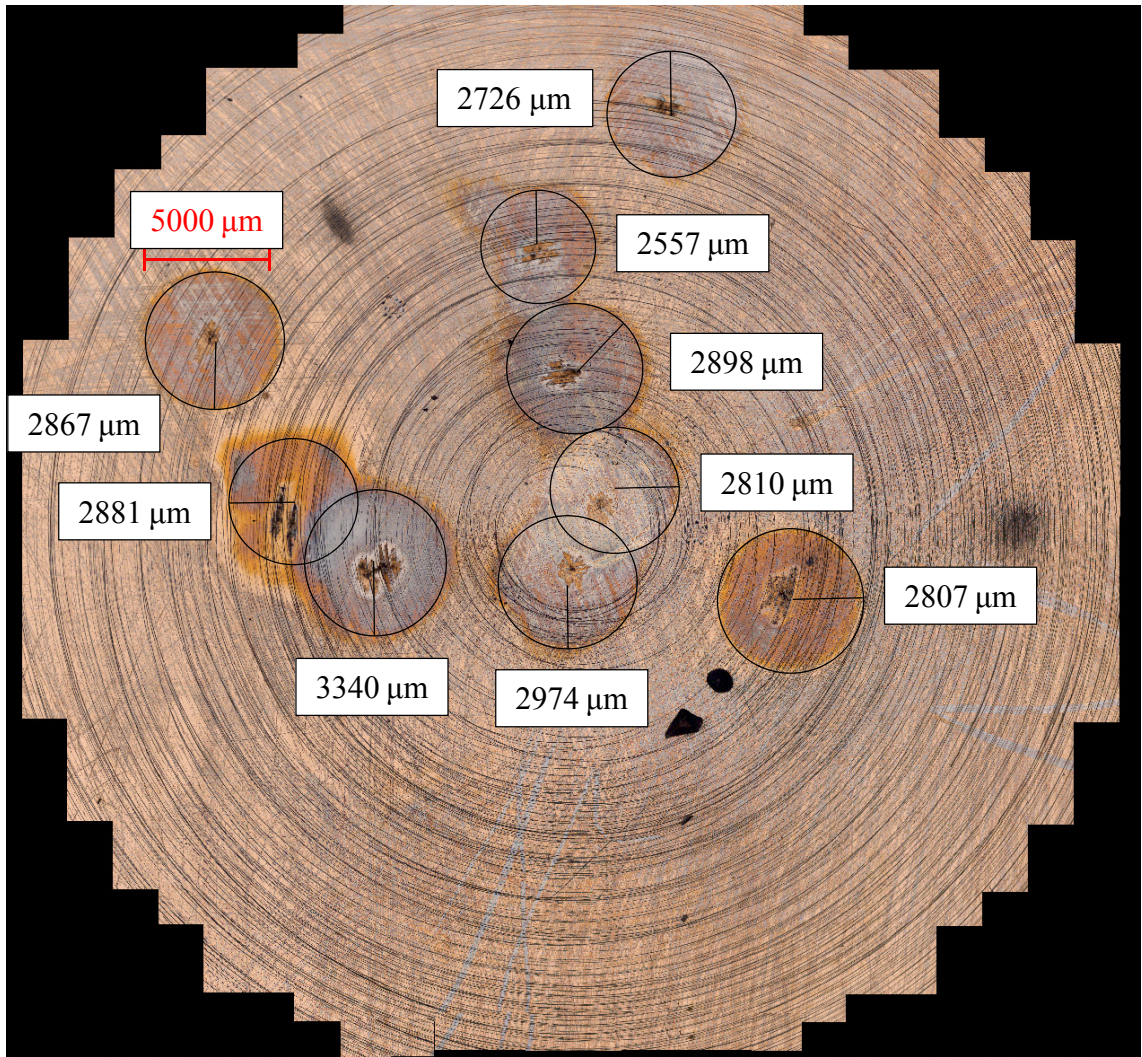
Figure 7.8: Microscope imaging showing the breakdowns that occurred in the centre of the plane electrode after the experiment.
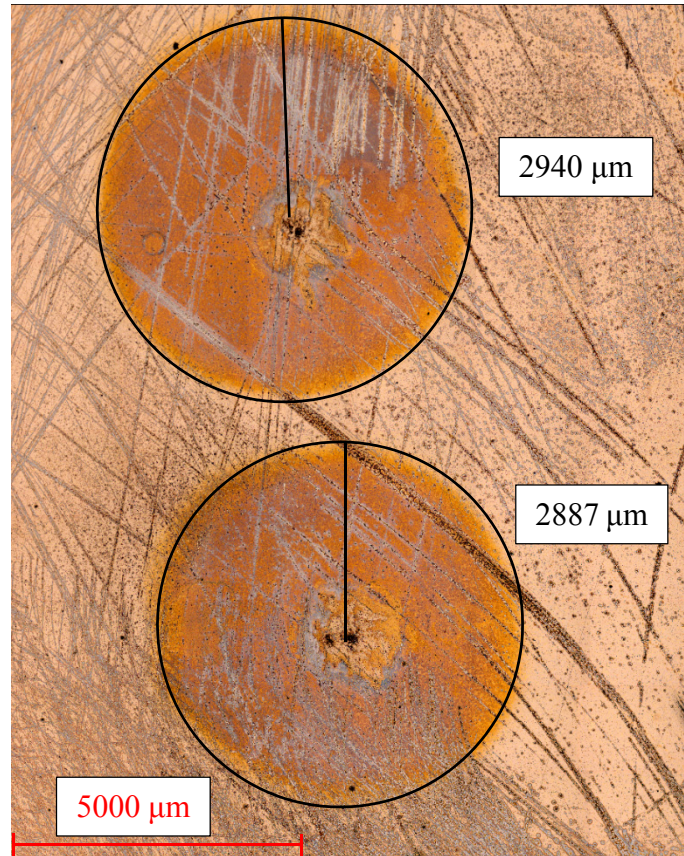
Figure 7.9: Microscope imaging of the two breakdowns that occurred closer to the edge of the plane electrode.

7.3 SEM Analysis

By-products will always be produced from gas discharge experiments, and as the contents of by-products increase the breakdown performance of the gas medium will reduce. A Hitachi TM3030 benchtop scanning electron microscope (SEM) with an EDX system was, therefore, used to perform an Energy Dispersive X-ray Spectroscopy (EDX/EDS) mapping of the elements for the post experimental analysis.

The sample was inserted into a vacuum chamber inside the SEM, which is necessary since small particles could deflect the electrons onto the sample, thus obscuring the results. This

method was applied to identify the elements from the depositions on the surface of the plane electrode after the experiment.

SEM analysis was carried out on the same plane electrode as shown in Figure 7.6 to investigate the by-products produced from the breakdown events. A mapped image was taken of the polished electrode prior to the experiment, as shown in Figure 7.10(a). Another image was taken after the experiment to analyse the decompositions around a pit (arc site) mark left by an electrical discharge as shown in Figure 7.10(b).

(a)   (b)
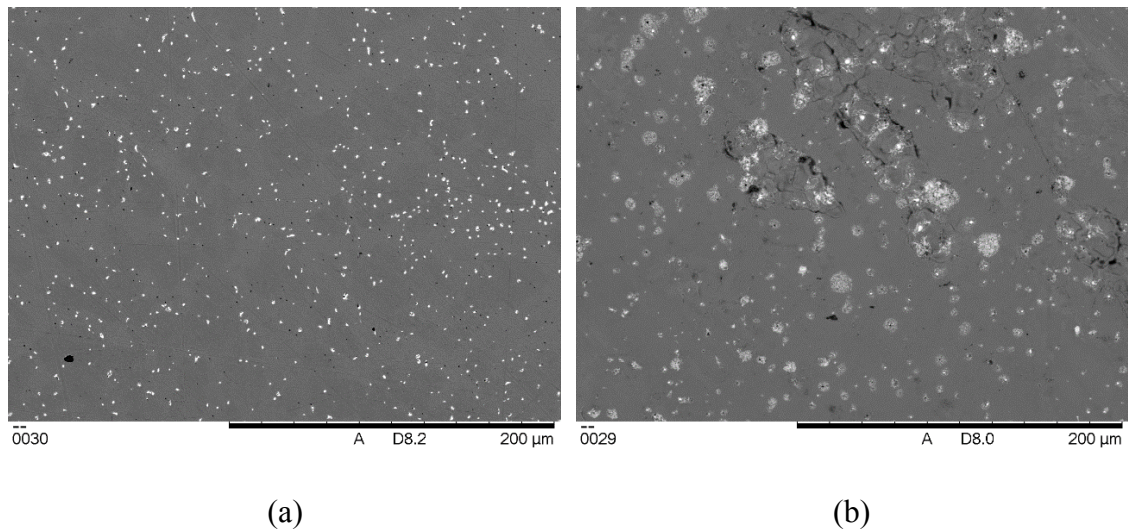
Figure 7.10: (a) Mapped image of the polished electrode and (b) mapped image of the location of an electric discharge post experiment; both images were taken from the centre of the plane electrode.

The spectrum analysis performed on the polished electrode is shown in Figure 7.11, and shows strong signals for two elements: zinc (Zn) and copper (Cu). This is expected since the plane electrode is made of brass, which is an alloy made of copper and zinc. To enhance the machinability of the brass, a very small concentration of lead (Pb) is often added in the manufacturing process, as illustrated by the weak signal of lead (Pb) shown in Figure 7.11.
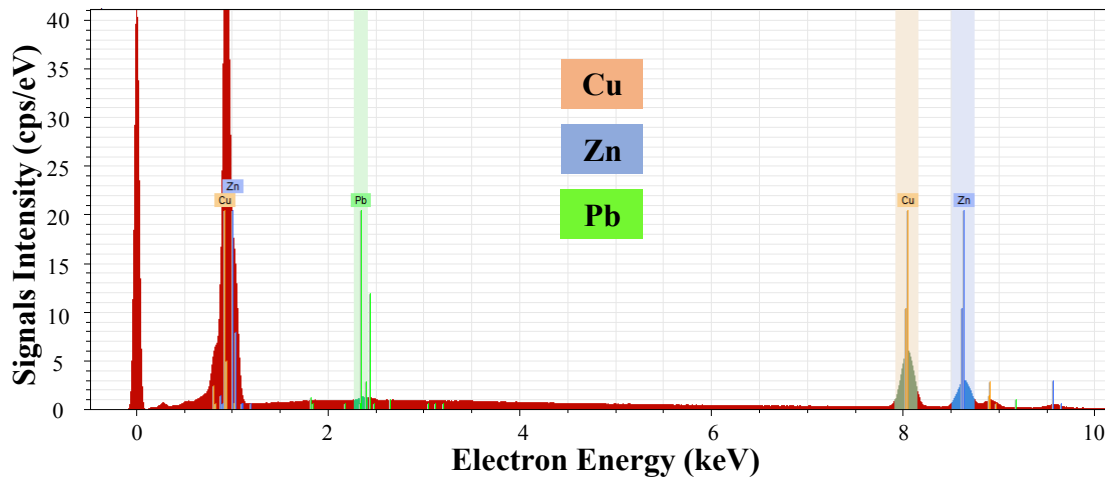
Figure 7.11: Spectrum analysis on the central area of the polished electrode surface.

In the post-experimental analysis, additional signals were detected for carbon (C), iodine (I), oxygen (O), and rhenium (Re), as shown in Figure 7.12. It can be seen from the figure that the iodine content is relatively low, that is, a few percent of the total composition for all detected elements. Taking into consideration that only nine breakdowns occurred in the central area of the plane electrode, however, it is important to note that there is such quick build-up of iodine on the electrode's surface. The detection for Re was unexpected, but it may just be noise signal overlapped with signal for Zn at 8 keV.
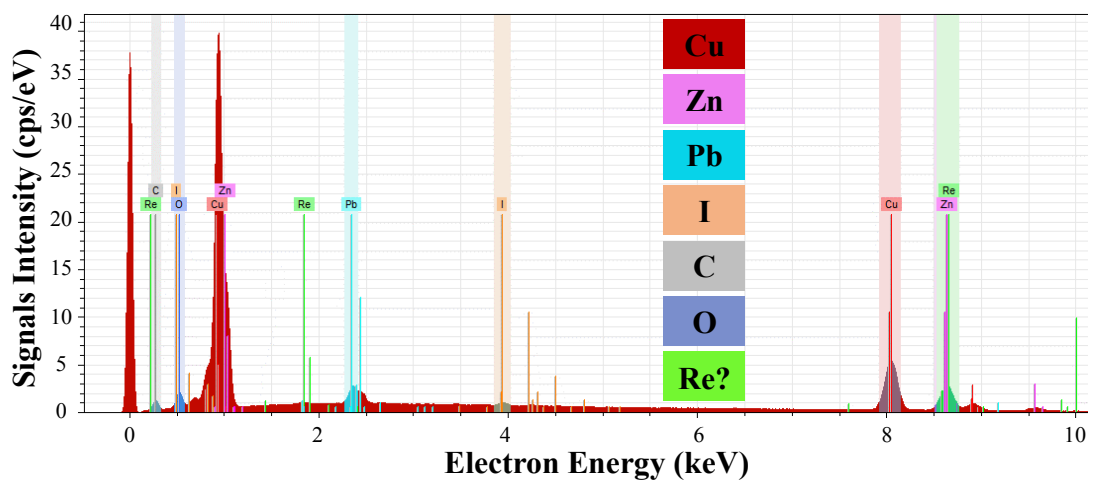
Figure 7.12: Spectrum analysis on the electrode surface after the experiment in the same location where an electrical discharge occurred.

157

Figure 7.13 shows individual pictures of detected elements for the analysis carried out on the plane electrode after the experiment. The figure suggests that, after a breakdown, iodine breaks apart from the weakly attached C-I bond and is scattered in the area near to where the breakdown took place. This means that after a succession of breakdown events, the iodine will build-up all over the electrode's surface. There is no evidence the iodine deposition would reduce the insulation strength of the CF$_3$I gas mixture.

(a)   (b)
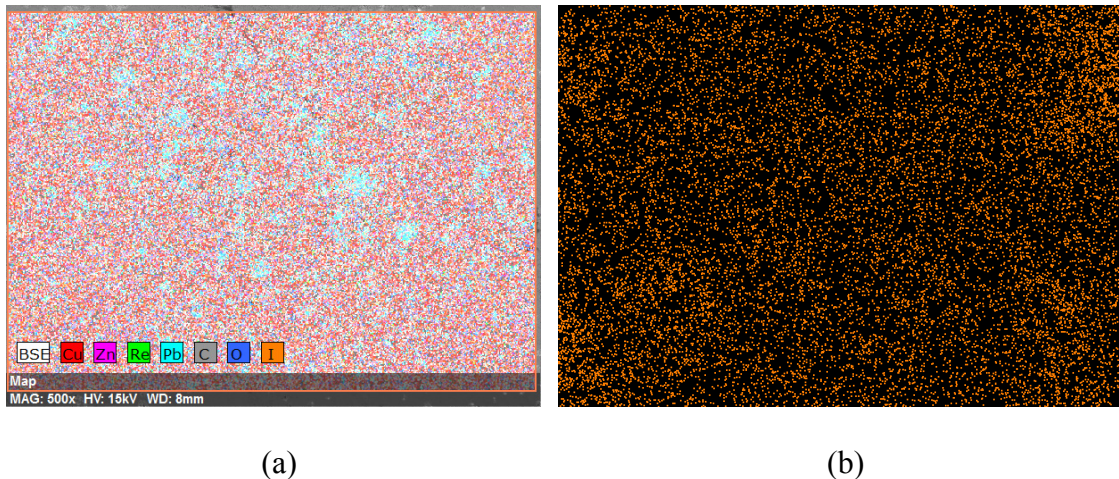
Figure 7.13: (a) Mapping distributions of all the elements and (b) mapping distribution of solely iodine element on the plane electrode after the experiment.

7.4   Comparative Study of Non-uniform Field Distribution

GIL as a passive system; it is designed to avoid direct breakdown when it is in operation. If breakdown events were to occur, these would normally be due to the influence of high electric field stress caused by the presence of a protrusion or a sharp point on the inner surface of the GIL enclosure. It is, therefore, important to characterise the performance of the 30/70% CF$_3$I/CO$_2$ gas mixture, a proposed alternative to SF$_6$ [8], [41], [129], especially in non-uniform field distribution. A rod-plane electrode configuration was, therefore, subjected to lightning impulse and steep-front square impulse waveforms; the measured results for breakdown and V-t characteristics were collected and analysed.

7.4.1 Effect of Gas Pressure, Gap Distance and Impulse Polarities

For this study, the breakdown characteristics of the 30/70% CF$_3$I/CO$_2$ gas mixture were extensively investigated in a non-uniform field distribution. The experimental work was carried out for gap distances of 10, 30 and 50 mm and gas pressures of 1 and 2 bar (abs.) for both positive and negative lightning impulses. The range of experimental data were able to provide an initial analysis of the influence of gas pressure, gap distance and impulse polarities for a 30/70% CF$_3$I/CO$_2$ gas mixture.

The effect of impulse polarity was tested using a standard lightning impulse waveform (1.2/50). Figure 7.14 shows the U$_{50}$ as a function of increasing gap length under 1 and 2 bars of pressure for both lightning impulse polarities. The U$_{50}$ increases with longer gap distances, however, more data points are required to provide clearer indication of the trend characteristic. Breakdowns for negative impulse polarity have a comparably higher U$_{50}$ than their equivalent for positive impulse polarity, and the difference widens as the gap distance increases. This can be explained by the corona inception and breakdown characteristics. For a small value of pressure spacing product, pd, the breakdown characteristics are almost the same for both polarities, as can be seen from the measured U$_{50}$ results on the 10 mm gap in Figure 7.14. As the value of pd increases, for positive breakdowns, there will be a sudden drop in breakdown strengths, whereas for negative polarity, the corona stabilised region then extends to much higher pd values. This behaviour was reported by Sangkasaad et al. [115] for SF$_6$ gas in non-uniform field gaps.

The measured results were then converted into pd values, which are graphically displayed in Figure 7.15. As explained previously, the negative breakdown voltages were shown to be higher than the positive breakdown voltages, especially at higher pd values. In the

literature [130], the same behaviour was reported for SF_6 gas, in that the breakdown

voltage of SF_6 gas shows a tendency to saturate towards a large electrode separation and

for non-uniform field gaps.

Figure 7.14: U₅₀ as a function of gap distance in a rod-plane configuration, tested for a 30/70% CF₃I/CO₂ gas mixture, for 10, 30 and 50 mm, at pressures of 1 and 2 bar (abs.) and for both lightning impulse polarities.
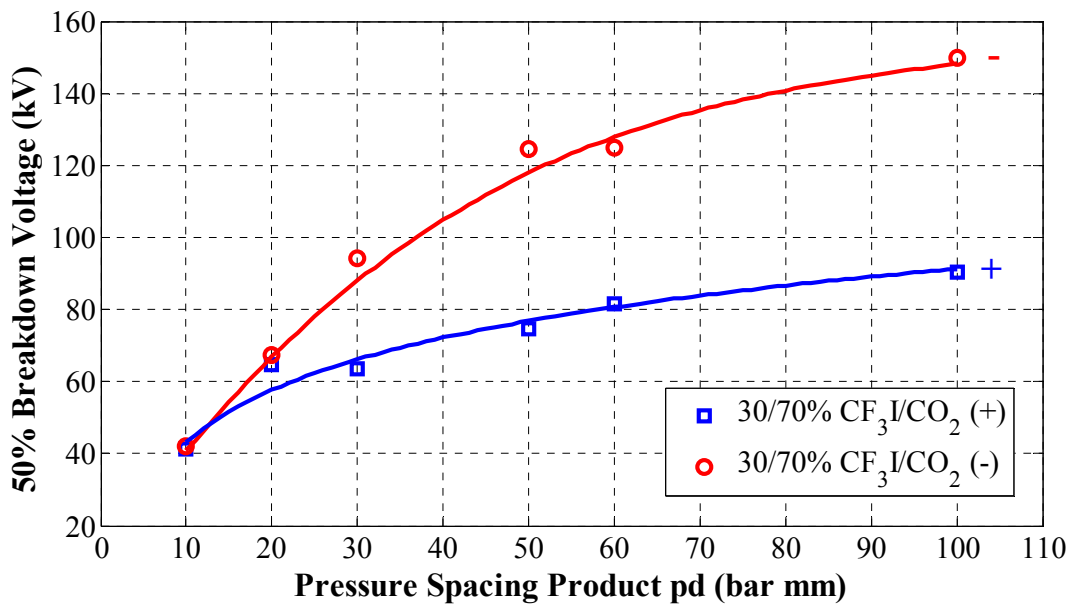
Figure 7.15: Measured U₅₀ as a function of pd tested for a 30/70% CF₃I/CO₂ gas mixture and for both lightning impulse polarities.

From the test results, the breakdown voltage and time to breakdown were also recorded. The V-t characteristics are shown in Figure 7.16 and Figure 7.17, at gas pressures of 1 and 2 bar respectively. It can be seen from both figures that as the gap length and gas pressure increase, the breakdown voltage also increases. For positive impulse polarity, at 1 pressure bar, most of the breakdowns occurred in less than 4 µs. At 2 bar, however, there is a more dispersion in the V-t results with more breakdown occurrences above 4 µs. The V-t characteristics for negative impulse polarity behave differently; for 1 bar, the average time to breakdown is much longer in comparison to the equivalent for positive impulse polarity but, for 2 bar, there is very little difference between the breakdown times for both impulse polarities.

Figure 7.16: V-t characteristics in a rod-plane configuration tested for a 30/70% CF₃I/CO₂ gas mixture, for 10, 30 and 50 mm gap distance, at pressure of 1 bar (abs.) and for both lightning impulse polarities.

Figure 7.17: V-t characteristics in a rod-plane configuration tested for a 30/70% CF₃I/CO₂ gas mixture, for 10, 30 and 50 mm gap distance, at pressure of 2 bar (abs.) and for both lightning impulse polarities.

7.4.2   Breakdown Characteristics of Steep-front Square Impulse

Studies were carried out for the rod-plane configuration on the effect of gap distance, gas pressure and fast impulse waveform. The multi-level method was applied and the U_{50} and standard deviation values were obtained by plotting the results on probability graph paper. Figure 7.18 shows a relatively linear relationship between U_{50} and gap distance while, for the breakdown voltages, it increases linearly with pressure up to 3 bar (abs.). Similar trend characteristics were observed for SF_6 in a rod-plane gap using lightning impulse as reported in [130]. Since the waveform, insulation gas and rod geometry are different, a direct comparison cannot be made between the breakdown results. It was suggested in [130] that the critical field strength of a rod-plane gas gap subjected to lightning impulse could be given as a linear function of pressure "p" up to about 4 bar, a characteristic that can also be observed from Figure 7.18.
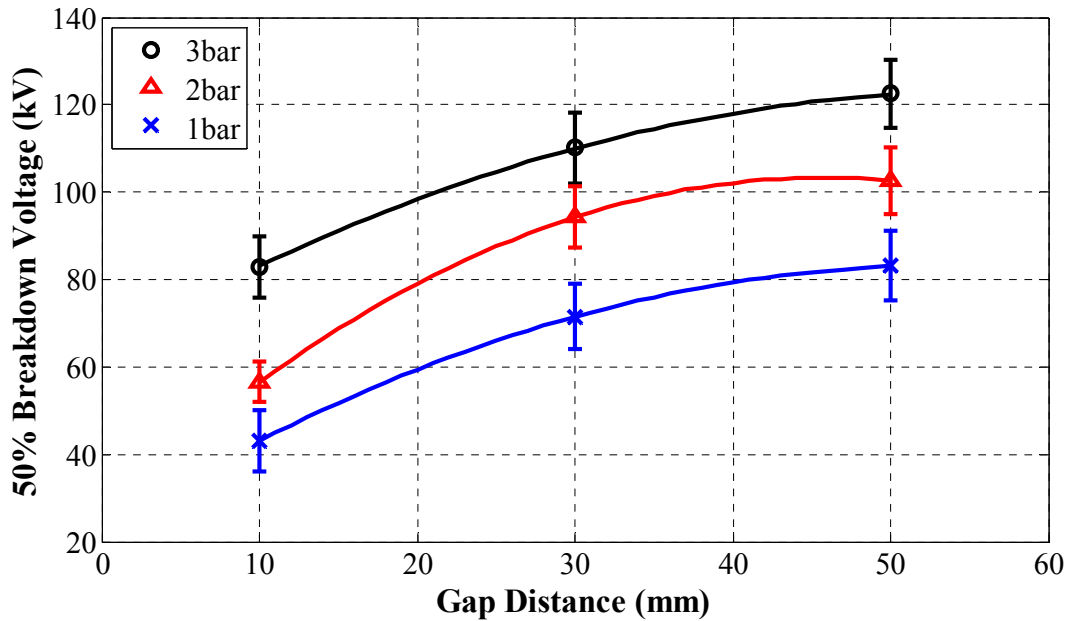
Figure 7.18: Breakdown voltage, U_{50}, as a function of gap distance for rod-plane gaps, tested for a 30/70% CF_3I/CO_2 gas mixture, for 10, 30 and 50 mm, at gas pressures of 1, 2 and 3 bar (abs.) and for positive steep-front square impulse polarity.

The V-t characteristics of a rod-plane configuration were obtained based on the recorded results from the multi-level tests. The effects of gas pressure on the V-t characteristics are as shown in Figure 7.19, Figure 7.20 and Figure 7.21 for a gap length of 10, 30 and 50 mm respectively. In general, an increase in gap distance and pressure is accompanied by a higher breakdown voltage. The majority of the breakdown events shown in the figures occurred below 10 μs. From the figures, it can be said that the average breakdown time is shorter at a longer gap distance when compared to the breakdown time at a smaller gap distance. The increase in pressure resulted in a shorter average breakdown time when compared with the results at lower pressure. From all the measured results for V-t characteristics, two main patterns can be observed: (i) almost flat V-t curves and (ii) V-t curves rising steeply in the short-time region. The second pattern is generally observed at low pressure and small gap distance.
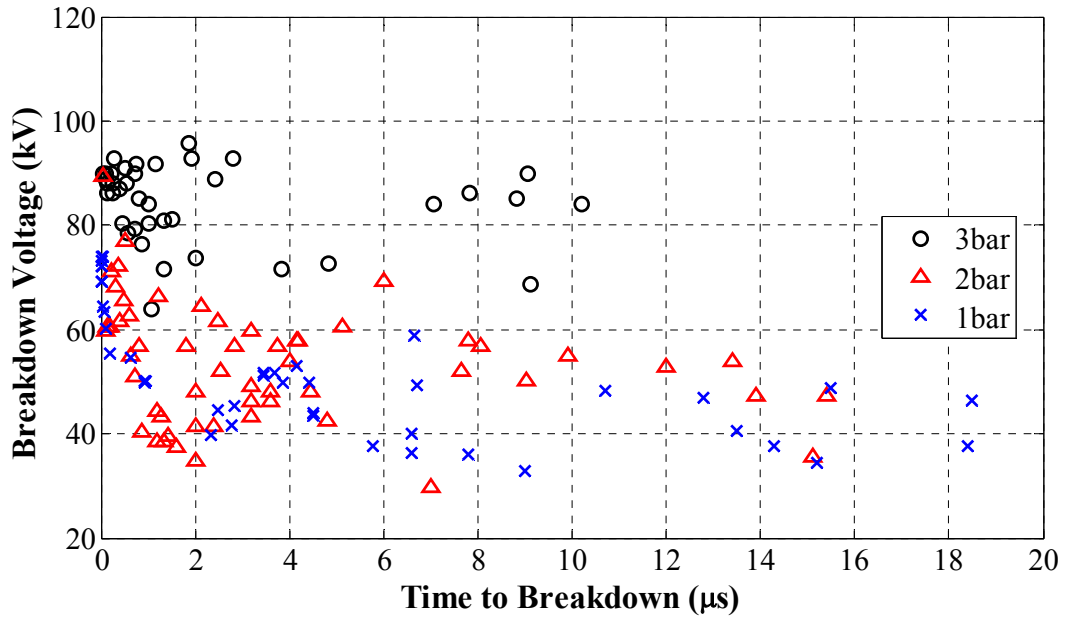
Figure 7.19: V-t characteristics in a rod-plane configuration, tested for a 30/70% CF₃I/CO₂ gas mixture, for gap distance of 10 mm, at pressures of 1, 2 and 3 bar (abs.) and for positive steep-front square impulse polarity.
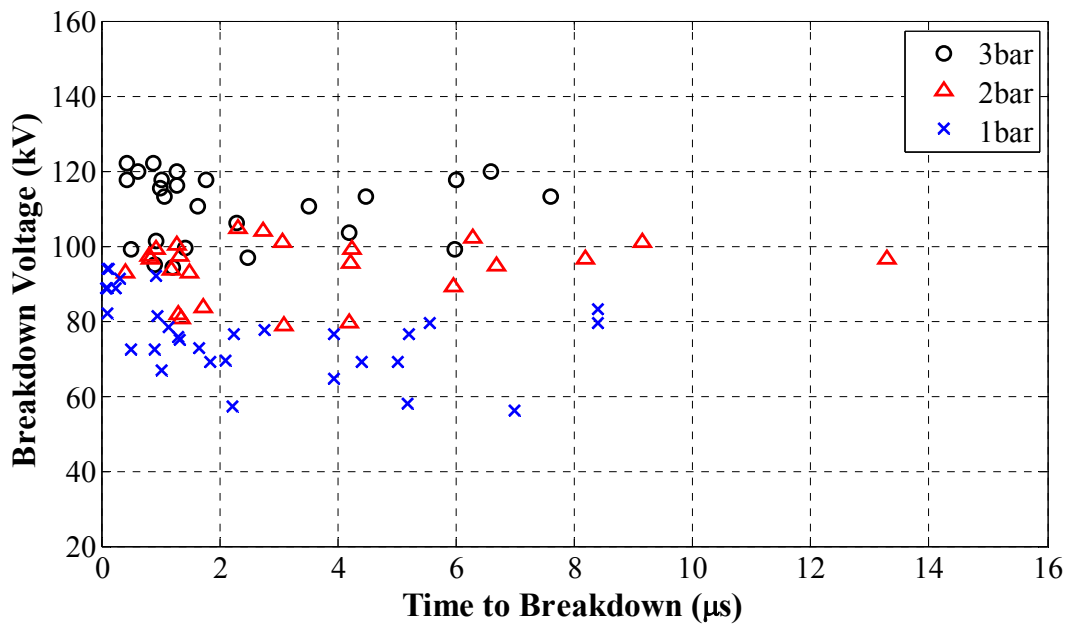
Figure 7.20: V-t characteristics in a rod-plane configuration, tested for a 30/70% CF₃I/CO₂ gas mixture, for gap distance of 30 mm, at pressures of 1, 2 and 3 bar (abs.) and for positive steep-front square impulse polarity.
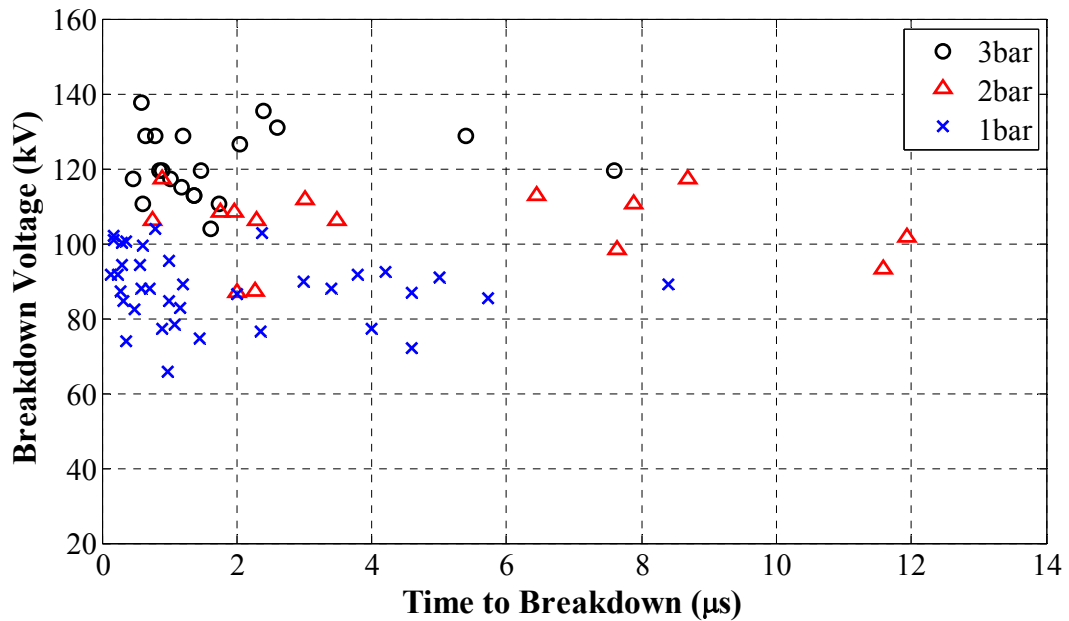
Figure 7.21: V-t characteristics in a rod-plane configuration, tested for a 30/70% CF₃I/CO₂ gas mixture, for gap distance of 50 mm, at pressures of 1, 2 and 3 bar (abs.) and for positive steep-front square impulse polarity.

7.4.3 Comparison of Lightning Impulse and Steep-front Square Impulse Waveforms

Based on the results obtained from the lightning impulse and steep-front square impulse waveforms, the breakdown voltages of both waveforms are compared in Figure 7.22 as a function of gap distance. As can be seen in the figure, for a 10 mm gap, the measured breakdown voltages are comparable between the two generators. The rate of increase for the breakdown voltage becomes more gradual with higher gap spacing and gas pressure.

It can be seen from Figure 7.18 that for a longer gap, the breakdown voltage obtained from the steep-front square impulse waveform is considerably higher than its equivalent obtained from the lightning impulse. This behaviour is related to the event of a breakdown. To initiate a breakdown event, an initial electron must be present to start the electron

avalanche. When the power source is AC or DC with slowly rising voltages, there will be sufficient initiatory electrons from naturally occurring radioactive sources. In the case of lightning impulse and steep-front square impulses, with a time duration of less than 1 μs, breakdown may not occur unless the initiatory electrons are available through artificial irradiation, i.e. using a higher applied voltage to introduce a higher field stress. A steep-front square impulse waveform has a rise time in the nanosecond range, whereas a standard lightning impulse waveform has a longer rise time of 1.2 μs. Since there is less time for the leader to propagate into the gap, a much higher applied voltage is required for the leader to cross the gap and initiate a full breakdown. This may be the reason behind the higher average breakdown voltage for steep-front square impulse waveforms in comparison to their equivalent lightning impulse voltage waveforms.
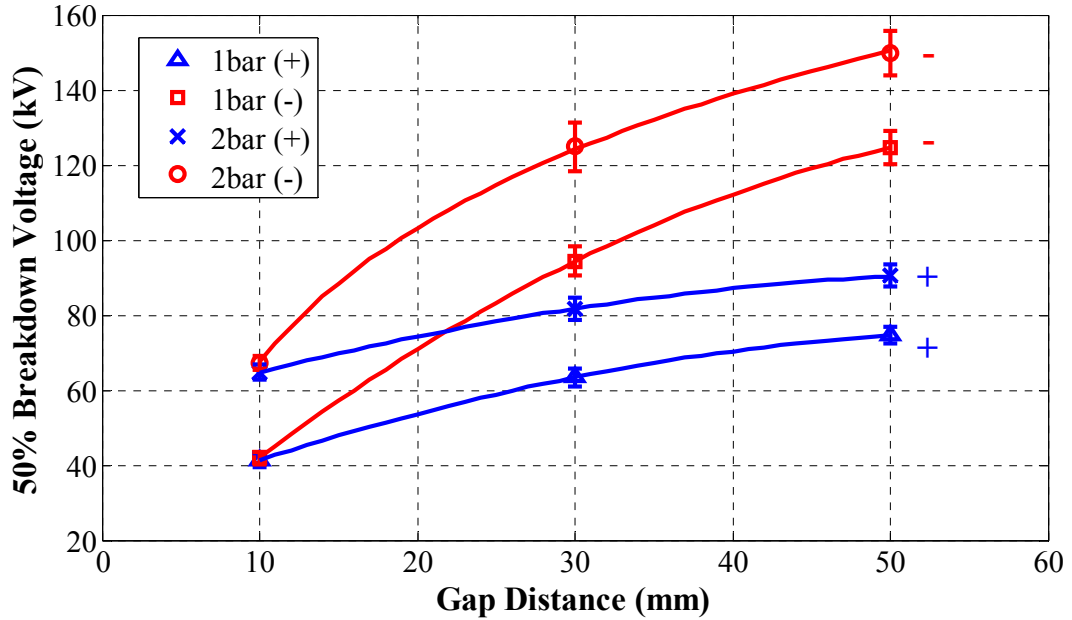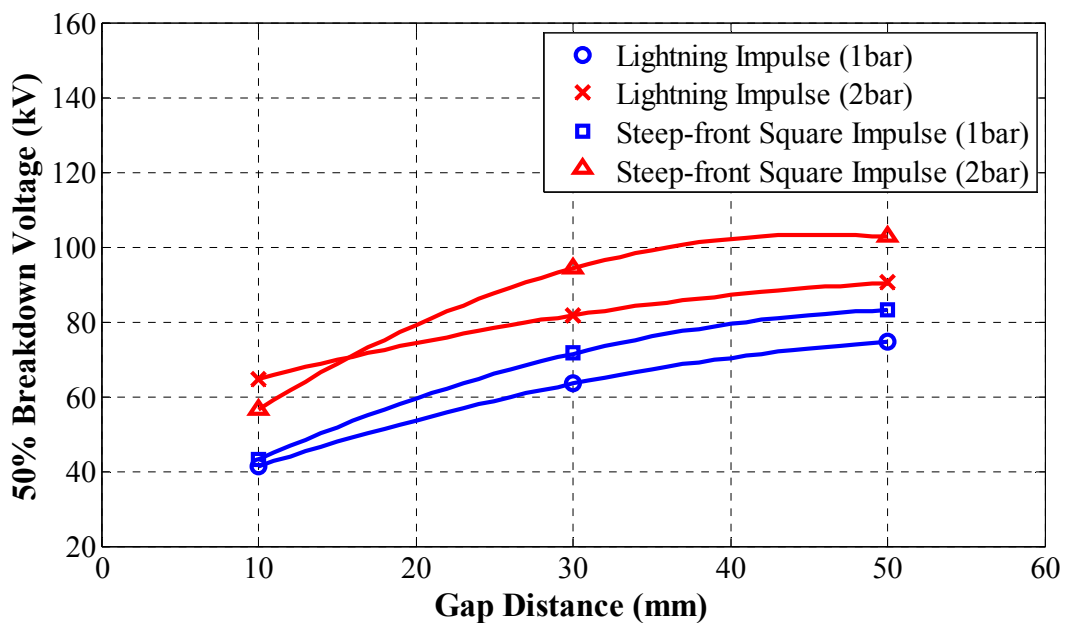

Figure 7.22: U_{50} as a function of gap distance in a rod-plane configuration, tested for a 30/70% CF₃I/CO₂ gas mixture, for 10, 30 and 50 mm, at pressures of 1 and 2 bar (abs.) and for both positive steep-front square and lightning impulse polarity.

When a sufficiently high value of voltage (lightning impulse or steep-front square impulse) is applied to a gap, a breakdown event will occur across the gap. The time to full

breakdown is dependent on the field uniformity of the electrode configuration and the rate of overvoltage applied. Hence, for every electrode configuration, the electrode gap is subjected to a number of voltage applications, so a different V-t characteristic can be constructed. The comparison of V-t characteristics for both the lightning impulse and the steep-front square impulse waveforms are plotted in Figure 7.23 and Figure 7.24. These show that there appears to be less breakdown time dispersion for the V-t results obtained through a lightning impulse. The V-t characteristics suggest a longer average breakdown time for a lightning impulse at higher pressure, whereas with a steep-front square impulse, the average breakdown time is shorter at higher pressure. The data show a range of scattered results with no clear correlation between the time to breakdown and the increase in breakdown voltage.

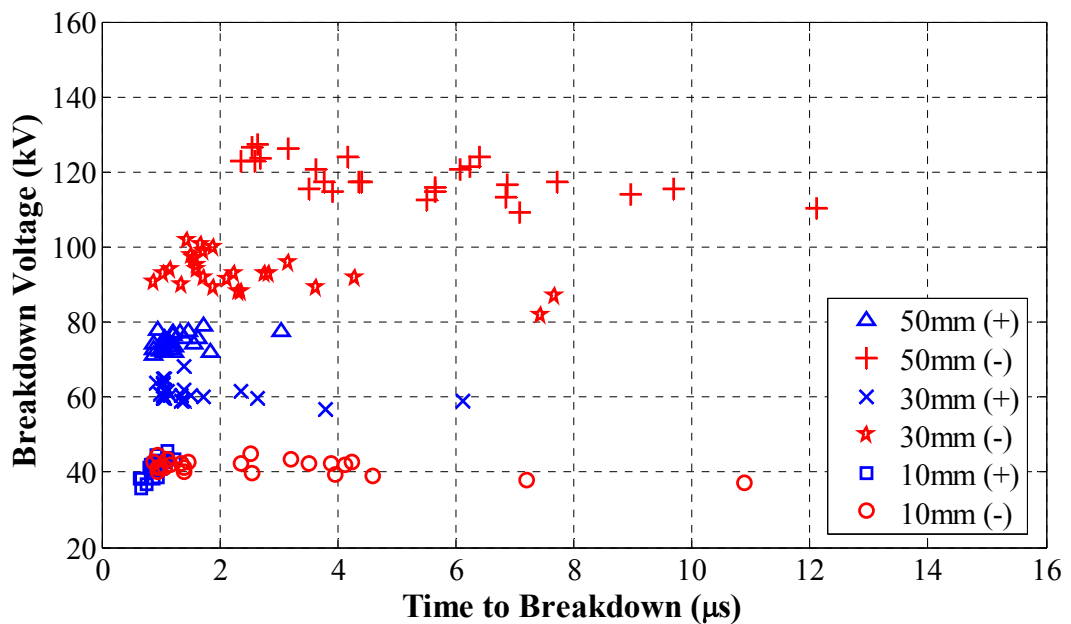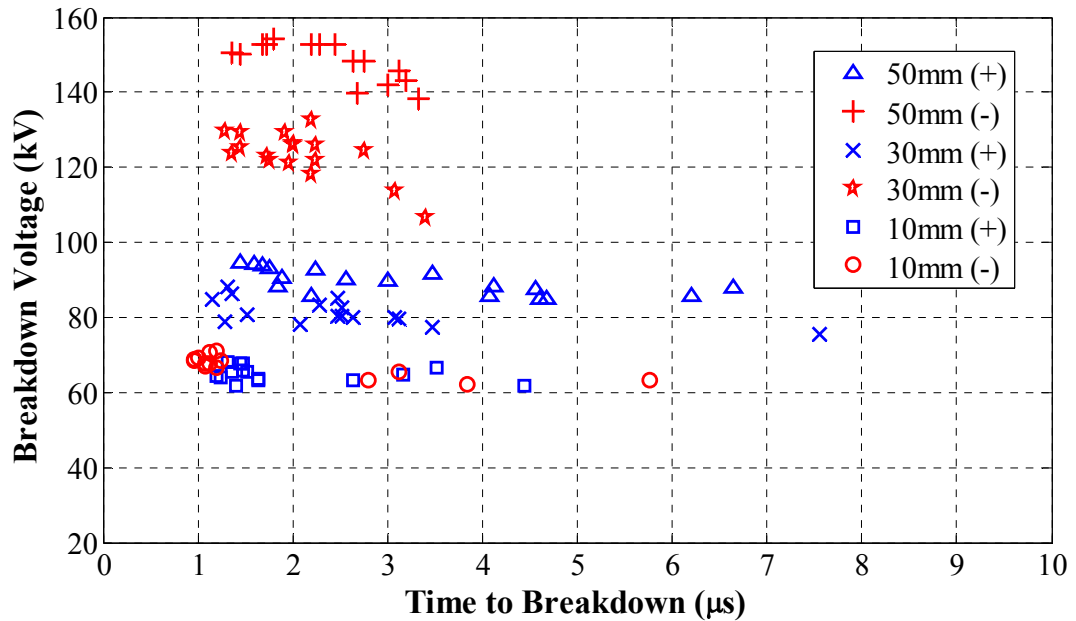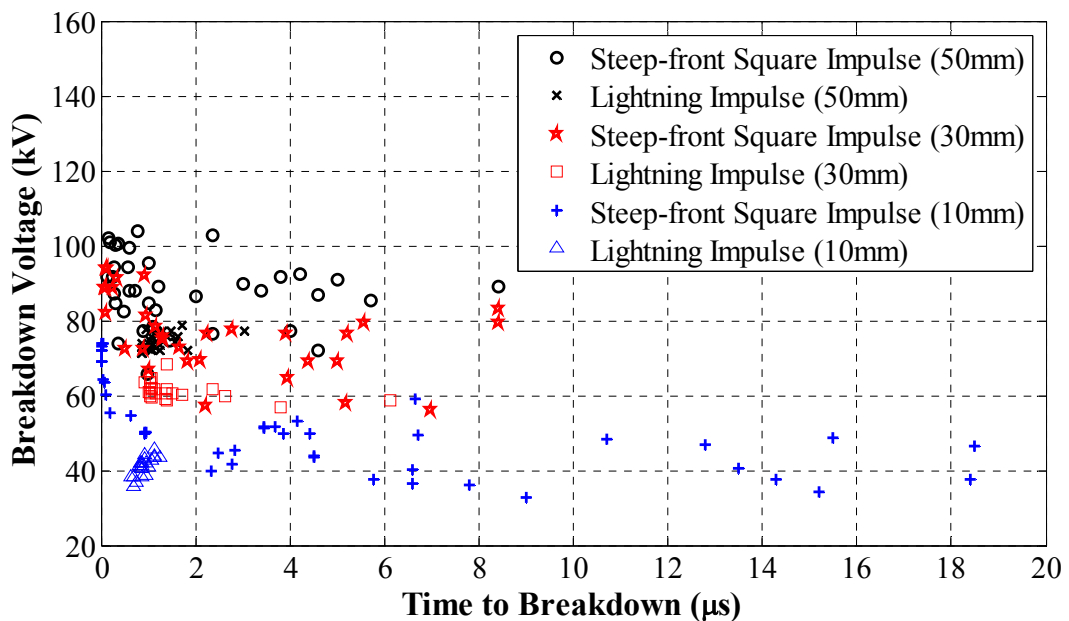**Figure 7.23: V-t characteristics in a rod-plane configuration, tested for a 30/70% CF₃I/CO₂ gas mixture, for 10, 30 and 50 mm, at pressure of 1 bar (abs.) and for both positive steep-front square impulse and positive lightning impulse waveforms.**
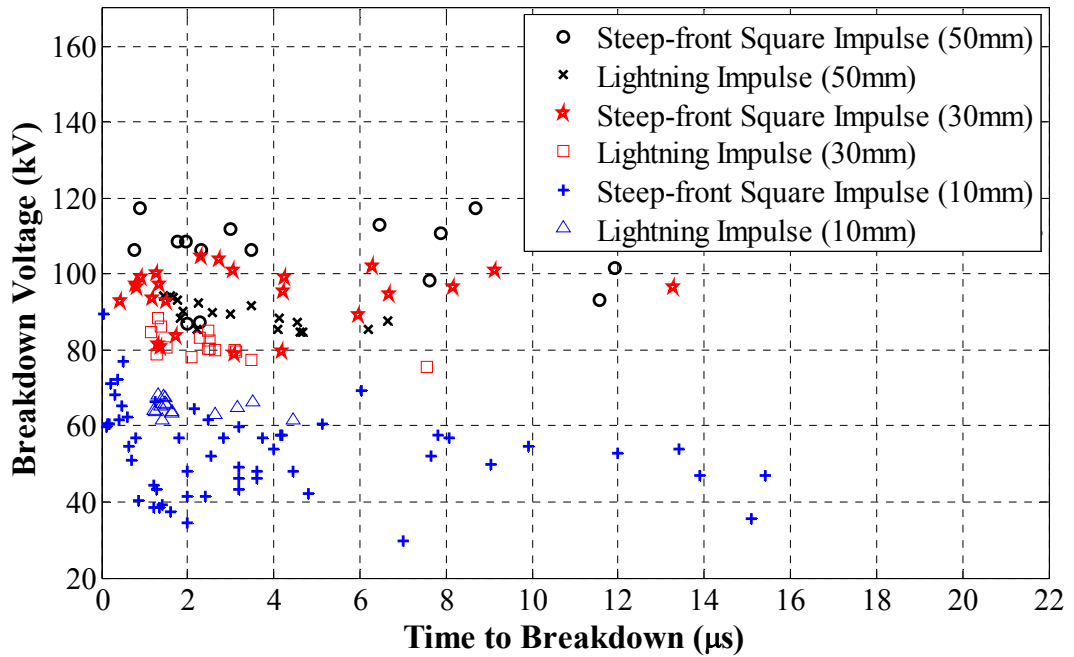
Figure 7.24: V-t characteristics in a rod-plane configuration, tested for a 30/70% CF₃I/CO₂ gas mixture, for 10, 30 and 50 mm, at pressure of 2 bar (abs.) and for both positive steep-front square impulse and positive lightning impulse waveforms.

7.5   Breakdown Characteristics in Uniform Field Distribution

Analysis was carried out on 30/70% CF₃I/CO₂ gas mixture for a more uniform field distribution, represented by a plane-plane configuration. Due to the limitation of the high-voltage bushing, the plane-plane electrode was investigated only up to a 30 mm gap at atmospheric pressure.

7.5.1   Effect of Gas Pressure, Gap Distance and Impulse Polarities

An investigation was carried out using the up-down method on 30/70% CF₃I/CO₂ gas mixture for a 10, 20 and 30 mm gap distances and under both polarities. The results were plotted to demonstrate a comparison to the data for SF₆ and air obtained from the literature. For SF₆, Kawaguchi et al. [131] examined the breakdown gradient potential using the up-down method for SF₆ at pressures of up to 4 bar (abs.) for a standard impulse voltage

(1/40). Rogowski profiled aluminium electrodes representing a nearly uniform field tested at a gap spacing of 20, 40 and 60 mm.

Regarding air as an insulation medium, Kuffel et al. [74] reported that the breakdown voltage (U_b) and the breakdown field strength (E_b) can be calculated for air at a standard temperature and pressure. The calculated data agree well with the experimental values for gap distances extending from 1 mm to 100 mm using (7.1), derived from Paschen's law.

$$\frac{U_b}{pd} = \frac{E_b}{p} = \frac{6.72}{\sqrt{pd}} + 24.36 \frac{kV}{cm \cdot bar} \qquad (7.1)$$

Based on the findings from the literature, the breakdown strength of 30/70% CF_3I/CO_2 can be compared directly against SF_6 and air, as shown in Figure 7.25. It is well known that in uniform field gaps, SF_6 has a breakdown strength around three times higher than air, and this ratio can be seen at a 30 mm gap. The breakdown strength of a 30/70% CF_3I/CO_2 gas mixture is around 70% of SF_6 for a 30 mm uniform gap. This is promising considering that CF_3I is only used in a small proportion to total gas mixture.

It can be seen in Figure 7.25 that in uniform gaps the positive breakdown voltage is higher than the negative breakdown voltage for 30/70% CF_3I/CO_2 gas mixture. Similar characteristic was also shown in Figure 7.26 which was reported by Manjunath et al. [132]. The investigation determined the U_{50} in SF_6 gas over the pressure range of 1.4 to 4.5 bar (abs.), using the lightning impulse (1.2/50) voltage for a uniform field gap and two electrodes of a Rogowski profile, with gap distances from 4 mm to 30 mm [132]. For SF_6 in gap distances of 20 and 30 mm, the measured positive breakdown voltages are higher than the breakdowns that occurred in negative impulse polarity.
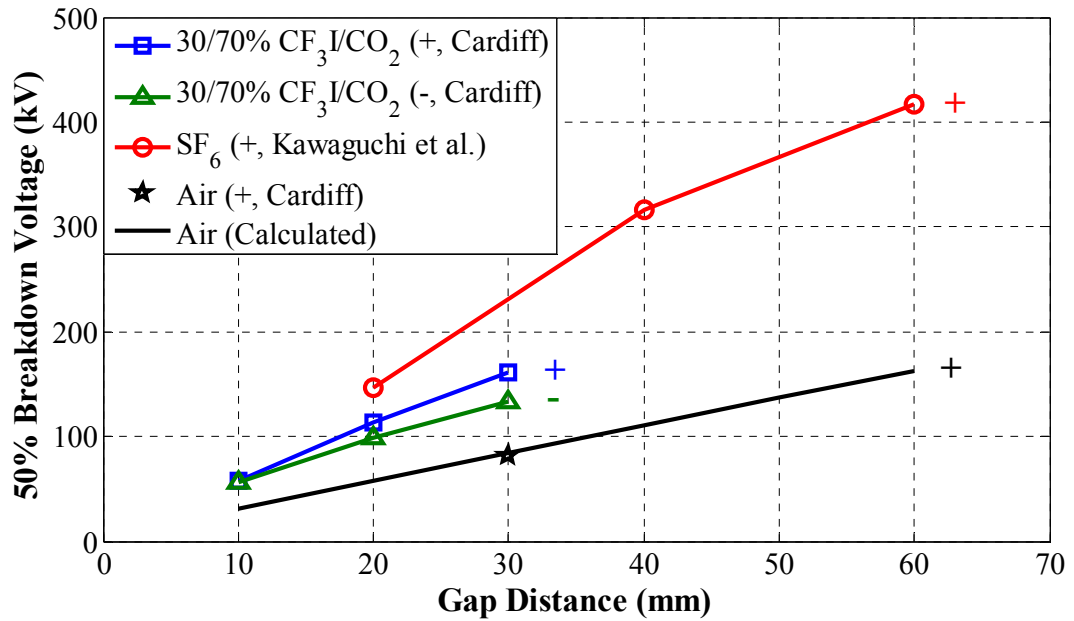
Figure 7.25: Breakdown voltage as a function of gap distance in uniform field gaps in air [8], SF₆ [131] and a 30/70% CF₃I/CO₂ gas mixture [73], at pressure of 1 bar (abs.) and using lightning impulse.
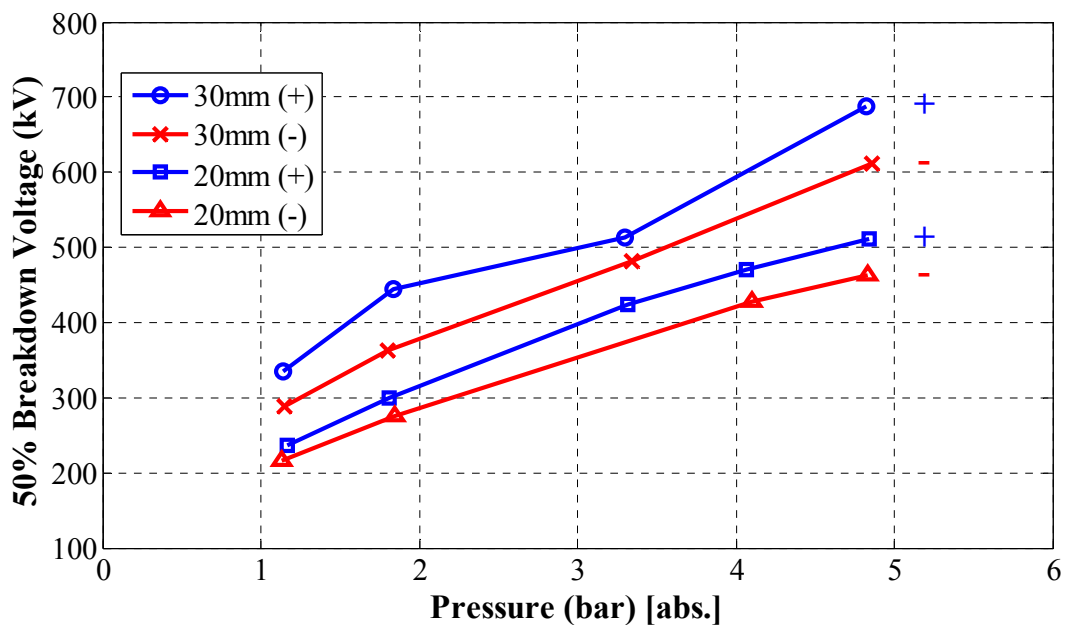
Figure 7.26: Breakdown voltage as a function of pressure in uniform field gaps, tested using SF₆ gas, for 20 and 30 mm, at pressure range from 1 to 5 bar (abs.) and for both lightning impulse polarities [132].

In uniform or quasi-uniform field gaps, the V-t characteristics show a clearly defined trend. For longer gap spacing, as the overvoltage level increases, the breakdown time decreases, which results in a steep rising slope below the 2 μs region. The time to breakdown, however, is less sensitive to the increase in the overvoltage level for non-uniform field gaps. There is a greater variation in the V-t results and, normally, the data will fall into a dispersion band as shown in Figure 2.16 [74]. The generic V-t characteristics trends for uniform and non-uniform gaps can be seen in Figure 7.27, where the results for a rod-plane show greater dispersion.
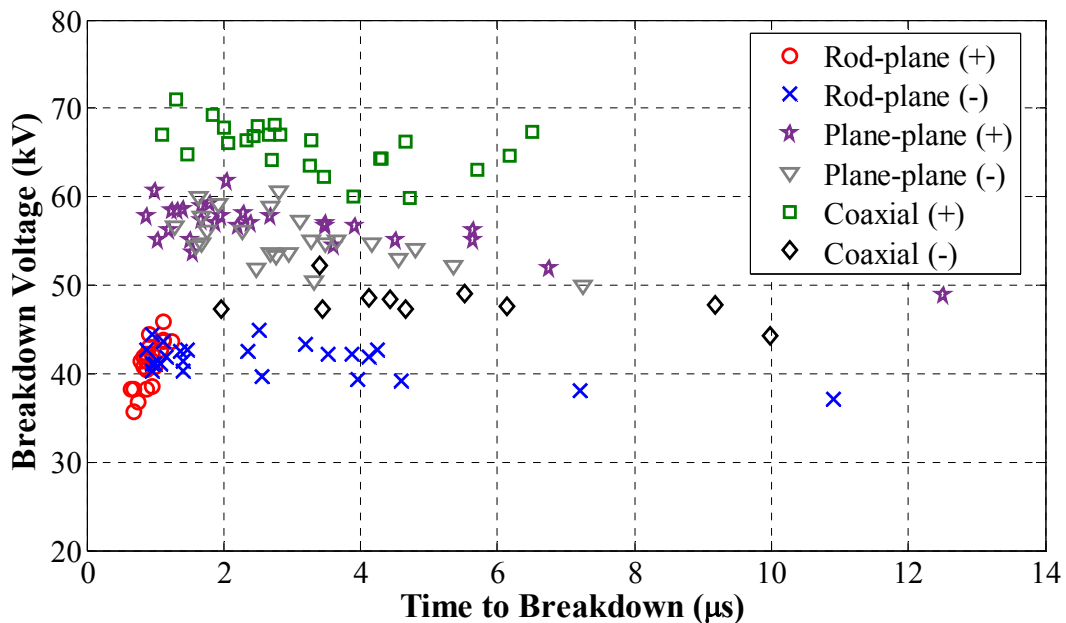
Figure 7.27: V-t characteristics in rod-plane, plane-plane and coaxial (10/30 mm) configurations, tested for a 30/70% CF₃I/CO₂ gas mixture, for 10 mm gap, at pressure of 1 bar (abs.) and for both lightning impulse polarities.

7.5.2   Breakdown Field Strength of Uniform Gap

The conditions for the measured breakdown results for 30/70% CF_3I/CO_2 [73], SF_6 [131], [132] and air [8] were converted into the product of pressure and gap distance, pd, as shown in Figure 7.28. A linear regression line can be fitted onto the scattered data of U_{50} as a function of pd.
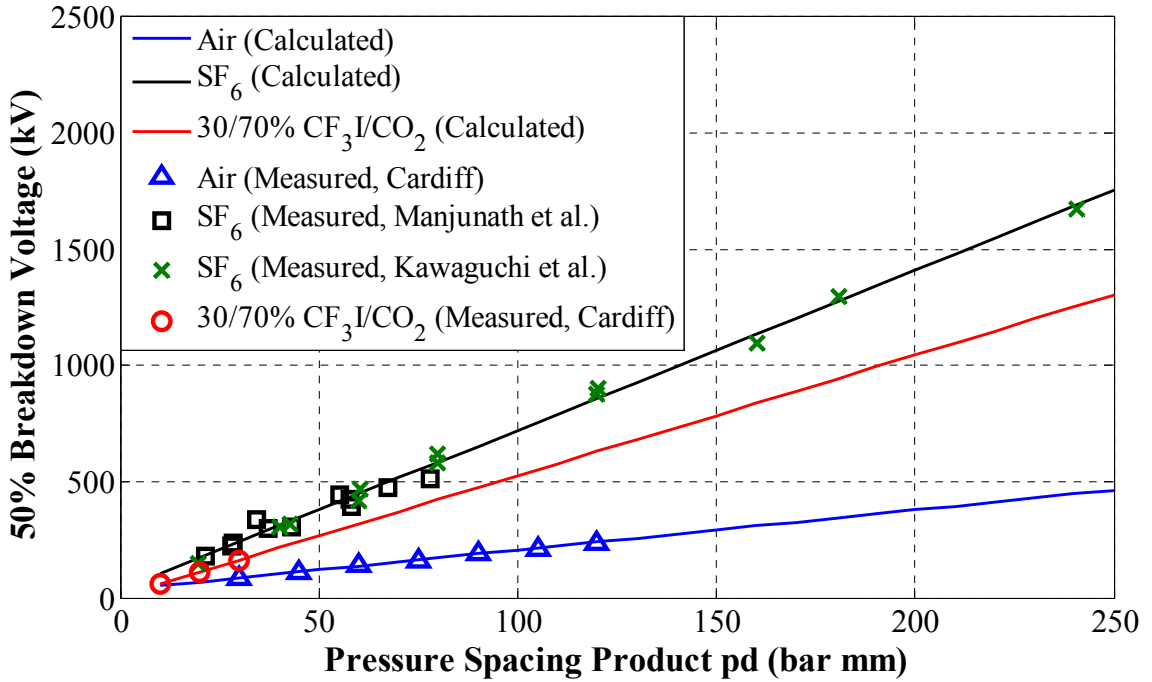
Figure 7.28: Measured and calculated U₅₀ as a function of pd in uniform field gaps, tested for air [8], SF₆ [131], [132] and a 30/70% CF₃I/CO₂ gas mixture [73] and for positive lightning impulse polarity.

The breakdown field strength for a gas such as SF_6 and air, or a 30/70% CF_3I/CO_2 gas mixture, can be obtained in uniform field gaps using (7.2) [74].

$$\frac{E_b}{p} = \left(\frac{E}{p}\right)_{crit} + \frac{K}{k(pd)}\left[\frac{kV}{mm}\right] \tag{7.2}$$

For 30/70% CF_3I/CO_2 gas mixture, the $(E/p)_{crit}$ = 5.53 kV/mm/bar, k = 23.9 kV^{-1}, which is the primary ionization coefficient, and K = 18 for the streamer mechanism. The $(E/p)_{crit}$ and k values are obtained using the BOLSIG+ software for when $(\alpha - \eta) = 0$ for each gas or gas mixture. Substituting those numbers into (7.2), the breakdown field strength can be re-written for gas pressure and gap distance as (7.3).

$$\frac{E_b}{p} = 5.53 + \frac{0.75}{d}\left[\frac{kV}{mm}\right] \tag{7.3}$$

Based on Equation (7.3), the critical breakdown field strengths in uniform field gaps are shown in Figure 7.29 for 30/70% CF_3I/CO_2, SF_6 and air. It can be seen from the figure

that the critical breakdown field strength for SF₆ is approximately three times that of air, which is consistent with the reports from the literature. There is good agreement between the measured and calculated results, as can be seen in Figure 7.28 and Figure 7.29.
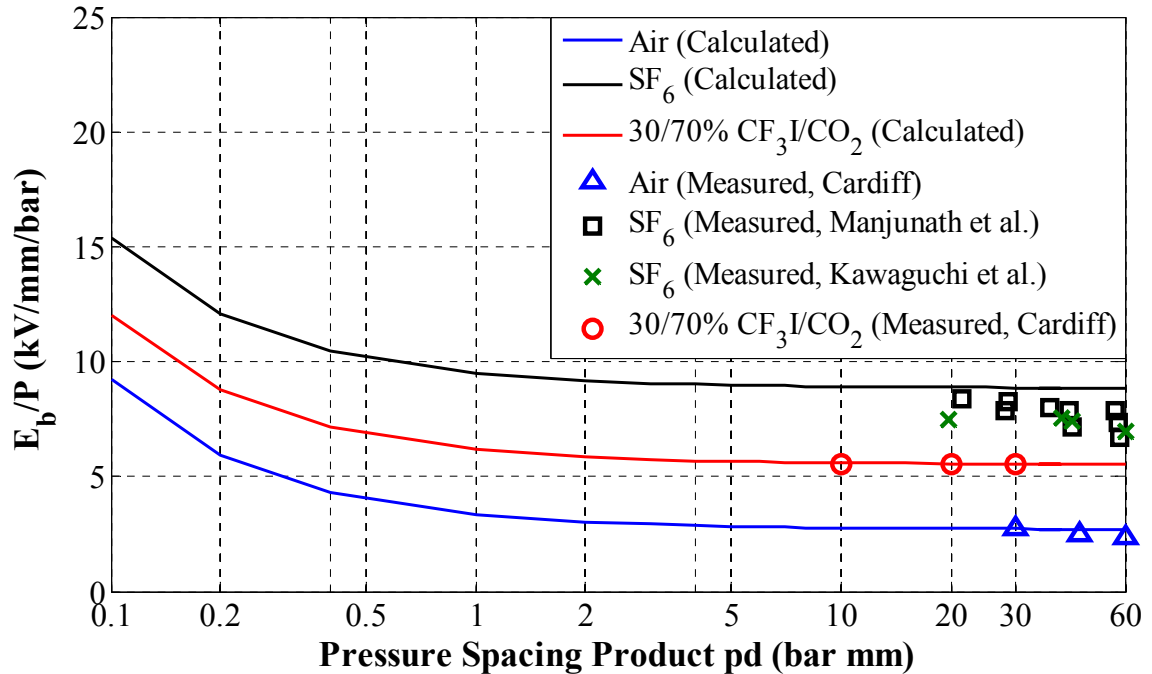
Figure 7.29: Breakdown field strength in uniform gaps for air [8], SF₆ [131], [132] and a 30/70% CF₃I/CO₂ gas mixture [73] for both calculated and measured data and for positive lightning impulse polarity.

For a uniform field gap, (7.3) can be converted to (7.4) for calculating Paschen dependent breakdown voltages. However, Equation (7.4) cannot be used for calculating the breakdown voltage at a lower pd, which is the left-hand side of a Paschen curve.

$$U_b = 0.75 + 5.53(pd)\,[kV] \tag{7.4}$$

7.6   Conclusion

This chapter has investigated the breakdown characteristics of a 30/70% CF₃I/CO₂ gas mixture in non-uniform and uniform field gaps, which were represented by a rod-plane and a plane-plane electrode configuration respectively. For non-uniform field gaps, a

comparative study was carried out between a standard lightning impulse waveform and a steep-front square impulse voltage waveform. In terms of the breakdown characteristics, the measured U_{50} were plotted as a function of the product of pressure and gap distance. The results were compared to SF_6 and air for similar test electrodes performed under similar test conditions and the breakdown strength of 30/70% CF_3I/CO_2 gas mixture is two times higher than air at pd value of 30 bar·mm. This is promising as CF_3I is only used in small proportion of the total gas mixture. Another characteristic which was investigated is the V-t, which is mainly used for establishing the breakdown strength of the insulation medium and for the design of the protection level against overvoltage. From the obtained results, two different patterns can be observed: (i) flat V-t curves and (ii) V-t curves rising steeply in the short-time region. V-t characteristics may vary depending on the field uniformity of the test gaps; for a non-uniform gap, there will be a much larger dispersion in the V-t results and, hence, a dispersion band is used to define the characteristics. The time to breakdown of non-uniform field gaps is also less dependent on the rise of the applied voltage in comparison to uniform field gaps. This is one of the reasons why quasi-uniform field gaps, like sphere-sphere electrodes, are often used in devices protecting against overvoltage in power systems.

By-product analysis was carried out to determine the elements on the surface of the plane electrode after the experiment. This confirms the build-up of iodine elements after a succession of breakdown events. A more systematic method needs to be devised to determine the impact of iodine contents on the performance of CF_3I gas mixture.

8 CONCLUSION AND FUTURE WORK

8.1   General Conclusions

In this thesis, research investigations were carried out on CF_3I gas mixtures to evaluate the feasibility of using a CF_3I gas mixture as an alternative to SF_6 in GIL applications, particularly for 400 kV rated GIL. Researchers have spent years trying to find an alternative insulation medium to replace SF_6 in high-voltage gas-insulated equipment. There are gas candidates that have a much higher dielectric strength than SF_6; however, they all possess some negative characteristics, such as a high boiling point, high GWP, harmful by-products or voltage-withstand limitations. Due to the high costs of building a full-scale 400 kV GIL system, a reduced-scale coaxial prototype was fabricated with a similar electric field distribution to a full-scale GIL system. The coaxial test system was then incorporated into a pressure vessel integrated with a control/measurement system, and a gas recovery unit, which made it possible to recycle the tested gas mixtures for further use. To investigate the feasibility of CF_3I gas and its mixtures, investigations were carried out on the gas analysis of CF_3I, which was to evaluate the insulation strength and the boiling point of each CF_3I gas mixture, and the breakdown characteristics of CF_3I gas mixtures, which were obtained through large numbers of breakdown tests using various electrode configurations.

Previous investigations into CF_3I gas and its mixtures were described in Chapter 2. The review highlights the need for a greater understanding of CF_3I gas mixtures before full deployment in gas-insulated equipment. CF_3I and SF_6 share many similar properties

because both gases are chemically inert and nonflammable. A review of the by-products of CF_3I suggests that it may not be suitable for a GIS application where a large number of switching/interruption operations are required. The literature also indicates that CF_3I has a better breakdown strength than SF_6 in a uniform electric field, which may be promising in GIL applications, since they use a quasi-uniform electric field. There is a gap in the research, however, in terms of coaxial cylindrical configurations for CF_3I or other alternative gases. This may be because GIS applications are more widely deployed in industry, and the switch contact has a non-uniform electric field distribution, in which CF_3I has a much lower breakdown strength when compared to SF_6.

Preliminary tests were conducted on a trial coaxial prototype and the results shown evidences of breakdown occurrences near the edge of the enclosure as a result of end effects. Based on the findings, modifications were made to the initial design and a reduced-scale coaxial GIL test system was then fabricated. Using the coaxial test system, investigations were carried out on the breakdown characteristics of CF_3I/CO_2 and CF_3I/N_2 gas mixtures in terms of mixture content, gas pressure, gap distance and impulse polarity. From the obtained results, five observations can be made: (i) higher CF_3I content results in a higher breakdown voltage, (ii) the breakdown voltage increases with increasing pressure, (iii) highest breakdown voltage was achieved for coaxial geometry with $\ln(R_b/R_a)$ quantity closest to unity, (iv) the breakdown voltages obtained for positive impulse were higher than their equivalent for negative impulse, and, (v) the breakdown voltages for CF_3I/CO_2 gas mixtures were comparably higher than CF_3I/N_2 gas mixtures equivalent, especially at higher pressures. The first three observations were supported by reports in the literature, described in Chapter 6. The breakdown voltage for positive polarity is higher than negative polarity, as was reported for N_2 and SF_6 gases in the

literature for coaxial configuration. However, it is unexpected that the breakdown voltage in CF_3I/CO_2 gas mixtures are higher than their CF_3I/N_2 equivalent despite CF_3I/N_2 gas mixtures having comparably higher $(E/p)_{crit}$ values. The breakdown results were converted into pressure-reduced maximum breakdown field strength $(E_{max}/p)_B$ and compared with the SF_6 results obtained on coaxial systems with a similar geometric ratio, as was found in the literature. It was demonstrated that for a 30/70% CF_3I gas mixture, the $(E_{max}/p)_B$ value under 4 bar (abs.) pressure is around 80% that of SF_6. Thus, it can be inferred that CF_3I gas and its mixtures have a promising insulation capability, and may be a feasible alternative to SF_6 in a GIL system.

At low pressures (1−3 bar), the breakdown trend appears to increase linearly and towards 4 bar, and the trend appears to saturate, as was reported for SF_6 gas. It is stated in the literature that leader breakdown can occur at lower voltage than streamer breakdown, which suggests that at higher pressures, the breakdown occurrences are likely to be leader discharge. To evaluate this further, a two-stage streamer and leader breakdown model was developed based on the positive breakdown data in coaxial geometry. The breakdown model introduced criteria such as leader channel extent, C_L, and leader field, E_L, which were deduced from the measured breakdown voltage U_{50}. This breakdown model cannot be used to predict the breakdown results of larger coaxial test systems without first determining the general validity of the value of the leader field E_L, which was obtained from the breakdown tests. From which, the ratio of the E_L in the leader channel to the critical field E_{crit} can be represented as ratio K. Based on the evaluation from the streamer/leader breakdown model, the experimental data indicated the following:

- At lower pressures, streamer breakdown occurs at a voltage given by $E_{crit} \cdot (R_b − R_a)$.

- At higher pressures, leader breakdown occurs at a voltage given by $K \cdot E_{crit} \cdot (R_b - R_a)$.

- At intermediate pressures, the breakdown voltage lies between these limits, and will be dependent on the criteria that are necessary for streamer to leader transition within the inter-electrode gap in coaxial geometry.

- A comparison of ratio K as a function of pressure shown that, for the available data, K is almost independent of the insulation medium, gas pressure and, more importantly, the size of the coaxial geometry, provided that the geometric ratio remains the same.

Further experimental work and analysis are required to find out the behaviour of ratio K at high gas pressures for CF_3I gas mixtures. In order to predict the breakdown voltage, the criterion for the creation of the leader channel needs to be determined. This allows the calculation of E_L which can be used to obtain the estimated breakdown voltage without recourse to experiment.

The breakdown characteristics of a 30/70% CF_3I/CO_2 gas mixture in non-uniform field gaps were compared for (i) a lightning impulse waveform (1.2/50) and (ii) a steep-front square impulse voltage waveform (rise time of 16 ns). Breakdown tests using lightning impulse and steep-front square impulse revealed that the measured U_{50} values obtained at a longer gap distance for a steep-front square impulse are comparatively higher than the lightning impulse equivalents. This may have been caused by the significant difference in the rise times of the voltage generated by the two sources. The results obtained for the V-t characteristics show that, for the lightning impulse, there is less dispersion in time to breakdown. At higher gas pressures, the characteristics indicate a longer average

breakdown time for the lightning impulse in comparison to the steep-front square impulse. The results show that the V-t characteristic of a 30/70% CF_3I/CO_2 gas mixture changes depending on the gap spacing and the gas pressure.

Two types of gas analysis were conducted on CF_3I gas mixtures: (a) the effective ionisation coefficients of different gases and gas mixtures were computed using BOLSIG+, which was used to calculate the gas parameters, such as the effective ionisation coefficient, $(\alpha - \eta)$ for different gases or gas mixtures. The corresponding E/p value at $(\alpha - \eta) = 0$ gave an indication of the critical reduced field strength $(E/p)_{crit}$ of each gas or gas mixture. The obtained $(E/p)_{crit}$ values were used in breakdown analysis in uniform field geometry and breakdown modelling in coaxial geometry. In uniform field gaps, the calculated data of air, SF_6 and 30/70% CF_3I/CO_2 gas mixture were in good agreement with the measured data in the literature up to a pd value of 250 bar·mm. The $(E/p)_{crit}$ values were also used in the breakdown model for CF_3I data in coaxial geometry. As $(E/p)_{crit}$ is specific to each CF_3I gas mixture, the calculated value for ratio K is then independent of gas mixtures, (b) A second gas analysis was conducted to examine the boiling point of CF_3I/CO_2 and CF_3I/N_2 gas mixtures. The measured results were correlated using a calculation model, and the comparison indicated a relatively small difference between the measured and the calculated results. It was observed that CF_3I/N_2 gas mixtures have lower boiling points than their CF_3I/CO_2 equivalents. At high temperatures, higher pressures would be required for the gas to liquefy. Conversely, lower pressures were recorded for tests carried out at lower temperatures for CF_3I gas mixtures. From the results, it can be seen that CF_3I/N_2 gas mixtures have comparably lower boiling points than their equivalents in CF_3I/CO_2 gas mixtures. This is as expected, since N_2 has a much lower boiling point than CO_2. For the CF_3I-GIL to be used in an extremely cold

area, a heating device would be required in order to heat up the line sections should the temperature drop below a pre-determined value. At normal working temperatures, however, 20-30% CF_3I gas mixtures can be used up to the current operating pressure of GIL without the risk of liquefaction occurring.

In the SEM analysis, iodine was detected on the plane electrode after tests. It was reported for pure CF_3I gas that breakdown voltage was reduced by 11% after 1300 breakdown occurrences. The density of iodine generated for a 20-30% CF_3I gas mixture is significantly less than pure CF_3I under the same test interruption current, as was reported in the literature. Considering the significantly less number of discharges per experiment and less anticipated iodine by-products in gas mixtures, therefore, it can be assumed that the effect of iodine deposition on the measured results of CF_3I gas mixtures is minimal.

8.2   Future Work

The research work of this thesis has shown the potential of using CF_3I/CO_2 and CF_3I/N_2 gas mixtures in GIL applications. The next step of this research is to construct a full-scale 400 kV GIL demonstrator. Extensive testing and optimisation of this demonstrator system will prove whether CF_3I gas and its mixtures can be used in fully practical GIL systems. This section will discuss three potential project ideas for developing an environmentally friendly GIL using a CF_3I gas mixture.

8.2.1   400 kV GIL Demonstrator

The only way of verifying the feasibility of CF_3I gas mixtures is to carry out high-voltage testing directly in a full-scale GIL demonstrator. Gas-insulated equipment includes line sections, bushings, suitable terminations and a range of fitting assemblies. Direct

breakdown testing would be an inappropriate investigation method since the expensive demonstrator system would sustain significant damage. Instead, ultra-high frequency (UHF) sensors should be fitted to the GIL to identify free moving particles inside the GIL enclosure. For current SF_6-GIL systems, partial-discharge measurement is used at the start of the commissioning process, until the particles are trapped by a particle trap device implemented in the GIL. CF_3I may behave differently to SF_6, however, and an extensive partial-discharge testing programme would be required to establish whether any design modifications need to be made to the current SF_6-GIL system.

8.2.2   Continued Research Work on Scaled Prototypes

To address the various points identified in this thesis that have not been fully explained, coaxial test systems with larger geometrical dimension than Prototype I & II could be manufactured. Extensive testing on the new scaled coaxial test system will provide a better indication of the breakdown characteristics of various CF_3I/CO_2 and CF_3I/N_2 gas mixtures, the polarity effect at a much larger gap spacing, and further investigation on the V-t characteristics of coaxial geometries.

It would also be useful to carry out preliminary testing on a larger coaxial test system to establish the behavioural trends of CF_3I in comparison to SF_6 used under partial-discharge. Sharp protrusions in the electrodes and particles on the insulator surfaces could be engineered to further evaluate the performance of CF_3I gas mixtures. This would allow a detailed investigation to be carried out and would establish a more precise testing programme before tests are carried out that may cause significant damage to an expensive GIL demonstrator system.

8.2.3   Gas Analysis of CF_3I Gas Mixtures

The results in this thesis show that 30/70% CF_3I gas mixtures have a comparable insulation performance with SF_6 up to 4 bar (abs.). The phase equilibrium experiment indicates that 30/70% CF_3I gas mixtures can be used in GIL in most places in the UK, though, in severely cold weather, a heating device would be required to heat up the line sections. The other main concern is the inherent ability of CF_3I to produce iodine as a by-product and the potential effect to the safe operation of GIL using CF_3I gas mixtures. For example, the potential risk of flashover occurrence along the surface of insulators with significant build-up of iodine. A compatibility test could be carried out to investigate the effectiveness of various absorbents that may react with iodine to prevent the build-up of iodine deposition on the surface of insulators and metal conductor/enclosure. This could then lead to a long-term testing programme to assess the effects of the ageing phenomenon on the insulation properties of the gas and support insulators in the GIL. The monitored data obtained continuously throughout the programme will clarify any new observed phenomena or anomalies that arise when working with CF_3I in GIL applications. This can then contribute to the establishment of new gas handling and safety procedures for the industrial deployment of a CF_3I-GIL system.

The by-products reported in the literature for CF_3I were measured after breakdown events. CF_3I decomposition can also be formed by partial discharge due to the energy dissipated in each partial discharge pulse. A gas diagnostic tool for CF_3I gas and its mixtures could be developed to detect the presence of partial discharge inside the GIL demonstrator by detecting the presence of the by-products.

REFERENCES

[1]   O. Farish, M. D. Judd, B. F. Hampton and J. S. Pearson, "SF_6 Insulation Systems and their Monitoring", *in Advances in High Voltage Engineering*, edited by A. Haddad and D. Warne, London, UK: IET, ch.2, pp.38–45, 2004.

[2]   EPA, "Inventory of U.S. Greenhouse Gas Emissions and Sinks: 1990-2000", *Office of Atmospheric Programs, U.S. Environmental Protection Agency,* Washington (USA), 2002.

[3]   L. G. Christophorou and J. K. Olthoff, "Electron Interactions with CF_3I", *Journal of Physical and Chemical Reference Data*, vol.29, no.4, pp.553–569, 2000.

[4]   H. Toyota, S. Matsuoka, and K. Hidaka, "Measurement of Sparkover Voltage and Time Lag Characteristics in CF_3I-N_2 and CF_3I-Air Gas Mixtures by using Steep-Front Square Voltage", *Electrical Engineering in Japan*, vol.157, no.2, pp.1–7, 2006.

[5]   H. Koch, "Future needs of high power interconnections solved with gas-insulated transmissione lines (GIL)", *International Conference Power System Technology*, vol.3, pp.1851–1855, Kunming (China), 2002.

[6]   "Gas Insulated Transmission Lines (GIL)", *CIGRE Brochure 218*, pp.1–48, 2003.

[7]   P. Widger, "Investigation into CF_3I-CO_2 Gas Mixtures for Gas-Insulated Distribution", Ph.D. thesis, Cardiff University, UK, 2014.

[8]   M. S. Kamarudin, "Experimental Investigation of CF_3I-CO_2 Gas Mixtures on the Breakdown Characteristics in Uniform and Non-Uniform Field Configurations", Ph.D. thesis, Cardiff University, UK, 2013.

[9]   "GIL – Power transmission technology for the 245 to 550 kV range", [Online]. Available: www.siemens.de/hv-gil [Accessed: 01-Mar-2014].

[10]   J. M. Braun, N. Fujimot, G. C. Stone, S. A. Boggs, G. Addis, K. J. Diederich, A. Diessner, G. Luxa, and A. Girodet, "Long term reliability of cast epoxy insulators in gas insulated equipment", *CIGRE Session 33*, 15/33–07, Paris (France), 1990.

[11]   H. Koch, *Gas-Insulated Transmission Lines*, Chichester, UK: John Wiley & Sons, Ltd, 2012.

[12]   T. Hillers and H. Koch, "Gas insulated transmission lines for high power transmission over long distances", *International Conference Energy Management and Power Delivery*, vol.2, pp.613–618, Singapore, 1998.

[13]   R. Benato, C. Mario, and H. Koch, "High-Capability Applications of Long Gas-Insulated Lines in Structures", *IEEE Transactions on Power Delivery*, vol.22, no.1, pp.619–626, 2007.

[14] H. Koch and T. Hillers, "Second-generation gas-insulated line", *Power Engineering Journal*, vol.16, no.3, pp.111–116, 2002.

[15] E. Johnson, "When Cables Won't Do", *Living Energy*, no.6, pp.40–45, 2012.

[16] "Respecting the environment", *Alstom Grid Brochure*, pp.12–17, 2010.

[17] "Gas-insulated transmission lines (GIL) – High-power transmission technology", *Siemens AG*, Erlangen (Germany), pp.2–7, 2012.

[18] G. Schoffner, D. Kunze, and I. Smith, "Gas insulated transmission lines-successful underground bulk power transmission for more than 30 years", *8th International Conference on AC-DC Power Transmission*, vol.1, pp.271–275, London (UK), 2006.

[19] "Substations Committee GIS Subcommittee K2 Module – Gas Insulated Transmission Line (GIL) Applications", *IEEE/PES Substation Committee*. [Online]. Available: http://ewh.ieee.org/cmte/ [Accessed: 20-Mar-2010].

[20] V. Piputvat, W. Rochanapithyakorn, T. Hillers, H. Koch, S. Poehler, and G. Schoeffner, "550 kV Gas-Insulated Transmission Line for High Power Rating in Thailand", *CIGRE Session 40*, B1–107, 2004.

[21] W. Boeck, "Long-term Performance of SF_6 Insulated Systems", by Task Force 15.03.07 of Working Group 15.03 on behalf of Study Committee 15, *CIGRE Session 39*, 15–301, Paris (France), 2002.

[22] H. Koch, "Gas-insulated line (GIL) of the 2nd generation", 7th *International Conference on AC-DC Power Transmission*, pp.39–43, London (UK), 2001.

[23] H. Koch, "Experience with 2nd Generation Gas-Insulated Transmission Lines (GIL)", 8th *International Conference on Insulated Power Cables*, Versailles (France), 2003.

[24] Intergovernmental Panel on Climate Change, *Climate Change 2001: The Scientific Basis*, New York, USA:University Press, 2001.

[25] C. Neumann, "Gas-Insulated Lines Provide EHV Solution", *Transmission & Distribution World* Magazine, Issue February 2010, [Online]. Available: http://tdworld.com/underground_transmission_distribution/gas-insulated-lines-20100201/2010 [Accessed: 15-Mar-2015].

[26] "Siemens completes the world's longest and highest capacity GIL connection in China", Siemens Press, Issue October 2013, [Online]. Available: http://www.siemens.com/press/en/feature/2013/energy/2013-10-xiluodu.php [Accessed: 01-Mar-2015].

[27] "CGIT Systems Worldwide Experience List", *CGIT Technical Brouchure*, Medway (USA), 2012.

[28] A. Drews, C. Rathke, M. Siebert, D. Heinemann, L. Hofmann, B. Hühnerbein, H. Koch, D. Kunze, H.-J. Hoppensack, H. Lohrenscheit, T. Roggenberg, and F. Wendt, "Network of offshore wind farms connected by gas insulated transmission lines?", in *European Wind Energy Conference & Exhibition*, PO.260, Brussels (Belgium), 2008.

[29] L. G. Christophorou and J. K. Olthoff, "Electron Interactions with SF_6", *Journal of Physical and Chemical Reference Data,* vol.29, no.3, pp.267–330, 2000.

[30] D. Koch, "SF_6 properties, and use in MV and HV switchgear", *Schneider Electric*, cahier technique no.188, pp.3–22, 2003.

[31] B. Darwent, "Bond Dissociation Energies in Simple Molecules", *NIST*, Washington (USA), pp.1–9, 1970.

[32] Subcommittee on Iodotrifluoromethane, *Iodotrifluoromethane: Toxicity Review*, Washington, USA: The National Academies Press, 2004.

[33] S. Solomon, B. Burkholder, A. R. Ravishankara, and R. Garcia, "Ozone depletion and global warming potentials of CF_3I", *Journal of Geophysical Research*, vol.99, no.D10, pp.20929–20935, 1994.

[34] Y. Li, K. O. Patten, D. J. Wuebbles, and D. Youn, "Potential impacts of CF_3I on ozone as a replacement for CF_3Br in aircraft applications", *Atmospheric Chemistry and Physics*, vol.6, no.12, pp.4559–4568, 2006.

[35] R. G. Gann, "Suitability of CF_3I to replace Halon 1301 as the inerting agent in wing fuel tanks on the F-16 aircraft", 13th *Proceedings of Halon Options Technical Working Conference*, pp.1–13, Albuquerque (USA), 2003.

[36] S. Solomon, R. R. Garcia, and A. R. Ravishankara, "On the role of iodine in ozone depletion", *Journal of Geophysical Research*, vol.99, no.D10, pp.20491–20499, 1994.

[37] Y. Duan, M. Zhu, and L. Han, "Experimental vapor pressure data and a vapor pressure equation for trifluoroiodomethane (CF_3I)", *Fluid Phase Equilibria*, vol.121, pp.227–234, 1996.

[38] M. S. Kamarudin, L. Chen, P. Widger, K. H. Elnaddab, M. Albano, H. Griffiths, and A. Haddad, "CF_3I Gas and Its Mixtures: Potential for Electrical Insulation", *CIGRE Session 45*, D1–308, Paris (France), 2014.

[39] Y.-K. Deng and D.-M. Xiao, "The effective ionization coefficients and electron drift velocities in gas mixtures of CF_3I with N_2 and CO_2 obtained from Boltzmann equation analysis", *Chinese Physics B*, vol.22, no.3, pp.1–6 (035101), 2013.

[40] T. Takeda, S. Matsuoka, A. Kumada, and K. Hidaka, "By-product Generation through Electrical Discharge in CF_3I Gas and its Effect to Insulation Characteristics", *IEEJ Transactions on Power Energy*, vol.131, no.10, pp.859–864, 2011.

[41]   H. Katagiri, H. Kasuya, H. Mizoguchi, and S. Yanabu, "Investigation of the performance of CF_3I Gas as a Possible Substitute for SF_6", *IEEE Transactions on Dielectrics and Electrical Insulation*, vol.15, no.5, pp.1424–1429, 2008.

[42]   Y. F. Wang, M. Shih, C. H. Tsai, and P. J. Tsai, "Total toxicity equivalents emissions of SF_6, CHF_3, and CCl_2F_2 decomposed in a RF plasma environment", *Chemosphere*, vol.62, no.10, pp.1681–1688, 2006.

[43]   W. C. Mccain and J. Macko, "Toxicity Review for Iodotrifluoromethane (CF_3I)", in *Halon Options Technical Working Conference*, project no.85-8823-99, pp.242–253, Albuquerque (USA), 1999.

[44]   "CGA P-20: Standard for the Classification of Toxic Gas Mixtures", *Compressed Gas Association*, 3rd ed., 2013.

[45]   "BS ISO 10298:2010: Determination of toxicity of a gas or gas mixture", *British Standard Institutions*, 2010.

[46]   C. N. Works and T. W. Dakin, "Dielectric Breakdown of Sulfur Hexafluoride in Nonuniform Fields", *Transactions on American Institute of Electrical Enginers, Part I: Communication and Electronics*, vol.72, no.5, pp.682–689, 1953.

[47]   S. F. Philp, "Compressed Gas Insulation in the Million-Volt Range: A Comparison or SF_6 with N_2 and CO_2", *IEEE Transactions on Power Apparatus and System*, vol.82, no.66, pp.356–359, 1963.

[48]   H. C. Doepken, "Compressed-Gas Insulation in Large Coaxial Systems", *IEEE Transactions on Power Apparatus and System*, vol.PAS–88, no.4, pp.364–369, 1969.

[49]   S. Menju, H. Aoyagi, K. Takahashi, and H. Qhno, "Dielectric Breakdown of High Pressure SF_6 in Sphere and Coaxial Cylinder Gaps", *IEEE Transactions on Power Apparatus and System*, vol.PAS–93, no.5, pp.1706–1712, 1974.

[50]   M. H. Bottero, "Breakdown of a Coaxial-Cylinder Gap in SF_6 under Switching Impulse Voltages", *IEEE Transactions on Power Apparatus and System*, vol.PAS–103, no.4, pp.849–854, 1984.

[51]   N. H. Malik and A. H. Qureshi, "Breakdown Mechanisms in Sulphur-Hexafluoride", *IEEE Transactions on Electrical Insulation*, vol.EI–13, no.3, pp.135–145, 1978.

[52]   J. C. Devins, "Replacement Gases for SF_6", *IEEE Transactions on Electrical Insulation*, vol.EI–15, no.2, pp.81–86, 1980.

[53]   F. Rizk and M. Eteiba, "Impulse Breakdown Voltage-Time Curves of SF_6 and SF_6-N_2 Coaxial-Cylinder Gaps", *IEEE Transactions on Power Apparatus and System*, vol.PAS–101, no.12, pp.4460–4471, 1982.

[54] N. H. Malik and A. H. Qureshi, "Breakdown Gradients in SF_6-N_2, SF_6-Air and SF_6-CO_2 Mixtures", *IEEE Transactions on Electrical Insulation*, vol.EI–15, no.5, pp.413–418, 1980.

[55] R. S. Nema, S. V. Kulkarni, and E. Husain, "On calculation of breakdown voltages of mixtures of electron attaching gases", *IEEE Transactions on Electrical Insulation*, vol.EI–17, no.5, pp.434–440, 1982.

[56] M. Piemontesi, F. Koenig, L. Niemeyer, and C. Heitz, "Insulation performance of 10% SF_6/90% N_2 mixture", IEEE *Conference on Electrical Insulation and Dielectric Phenomena*, vol.1, pp.395–398, Austin (USA), 1999.

[57] N. H. Malik and A. H. Qureshi, "A review of electrical breakdown in mixtures of SF_6 and other gases", *IEEE Transactions on Electrical Insulation*, vol.EI–14, no.1, pp.1–13, 1979.

[58] K. P. Brand, "Dielectric strength, boiling point and toxicity of gases - different aspects of the same basic molecular properties", *IEEE Transactions on Electrical Insulation*, vol.EI-17, no.5, pp.451–456, 1982.

[59] M. Rabie and C. Franck, "Computational screening of new high voltage insulation gases with low global warming potential", *IEEE Transactions on Dielectrics and Electrical Insulation*, vol.22, no.1, pp.296–302, 2015.

[60] M. Rabie, P. Haefliger, a Chachereau, and C. M. Franck, "Obtaining electron attachment cross sections by means of linear inversion of swarm parameters", *Journal of Physics D: Applied Physics*, vol.48, no.7, pp.1–7 (075201), 2015.

[61] M. Rabie, D. Dahl, S. M. a Donald, M. Reiher, and C. Franck, "Predictors for gases of high electrical strength", *IEEE Transactions on Dielectrics and Electrical Insulation*, vol.20, no.3, pp.856–863, 2013.

[62] Y. Kieffel, A. Girodet, F. Biquez, P. Ponchon, J. Owens, M. Costello, M. Bulinski, R. V. A. N. San, and K. Werner, "SF_6 alternative development for high voltage switchgears", *CIGRE Session 45, D1–305*, Paris (France), 2014.

[63] T. Yagi, "Electrical breakdown characteristics of CF_3I gas and its gas mixtures", M.S. thesis, University of Tokyo, Japan, 2012.

[64] K. Imai, "Discharge characteristics and suitability as insulation medium of CF_3I and its mixture", M.S. thesis, University of Tokyo, Japan, 2011.

[65] T. Takeda, "Basic Study on Insulation Performance of CF_3I Gas", Ph.D. thesis, University of Tokyo, Japan, 2010.

[66] H. Toyata, "Nanosecond Range Electrical Discharge Phenomena in Insulation Gases", Ph.D. thesis, University of Tokyo, Japan, 2004.

[67] M. Taki, D. Maekawa, H. Odaka, H. Mizoguchi, and S. Yanabu, "Interruption capability of CF_3I Gas as a substitution candidate for SF_6 gas", *IEEE Transactions on Dielectrics and Electrical Insulation*, vol.14, no.2, pp.341–346, 2007.

[68] M. K. Mohd Jamil, S. Ohtsuka, M. Hikita, H. Saitoh, and M. Sakaki, "Gas by-products of CF_3I under AC partial discharge", *Journal of Electrostatics*, vol.69, no.6, pp.611–617, 2011.

[69] J. de Urquijo, A. M. Juárez, E. Basurto, and J. L. Hernández-Ávila, "Electron impact ionization and attachment, drift velocities and longitundinal diffusion in CF_3I and CF_3I-N_2 mixtures", *Journal of Physics D: Applied Physics*, vol.40, no.7, pp.2205–2209, 2007.

[70] J. de Urquijo, A. Mitrani, G. Ruíz-Vargas, and E. Basurto, "Limiting field strength and electron swarm coefficients of the CF_3I–SF_6 gas mixture", *Journal of Physics D: Applied Physics*, vol.44, no.34, pp.1–3 (342001), 2011.

[71] M. Kimura and Y. Nakamura, "Electron swarm parameters in CF_3I and a set of electron collision cross sections for the CF_3I molecule", *Journal of Physics D: Applied Physics*, vol.43, no.14, pp.1–6 (145202), 2010.

[72] S. Kawaguchi, K. Satoh, and H. Itoh, "Electron transport in CF_3I and CF_3I-N_2 mixtures", *The European Physical Journal D*, vol.68, no.4, pp. 1–6 (100), 2014.

[73] M. S. Kamarudin, A. Haddad, and S. J. Macgregor, "Experimental investigation of CF_3I-CO_2 gas mixtures under lightning impulses", *20th International Conference on Gas Discharges and their Applications*, C–4, Orleans (France), 2014.

[74] E. Kuffel, W. S. Zaengl, and J. Kuffel, *High Voltage Engineering - Fundamentals*, 2nd ed., Oxford, UK: Newnes, 2000.

[75] L. G. Christophorou, J. K. Olthoff, and D. S. Green, "Gases for Electrical Insulation and Arc Interruption: Possible Present and Future Alternatives to Pure SF_6", *NIST Technical Note 1425*, Washington (USA), pp.1–44, 1997.

[76] H. Toyota, S. Nakauchi, S. Matsuoka, and K. Hidaka, "Voltage-time Characteristics in SF_6 and CF_3I Gas within Non-uniform Electric Field", *14th International Symposium on High Voltage Engineering*, H–04, Beijing (China), pp.466–471, 2005.

[77] "IEC/BS EN 60137: Insulated Bushing for Alternating Voltages Above 1000 V", *British Standard Institutions*, 2008.

[78] "Datasheet: Miniature Linear Motion Series • L12", *Firgelli Technologies Inc.*, vol.1, no.206, pp.1–7, 2008.

[79] "Product Manual 1066 – PhidgetAdvancedServo 1-Motor", *Phidgets Inc.*, pp.1–14, 2009.

[80] S. Ohtsuka, M. Koumura, M. Cho, Y. Hashimoto, M. Nakamura, and M. Hikita, "Insulation Properties of CO_2/N_2 Gas Mixture with a Small Amount of SF_6", *9th International Symposium on Gaseous Dielectrics*, sec.5, pp.295–300, 2001.

[81] "IEC/BS EN 60060-1: High-voltage test techniques – Part 1: General definitions and test requirements", *British Standard Institutions*, 2010.

[82] T. Takeda, S. Matsuoka, A. Kumada, and K. Hidaka, "Breakdown Characteristics of CF_3I Gas in Uniform and Non-Uniform Field Gap Under Various Voltage Applications of Nanosecond Pulse to AC", *15th International Symposium on High Voltage Engineering*, T9–647, Ljubjana (Slovenia), 2007.

[83] T. Takeda, S. Matsuoka, A. Kumada, and K. Hidaka, "Sparkover and Surface Flashover Characteristics of CF_3I Gas under Application of Nanosecond Square Pulse Voltage", *16th International Symposium on High Voltage Engineering*, C–55, pp.812–817, Cape Town (South Africa), 2009.

[84] W. Hauschild and W. Mosch, "Up-and-down method", *Statistical Techniques for High-Voltage Engineering*, Reprinted. London (UK): IET, 2007.

[85] S. Chakravorti and H. Steinbigler, "Capacitive-resistive Field Calculation on HV Bushings using the Boundary-element Method", *IEEE Transactions on Dielectrics and Electrical Insulation*, vol.5, no.2, pp.237–244, 1998.

[86] "Compressed Gas Insulated Transmission Bus Systems – Proven Solutions For Power Transmission", *CGIT Westboro Inc.*, 2004.

[87] S. Obayashi, N. Takinami, and A. Miyazaki, "Application of the world's longest gas insulated transmission line (GIL)", *IEEE Power Engineering Society General Meeting*, vol.4, Toronto (Canada), 2003.

[88] H. Koch and A. Chakir, "Thermal calculations for buried gas-insulated transmission lines (GIL) and XLPE-cable", *IEEE Power Engineering Society Winter Meeting*, vol.2, pp.857–862, Columbus (USA), 2001.

[89] H. Koch, "Basic Information on Gas Insulated Transmission Lines (GIL)", *IEEE Power and Energy Society General Meeting – Conversion and Delivery of Electrical Energy in the 21st Century*, pp.1–4, Pittsburgh (USA), 2008.

[90] "Introduction to AC/DC Module", *COMSOL Module*, pp.5–45, 2012.

[91] "Dielectric properties of materials", *National Physical Laboratory*, [Online]. Available: http://www.kayelaby.npl.co.uk/general_physics/2_6/2_6_5.html [Accessed: 31-Feb-2013].

[92] E. F. D'Azevedo, "Are Bilinear Quadrilaterals Better Than Linear Triangles?", *SIAM Journal on Scientific Computing*, vol.22, no.1, pp.198–217, 2000.

[93] "Datasheet for Polypropylene", *Plastim Ltd*, p.27, 2013.

[94] C. M. Franck, D. A. Dahl, M. Rabie, P. Haefliger, and M. Koch, "An Efficient Procedure to Identify and Quantify New Molecules for Insulating Gas Mixtures", *Contributions to Plasma Physics*, vol.54, no.1, pp.3–13, 2014.

[95] X. Dong, M. Gong, J. Liu, and J. Wu, "Experimental measurement of vapor pressures and (vapor + liquid) equilibrium for {1,1,1,2-tetrafluoroethane (R134a) + propane (R290)} by a recirculation apparatus with view windows", *Journal of Chemical Thermodynamics*, vol.43, no.3, pp.505–510, 2011.

[96] G. J. M. Hagelaar and L. C. Pitchford, "Solving the Boltzmann equation to obtain electron transport coefficients and rate coefficients for fluid models", *Plasma Sources Science and Technology*, vol.14, no.4, pp.722–733, 2005.

[97] D. Tanaka, A. Kumada, and K. Hidaka, "Numerical Simulation of Streamer Development in CF_3I-N_2 Gas Mixtures", *17th International Symposium on High Voltage Engineering*, A–14, Hannover (Germany), 2011.

[98] X. Dong, M. Gong, J. Shen, and J. Wu, "Experimental measurement of vapor–liquid equilibrium for (trans-1,3,3,3-tetrafluoropropene (R1234ze(E))+propane (R290))", *International Journal of Refrigeration*, vol.34, no.5, pp.1238–1243, 2011.

[99] X. Dong, M. Gong, and J. Wu, "Phase equilibrium for the binary azeotropic mixture of trifluoroiodomethane (R13I1)+1,1,2,2-tetrafluoroethane (R134) at temperatures from 258.150 to 283.150K", *Fluid Phase Equilibria*, vol.315, pp.35–39, 2012.

[100] H. Guo, M. Gong, X. Dong, and J. Wu, "(Vapour+liquid) equilibrium data for the binary system of {trifluoroiodomethane (R13I1)+trans-1, 3, 3, 3-tetrafluoropropene (R1234ze (E))} at various temperatures from (258.150 to 298.150)K", *The Journal of Chemical Thermodynamics*, vol.47, pp.397–401, 2012.

[101] H. Guo, M. Gong, X. Dong, and J. Wu, "Measurements of (vapour + liquid) equilibrium data for {trifluoroiodomethane (R13I1) + isobutane (R600a)} at temperatures between (263.150 and 293.150) K", *The Journal of Chemical Thermodynamics*, vol.58, pp.428–431, 2013.

[102] M. Gong, H. Guo, X. Dong, H. Li, and J. Wu, "(Vapor+liquid) phase equilibrium measurements for {trifluoroiodomethane (R13I1)+propane (R290)} from T=(258.150 to 283.150)K", *The Journal of Chemical Thermodynamics*, vol.79, pp.167–170, 2014.

[103] D. Peng and D. B. Robinson, "A New Two-Constant Equation of State", *Industrial & Engineering Chemistry Fundammentals*, vol.15, no.1, pp.59–64, 1976.

[104] "IEC/BS EN 62271-203: High-voltage switchgear and controlgear – Part 203: Gas-insulated metal-enclosed switchgear for rated voltages above 52 kV", *British Standard Institutions*, 2012.

[105] L. A. Weber, "Some vapor pressure and P, V, T data on nitrogen in the range 65 to 140 K", *The Journal of Chemical Thermodynamics*, vol.2, no.6, pp.839–846, 1970.

[106] W. Duschek, R. Kleinrahm, and W. Wagner, "Measurement and correlation of the (pressure, density, temperature) relation of carbon dioxide I. The homogeneous gas and liquid regions in the temperature range from 217 K to 340 K at pressures up to 9 MPa", *The Journal of Chemical Thermodynamics*, vol.22, no.9, pp.827–840, 1990.

[107] W. Duschek, R. Kleinrahm, and W. Wagner, "Measurement and correlation of the (pressure, density, temperature) relation of carbon dioxide II. Saturated-liquid and saturated-vapour densities and the vapour pressure along the entire coexistence curve", *The Journal of Chemical Thermodynamics*, vol.22, no.9, pp.841–864, 1990.

[108] "Sulphur Hexafluoride", *Solvay Special Chemicals Technical Brouchure*, pp.5–51, 2014.

[109] R. Waters, "Flashover and PD Modelling in CF_3I Mixtures", *Internal Report*, Advanced High Voltage Engineering Research Centre, Cardiff University, 2015.

[110] H. Anis and K. D. Srivastava, "Particle-Initiated Breakdowns in Compressed Gas Insulation under Time-varying Voltages", *IEEE Transactions on Power Apparatus and System*, vol.PAS–100, no.8, pp.3694–3702, 1981.

[111] A. H. Cookson and O. Farish, "Particle-initiated Breakdown between Coaxial Electrodes in Compressed SF_6", *IEEE Transactions on Power Apparatus and System*, vol.PAS–92, no.3, pp.871–876, 1973.

[112] O. Farish, O. E. Ibrahim, and B. H. Crichton, "Effect of electrode surface roughness on breakdown in nitrogen/SF_6 mixtures", *Proceedings of the Institution of Electrical Engineers*, vol.123, no.10, pp.1047–1050, 1976.

[113] C. M. Cooke, "Ionization, Electrode Surfaces and Discharges in SF_6 at Extra-High-Voltages", *IEEE Transactions on Power Apparatus and System*, vol.PAS–94, no.5, pp.1518–1523, 1975.

[114] A. Pedersen, "The Effect of Surface Roughness on Breakdown in SF_6", *IEEE Transactions on Power Apparatus and System*, vol.PAS–94, no.5, pp.1749–1754, 1975.

[115] S. Sangkassad, "Dielectric Strength of Compressed SF_6 in Nonuniform Fields", Ph.D. thesis, ETH Zurich, Switzerland, 1976.

[116] P. R. Howard, "Insulation Properties of Compressed Electronegative Gases", *Proceedings of the IEE Part A: Power Engineering*, vol.104, no.14, pp.123–137, 1957.

[117] T. Nitta, N. Yamada, and Y. Fujiwara, "Area Effect of Electrical Breakdown in Compressed SF$_6$", *IEEE Transactions on Power Apparatus and System*, vol.PAS–93, no.2, pp.623–629, 1973.

[118] E. H. Cohen, "The Electric Strength of Highly Compressed Gases", *Proceedings of the IEE Part A: Power Engineering*, vol.103, no.7, pp.57–68, 1956.

[119] T. Shioiri, T. Kamikawji, E. Kaneko, M. Homma, H. Takahashi, and I. Ohshima, "Influence of Electrode Area on the Conditioning Effect in Vacuum", *IEEE Transactions on Dielectrics and Electrical Insulation*, vol.2, no.2, pp.317–320, 1995.

[120] K. Kato, Y. Fukuoka, H. Saitoh, M. Sakaki, and H. Okubo, "Effect of Electrode Surface Roughness on Breakdown Conditioning under Non-uniform Electric Field in Vacuum", *IEEE Transactions on Dielectrics and Electrical Insulation*, vol.14, no.3, pp.538–543, 2006.

[121] T. Yasuoka, T. Kato, K. Kato, and H. Okubo, "Discussion of Electrode Conditioning Mechanism Based on Pre-breakdown Current under Nonuniform Electric Field in Vacuum", *23rd International Symposium on Discharges and Electrical Insulation in Vacuum*, Bucharest (Romania), 2008.

[122] N. Wiegart, "A Model for the Production of Initial Electrons by Detachment of SF$_6$-Ions", *IEEE Transactions on Electrical Insulation*, vol.EI–20, no.3, pp.587–594, 1985.

[123] N. Wiegart, L. Niemeyer, F. Pinnekamp, W. Boeck, J. Kindersberger, R. Morrow, W. Zaengl, M. Zwicky, I. Gallimberti, and S. A. Boggs, "Inhomogeneous field breakdown in GIS – the prediction of breakdown probabilities and voltages. II. Ion density and statistical time lag", *IEEE Transactions on Power Delivery*, vol.3, no.3, pp.931–938, 1988.

[124] N. Wiegart, L. Niemeyer, F. Pinnekamp, W. Boeck, J. Kindersberger, R. Morrow, W. Zaengl, M. Zwicky, I. Gallimberti, and S. A. Boggs, "Inhomogeneous field breakdown in GIS – the prediction of breakdown probabilities and voltages. III. Discharge development in SF$_6$ and computer model of breakdown", *IEEE Transactions on Power Delivery*, vol.3, no.3, pp.939–946, 1988.

[125] N. Wiegart, L. Niemeyer, J. Kindersberger, R. Morrow, W. Zaengl, I. Gallimberti, and S. A. Boggs, "Inhomogeneous field breakdown in GIS – the prediction of breakdown probabilities and voltages. I. Overview of a theory for inhomogeneous field breakdown in SF$_6$", *IEEE Transactions on Power Delivery*, vol.3, no.3, pp.923–930, 1988.

[126] L. Niemeyer, L. Ullrich, and N. Wiegart, "The Mechanism of Leader Breakdown in Electronegative Gases", *IEEE Transactions on Electrical Insulation*, vol.24, no.2, pp.309–324, 1989.

[127] M. Seeger, L. Niemeyer, and M. Bujotzek, "Partial discharges and breakdown at protrusions in uniform background fields in SF_6", *Journal of Physics D: Applied Physics*, vol.41, no.18, pp.1–14 (185204), 2008.

[128] "Axio Imager 2 – Progress Meets Performance", *Carl Zeiss*, pp.2–25, 2009.

[129] H. Kasuya, Y. Kawamura, H. Mizoguchi, Y. Nakamura, and S. Yanabu, "Interruption Capability and Decomposed Gas Density of CF_3I as a Substitute for SF_6 Gas", *IEEE Transactions on Dielectrics and Electrical Insulation*, vol.17, no.4, pp.1196–1203, 2010.

[130] T. Takuma, "Discharge Characteristics of Gaseous Dielectrics", *IEEE Transactions on Electrical Insulation*, vol.EI–21, no.6, pp.855–867, 1986.

[131] Y. Kawaguchi, K. Sakata, and S. Menju, "Effect of a Grounded Cylinder Enclosure on the Breakdown Gradient of Rod Gaps in SF_6", *IEEE Transactions on Power Apparatus and System*, vol.PAS–90, no.3, pp.1079–1085, 1970.

[132] B. S. Manjunath, K. Dwarakanath, K. S. Arunachala Sastry, and K. N. Ravi, "Uniform field breakdown in SF_6 gas at high pressures under lightning and switching surge voltages", IEEE *Conference on Electrical Insulation and Dielectric Phenomena*, pp.329–333, Ottawa (Canada), 1988.

APPENDIX A

Gas	Breakdown Strength E_r	Boiling point (1bar) T_b / K	Ion Potential ε_i / eV	Polarizability α / 10^{-30} m^3	Toxicity mac / ppm-Vol.
Ne	0.006	27.25	21.564	0.395	nontoxic
Ar	0.07	87.45	15.759	1.64	nontoxic
H_2	0.18	20.35	15.427	0.808	nontoxic
O_2	0.33	90.19	12.07	1.6	hyperoxia
N_2	0.38	77.35	15.576	1.76	nontoxic
N_2O	0.47	184.7	12.922	2.92	slightly narcotic
CO	0.4	81.68	14.013	1.95	50
CO_2	0.31	194.7	13.786	2.59	5000
SO_2	1	263.2	12.34	3.78	5
SF_6	1	209.4	15.75	4.48	1000
CH_4	0.43	109.2	12.8	2.56	>1000 (nontoxic)
CH_3Cl	0.49	249	11.24	4.56	100
CH_3Br	0.65	276.7	10.535	5.65	20
CH_3I	1.15	315.6	9.538	7.67	5
CH_2F_2	0.3	221.6	12.6	2.75	slightly toxic
CH_2Cl_2	0.73	313.2	12.12	6.48	500
$CHCl_3$	1.67	334.9	11.42	8.23	50
$CHClF_2$	0.42	232.4	12.45	4.61	1000
$CHCl_2F$	0.99	282.2	12.39	6.45	1000
CF_4	0.41	144.2	14.36	2.82	>10 (medium toxic)
CCl_2F_2	1.01	243.4	12.31	6.76	1000
CCl_3F	1.72	297	11.77	8.36	1000
$CBrF_3$	0.75	214.2	11.89	5.73	1000
CH_3CN	0.8	354.8	12.21	4.5	40
C_2F_6	0.8	194.2	14.6	4.6	(nontoxic)
1,1,1-$C_2Cl_3F_3$	2.49	319	11.78	10.6	1000
1,1,2-$C_2Cl_3F_3$	2.3	320.9	11.99	10.6	1000
CF_2CClF	0.69	244.8	10.4	6.4	2
C_2H_2	0.42	189.2	11.4	4.26	5000
C_3F_8	0.94	236.5	17.1	6.96	na
CH_2CHCF_3	0.8	248.2	10.9	6.38	na
C_3F_6	0.97	243.8	11.11	6.56	0.8
c-C_4F_8	1.27	269.2	12.1	8.24	na
CF_3CCCF_3	2.22	248.6	12.3	7.57	acute inhal. toxic
c-C_6F_{12}	2.35	na	13.2	12.36	na
CCl_4	2.36	349.7	11.47	10.2	10
1,1-$C_2Cl_2H_4$	1.01	330.4	11.12	8.4	na

APPENDIX B